Dual modification of predator and prey cell shapes during predation by *Bdellovibrio bacteriovorus*

Thesis submitted to the University of Nottingham for the degree of Doctor of Philosophy

Emma Jane Banks M.Res.

February 2022

Abstract

Bdellovibrio bacteriovorus HD100 is a vibrioid-shaped Gram-negative bacterium with an unusual predatory lifestyle. *B. bacteriovorus* attaches to, invades, and then replicates within Gram-negative prey bacteria including multi-drug resistant bacterial pathogens. Due to an extensive range of Gram-negative prey targets which are also incapable of developing genetic resistance to the invading predator, *B. bacteriovorus* presents itself as a potential novel antibacterial therapeutic within the worsening global antibiotic resistance crisis.

The predatory lifecycle of *B. bacteriovorus* involves numerous different effector proteins including peptidoglycan (PG)-modifying enzymes which remodel the PG cell walls of both predators and prey. Following attachment to prey via type IV pili, *B. bacteriovorus* secretes hydrolytic PG enzymes into the prey periplasm to sculpt an entry 'porthole' within the prey wall. The predator cell also secretes DD-endopeptidase (DacB) PG enzymes into the prey periplasm which cut crosslinks in the prey PG, causing it to become more malleable. This results in the transformation of rod-shaped prey cells into spherical prey bdelloplasts. *B. bacteriovorus* enters its prey through the porthole, reseals it, and then consumes the DNA and protein nutrients of the prey, elongating as a filament within the inner periplasmic compartment. When prey nutrients are exhausted, the predator filament synchronously divides to give variable numbers of daughter cells which lyse the prey cell and escape to seek out new prey.

During my PhD I worked on two projects, characterising new proteins that are involved in the modification of prey cell shape and the generation of vibrioid-shaped *B. bacteriovorus* predator cells. I discovered that the lytic transglycosylase Bd3285 is naturally secreted into the prey bdelloplast by *B. bacteriovorus* during predation and, when heterologously-expressed in *Escherichia coli*, localises to the septum of dividing *E. coli* cells. In the absence of *bd3285*, prey bdelloplasts form three different shapes: spheres, rods, and 'dumbbells', in comparison to wild-type

bdelloplasts which are all spherical. Dumbbell-shaped prey bdelloplasts are derived from *E. coli* prey which were in the process of dividing at the moment of invasion by *B. bacteriovorus*. Pre-labelling of *E. coli* prey PG with a fluorescent D-amino acid dye revealed that the dumbbell bdelloplasts observed in the Δ*bd3285* mutant contained an intact PG septum, indicating that Bd3285 cleaves septal PG. It is probable that Bd3285 cutting of septal PG is required to allow DD-endopeptidase DacB access to PG crosslinks at the mid-cell and facilitate rounding of prey bdelloplasts. Bd3285 is a homologue of the *E. coli* lytic transglycosylase MltA. There are two other MltA homologues in *B. bacteriovorus* strain HD100: Bd0599 and Bd0519. During my PhD I characterised Bd0599, showing that although it is also secreted into the prey bdelloplast and can localise to the *E. coli* septum, it is dispensable for prey shape transformation as all prey bdelloplasts were spherical in shape.

In the second part of my thesis, I followed up my work from my short MRes project in which I identified the cell curvature-determinant of *B. bacteriovorus* strain HD100. In my PhD, I characterised this shape determinant, Bd1075, further, discovering that it is broadly conserved across *Bdellovibrio* strains, including a rod-shaped strain: strain 109J. Through cross-complementation experiments and analysis of PG wall composition (with collaborators), I discovered that a truncation of 171 bp within the $bd1075_{109J}$ gene renders strain 109J unable to generate cell curvature. Collaborating with Prof Waldemar Vollmer's group at Newcastle University, I determined that Bd1075 generates cell curvature by exerting LD-carboxypeptidase activity upon the *B. bacteriovorus* cell wall. My co-supervisor and collaborator Prof Andrew Lovering and his group solved the crystal structure of Bd1075, revealing novel properties unique to this shape enzyme. I also discovered that Bd1075 specifically localises to the outer convex face of *B. bacteriovorus* cells and that the protein is targeted by its cryptic nuclear transport factor 2-like domain. Finally, I discovered benefits for cell curvature during *B. bacteriovorus* predation: faster invasion of curved predators into prey bacteria and

potentially more optimal growth of curved predators within spherical prey bdelloplasts.

These two studies revealed important new insights into the generation and remodelling of predator and prey cell shapes during bacterial predation by *B. bacteriovorus*.

Acknowledgements

I would firstly like to thank my primary supervisor: Professor Liz Sockett for supervising and supporting me throughout my PhD. Thank you for the opportunity to work on such a fascinating bacterium and two amazing projects. I still can't think of another PhD that I would have rather done.

Thank you to Professor Andrew Lovering for co-supervising me during my PhD and your amazing insights into the world of proteins. Thank you also to Amber Wilson and Ian Cadby in Andy's group at the University of Birmingham for their work in purifying Bd1075 and particular thanks go out to Mauricio Valdivia-Delgado for solving the crystal structure of a somewhat difficult protein! Thank you to Professor Waldemar Vollmer and Dr Jacob Biboy at Newcastle University for kindly analysing peptidoglycan for me. Together, these two collaborations were vital for elucidating the function of Bd1075. Thank you! Thank you also to my MSci project student Samuel Mason who I supervised for 3 months and christened a new shape of bdelloplast: the 'dumbbell'.

I'd also like to thank everyone in our lab C15 at the University of Nottingham for their friendly support and constant supplies of chocolate! Special thanks go out to Dr Carey Lambert for being a font of *Bdellovibrio* knowledge and teaching me so much. Thank you to Rob Till for supplying the lab with media, to the C3 prep room team for technical support and to James Briggs for ensuring reliable deliveries - especially in challenging times. I completed my PhD during the global COVID-19 pandemic which brought inevitable challenges. Thank you to everyone who helped us swiftly shut down and then safely re-open our lab after lockdown.

Finally, I'd like to thank the Wellcome Trust for funding my Antimicrobials and Antimicrobial Resistance doctoral training programme PhD, and my parents for their unwavering support throughout.

Table of contents

Table of figures

Table of tables

List of abbreviations

%	percentage
=	equals
<	less than
≤	less than or equal to
>	greater than
≥	greater than or equal to
±	plus or minus
~	approximately
&	and
°C	degrees centigrade
16S	component of the 30S ribosomal subunit
3’	3 prime hydroxyl end of DNA or RNA
5’	5 prime phosphate end of DNA or RNA
Å	angstrom
α	alpha
β	beta
δ	delta
Δ	delta (gene deletion)
ε	epsilon
µg	microgram
µl	microlitre
µm	micrometre
µM	micromolar
π	pi
aa	amino acid
Amp	ampicillin
AP	attack-phase
ATP	adenosine triphosphate
ATPase	protein that hydrolyses ATP
BLAST	basic local alignment search tool
bp	base pair

BSA	bovine serum albumin
CFU	colony forming unit
CI	confidence interval
CPase	carboxypeptidase
CPRG	chlorophenol red-β-D-galactopyranoside
Da	dalton
D-Ala	D-alanine
D-Glu	D-glutamate
DNA	deoxyribonucleic acid
dNTPs	deoxyribonucleotide triphosphates
e.g.	for example
EDTA	ethylenediaminetetraacetic acid
EM	electron microscopy
EPase	endopeptidase
etc.	et cetera
FOV	field(s) of view
g	gram
g	gravitational acceleration force
Gent	gentamicin
GFP	green fluorescent protein
Glc*N*Ac	N-acetylglucosamine
GTase	glycosyltransferase
GTP	guanosine triphosphate
GTPase	protein that hydrolyses GTP
h	hour
HD	host-dependent
HI	host-independent
HPLC	high performance liquid chromatography
IM	inner membrane
IPTG	isopropyl-β-D-thiogalactopyranoside
Kan	kanamycin
kb	kilobase, 1000 bp
kDa	kilodalton
kg	kilogram

KO	gene knockout
kV	kilovolt
l	litre
L-Ala	L-alanine
L-ara	L-arabinose
Lpp	Braun's lipoprotein
LPS	lipopolysaccharide
LT	lytic transglycosylase
M	molar
Mb	megabase, 1,000,000 bp
mCerulean3	monomeric cerulean fluorescent protein
mCherry	monomeric red fluorescent protein
mCitrine	monomeric citrine fluorescent protein
m-Dap	*meso*-diaminopimelic acid
mg	milligram
min	minutes
ml	millilitre
mm	millimetre
mM	millimolar
MOI	multiplicity of infection
MS	mass spectrometry
Mur*N*Ac	N-acetylmuramic acid
N/A	not applicable
NCBI	national centre for biotechnology information
ng	nanogram
nm	nanometre
nM	nanomolar
OD	optical density
OD_{600}	optical density at 600 nm
OD_{574}	optical density at 574 nm
OD_{750}	optical density at 750 nm
OM	outer membrane
ONPG	2-Nitrophenyl β-D-galactopyranoside
PBP	penicillin-binding protein

PBS	phosphate buffered saline
PCR	polymerase chain reaction
PDB	protein data bank
Pfam	protein families database
PFU	plaque forming unit
PG	peptidoglycan
pH	negative $\log_{10}$ of the hydrogen ion concentration
^{R}	resistant
RNA	ribonucleic acid
rpm	revolutions per minute
RT-PCR	reverse-transcriptase polymerase chain reaction
s	second
S	Svedberg unit of sedimentation rate
SDS	sodium dodecyl sulphate
SDS-PAGE	sodium dodecyl sulphate polyacrylamide gel electrophoresis
SEDS	shape, elongation, division and sporulation
SignalP	prediction of signal peptides server
TE	tris-EDTA
TEM	transmission electron microscopy
TPase	transpeptidase
UV	ultraviolet
V	volt
v/v	volume by volume concentration
vs	versus
w/v	weight by volume concentration
WT	wild-type
xBASE	database of bacterial genomes
X-Gal	5-bromo-4-chloro-3-indolyl- β-D-galactopyranoside

Chapter 1. Introduction

1.1. Predatory bacteria

Bacterial predation is a fascinating and complex microbial lifestyle which has been observed and studied for over 80 years[1]. Predatory bacteria have a natural environmental role in shaping the ecological biodiversity of bacterial communities and ecosystems[1]. In addition, predatory bacteria are of increasing scientific interest due to potential applications in industry and medicine – for example as a therapeutic to treat animal and plant infections[2, 3].

Heterobacteriolytic action of *Bacterium bacteriovorus* on *Bacillus danicus* was described as early as 1927[4] and studies on the secretion of bacteriolytic secondary metabolites by *Streptomyces* species in the 1940s were critical to the discovery of streptomycin and many other antibiotics[5, 6]. It is unclear whether these lytic behaviours should be described as predatory, as true predators must not only kill their prey but also utilise prey nutrients for growth. The Gram-negative δ-proteobacterium *Myxococcus xanthus* was therefore the first definitively predatory bacterium to be characterised[7, 8]. *M. xanthus* uses gliding motility and cooperative cell swarming behaviour to locate its prey in a hunting strategy termed 'wolfpack predation'[9]. Prey lysis occurs through *M. xanthus* secretion of outer membrane vesicles (OMVs) which contain antibiotics and degradative exoenzymes that either fuse with prey membranes or release lethal cargo in close prey proximity[10].

To date, predatory bacteria have been identified in most phylogenetic branches of Gram-negative bacteria as well as in Gram-positive bacteria, strongly suggesting that predation evolved independently on multiple occasions[11]. Predatory bacteria are generally classified into one of three groups on the basis of their predatory strategy: I) group-attack predators which hunt prey in social groups (such as the aforementioned

myxobacteria); II) epibiotic predators which attach to and leach nutrients from their prey without physical invasion (such as *Micavibrio* spp.[12], *Bdellovibrio exovorus*[13] and *Vampirovibrio chlorellavorus*[14]); and III) endobiotic predators which physically invade and replicate within either the cytoplasm (*Daptobacter*[14]) or periplasm (*Bdellovibrio bacteriovorus*[15]) of prey. The endobiotic *B. bacteriovorus* is one of the better characterised predatory bacteria and the subject of this PhD thesis.

1.2. *Bdellovibrio bacteriovorus*

1.2.1. Discovery of *B. bacteriovorus*

B. bacteriovorus, an aerobic, intracellular bacterial predator was discovered serendipitously in 1962 by Heinz Stolp who was isolating bacteriophage from German soils[16]. Bacteriophage plaques usually arise on double layer agar plates following a single day's incubation, however Stolp failed to detect any plaques after 24 h. The plates would typically have been discarded at this point but were not, and after several further days, Stolp noticed the emergence of plaques which continued to increase in size, unlike phage plaques. Upon microscopic visualisation of the plaque content, he observed tiny, rapidly-swimming bacteria which frequently collided with larger bacteria at high velocity and concluded that he had isolated a bacterial predator with phage-like characteristics. Stolp continued the study of his new bacterium in the United States with Mortimer Starr where the pair succeeded in isolating 12 additional predatory strains from Californian soil and sewage[17]. The subsequent characterisation of these strains led to a seminal publication that described both a new genus and species of Gram-negative δ-proteobacteria (recently re-classified as Oligoflexia[18]): *Bdellovibrio bacteriovorus*. 'Bdello' is derived from the Greek word for leach, 'vibrio' describes the curved, vibrioid cell shape, and 'bacteriovorus' means 'bacteria-eater'. *B. bacteriovorus* strain HD100, isolated on *Pseudomonas phaseolicola* prey, was designated as the species Type

strain. The genome of strain HD100 was also the first *Bdellovibrio* genome to be sequenced[19] and HD100 is the strain of *B. bacteriovorus* that is predominantly used in the research of our laboratory. *B. bacteriovorus* strain 109J is commonly cultured in other *Bdellovibrio* research laboratories and is discussed further in **Chapter 4 Section 4.3.4**.

Although originally described as an 'ectoparasite', *B. bacteriovorus* was soon proven to be an endobiotic invasive predator with the aid of electron microscopy which also revealed key stages in its prey/host-dependent (HD) intracellular lifecycle[15].

1.2.2. Attack-phase *B. bacteriovorus*

The free-swimming form of prey (alternatively called host)-dependent *B. bacteriovorus* cells is called the 'attack-phase' (AP). *B. bacteriovorus* AP cells are very small (~ 1 µm long and 0.3 µm wide), comma-shaped rods with a single polar flagellum[17] (Figure 1.1). AP cells cannot replicate in the absence of prey and therefore rely upon swimming or gliding motility mechanisms to locate sources of prey. *B. bacteriovorus* AP cells rapidly starve in the absence of prey nutrients, with cell viability decreasing by up to 50% after 10 h of incubation in buffer alone[20]. This swift loss of predator viability is probably due to a very high rate of endogenous respiration in *B. bacteriovorus*, which respires 3% of its carbon/h in contrast to *E. coli* which respires 0.6% of carbon/h and remains viable for longer under starvation conditions[20]. Hespell *et al*., (1974) calculated that 20-40% of the energy pool of *B. bacteriovorus* AP cells is directed into locomotion[20], implicating a critical role for motility in *B. bacteriovorus* survival.

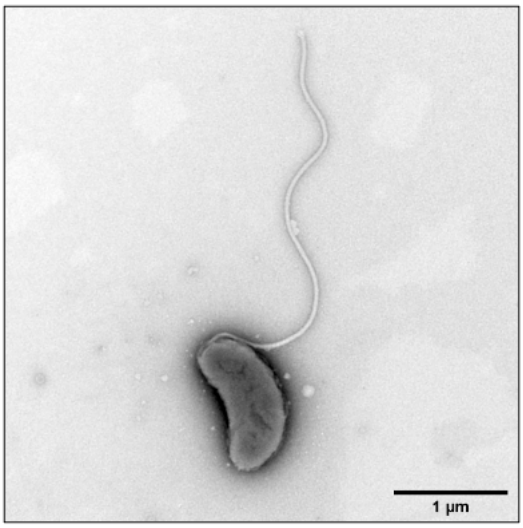

Figure 1.1. Electron micrograph of an attack-phase *B. bacteriovorus* HD100 cell

Transmission electron micrograph of a representative attack-phase *B. bacteriovorus* HD100 cell. *B. bacteriovorus* HD100 attack-phase cells are curved, vibrioid rods, approximately 1 µm in length and 0.3 µm wide with a single, polar, sheathed flagellum that is continuous with the outer membrane. Image acquired during my PhD.

Indeed, *B. bacteriovorus* is one of the fastest-known bacterial swimmers, capable of reaching speeds of up to 160 µm/s (over 100 cell lengths per second)[21]. Swimming motility is powered by the energy-dependent rotation of the polar flagellum which is a semi-rigid helix in most bacteria but has several uncommon features in *B. bacteriovorus*: the presence of a sheath that surrounds the core filament and is continuous with the outer membrane of the cell body[22], and a damped waveform (as opposed to a constant periodicity) wherein the third flagellum period has diminished 3-fold in size compared to the first period[23]. *B. bacteriovorus* flagella lengthen with cell culture age (flagella >11 µm have been observed) and AP cells retain the ability to regenerate flagella[23]. The flagellar sheath is only loosely associated with the core filament and contains less protein and a greater proportion of phospholipids than the outer membrane of the cell body – both of which may confer greater flagellar fluidity and flexibility[24].

B. bacteriovorus can also use gliding motility to locate prey on surfaces. Gliding motility does not utilise external surface appendages such as flagella or pili[25], however the mechanism underpinning bacterial gliding has not been fully elucidated and remains particularly cryptic in *B. bacteriovorus* due to the existence of 4 gliding operons which each encode 8-10 genes[19]. Slow *B. bacteriovorus* gliding (16 μm/h) was observed on agarose pads, with speeds increasing to 35 μm/h upon contact with prey cells which were often encircled by gliding predators[26]. Prey invasions that occurred following gliding-mediated encounters also culminated in the release of gliding predators from the host cell[26].

Many bacteria are positively chemotactic towards regions of strong nutrient concentration[27]. Chemotaxis has proven difficult to study in *B. bacteriovorus*, however research has shown that bdellovibrios exhibit chemotaxis towards yeast extract[28] and were weakly attracted to a limited number of L- amino acids which it is generally incapable of metabolising (but could be oxidised by *E. coli*)[29]. Bdellovibrios did not appear to be chemotactic towards prey exudates and were only chemotactic towards potential prey at very high prey densities of $>10^8$ cells/ml[30]. From the results of these early studies, it was considered most likely that bdellovibrios are weakly chemotactic towards amino acids that attract prey bacteria, however this has not been examined further. In contrast, a more recent publication proposed that chemotaxis may play a minor role in the location of prey bacteria[31]. The authors instead discovered that bacterial motility generated hydrodynamic flow fields which directed both predators and prey towards surfaces, reducing the wide predatory search space from three to two dimensions and improving the chances of random predator-prey collisions[31].

1.2.3. Overview of the *B. bacteriovorus* predatory lifecycle

Briefly, the predatory cycle (Figure 1.2) begins with *B. bacteriovorus* free-swimming 'attack-phase' cells which locate and attach to Gram-negative prey bacteria[26, 32]. A porthole is created in the prey cell wall through which the predator traverses to enter the inner periplasmic space and then reseals[32, 33]. Through the secretion of hydrolytic enzymes, *B. bacteriovorus* degrades and takes up components of prey proteins and nucleic acids which it utilises for growth and replication of new predator genomes[34, 35, 36]. The predator elongates as a filament inside the dead prey cell until nutrients have been exhausted[36]. *B. bacteriovorus* then divides to produce multiple progeny cells which secrete hydrolytic enzymes to lyse the prey, escape and reinitiate the predatory cycle[37, 38]. Each of these individual stages is described in much greater depth later in **Section 1.4**.

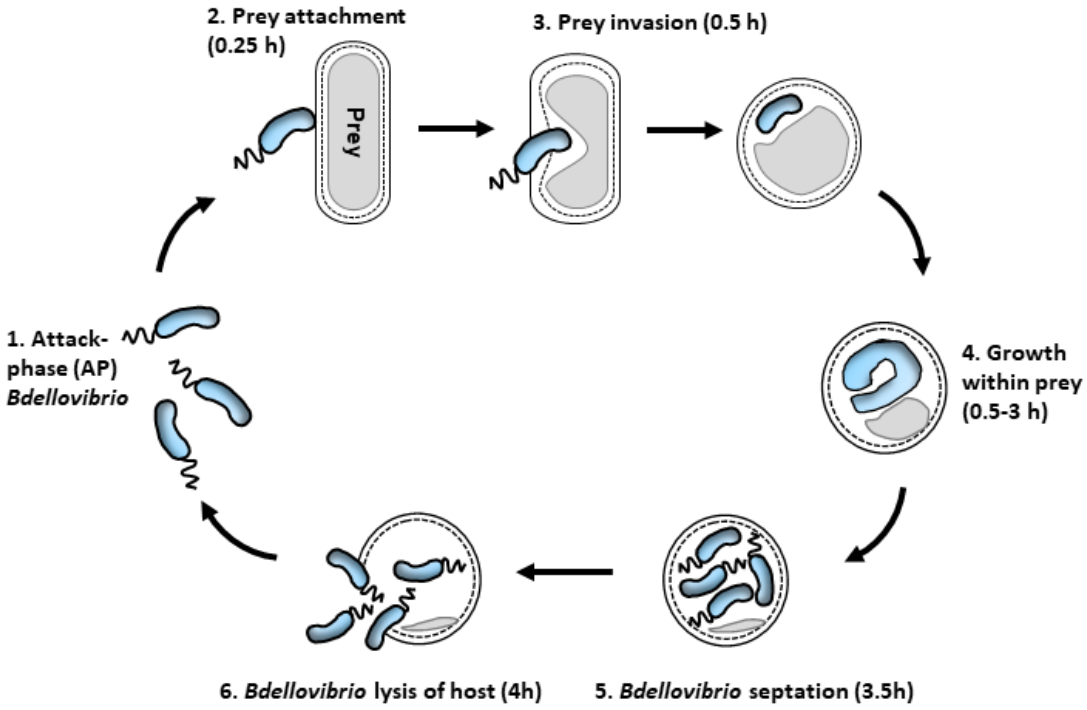

Figure 1.2. The prey-dependent life cycle of *Bdellovibrio bacteriovorus*

Predatory attack-phase (AP) *B. bacteriovorus* cells (**1**) use either swimming or gliding motility to seek out Gram-negative prey. The predator attaches to its prey with type IV pili (**2**) and then invades through the prey outer membrane and cell wall to enter the inner periplasmic compartment (**3**). The predator utilises prey nutrients to elongate as a filament inside the dead prey cell (**4**) until nutrients are exhausted. *B. bacteriovorus* then septates and divides to give odd or even-numbered daughter cells (**5**) which lyse the prey to escape (using either swimming or gliding motility) and seek out new prey to invade (**6**). The timepoints (0.25 – 4 h) indicate the approximate time at which each stage occurs (0 h = mixing of predators and prey) during a predatory timecourse in liquid culture in the laboratory.

1.2.4. The prey-independent lifecycle of *B. bacteriovorus*

Stolp & Starr[17] also identified an alternative and less common (at least in the laboratory) prey/host-independent (HI) lifecycle of *B. bacteriovorus*.

Under specific conditions, *B. bacteriovorus* can enter a prey (alternatively called host)-independent (HI) lifecycle that does not involve predation[17]. The ability to survive and replicate independently from a host may account for the surprisingly large genome size (3.8 Mb) of *B. bacteriovorus*[19]. In rich media and at high population density, *B. bacteriovorus* cells can transition to a HI lifecycle[17]. This lifecycle switch often occurs due to a mutation at a particular genetic location: the host interaction (*hit*) locus[39]. Mutations in the *hit* locus occur at a frequency of approximately 1 in 10^7 cells and confer the ability to grow independently from prey[17]. The mechanism for this is not well understood but the mutation affects the extrusion/retraction status of predator pili[40]. HI strains also retain predatory ability if introduced to prey bacteria. The HI lifecycle was originally thought to be a laboratory phenomenon until the identification of a new species, *B. bacteriovorus* Tiberius, isolated from the river Tiber, which could simultaneously grow host-dependently and host-independently[41].

In contrast to HD strains, HI strains are pleomorphic, existing in a range of shapes such as spheres, curved rods and long serpentine-shaped filaments[17]. HI strains are very slow-growing and difficult to culture and manipulate in the laboratory. The HI lifecycle is important to consider during the construction of genetic knockouts in HD strains, since if a particular gene is essential for predation, then it would only be possible to isolate the mutant as an HI strain. This was not necessary during my PhD as the gene knockouts that I generated could be obtained in the HD lifecycle and were not essential for predation. HI strains are therefore not discussed further in this thesis.

1.2.5. Predatory bacteria as 'living antibiotics'

My PhD was funded by a Wellcome Trust Antimicrobials and Antimicrobial Resistance doctoral training programme (DTP) which aims to train new researchers to tackle the growing crisis of antimicrobial resistance. Antimicrobial resistance is serious global issue and currently the leading cause of deaths worldwide[42]. The rapid development of resistance and paucity of new antibiotic discovery has led to renewed interest in alternative therapeutics such as phage therapy, however pathogens can still develop genetic resistance to bacteriophages.

Predatory bacteria such as *B. bacteriovorus* have considerable potential as a novel antibacterial therapeutic (a 'living antibiotic') for several reasons. Firstly, *B. bacteriovorus* has an extremely broad prey range, capable of preying upon virtually all Gram-negative bacteria including clinically important and antibiotic-resistant pathogens such as *Klebsiella pneumoniae* and *Pseudomonas aeruginosa*[3].

Secondly, prey bacteria are unable to develop genetic resistance to *B. bacteriovorus*. Genetic resistance has never been observed since the species was first isolated in 1962[3]. It is probable that genetic resistance cannot occur because *B. bacteriovorus* uses an extensive range of enzymatic activities to kill and invade its prey and any mutations within a handful of prey genes are insufficient to overcome death by multiple mechanisms.

To be a viable therapeutic, *B. bacteriovorus* must not be harmful to humans. Data thus far are encouraging, having demonstrated that *B. bacteriovorus* was not cytotoxic to human cell lines[43, 44]. Numerous studies have revealed the efficacy of *B. bacteriovorus* predation *in vivo* within a range of animal models. An early study by Atterbury *et al*. (2011)[45] showed that *B. bacteriovorus* could effectively treat chickens that had been colonised by *Salmonella* Typhimurium, significantly reducing pathogen burden. The authors noted however, that oral

administration of *B. bacteriovorus* resulted in changes to the chicken gut microbiome which would be expected due to the broad prey range of *B. bacteriovorus*[45]. For this reason, *B. bacteriovorus* might function most effectively as a topical antibacterial agent to treat wound infections, thereby avoiding disruption of the human gut microflora. *B. bacteriovorus* can also prey on pathogens in other animals including rats[46]. A pivotal study by Willis *et al*. (2016)[47] used a zebrafish larvae model to visualise predation *in vivo* using fluorescence microscopy. Injected *B. bacteriovorus* was used to treat zebrafish larvae that had been infected with *Shigella flexneri*, increasing zebrafish survival by 35%[47]. The authors also demonstrated that *B. bacteriovorus* worked synergistically with zebrafish macrophages and neutrophils to clear the infection, and that *B. bacteriovorus* itself was eventually cleared by the zebrafish immune system[47]. More recently, Raghunathan *et al*. (2019)[48] showed that *B. bacteriovorus* predators are engulfed by cultured human macrophage-like U937 cells and that they can survive for up to 48 h post-engulfment prior to clearance.

To advance the potential development of *B. bacteriovorus* as a novel antibacterial agent, further studies that demonstrate the efficacy and safety of *B. bacteriovorus* predation *in vivo* are needed. We also require a deeper understanding of the molecular mechanisms that facilitate the predatory lifecycle of this unusual species – which is what my PhD research aims to address.

1.3. Bacterial cell wall peptidoglycan

1.3.1. Structure of the Gram-negative cell wall

Bacteria can be categorised into two different groups based on their cell envelope composition: Gram-positive and Gram-negative bacteria. Gram-positive bacteria have a more simple envelope composition. The inner phospholipid membrane is surrounded by thick (~ 30-100 nm) layers of PG through which teichoic acids are threaded[49]. Teichoic acids comprise ~ 60% of the cell wall mass and can be covalently linked to PG (wall teichoic acids) or attached to phospholipids (lipoteichoic acids)[49]. Unlike Gram-negative bacteria, Gram-positives do not have an outer membrane, however the outer PG layer is decorated with proteins that are attached to PG or wall teichoic acids[49]. The composition of Gram-positive PG contains some differences to Gram-negative PG, however I will not discuss these here since my PhD work focussed entirely upon Gram-negative bacteria. The Gram-negative cell envelope comprises 3 layers: an inner phospholipid membrane, a thin (~ 2-8 nm) PG cell wall, and a unique outer membrane with a lipopolysaccharide (LPS) layer[50] (Figure 1.3a).

The Gram-negative PG cell wall is a complex macromolecular structure that is sometimes called a sacculus. The PG wall confers osmotic integrity to the cell and serves as an important permeability barrier, restricting the diffusion of potentially damaging extracellular molecules[49]. PG also defines bacterial shape which is integral to this thesis and is discussed in greater depth in **Chapter 4**.

Gram-negative PG consists of glycan chains comprising alternating residues of N-acetylglucosamine (Glc*N*Ac) and N-acetylmuramic acid (Mur*N*Ac) which are connected by chains of amino acids (stem peptides) attached to Mur*N*Ac residues[50] (Figure 1.3b). Peptide bond crosslinks between stem peptides link glycan chains and confer rigidity and structure to the PG wall[50] (Figure 1.3b). Biosynthesis and degradation of

the PG wall allow dynamic bacterial growth and division and each are discussed in the following sections.

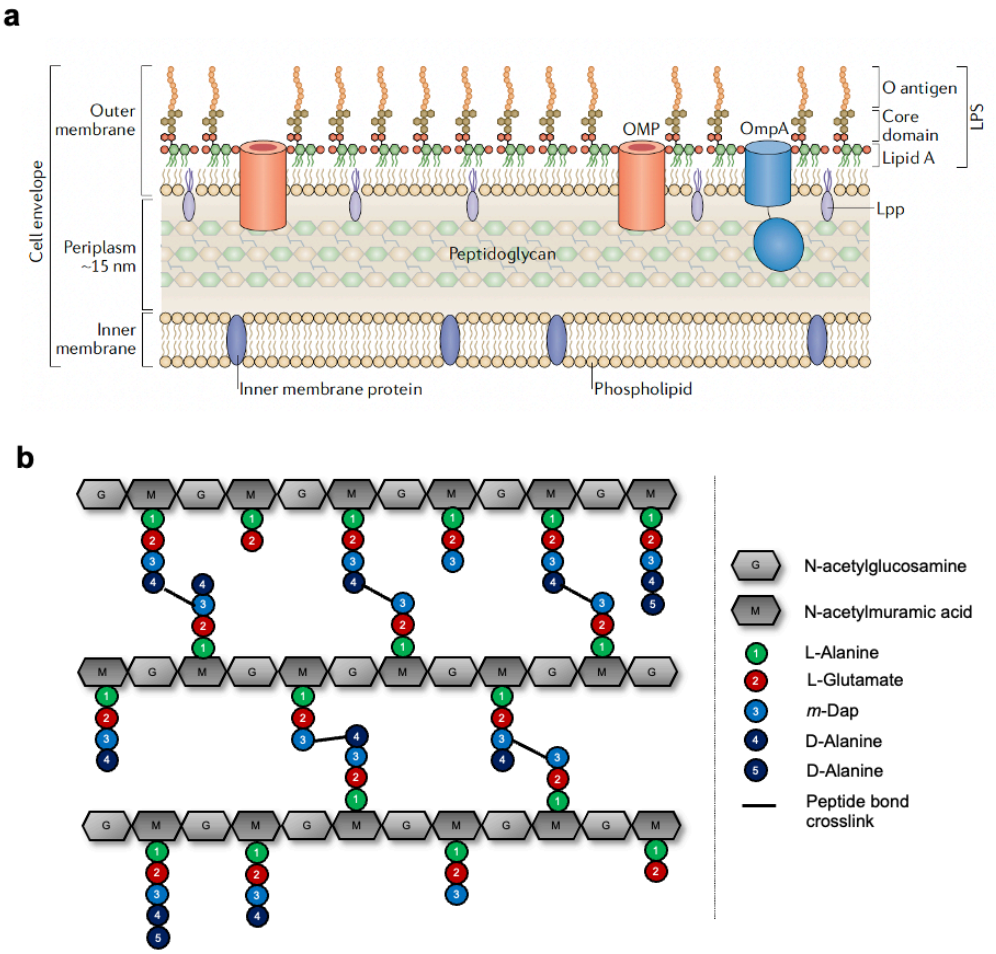

Figure 1.3. The Gram-negative cell envelope

a) Structure of a typical Gram-negative cell envelope. An inner membrane (IM) comprising phospholipids and proteins surrounds the cytoplasm. This, in turn, is surrounded by the periplasm which contains the peptidoglycan (PG) cell wall. The periplasm is surrounded by the outer membrane (OM) which consists of a phospholipid membrane attached to a lipopolysaccharide (LPS) layer. LPS consists of lipid A, a core domain and O-antigen. The OM contains outer membrane proteins (OMPs) and Lpp (Braun's lipoprotein) - a common OM-anchored lipoprotein which links the OM and PG wall. Figure from Sun *et al*. (2021)[51] **b**) Structure of the Gram-negative PG cell wall which consists of N-acetylglucosamine (G) and N-acetylmuramic acid (M) sugar residues linked by β-1,4-glycosidic bonds. Glycan chains are connected by peptide bonds that form between chains of amino acids (shown as coloured beads).

1.3.2. Cell wall biosynthesis

1.3.2.1. Insertion of new PG precursors into the cell wall

PG biosynthesis – which has been most extensively studied in *E. coli* - is a complex, multi-step process that begins in the cytoplasm with the Mur pathway[52, 53] (Figure 1.4). MurA and MurB synthesise two PG precursor molecules: uridine-diphosphate-N-acetyl-glucosamine (UDP-NAG) and uridine-diphosphate-N-acetyl-muramic acid (UDP-NAM)[52, 53]. Peptides are sequentially added to UDP-NAM by a series of enzymes: MurC (adds L-Ala), MurD (adds D-Glu), MurE (adds *m*-Dap), and MurF (adds a D-Ala dipeptide made by DdlA)[52, 53]. The racemase enzymes MurI and Alr/DadX convert the precursor L-amino acids L-Glu and L-Ala to D-Glu and D-Ala where required, respectively[52, 53]. The pentapeptide moiety is then attached to an inner membrane-anchored C_{55} lipid carrier by MraY, forming the molecule lipid I[54]. The UDP-NAG precursor is then attached to lipid I by MurG to form lipid II[54]. Finally, the lipid II PG precursor is flipped onto the periplasmic face of the inner membrane by MurJ or FtsW[55]. The PG precursor is then inserted into existing PG chains through the action of class A penicillin-binding proteins (PBPs) which are bi-functional, having both glycosyl transferase (GTase) and transpeptidase (TPase) activities[50]. In *E. coli*, these are PBP1A and PBP1B[50]. GTase activity firstly attaches lipid II to the reducing end of a growing PG chain and then TPase activity crosslinks the pentapeptide chain of lipid II to the stem peptide of another PG chain[50]. Other classes of PBPs can be more specialised such as class B PBPs which only have TPase activity and are involved in cell elongation (*E. coli* PBP2) and cell division (*E. coli* PBP3)[56].

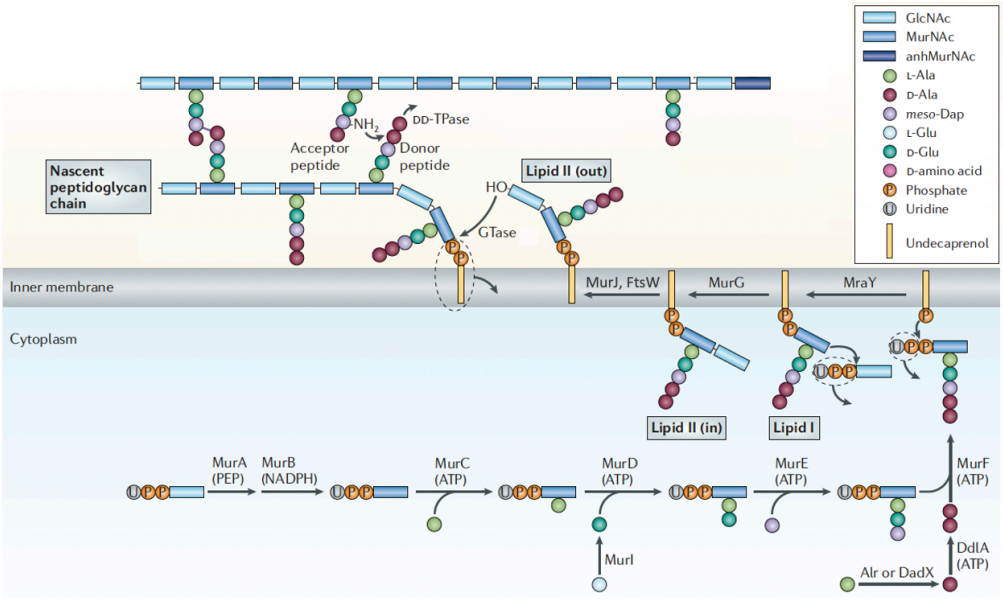

Figure 1.4. Biosynthesis of Gram-negative peptidoglycan

The peptidoglycan precursors uridine-diphosphate-N-acetyl-glucosamine (UDP-NAG) and uridine-diphosphate-N-acetyl-muramic acid (UDP-NAM) are synthesised in the cytoplasm by the Mur pathway, processed by MraY and MurG and then flipped onto the periplasmic face of the inner membrane by MurJ/FtsW. GTase activity connects the lipid II precursor to a nascent peptidoglycan chain. DD-TPase activity links two glycan chains by catalysing a peptide bond between the pentapeptide donor stem peptide and a tetrapeptide acceptor peptide. Glc*N*Ac: N-acetylglucosamine; Mur*N*Ac: N-acetylmuramic acid; L-Ala: L-alanine; D-Ala: D-alanine, *meso*-Dap: *meso*-diaminopimelic acid; L-Glu: L-glutamate; D-Glu: D-glutamate; Alr, DadX and MurI: L-amino acid racemases; PEP: phosphoenolpyruvate. Figure adapted from Typas *et al*. (2011)[56].

In *E. coli*, PBP1A and PBP1B are partially redundant as one enzyme can compensate for the deletion of the other[57]. Despite having a general role in the insertion of new PG into the cell wall sacculus, PBP1A preferentially localises to the cell periphery during growth, interacting with PBP2, whereas PBP1B localises to the mid-cell during cell division, interacting with PBP3 and other divisome proteins[58] (which are introduced in **Section 1.3.3**). The activities of PBP1A and PBP1B are stimulated by Lpo lipoproteins which are anchored in the outer membrane and span the breadth of the periplasm[59, 60]. LpoA and LpoB stimulate PBP1A and PBP1B activity respectively, potentially sensing and responding to changes in PG pore sizes[59, 60].

1.3.2.2. Peptidoglycan crosslinking

The structural integrity of the PG wall is increased by peptide bond formation between stem peptides in different glycan strands[50]. As discussed earlier, the immature PG lipid II moiety has a pentapeptide chain attached to the Mur*N*Ac residue. During transpeptidation by PBP1b, the 5th amino acid (D-Ala) is removed to catalyse bond formation between the now terminal 4th amino acid (also D-Ala) and the 3rd amino acid (*m*-Dap) of a different stem peptide[50]. This DD-transpeptidase (DD-TPase) activity forms 4-3 (named for the amino acid position) peptide bond crosslinks, strengthening the PG sacculus[50]. The 4-3 linkage is generally the most common type of PG cross-linkage, however an alternative and less common 3-3 cross-link between two *m*-Dap residues can be catalysed by LD-transpeptidase (LD-TPase) activity[61]. Mycobacterial species are an exception, having a greater abundance of 3-3 bonds than 4-3 bonds[62]. In *E. coli*, however, the proportions of the two different types of cross-linkage alter depending on cell cycle stage and environmental conditions[63]. During the transition from log phase to stationary phase, the proportion of 3-3 cross-links in the *E. coli* PG sacculus increases from ~2-10% up to 16%[64, 65]. Unlike DD-TPases, LD-transpeptidase (Ldt) enzymes are insensitive to penicillin and a higher degree of 3-3 crosslinks has been observed in β-lactam resistant strains,

implicating Ldt enzymes in antibiotic resistance[66, 67, 68]. Some *E. coli* Ldts catalyse 3-3 bond formation between stem peptides (LdtD, LdtE, LdtF), however others (LdtA, LdtB, LdtC) instead connect Braun's lipoprotein (Lpp) to the PG wall[61, 69]. Ldts can also have specialised roles such as remodelling PG to repair cell envelope damage (LdtD)[70] and facilitating the secretion of *Salmonella* Typhi toxin[71]. The grouping and potential roles of Ldts in *B. bacteriovorus* are introduced in **Chapter 4 Section 4.1.2**.

1.3.2.3. Cell elongation via the Rod complex and MreB

In most bacteria, cell growth and elongation generally occurs via the insertion of new PG precursors along the side-walls of the cell (lateral growth). Elongation is controlled by a macromolecular protein machine called the Rod complex[72] (Figure 1.5). The Rod complex comprises the proteins RodA, RodZ, PBP2, MreB, MreC and MreD[56]. RodA is an essential GTase from the SEDS (shape, elongation, division, sporulation) family of proteins[73]. RodA interacts with (and is stimulated by) PBP2 to synthesise new PG[74]. PBP2 also interacts with PBP1A during PG synthesis[75]. RodZ is an adaptor molecule in the inner membrane that connects the PG synthesising activities of RodA, PBP2 and PBP1A with the cytoskeleton via MreB[76, 77].

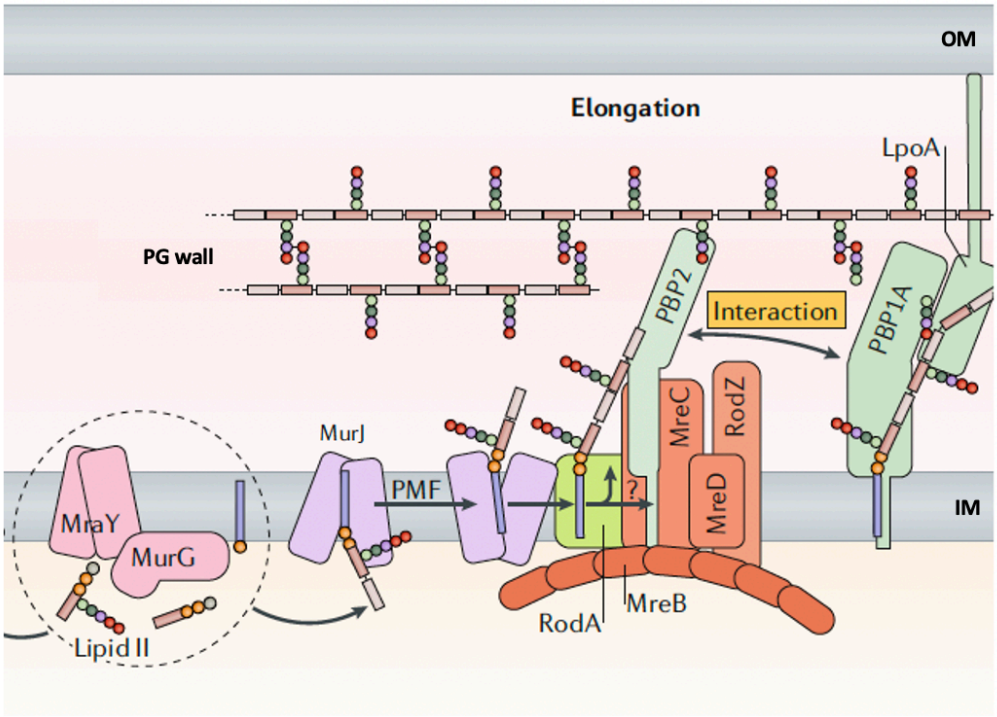

Figure 1.5. The Rod complex for cell elongation

Cell elongation proceeds via PG synthesis that is coordinated by the multi-protein Rod complex. MraY attaches lipid I to the inner membrane which is converted to lipid II by MurG and then flipped onto the periplasmic face of the inner membrane (IM) by MurJ using proton motive force (PMF). RodA is a glycosyl transferase (GTase) that incorporates lipid II into an existing PG chain. PBP2 catalyses transpeptidation between chains, interacting with the bifunctional PBP1A which is stimulated by its cognate protein LpoA. RodZ acts as an adaptor molecule that connects the periplasmic proteins with the MreB cytoskeleton. MreB interacts with MreC and MreD and rotates around the cell circumference, directing the Rod machinery to areas of negative Gaussian curvature, straightening cells as they elongate. Figure adapted from Egan *et al*. (2020)[72].

MreB is an important cytoskeletal protein that is homologous to eukaryotic actin[78]. MreB is strongly conserved across rod-shaped bacteria (except for *Rhizobium* and *Agrobacterium* species) and is the primary determinant of bacterial rod-shape[79]. Most Gram-negative rods have a single essential copy of MreB, however some species have multiple copies such as *Bacillus subtilis* which has 3 isoforms of MreB[80] and *B. bacteriovorus* which has 2 copies[19] (the roles of which are detailed in **Section 1.4.3**).

MreB rotates around the circumference of the cell, directing PG synthesis to sites of negative Gaussian curvature which results in cell straightening and maintenance of bacterial rod shape[81]. MreB was originally thought to form long helical structures that dynamically rotate around the cell[82, 83, 84], however high-resolution microscopy revealed that MreB moves bidirectionally across the cell as dynamic patches[85]. The energy for the processive movement of MreB was shown by to be driven by PG synthesis itself[85, 86, 87]. Subsequent studies again suggested the existence of long MreB helical filaments in *B. subtilis*[88, 89], leading to the attempted revival of the helix model[90]. Recent work contradicts this, showing that the previous observations of micron-long helical MreB filaments were an artefact of GFP-MreB accumulation in stationary phase[91]. MreB instead forms nanofilaments <200 nm in length in *B. subtilis*[91].

MreB interacts with MreC and MreD which are also involved in elongation and maintenance of rod shape[92, 93]. MreB is required for a general rod shape, however the generation of more complex shapes like curved rods and corkscrews is determined by additional specific shape proteins that are discussed in detail in **Chapter 4 Section 4.1.1**.

1.3.3. Bacterial cell division

1.3.3.1. Assembly of the Z-ring and septal PG synthesis

While MreB primarily directs and controls the elongasome for lateral PG synthesis and growth, the cytoskeletal element FtsZ controls cell division[94]. FtsZ is a tubulin homologue and the master regulator of bacterial cell division[94]. FtsZ localises to the mid-cell and forms a dynamic ring structure called the Z-ring[94] (Figure 1.6a). FtsZ is a GTPase which dynamically polymerises and depolymerises upon GTP binding and hydrolysis[95]. Super-resolution microscopy has revealed that FtsZ moves circumferentially around the site of cell division, turning over protein subunits in a process called treadmilling[96, 97, 98]. The early divisome proteins FtsA and ZipA then localise to mid-cell, interacting with and stabilising the FtsZ ring[99, 100]. The Zap proteins ZapA-E also stabilise and regulate FtsZ activity[101]. The PG synthase PBP1B is recruited to the Z-ring via ZipA interactions to carry out pre-septal PG synthesis[102]. The arrival of FtsK at the divisome signals the transition from early to mid-late stages of cell division, interacting with components of the divisome and participating in DNA segregation[94]. The main septal PG synthase PBP3 is recruited along with FtsW, a GTase of the SEDS family and a lipid II flippase[102]. PBP3 PG synthesis is regulated by the FtsQLB complex[103]. Sufficient accumulation of FtsN – which binds septal PG via its SPOR domain – signals to FtsA that septation is complete and triggers the final stage of cell division: daughter cell separation[104] (Figure 1.6b).

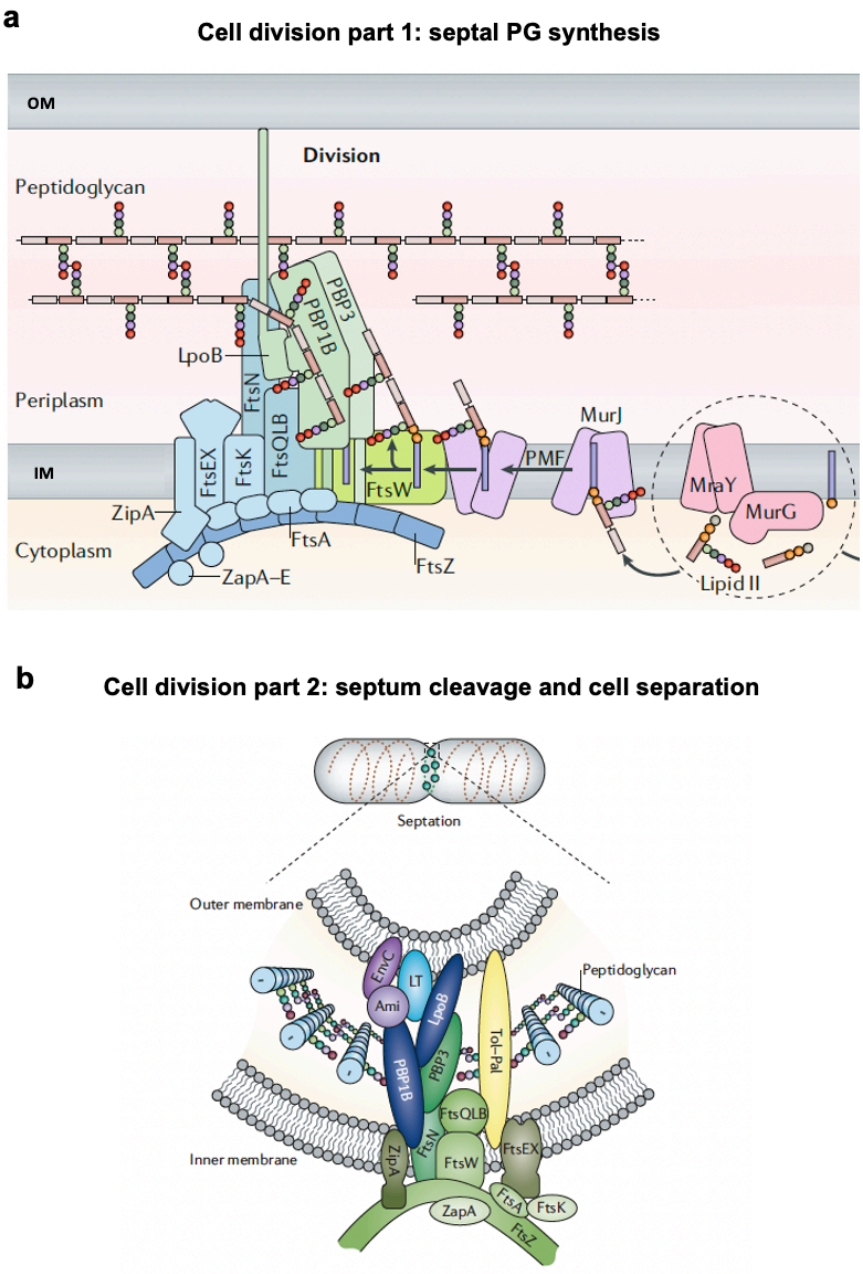

Figure 1.6. Synthesis and cleavage of septal PG during cell division

a) Cell division begins with localisation of FtsZ to the mid-cell, generating the Z-ring divisome. Early divisome proteins FtsA, ZipA and ZapA-E are recruited, interacting with PBP1B which synthesises early septal PG. Late-associating proteins FtsK, FtsQLB and FtsW are then recruited, regulating PBP3 which synthesises most of septal PG. Accumulation of FtsN above a threshold level signals that septal PG synthesis is complete and triggers PG cleavage and cell separation (**b**). The amidases AmiA-C and their activators EnvC and NlpD are required for PG cleavage, alongside lytic transglycosylase (LT) activity. Finally, the Tol-Pal complex facilitates invagination of the outer membrane, resulting in cell separation. Figures adapted from Egan *et al*. (2020)[72] and Typas *et al*. (2011)[56].

1.3.3.2. Cleavage of septal PG and daughter cell separation

In Gram-negative bacteria, cleavage of the newly-synthesised septum and daughter cell separation occur almost simultaneously[105]. In *E. coli*, the 3 amidases AmiA, AmiB and AmiC are responsible for most septal PG cleavage[106, 107]. Amidases remove the stem peptide from Mur*N*Ac residues in the glycan chain[105]. This results in septal PG which has a different composition to lateral PG: the septal PG lacks amino acids chains and consists of 'denuded' or 'naked' glycans (Figure 1.7a). A triple deletion of all 3 *E. coli* amidases resulted in a severe cell chaining defect[106, 107]. The *E. coli* amidases are regulated by EnvC (AmiA and AmiB) or the lipoprotein NlpD (AmiC)[108, 109].

In *E. coli*, lytic transglycosylases (LTs) cut β-1,4-glycosidic bonds between Glc*N*Ac and Mur*N*Ac and have a relatively minor role in cell division along with DD-endopeptidases (which cut bonds between stem peptides)[106, 110]. In *V. cholerae* and *P. aeruginosa*, however, the LT rare lipoprotein A (RlpA) has a more important role in separation of daughter cells[111, 112]. *P. aeruginosa* RlpA binds to PG via its SPOR domain and has specific activity on denuded glycans[112]. Denuded glycans are enriched in septal PG following amidase activity that cleaves stem peptide chains[112]. In *V. cholerae*, amidase activity alone is insufficient for separation of daughter cells and requires RlpA and another LT, MltC[111]. Due to the chaining phenotype of Δ*rlpA*Δ*mltC*, the authors proposed that septal PG must contain PG strands that are inaccessible to amidases and require the activity of specific LTs to be cut[111]. Most studies suggest that PG is inserted perpendicular to the long axis of the cell. The authors therefore suggest a model whereby, during cell division, PG synthases deposit some new septal PG at a sub-optimal angle transecting the septal plane and bridging the two daughter cells[111] (Figure 1.7b). These PG strands could be accessible to LTs but not amidases[111]. In *P. aeruginosa*, it was further suggested that RlpA follows AmiB, cutting the remaining bridging PG strands[112]. The role of LTs in *B. bacteriovorus* bacterial predation is investigated in **Chapter 3** of my thesis.

Finally, constriction of the outer membrane allows daughter cell separation. This involves the Tol-Pal system, comprising the proteins TolQ, TolR, TolA, TolB and Pal, which interact with PBP1B to facilitate outer membrane constriction and ultimately cell separation[113].

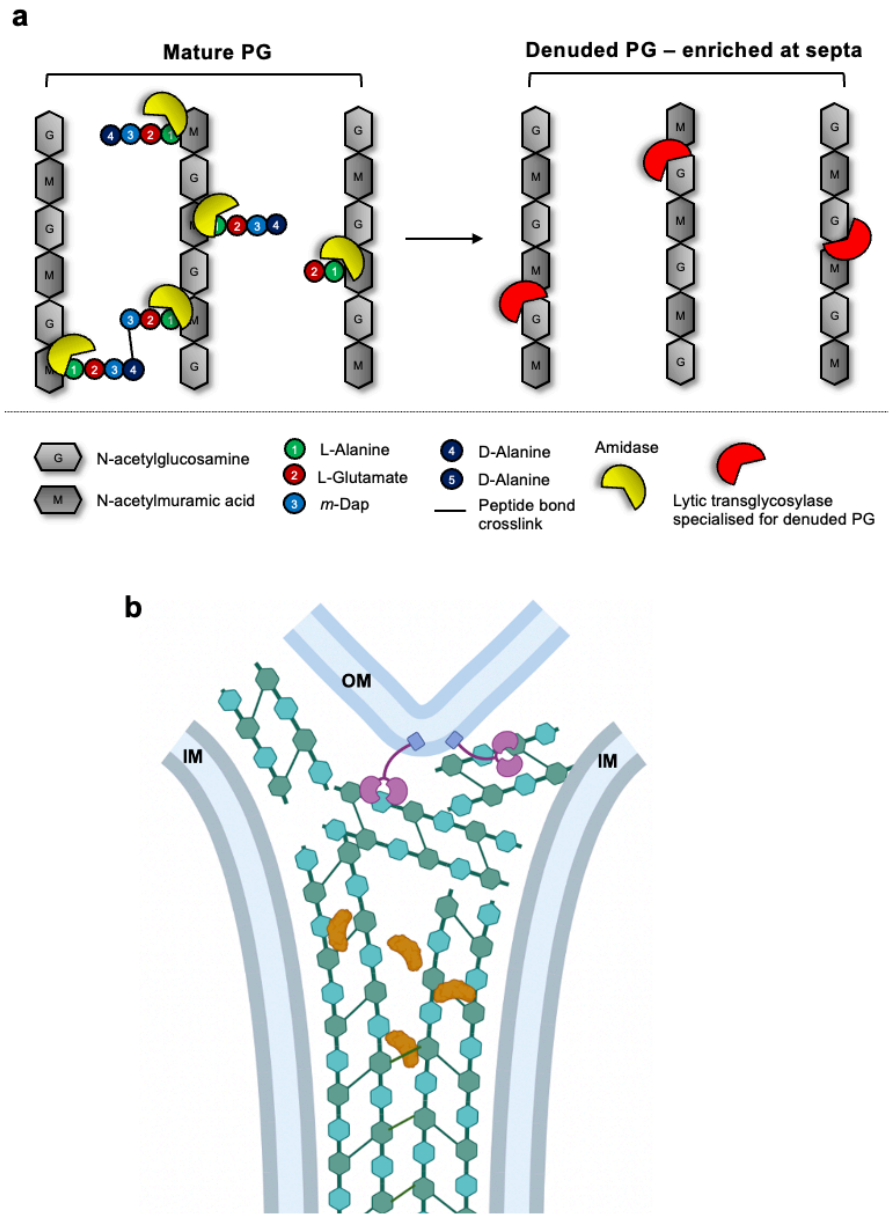

Figure 1.7. Composition and cutting of septal PG during cell division

a) Schematic showing the conversion of mature cross-linked PG to denuded PG (enriched at septa) by the activity of cell wall amidases which cleave the amide bond between L-Alanine (green bead) and N-acetylmuramic acid (M) to remove peptide

chains. Some lytic transglycosylases like *P. aeruginosa* RlpA then specifically cleave denuded glycan chains. **b**) Model proposed by Weaver *et al*. (2019)[111] for *V. cholerae* cell separation in which amidases (orange) cleave peptide chains but the deposition of some glycan chains at a sub-optimal angle during septal PG synthesis cannot be accessed by amidases. These require lytic transglycosylases like RlpA or MltC (purple) to be resolved, facilitating daughter cell separation. Figure created in BioRender.

1.3.4. Summary of peptidoglycan remodelling enzymes

To elongate and divide, PG must be constantly remodelled by polymerising and cutting enzymes[72]. Some remodelling enzymes have already been introduced in this chapter. I will summarise these here and introduce additional enzymes since remodelling of predator and prey PG is central to my PhD (Figure 1.8).

To initially insert new PG precursor units into a nascent glycan chain, the existing PG sacculus must first be nicked. This cutting is generally fulfilled by lytic transglycosylases (LTs) which cleave β-1,4-glycosidic bonds between Glc*N*Ac and Mur*N*Ac residues in the glycan chain[105]. LTs can be either exolytic (cleaving from the glycan chain terminus) or endolytic (cleaving in the middle of the glycan chain)[114] (Figure 1.8). LTs can also cleave PG to allow the insertion of macromolecular machinery like pili and secretion systems[114]. Alongside amidases (which cleave the peptide bond between the first amino acid L-Ala and Mur*N*Ac), LTs also participate in cell division, cleaving glycan chains prior to cell separation[114] (Figure 1.8). LTs in *B. bacteriovorus* are the subject of **Chapter 3** where they are discussed in greater detail.

The key bond-forming enzymes are DD-transpeptidases and LD-transpeptidases (Ldts) which catalyse 4-3 and 3-3 bond formation between stem peptide chains, respectively[50, 61] (Figure 1.8). The 4-3 and 3-3 peptide crosslinks can subsequently be cut by DD-endopeptidases (also called DacB enzymes) or LD-endopeptidases (rare), respectively[105] (Figure 1.8). *B. bacteriovorus* DacB enzymes Bd0816 and Bd3459 are secreted from predator cells to cleave crosslinks in the prey PG, facilitating the transformation of rod-shaped prey into rounded prey bdelloplasts[115]. These DacB enzymes are important within the context of **Chapter 3** results.

Finally, bonds can be cut between amino acids comprising a single stem peptide by carboxypeptidase enzymes[116]. DD-carboxypeptidases (DD-

CPases), LD-carboxypeptidases (LD-CPases) and DL-carboxypeptidase (DL-CPases) remove the terminal amino acid from pentapeptides (which is a D-Ala), tetrapeptides (a D-Ala) or tripeptides (*m*-Dap), respectively[116] (Figure 1.8). Some carboxypeptidases can also cleave the terminal amino acid from crosslinked stem peptides[116]. LD-CPases are of particular importance in **Chapter 4**.

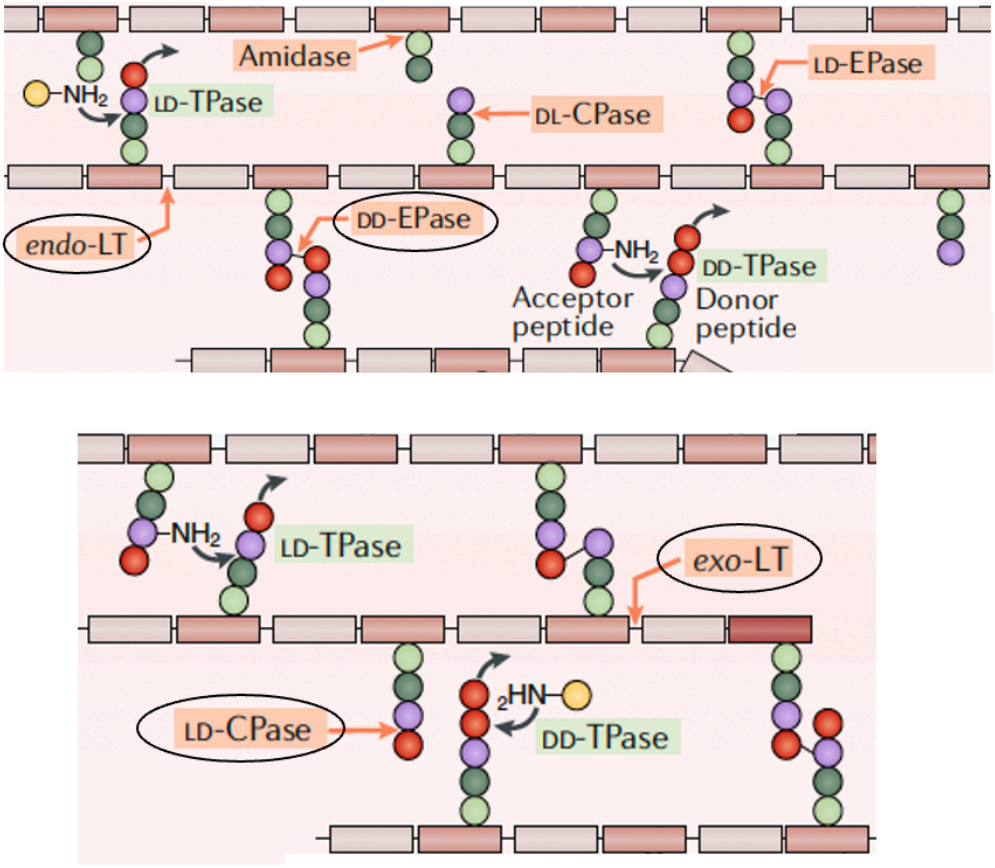

Figure 1.8. Peptidoglycan remodelling enzymes

Examples of enzymes involved in remodelling of the PG cell wall. endo-LT and exo-LT: lytic transglycosylases that cleave the β-1,4-glycosidic bond between Glc*N*Ac and Mur*N*Ac residues at either the chain terminus (exo-) or chain middle (endo-). Amidases cleave the amide bond between L-Ala and Mur*N*Ac to completely remove a stem peptide. DD-TPases form a 4-3 crosslink between the D-Ala of one stem peptide and the *m*-Dap of another. LD-TPases (Ldts) form a 3-3 crosslink between the *m*-Dap residues of two stem peptides. DD-EPases and LD-EPases cut 4-3 and 3-3 peptide bonds, respectively. DD-CPases, LD-CPases, and DL-CPases remove the terminal (5^{th},

4th or 3rd, respectively) amino acid from a stem peptide. Enzymes of most importance in *B. bacteriovorus* in this thesis are encircled. Figure adapted from Egan *et al*. (2020)[72].

1.4. The *B. bacteriovorus* predatory lifecycle involves PG modifications

1.4.1. Attachment to prey

After locating its prey, *B. bacteriovorus* attaches to and invades the prey host cell (Figure 1.9a-b). Attack-phase *B. bacteriovorus* cells collide with potential prey and form an initially reversible attachment to the cell surface[17]. *B. bacteriovorus* then receives an unknown signal which results in one of two possible outcomes: either the predator recognises that the surface is not suitable for predation (for example Gram-positive bacteria or a non-biological surface) and dissociates from the surface, or the predator identifies the surface as potential prey and forms a strong irreversible attachment to the bacterium[17]. The molecular basis for this two-step attachment is not fully understood but is likely to involve *B. bacteriovorus* type IV pili.

Type IV pili were first observed in early electron micrographs in which the structures were described as fine cellular filaments protruding from the anterior non-flagellated pole of attack-phase *B. bacteriovorus*[32]. The significance of *B. bacteriovorus* pili was not fully revealed until a later study by Evans *et al*. (2007)[117] which demonstrated that deletion of the major pilin protein, PilA, completely abolished predatory capability[117]. Subsequent work supported an invasive role for *B. bacteriovorus* pili through the detection of PilA at the predator-prey attachment interface by immunofluorescence[118] and observations that deletion of a pilus retraction ATPase, PilT2, (pers. comm. from Dr Carey Lambert) or application of anti-PilA antiserum (which could block the pilus recognition site)[118] abolished or greatly reduced the efficiency of predation, respectively. Despite the evident necessity for *B. bacteriovorus* type IV pili in the process of prey entry, the exact mechanism by which the invasive pili function remains to be fully determined. It is possible that pili help to firmly anchor the predator to the prey cell before penetration and that the invasive movement is by gliding motility, or that pili retract to

facilitate the physical entry of *B. bacteriovorus* into prey in a ‘ratcheting’ manner.

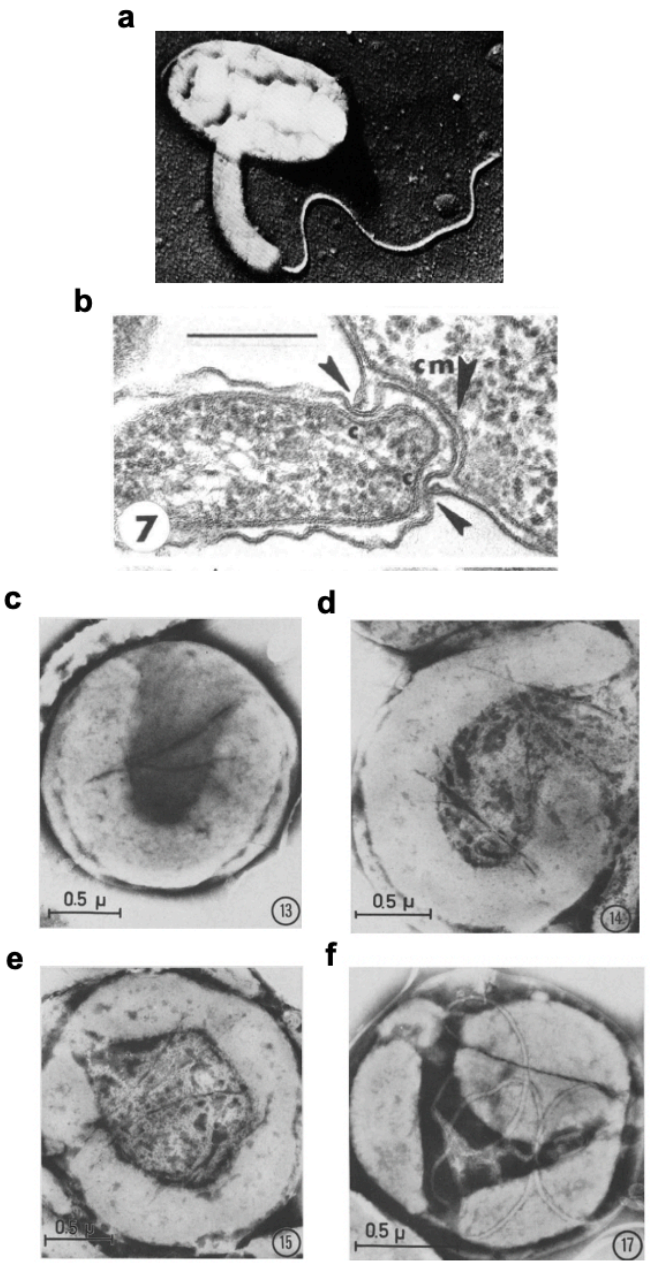

Figure 1.9. Electron micrographs of the *B. bacteriovorus* predatory lifecycle within prey

A selection of electron micrographs showing the stages of the *B. bacteriovorus* predatory lifecycle. *B. bacteriovorus* attaches to a Gram-negative prey cell (**a**) and invades its prey (**b**). The invasive nose becomes constricted (indicated by black arrows) as the predator squeezes through the outer membrane and porthole. *B. bacteriovorus* becomes established inside (**c**) and then elongates within the prey bdelloplast (**d**) until septation into daughter cells (**e**), cell division, and regeneration of new flagella prior to lysis (**f**). Electron micrographs are reproduced from Stolp & Starr (1963)[17] (a), Abraham *et al*. (1974)[119] (b), and Shilo (1969)[32] (c-f).

1.4.2. Prey invasion

1.4.2.1. The entry porthole

One of the critical stages of invasion is the creation of a small 'porthole' within the prey cell wall[32] (Figure 1.10). Early work demonstrated that invasion (and by extension the creation of the porthole) is an enzymatic process as it is inhibited in the presence of the antibiotics streptomycin or chloramphenicol which block protein synthesis[120]. These antibiotics did not inhibit attachment[120]. It was also initially theorised that the rapid rotation of the flagellum may exert a degradative 'drilling' action on the prey cell wall to enable entry. The drilling hypothesis and any invasive role by flagellar rotation was later disproved via the demonstration that non-motile *B. bacteriovorus* cells (generated by inactivation of a key flagellin component FliC3) remained capable of prey penetration when predators were directly applied to prey[121]. Flagellar motility was required to reach areas of prey but not for invasion into prey cells[121].

Constriction of the *B. bacteriovorus* invasive nose allows the predator to squeeze through the smaller porthole and enter the inner periplasmic space[15, 122] which expands asymmetrically to accommodate the invading predator[119]. The porthole is then resealed to secure the predator inside its new niche and prevent the leakage of prey contents. The mechanistic basis for the creation and ultimate re-sealing of the entry porthole is still under investigation and is likely to involve a large arsenal of PG hydrolytic and synthetic enzymes, respectively. Although the identity of these proteins is limited thus far, Lerner (2012)[123] showed that deletion of the *B. bacteriovorus* lytic transglycosylase Bd3575 significantly increased the entry time of *B. bacteriovorus* into prey from 4 min to 12 min, indicating that Bd3575 may constitute one of the hydrolytic invasion enzymes[123]. Furthermore, the recent discovery of a novel predatory vesicle made by *B. bacteriovorus* has important implications for the study of prey invasion (unpublished work, Sockett group). The vesicle contents might include enzymes required for the formation and/or resealing of the entry porthole.

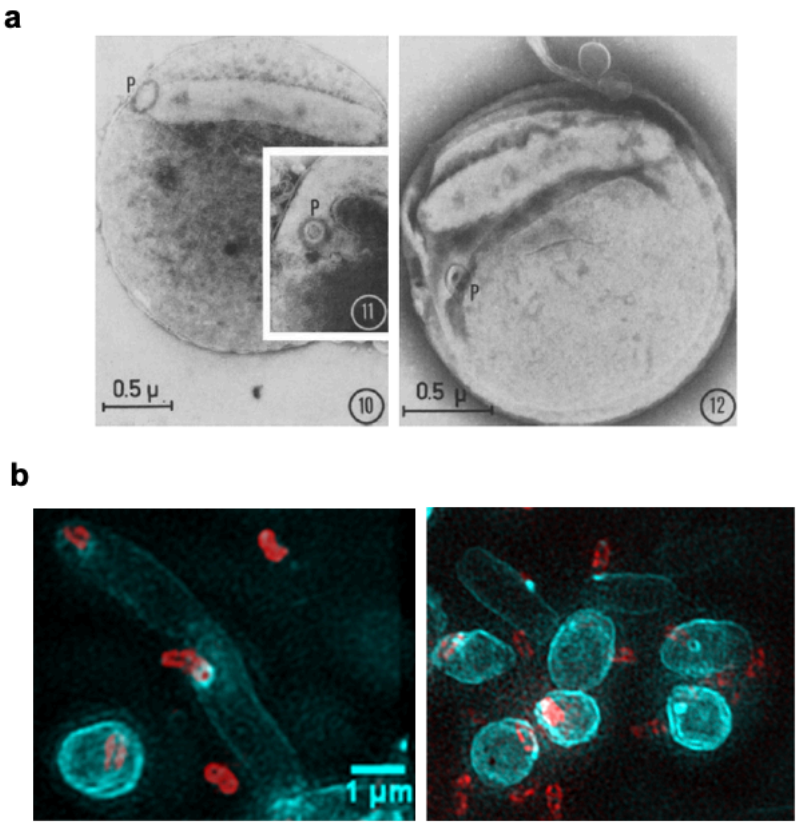

Figure 1.10. *B. bacteriovorus* invades prey by creating an entry porthole within the prey cell wall

a) Electron micrograph showing the invasion of *B. bacteriovorus* strain 109J (rod-shaped) into a rounded prey bdelloplast. 'P' denotes the porthole created by the predator to allow traversal through the PG wall of the prey and access to the inner periplasmic compartment. Images are reproduced from Shilo (1969)[32]. **b**) 3D-SIM fluorescence microscopy images showing *B. bacteriovorus* predators (labelled red by the D-amino acid BADA) invading *E. coli* prey (labelled blue by pulses of the D-amino acid HADA). HADA pulses label prey PG that is actively being modified, illuminating the entry porthole around the invasive nose of *B. bacteriovorus*. Rod-shaped prey are rounded into spherical bdelloplasts by the action of two DD-endopeptidases. Images are reproduced from Kuru, Lambert *et al*. (2017)[33].

1.4.2.2. Prey damage and death occurs rapidly

Evidence indicates that prey become rapidly and severely damaged during invasion[124]. Synthesis of RNA and protein by the prey is inhibited after just 3 min and 5 min of predatory contact, respectively[125]. The addition of streptomycin which prevents predator penetration did not prevent this inhibition, therefore processes occurring during attachment alone are sufficient to cause prey damage[125]. The permeability of prey to lactose and ONPG substrates increased during the first 45 min of predation and the ability of prey to respire a variety of substrates such as succinate or malate rapidly decreased after predator-prey contact[124]. In contrast, the respiration of *B. bacteriovorus* increases[124]. These results suggest that the prey cytoplasmic membrane, which functions as a permeability barrier and contains components of the electron transport chain and TCA cycle (both required for respiration) becomes damaged during predatory contact[124]. Electron micrographs show apparent contact of the predator nose with the prey cytoplasmic membrane during invasion, with contact sites appearing to correspond to 'blister sites and scars' on the surface of cytoplasmic membrane[126]. Despite the maintenance of an otherwise intact prey cytoplasmic membrane, it is possible that this contact may exert localised damage that is sufficient to disrupt the cytoplasmic membrane potential and cause prey death[124].

1.4.2.3. Biochemical modifications to the prey envelope

Numerous biochemical modifications occur during invasion of *B. bacteriovorus* into prey. *Bdellovibrio* researchers in the 1970s discovered that one of the first prey modifications is the limited solubilisation of prey LPS (~27% of LPS sugars) by an unknown *B. bacteriovorus* 'LPSase' enzyme[127] which may aid predatory traversal through the LPS layer. The second important modification of prey cells is the alteration of linkages in the prey cell envelope and the creation of an entry porthole within the PG cell wall (Figure 1.10). Braun's lipoprotein (Lpp) is the most abundant protein in *E. coli*[128] and forms a covalent connection to both the outer membrane (via the attachment of three acyl groups to its N-terminal

cysteine[129]) and the PG wall (via a covalent *m*-Dap-C-terminal lysine bond[130]). Lpp functions to stabilise the cell envelope by tethering the outer membrane to PG wall[131], although the protein is not essential in *E. coli*[132]. The length of Lpp protein also dictates the width of the outer periplasm[133, 134]. During *B. bacteriovorus* prey invasion, approximately 75% of *E. coli* Lpp is removed from the prey cell envelope and replaced with the long-chain fatty acids palmitic acid (60%) and oleic acid (20%) from *B. bacteriovorus*[135]. *B. bacteriovorus* fatty acids are attached to bdelloplast PG via the formation of a carboxylic-ester bond by an unknown acylase enzyme[135]. It is likely that removal of *E. coli* Lpp helps to destabilise the prey cell envelope at a localised point to facilitate predator invasion and that the addition of *B. bacteriovorus* PG-linked fatty acids subsequently reinforces the invaded host bdelloplast[135].

The creation of the small entry porthole can be observed via the incorporation of new PG (a reinforcing 'collar') around a pore in the PG wall (Figure 1.10). Pore formation must involve the specifically localised and controlled degradation of prey PG. Approximately 10% of *E. coli* prey PG glucosamine becomes solubilised during the first 20 min of invasion[127]. Glucosamine degradation then pauses until prey lysis which results in complete solubilisation of the remaining PG glucosamine[127]. Glucosamine solubilisation was prevented in the presence of chloramphenicol, indicating that the process is enzymatic[127]. The PG wall is additionally modified by the removal of *m*-Dap residues from the third position of the PG stem peptide[127]. Solubilisation of approximately 25% of *E. coli m*-Dap was detected within the first hour of predation which then remained low until complete solubilisation of remaining *m*-Dap during prey cell lysis[127]. As with glucosamine degradation, removal of *m*-Dap was inhibited by chloramphenicol[127]. *B. bacteriovorus* did not take up the released exogenous *m*-Dap[136]. Interestingly, 2% of the released *m*-Dap was re-incorporated into the prey bdelloplast cell wall in approximately the same time period as solubilisation[136]. It is possible that re-incorporation is temporally separated from solubilisation and occurs immediately after *B. bacteriovorus* entry into prey to reinforce the

bdelloplast wall and thus strengthen the predatory niche. The enzymes responsible for *m*-Dap cleavage and re-attachment are not known, however, the attachment enzyme is probably synthesised at an early timepoint as attachment was unaffected in the presence of chloramphenicol[136]. A subsequent study discovered that *m*-Dap attachment involved the synthesis of an amide bond and was inhibited by penicillin, however the identity of the enzyme responsible remains elusive[137].

Early *Bdellovibrio* research also demonstrated that prey bdelloplast PG is N-deacetylated by *B. bacteriovorus* early in predation (~ 20-60 min), conferring resistance to conventional lysozymes[138]. The authors proposed that this activity regulates invasive enzymes by inhibiting their action after invasion[138]. Recent work has revealed that N-deacetylation by the enzymes Bd0468 and Bd3279 differentiates predator PG from prey PG, facilitating the action of a novel *B. bacteriovorus* lysozyme specific for deacetylated PG during prey lysis[38, 139] (**Section 1.4.4**).

1.4.2.4. Conversion of rod-shaped prey into spherical prey bdelloplasts

During invasion, rod-shaped prey visibly change morphology from rod shapes into rounded spheres[15]. Although initially termed ‘spheroplasts’, invaded prey hosts were later renamed ‘bdelloplasts’ since very large prey bacteria become only partially rounded[126]. It was originally hypothesised that the peptidase enzyme(s) responsible for the removal of prey *m*-Dap may weaken the wall to allow prey rounding[127]. More recent work has shown that two DacB-like DD-carboxy/endopeptidases, Bd0816 and Bd3459, are secreted into prey and cleave the 4-3 *m*-Dap-D-Alanine cross-links between glycan strands of prey PG[115]. Deletion of both *bd0816* and *bd3459*, which resulted in rod-shaped bdelloplasts, was not lethal to predatory growth by *B. bacteriovorus* although predators took longer to enter prey[115]. Prey cell rounding probably occurs because of internal osmotic pressures pushing upon the weakened and more

malleable cell wall. The activity of these two DacB enzymes and the conversion of prey cell shape is the subject of **Chapter 3**. Additional work demonstrated that complexation of Bd0816 or Bd3459 with the ankyrin-repeat immunity protein, Bd3460, prevents potential *B. bacteriovorus* self-toxicity before secretion of the DD-endopeptidases into prey[140]. Deletion of *bd3460* resulted in the dramatic phenotype of *B. bacteriovorus* cells which self-rounded and then lost predatory viability upon attempted prey invasion[140].

1.4.3. Intracellular growth and replication

After *B. bacteriovorus* has completed prey invasion, the predator begins to grow and elongate inside the prey cell (Figure 1.9c-d). *B. bacteriovorus* requires a secure and stable niche within which to replicate that is protected from premature lysis. The secretion of two predator Ldt enzymes, Bd0886 and Bd1176, into prey results in the formation of 3-3 crosslinks in the prey bdelloplast PG, reinforcing the bdelloplast structure. This was observed via the additional incorporation of HADA into the cell wall of bdelloplasts containing *B. bacteriovorus* predators (Figure 1.10).

As *B. bacteriovorus* resides in the inner periplasmic compartment, the predator must somehow access the prey DNA and nutrients contained within the prey cytoplasm. Early *Bdellovibrio* studies proposed that *B. bacteriovorus* removes the outer membrane porin OmpF from prey and inserts it into its own envelope[141, 142]. This was later disproven by several studies which provided alternative evidence that *B. bacteriovorus* inserts its own OmpF porin into the prey inner membrane[143, 144, 145, 146]. One study detected OmpF in the prey membrane within minutes of predation which might suggest that porin insertion contributes to early prey death via disruption of inner membrane potential[146]. Critically, the predator porin could facilitate the transfer of prey nutrients across the inner membrane for absorption into *B. bacteriovorus*. *B. bacteriovorus* utilises nucleic acids of the prey to grow and replicate. *B. bacteriovorus* degrades ~50%

of prey ribosomes into ribonucleotides from which it constructs its own ribosomes[35]. The remaining prey ribosomes are used for energy metabolism and to build other predator macromolecules[147]. *B. bacteriovorus* replicates its genome by synthesising DNA nucleotides *de novo* but also by assimilating nucleotides from its prey, nicking prey DNA with a combination of endo- and exonucleases[34, 148].

B. bacteriovorus elongates as a curving filament until prey nutrients are exhausted. At that point, the filament synchronously septates and then divides to yield daughter cells[149]. The number of progeny produced is correlated with prey size; typically 4 daughter cells are produced from one *E. coli* cell with a genome size of 4 Mb[149, 150]. The signal for septation remains unclear and the cell division machinery is unknown, however a homologue of the Gram-positive division protein DivIVA is involved, controlling the size and morphology of progeny cells[151].

B. bacteriovorus encodes two MreB homologues, MreB1 and MreB2[19]. Neither MreB could be deleted in either predatory or non-predatory *B. bacteriovorus* strains, indicating that the two proteins are essential for growth in both lifecycles[152]. Fenton *et al*. (2010)[152] tagged each MreB at the protein C-terminus with the fluorophore mTFP which partially abrogated the native function of both MreBs, providing insights into the role of each protein. Perturbation of MreB1 resulted in *B. bacteriovorus* predators that could not form plaques on lawns of *E. coli* and took 5-7 times longer to lyse *E. coli* in liquid compared to the wild-type strain[152]. Visualisation of the *B. bacteriovorus* MreB1-TFP mutant inside bdelloplasts by DAPI staining showed that - despite consuming prey nutrients - 12% of predator cells had failed to develop correctly into an elongated filament after 24 h[152]. A small proportion of these stalled *B. bacteriovorus* cells had rounded up into spheroplasts which were incapable of bdelloplast lysis and completion of predation[152]. All *B. bacteriovorus* progeny cells that successfully completed the predatory lifecycle were, however, wild-type in shape[152].

In contrast, the MreB2-TFP strain was not deficient in predatory efficiency and predator cells elongated like the wild-type strain within bdelloplasts, however 37% of released attack-phase predator cells were non-wild-type in shape, existing as spherical, elongated, or branched cells[152]. These results suggested possible roles for MreB1 in the elongation and development of *B. bacteriovorus* and for MreB2 in the control of cell shape during later development[152].

1.4.4. Lysis and escape from prey

Following cell division, *B. bacteriovorus* daughter cells synthesise a new polar flagellum in preparation for escape from prey (Figure 1.9e-f). Little is known about the molecular mechanisms of prey lysis; thus far the role of one protein has been elucidated, DslA[38]. DslA (*bd0314*) is a lysozyme that specifically acts on N-deacetylated PG[38]. Early in predation, the two *B. bacteriovorus* enzymes Bd0468 and Bd3279 deacetylated prey bdelloplast PG, demarcating predator PG from prey PG[139]. The specificity of this enzyme action for deacetylated PG prevents any potential self-inflicted damage to the cell wall of *B. bacteriovorus*. Deletion of DslA increased the escape time of predator progeny cells by 54%, however the protein is not essential for prey lysis[38]. Similarly to prey invasion, it is likely that a cocktail of different enzymes including lysozymes and lytic transglycosylases act together to facilitate escape from prey.

1.5. Aims of my PhD research

The overall aim of my PhD research was to further understand the molecular mechanisms that facilitate bacterial predation by *B. bacteriovorus*. During my PhD I focussed on enzymes that modify prey PG at the stage of prey invasion (Chapter 3) and an enzyme that generates the vibrioid curvature of *B. bacteriovorus* (Chapter 4) and affects predatory fitness (Chapter 5). Although I began my PhD by working on *B. bacteriovorus* cell shape and then studied prey PG modifications, I present this work in the opposite order within my thesis to improve the logical flow of the narrative. Therefore, I firstly introduce prey cell shape changes during invasion (as this occurs early in the predatory cycle), followed by the generation of *B. bacteriovorus* cell shape which affects invasion but also subsequent intracellular growth within prey. More specific chapter aims are detailed below.

Chapter 3. Role of a lytic transglycosylase in prey cell rounding
In this chapter, I investigate the role of lytic transglycosylases of *B. bacteriovorus* during predation, examining the transcriptional pattern, subcellular localisation, and genetic deletion phenotypes of two proteins: Bd3285 and Bd0599.

Chapter 4. The vibrioid cell shape-determinant of *B. bacteriovorus*
In this chapter, I build on my previous work from a short project in which I identified the protein Bd1075 as the curvature-determinant of *B. bacteriovorus*. I determine the subcellular localisation of Bd1075 and - with help from collaborators - characterise the enzyme function and protein structure.

Chapter 5. The importance of *B. bacteriovorus* vibrioid cell shape
In this chapter, I investigate whether the vibrioid cell shape of *B. bacteriovorus* confers a particular evolutionary advantage since this has been observed for other bacterial species. I examine the impact of cell

curvature on overall predation efficiency and test the role of curvature at two specific stages: prey invasion and growth within prey bdelloplasts.

Chapter 2. Materials and Methods

2.1. Bacterial strains, primers, and plasmids

2.1.1. Bacterial strains used in this study

The subject under study in this thesis is the invasive predatory bacterium *B. bacteriovorus* HD100 - with some additional work on another lab strain: *B. bacteriovorus* 109J. Both bacterial strains were isolated from soil in 1962-63[17]. Predominantly, I used strain HD100 as it was the first *B. bacteriovorus* strain to be genome-sequenced (in 2004)[19] and, since then, has been investigated by many studies in our laboratory. *B. bacteriovorus* strains that were used in my PhD research are listed in the table below along with *E. coli* strains that were either used for cloning purposes or as prey for *B. bacteriovorus* cultivation. *E. coli* strain S17-1 cells in stationary phase were most commonly used as prey for *B. bacteriovorus*.

Table 2.1. Table of bacterial strains

Strain	Description	Source
***B. bacteriovorus* wild-type strains**		
B. bacteriovorus HD100	The Type strain of *B. bacteriovorus*, genome-sequenced, commonly used in research, vibrioid-shaped.	Stolp & Starr (1963)[17], Rendulic *et al*., (2004)[19] DSM 50701
B. bacteriovorus 109J	Strain of *B. bacteriovorus* also commonly used in research, genome-sequenced, straight rod-shaped.	Stolp & Starr (1963)[17], Wurtzel *et al*. (2010)[153]
***E. coli* cloning and prey strains**		

E. coli NEB5α	*E. coli* DH5α cloning strain (F- *endA1 hsdR17*(rk–mk–) *supE44* thi-1 *recA1 gyrA* (NalR) *relA1*Δ(lacIZYA-argF) U169 *deoR*(φ80dlacΔ(lacZ)M15)	Hanahan (1983)[154]
E. coli S17-1	*E. coli* strain used a prey for *B. bacteriovorus* cultivation. Also the donor strain for conjugation of plasmids into *B. bacteriovorus* (*thi*, *pro*, *hsdR*-, *hsdM*+, *recA*; integrated plasmid RP4- Tc::Mu-Kn::Tn7)	Simon *et al*. (1983)[155]
E. coli S17-1 (pZMR100)	*E. coli* S17-1 strain containing the pZMR100 plasmid to confer resistance to kanamycin. Prey strain used for kanamycin-resistant *B. bacteriovorus* strains.	Rogers *et al*. (1986)[156]
E. coli S17-1 (pUC19)	*E. coli* S17-1 strain containing the pUC19 plasmid to confer resistance to gentamicin. Prey strain used for gentamicin-resistant *B. bacteriovorus* strains	Our laboratory
E. coli TOP10	*E. coli* strain for arabinose-inducible gene expression (F- mcrA Δ(mrr-hsdRMS-mcrBC) φ80lacZΔM15 ΔlacX74 deoR recA1 araD139 Δ(araA-leu)7697 galU galK rpsL endA1 nupG)	Gift from Dr Ruth Griffin
E. coli BL21 (DE3)	*E. coli* expression strain for Bd1075 protein purification (F^- *ompT gal dcm lon hsdS*$_B$(r_B^- m_B^-) λ(DE3 [*lacI lacUV5-T7 gene 1 ind1 sam7 nin5*]) [*malB*$^+$]$_{K\text{-}12}$(λ^S)	Studier & Moffatt (1986)[157]
E. coli BW25113	*E. coli* strain from which PG sacculi were isolated to test Bd1075 activity (*lacI*$^+$*rrnB*$_{T14}$ Δ*lacZ*$_{WJ16}$ *hsdR*514 Δ*araBAD*$_{AH33}$ Δ*rhaBAD*$_{LD78}$ *rph-1* Δ*(araB–D)567* Δ*(rhaD–B)568* Δ*lacZ4787*(::*rrnB-3*) *hsdR514 rph-1*	Prof Waldemar Vollmer & Dr Jacob Biboy
E. coli S17-1 lux	*E. coli* S17-1 strain expressing the gene strawberry lux which produces luminescence	Gift to the lab from Dr Phil Hill
Further strains involved in Chapter 3		
HD100 Bd3285-mCherry SXO	*B. bacteriovorus* HD100 containing a single-crossover fluorescent fusion of Bd3285-mCherry (kan^R)	This study

HD100 Bd0064mCerulean3 DXO	*B. bacteriovorus* HD100 containing a double-crossover fluorescent fusion of Bd0064-mCerulean3	Our laboratory
HD100 Bd3285-mCherry SXO + Bd0064-mCerulean3 DXO	*B. bacteriovorus* HD100 containing both a single-crossover fluorescent fusion of Bd3285-mCherry and a double-crossover fluorescent fusion of Bd0064-mCerulean3	This study
HD100 Bd0064-mCherry SXO	*B. bacteriovorus* HD100 containing a single-crossover fluorescent fusion of Bd0064-mCherry (kan^R)	This study
HD100 Δ*bd3285*	*B. bacteriovorus* HD100 containing an in-frame silent deletion of the gene *bd3285*	This study
HD100 Δ*bd3285*Δ*bd0816*Δ*bd3459*	*B. bacteriovorus* HD100 containing triple in-frame silent deletions of the genes *bd3285, bd0816* and *bd3459*	This study
HD100 Δ*bd3285* (+ Bd0064-mCherry SXO)	*B. bacteriovorus* HD100 Δ*bd3285* containing a single-crossover fluorescent fusion of Bd0064-mCherry (kan^R)	This study
HD100 Δ*bd3285*Δ*bd0816*Δ*bd3459* (+ Bd0064-mCherry SXO)	*B. bacteriovorus* HD100 Δ*bd3285*Δ*bd0816*Δ*bd3459* a single-crossover fluorescent fusion of Bd0064-mCherry (kan^R)	This study
HD100 Δ*bd3285* (+ *bd3285* (WT) DXO comp)	*B. bacteriovorus* HD100 Δ*bd3285* containing a double-crossover re-introduction of the wild-type *bd3285* gene to complement the knockout	This study
HD100 Δ*bd3285* (+ *bd3285* (D321A) DXO comp)	*B. bacteriovorus* HD100 Δ*bd3285* containing a double-crossover re-introduction of the *bd3285* gene (with the mutation D321A) to test for complementation of the knockout	This study
HD100 Δ*bd3285* (+ *bd3285* (WT) DXO comp) (+ Bd0064-mCherry SXO)	*B. bacteriovorus* HD100 Δ*bd3285* containing a double-crossover re-introduction of the wild-type *bd3285* gene to complement the knockout and also a single-crossover fluorescent fusion of Bd0064-mCherry (kan^R)	This study
HD100 Δ*bd3285* (+ *bd3285* (D321A) DXO	*B. bacteriovorus* HD100 Δ*bd3285* containing a double-crossover re-	This study

comp) (+ Bd0064-mCherry SXO)	introduction of the *bd3285* gene (with the mutation D321A) to test for complementation of the knockout and also a single-crossover fluorescent fusion of Bd0064-mCherry (kan^R)	
E. coli TOP10 pBAD Bd3285 (WT)-mCherry	*E. coli* TOP10 strain containing a pBAD overexpression construct of wild-type *bd3285* fused to mCherry at the protein C-terminus (kan^R)	This study
E. coli TOP10 pBAD Bd3285 (D321A)-mCherry	*E. coli* TOP10 strain containing a pBAD overexpression construct of *bd3285* (with the mutation D321A) fused to mCherry at the protein C-terminus (kan^R)	This study
HD100 Bd0599-mCherry SXO	*B. bacteriovorus* HD100 containing a single-crossover fluorescent fusion of Bd0599-mCherry (kan^R)	This study
HD100 Bd0599-mCherry SXO + Bd0064-mCerulean3 DXO	*B. bacteriovorus* HD100 containing both a single-crossover fluorescent fusion of Bd0599-mCherry and a double-crossover fluorescent fusion of Bd0064-mCerulean3 (kan^R)	This study
HD100 Δ*bd0599*	*B. bacteriovorus* HD100 containing an in-frame markerless deletion of the gene *bd0599*	This study
HD100 Δ*bd0599*Δ*bd3285*	*B. bacteriovorus* HD100 double mutant containing in-frame markerless deletions of the two genes *bd0599* and *bd3285*	This study
HD100 Δ*bd0599* (+ Bd0064-mCherry SXO)	*B. bacteriovorus* HD100 Δ*bd0599* containing a single-crossover fluorescent fusion of Bd0064-mCherry (kan^R)	This study
HD100 Δ*bd0599*Δ*bd3285* (+ Bd0064-mCherry SXO)	*B. bacteriovorus* HD100 Δ*bd0599*Δ*bd3285* containing a single-crossover fluorescent fusion of Bd0064-mCherry (kan^R)	This study
E. coli TOP10 pBAD Bd0599-mCherry	*E. coli* TOP10 strain containing a pBAD overexpression construct of wild-type *bd0599* fused to mCherry at the protein C-terminus (kan^R)	This study
Further strains involved in Chapter 4		

HD100 Δ*bd1075*	*B. bacteriovorus* HD100 containing an in-frame markerless deletion of the gene *bd1075*	Banks (2018)[158]
HD100 Δ*bd1075* (pEV)	*B. bacteriovorus* HD100 Δ*bd1075* containing the empty pMQBAD plasmid ($gent^R$)	This study
HD100 Δ*bd1075* (p*bd1075*$_{HD100}$)	*B. bacteriovorus* HD100 Δ*bd1075* containing the pMQBAD plasmid expressing *bd1075* from strain HD100 ($gent^R$)	This study
HD100 Δ*bd1075* (p*bd1075*$_{109J}$)	*B. bacteriovorus* HD100 Δ*bd1075* containing the pMQBAD plasmid expressing *bd1075* from strain 109J ($gent^R$)	This study
109J (pEV)	*B. bacteriovorus* 109J containing the empty pMQBAD plasmid ($gent^R$)	This study
109J (p*bd1075*$_{HD100}$)	*B. bacteriovorus* 109J containing the pMQBAD plasmid expressing *bd1075* from strain HD100 ($gent^R$)	This study
E. coli BL21 Bd1075	*E. coli* BL21 expression strain containing the pET41 plasmid expressing the *bd1075* gene (minus the signal peptide and in-frame with a hexahistidine tag) for protein purification	This study (Dr Ian Cadby)
HD100 Bd1075-mCherry DXO	*B. bacteriovorus* HD100 containing a double-crossover fluorescent fusion of Bd1075-mCherry	Banks (2018)[158]
HD100 Bd1075-mCherry DXO + Bd0064-mCerulean3 SXO	*B. bacteriovorus* HD100 containing both a double-crossover fluorescent fusion of Bd1075-mCherry and a single-crossover fluorescent fusion of Bd0064-mCerulean3 (kan^R)	This study
HD100 Bd1075-mCitrine SXO	*B. bacteriovorus* HD100 containing a single-crossover fluorescent fusion of Bd1075-mCitrine (kan^R)	This study
HD100 Bd0064-mCitrine SXO merodiploid	*B. bacteriovorus* HD100 containing a single-crossover merodiploid fluorescent fusion of Bd0064-mCitrine (kan^R)	This study
HD100 Bd1075 (full length) - mCherry SXO	*B. bacteriovorus* HD100 containing a single-crossover fluorescent fusion of wild-type, full length Bd1075-mCherry (kan^R)	This study

HD100 Bd1075 (A304) - mCherry SXO	*B. bacteriovorus* HD100 containing a single-crossover fluorescent fusion of Bd1075 (terminating at residue A304) – mCherry (kan^R)	This study
HD100 Bd1075 (E302) - mCherry SXO	*B. bacteriovorus* HD100 containing a single-crossover fluorescent fusion of Bd1075 (terminating at residue E302) – mCherry (kan^R)	This study
HD100 Bd1075 (C156A) - mCherry SXO	*B. bacteriovorus* HD100 containing a single-crossover fluorescent fusion of Bd1075 (with a point mutation of C156A) – mCherry (kan^R)	This study
HD100 Bd1075 (Y274A) - mCherry SXO	*B. bacteriovorus* HD100 containing a single-crossover fluorescent fusion of Bd1075 (with a point mutation of Y274A) – mCherry (kan^R)	This study
HD100 Δ*bd1075* + Bd1075 (full length) - mCherry SXO	*B. bacteriovorus* HD100 Δ*bd1075* containing a single-crossover fluorescent fusion of wild-type, full length Bd1075-mCherry (kan^R)	This study
HD100 Δ*bd1075* + Bd1075 (A304) - mCherry SXO	*B. bacteriovorus* HD100 Δ*bd1075* containing a single-crossover fluorescent fusion of Bd1075 (terminating at residue A304) – mCherry (kan^R)	This study
HD100 Δ*bd1075* + Bd1075 (E302) - mCherry SXO	*B. bacteriovorus* HD100 Δ*bd1075* containing a single-crossover fluorescent fusion of Bd1075 (terminating at residue E302) – mCherry (kan^R)	This study
HD100 Δ*bd1075* + Bd1075 (C156A) - mCherry SXO	*B. bacteriovorus* HD100 Δ*bd1075* containing a single-crossover fluorescent fusion of Bd1075 (with a point mutation of C156A) – mCherry (kan^R)	This study
HD100 Δ*bd1075* + Bd1075 (Y274A) - mCherry SXO	*B. bacteriovorus* HD100 Δ*bd1075* containing a single-crossover fluorescent fusion of Bd1075 (with a point mutation of Y247A) – mCherry (kan^R)	This study
Further strains involved in Chapter 5		

HD100 Δ*bd1075* (+ *bd1075* SXO comp)	*B. bacteriovorus* HD100 Δ*bd1075* containing a single-crossover copy of wild-type *bd1075* for complementation (kan^R)	This study
HD100 Bd0064-mCerulean3 SXO	*B. bacteriovorus* HD100 containing a single-crossover fluorescent fusion of Bd0064-mCerulean3 (kan^R)	This study
HD100 Δ*bd1075* (+ Bd0064-mCerulean3 SXO)	*B. bacteriovorus* HD100 Δ*bd1075* containing a single-crossover fluorescent fusion of Bd0064-mCerulean3 (kan^R)	This study
HD100 Δ*bd0886*Δ*bd1176* (Δ2*ldt*)	*B. bacteriovorus* HD100 double deletion mutant containing two in-frame silent deletions of the genes *bd0886* and *bd1176* (Δ2*ldt*)	Kuru, Lambert *et al*. (2017)[33]
HD100 Δ*bd1075*Δ*bd0886*Δ*bd1176* (Δ*bd1075*Δ2*ldt*)	*B. bacteriovorus* HD100 triple deletion mutant containing three in-frame silent deletions of the genes *bd1075*, *bd0886* and *bd1176* (Δ*bd1075*Δ2*ldt*)	This study

2.1.2. Primers used in this study

Table 2.2. Table of primers

Primer	Description	Sequence (5'-3')
Testing for co-transcription of *bd0599* and *bd0600*		
0599_F	Amplifies a 1,092 bp product if the two genes are co-transcribed	GCCCAATGGTGAGGTTCATG
0600_R		GAATTTTCCTGACCCGCCAG
0599_F	Control for *bd0599* amplification	GCCCAATGGTGAGGTTCATG
0599_R		TTGCGATGATCCAGGTAGCC
0600_F	Control for *bd0600* amplification	GGGATATGTGACGATTGCC
0600_R		GAATTTTCCTGACCCGCCAG
Testing the transcriptional start site of *bd3285*		
3285_F2	F2 & R amplify a 566 bp product if the start codon of *bd3285* is correct. F3 & R amplify a 481 bp product if the start codon of *bd3285* was mis-annotated	ACCTATTTTCGTCACCTCGTT
3285_F3		GTCTCAAGGTCAGGAGTTT
3285_R		CTGTTTTCCGGGGCTTCTTC
Transcriptional pattern of *bd3285* across the predatory cycle		
3285_F1	Amplifies a ~ 100 bp product internal to the *bd3285* gene	CGGAGACCAAACCAGAAACC
3285_R		CTGTTTTCCGGGGCTTCTTC
Transcriptional pattern of *bd0599* across the predatory cycle		
0599_F	Amplifies a ~ 100 bp product internal to the *bd0599* gene	GCCCAATGGTGAGGTTCATG
0599_R		TTGCGATGATCCAGGTAGCC
Transcriptional pattern of *bd0519* across the predatory cycle		
0519_F	Amplifies a ~ 100 bp product internal to the *bd0519* gene	GGTCCGGGTTGAAATGCTTT
0519_R		CGTGAACATAACAGGCCCCT
Transcriptional patten of control gene *dnaK* across the predatory cycle		
dnaK_RT_F	Amplifies a ~ 100 bp product internal to the *dnaK* gene	TGAGGACGAGATCAAACGTG
dnaK_RT_R		AAACCAGGTTGTCGAGGTTG
Construction of Bd3285-mCherry single-crossover fusion		

3285_gene_mCh_F	Amplifies the *bd3285* gene (minus the start codon and signal peptide)	CGTTGTAAAACGACGGCCAGTGCCATGCGGGCAGATGAAGGCTG
3285_gene_mCh_R		CTTGCTCACCATTTTGGTGACCGCGTGACG
3285_mCh_F	Amplifies the *mCherry* gene	CGCGGTCACCAAAATGGTGAGCAAGGGCGAG
3285_mCh_R		GGAAACAGCTATGACCATGATTACGTTACTTGTACAGCTCGTCCATG
Construction of the Δ*bd3285* genetic deletion		
3285_up_F	Amplifies 1 kb of DNA upstream from *bd3285*	CGTTGTAAAACGACGGCCAGTGCCAAATTCAAAATCCGTCTCATTGC
3285_up_R		GGGACTATTTGGTACTCATATTCAAACTCCTGACC
3285_down_F	Amplifies 1 kb of DNA downstream from *bd3285*	TTGAATATGAGTACCAAATAGTCCCGCGTG
3285_down_R		GGAAACAGCTATGACCATGATTACGTGCGGCAAACTCAATGAG
Complementation of Δ*bd3285* with wild-type *bd3285* (double-crossover)		
3285_up_F	Amplifies the wild-type *bd3285* gene and 1 kb of upstream and downstream DNA	CGTTGTAAAACGACGGCCAGTGCCAAATTCAAAATCCGTCTCATTGC
3285_down_R		GGAAACAGCTATGACCATGATTACGTGCGGCAAACTCAATGAG
Complementation of Δ*bd3285* with *bd3285* (D321A) (double-crossover)		
3285_up_F	Amplifies the *bd3285* gene, mutating the aspartate residue at position 321 to an alanine, and 1 kb of upstream and downstream DNA	CGTTGTAAAACGACGGCCAGTGCCAAATTCAAAATCCGTCTCATTGC
3285_D321A_R		GTAAAGAACGCAAATCGGCCC
3285_D321A_F	Amplifies the *bd3285* gene, mutating the aspartate residue at position 321 to an alanine, and 1 kb of upstream and downstream DNA	GGGCCGATTTGCGTTCTTTAC
3285_down_R		GGAAACAGCTATGACCATGATTACGTGCGGCAAACTCAATGAG
Construction of Bd3285-mCherry in the arabinose-inducible vector pBAD		
3285_pBAD_F		TTTTGGGCTAACAGGAGGAATTAACCATGAGTAAGAAACATATTGCAATAC

3285_genemCh_pBAD_R	Amplifies the wild-type *bd3285* gene	CTTGCTCACCATTTTGGTGACCGCGTGACG
3285_genemCh_pBAD_F	Amplifies the *mCherry* gene	CGCGGTCACCAAAATGGTGAGCAAGGGCGAG
3285_mCh_pBAD_R		ACCCATTTGCTGTCCACCAGTCATGTTACTTGTACAGCTCGTCCATG
Construction of Bd3285 (D321A)-mCherry in the arabinose-inducible vector pBAD		
3285_pBAD_F	Amplifies the *bd3285* gene, mutating the aspartate residue at position D321 to an alanine	TTTTGGGCTAACAGGAGGAATTAACCATGAGTAAGAAACATATTGCAATAC
3285_D321A_R		GTAAAGAACGCAAATCGGCCC
3285_D321A_F	Amplifies the *bd3285* gene, mutating the aspartate residue at position D321 to an alanine	GGGCCGATTTGCGTTCTTTAC
3285_genemCh_pBAD_R		CTTGCTCACCATTTTGGTGACCGCGTGACG
3285_genemCh_pBAD_F	Amplifies the *mCherry* gene	CGCGGTCACCAAAATGGTGAGCAAGGGCGAG
3285_mCh_pBAD_R		ACCCATTTGCTGTCCACCAGTCATGTTACTTGTACAGCTCGTCCATG
Construction of Bd0599-mCherry single-crossover fusion		
0599_gene_mCh_F	Amplifies the *bd0599* gene and 300 bp of upstream DNA	CGTTGTAAAACGACGGCCAGTGCCAGAAAGCGCATTCCCAATATG
0599_gene_mCh_R		CTTGCTCACCATTTCTTGCTGCTCTTCCAG
0599_mCh_F	Amplifies the *mCherry* gene	AGAGCAGCAAGAAATGGTGAGCAAGGGCGAG
0599_mCh_R		GGAAACAGCTATGACCATGATTACGTTACTTGTACAGCTCGTCCATG
Construction of the Δ*bd0599* genetic deletion		
0599_up_F	Amplifies 500 bp of DNA upstream from *bd0599*	CGTTGTAAAACGACGGCCAGTGCCATCAAAATTGCCCGATCTCAAG
0599_up_R		CTGGGAAACCTCTTTCATGTTTGGGCCCTC
0599_down_F	Amplifies 500 bp of DNA downstream from *bd0599*	CCCAAACATGAAAGAGGTTTCCCAGGACTTAAAAAG
0599_down_R		GGAAACAGCTATGACCATGATTACGATCACATGCGGAAAAAGTTTTG
Construction of Bd0599-mCherry in the arabinose-inducible vector pBAD		

0599_pBAD_F	Amplifies the *bd0599* gene	TTTTGGGCTAACAGGAGGAATTAACCATGAAAATTTTCAGTCAGATTTTG
0599_genemCh_pBAD_R		CTTGCTCACCATTTCTTGCTGCTCTTCCAG
0599_genemCh_pBAD_F	Amplifies the *mCherry* gene	AGAGCAGCAAGAAATGGTGAGCAAGGGCGAG
0699_mCh_pBAD_R		ACCCATTTGCTGTCCACCAGTCATGTTACTTGTACAGCTCGTCCATG
Testing the transcriptional start site of *bd1075*		
1075_F1	F1 & R amplify a 331 bp product if the start codon of *bd1075* is correct. F2 & R amplify a 305 bp product if the start codon of *bd1075* was mis-annotated	GTCCTATTCGGGCATAATAGTATT
1075_F2		ATGAGACTATTGCTCACGG
1075_R		GAAGTAAATGCCTTCCGGC
Plasmid-based complementation with *bd1075*$_{HD100}$		
1075_HD100c_F	Amplifies the *bd1075*$_{HD100}$ gene with 100 bp of flanking DNA	CAGCTGGTACCATATGGGAATTCGAACTTTATTTACATTTAAATTACACGG
1075_HD100c_R		CTTCTCTCATCCGCCAAAACAGCCATATCGAGTTGATGAAAAAAGC
Plasmid-based complementation with *bd1075*$_{109J}$		
1075_109Jc_F	Amplifies the *bd1075*$_{109J}$ gene with 100 bp of flanking DNA	CAGCTGGTACCATATGGGAATTCGAACTTTATTTACATTTAAATTACACGG
1075_109Jc_R		CTTCTCTCATCCGCCAAAACAGCCAGTATCGAGTTGATGAAAAAAG
Testing the transcription of *bd1075*$_{109J}$		
1075_RT_F	Amplifies a 102 bp product internal to the *bd1075* gene	CAACGATCAGTTGCTGGTG
1075_RT_R		AAGTGTCACCGGACTTGAGG
Testing the presence of a truncation in the *bd1075*$_{109J}$ transcript		
RTtrunc_F	Amplifies either a 298 bp product (if there is no truncation) or a 127 bp product if *bd1075*$_{109J}$ contains a 171 bp truncation	TATTTGCGTTGAGTCTGCCG
RTtrunc_R		TGGCTCAGACGCTCTTGC
Construction of Bd0064-mCerulean3 as a single-crossover fusion		

64_gene_mCeru_F	Amplifies the *bd0064* gene	CGTTGTAAAACGACGGCCAGTGCCAGTGGAGGACACATATACAGTTC
64_gene_mCeru_R		CTTGCTCACCATTCCGACTTTTTTAAAGATCGTG
64_mCeru_F	Amplifies the *mCerulean3* gene	TAAAAAAGTCGGAATGGTGAGCAAGGGCGAG
64_mCeru_R		GGAAACAGCTATGACCATGATTACGTTACTTGTACAGCTCGTCCATG
Construction of Bd1075-mCitrine as a single-crossover fusion		
1075_gene_mCit_F	Amplifies the *bd1075* gene with 1 kb of upstream DNA	CGTTGTAAAACGACGGCCAGTGCCAATGAGACTATTGCTCACGG
1075_gene_mCit_R		GCCCTTGCTCACTTGCGTTTTCTGGGAAGAG
1075_mCit_F	Amplifies the *mCitrine* gene	CCAGAAAACGCAAGTGAGCAAGGGCGAGGAG
1075_mCit_R		GGAAACAGCTATGACCATGATTACGCTACTTGTACAGCTCGTCCATG
Construction of Bd0064-mCitrine as a merodiploid single-crossover fusion		
64mCit_up_F	Amplifies 1 kb of upstream DNA flanking *bd0064*	CGTTGTAAAACGACGGCCAGTGCCAAGCGTTTTCGATTTTCAG
64mCit_up_R		CGCCCTTGCTCACTCCGACTTTTTTAAAGATCG
64mCit_F	Amplifies the *bd0064* gene	TAAAAAAGTCGGAGTGAGCAAGGGCGAGGAG
64mCit_R		GTTTTTGCGGATCCTACTTGTACAGCTCGTCCATG
64mCit_down_F	Amplifies 1 kb of downstream DNA flanking *bd0064*	GCTGTACAAGTAGGATCCGCAAAAACAAAAAG
64mCit_down_R		GGAAACAGCTATGACCATGATTACGAGCTCTACGGTGACTGAATC
Construction of Bd1075-mCherry (full length) as a single-crossover fusion		
1075_up_F	Amplifies the full length *bd1075* gene with 1 kb of upstream DNA	CGTTGTAAAACGACGGCCAGTGCCAGACCATCGGAACCGCGTG
Full_1075_R		CTTGCTCACCATTTGCGTTTTCTGGGAAGAGG
Full_mCh_F	Amplifies the *mCherry* gene	CCAGAAAACGCAAATGGTGAGCAAGGGCGAG
1075_mCh_R		GGAAACAGCTATGACCATGATTACGTTACTTGTACAGCTCGTCCATG
Construction of Bd1075-mCherry (A304) as a single-crossover fusion		
1075_up_F	Amplifies the *bd1075* gene, terminating at residue A304	CGTTGTAAAACGACGGCCAGTGCCAGACCATCGGAACCGCGTG
A304_R		CTTGCTCACCATAGCCCATTCTTCTCGGATG
A304_mCh_F		AGAAGAATGGGCTATGGTGAGCAAGGGCGAG

1075_mCh_R	Amplifies the *mCherry* gene	GGAAACAGCTATGACCATGATTACGTTACTTGTACAGCTCGTCCATG
Construction of Bd1075-mCherry (E302) as a single-crossover fusion		
1075_up_F	Amplifies the *bd1075* gene, terminating at residue E302	CGTTGTAAAACGACGGCCAGTGCCAGACCATCGGAACCGCGTG
E302_R		CTTGCTCACCATTTCTTCTCGGATGATTTTATAAGTGTCAC
E302_mCh_F	Amplifies the *mCherry* gene	CATCCGAGAAGAAATGGTGAGCAAGGGCGAG
1075_mCh_R		GGAAACAGCTATGACCATGATTACGTTACTTGTACAGCTCGTCCATG
Construction of Bd1075-mCherry (C156A) as a single-crossover fusion		
1075_up_F	Amplifies the full length *bd1075* gene, mutating the cysteine residue at position 156 to an alanine	CGTTGTAAAACGACGGCCAGTGCCAGACCATCGGAACCGCGTG
C156A_R		CCGCGGGTCAAAGGCACC
C156A_F	Amplifies the full length *bd1075* gene, mutating the cysteine residue at position 156 to an alanine	CTCTCGCGGCGCGGTCGTTGTTCGTAACGACG
Full_1075_R		CTTGCTCACCATTTGCGTTTTCTGGGAAGAGG
Full_mCh_F	Amplifies the *mCherry* gene	CCAGAAAACGCAAATGGTGAGCAAGGGCGAG
1075_mCh_R		GGAAACAGCTATGACCATGATTACGTTACTTGTACAGCTCGTCCATG
Construction of Bd1075-mCherry (Y274A) as a single-crossover fusion		
1075_up_F	Amplifies the full length *bd1075* gene, mutating the tyrosine residue at position 274 to an alanine	CGTTGTAAAACGACGGCCAGTGCCAGACCATCGGAACCGCGTG
Y274A_R		GTTTTCACCAGCAACTGATC
Y274A_F	Amplifies the full length *bd1075* gene, mutating the tyrosine residue at position 274 to an alanine	CCTGCAGCGCGCGGAATCTGACAAAC
Full_1075_R		CTTGCTCACCATTTGCGTTTTCTGGGAAGAGG
Full_mCh_F	Amplifies the *mCherry* gene	CCAGAAAACGCAAATGGTGAGCAAGGGCGAG
1075_mCh_R		GGAAACAGCTATGACCATGATTACGTTACTTGTACAGCTCGTCCATG
Single-crossover based complementation of Δ*bd1075*		

1075_up_F	Amplifies the *bd1075*$_{HD100}$ gene with 1 kb of upstream DNA	CGTTGTAAAACGACGGCCAGTGCCAGACCATCGGAACCGCGTG
1075_SXOcomp_R		GGAAACAGCTATGACCATGATTACGTTATTGCGTTTTCTGGGAAGAG
Deletion of *bd1075* in the double Δ*bd0886*Δ*bd1176* deletion strain		
1075_up_F	Amplifies 1 kb of upstream DNA flanking *bd1075*	CGTTGTAAAACGACGGCCAGTGCCAGACCATCGGAACCGCGTG
1075_up_R		CTAGTTTATTGCGTCTCATAAATACTATTATGCCCGAATAGGAC
1075_down_F	Amplifies 1 kb of downstream DNA flanking *bd1075*	AGTATTTATGAGACGCAATAAACTAGGCTGTAAAG
1075_down_R		GGAAACAGCTATGACCATGATTACGAGCCAAGTTGGTTTTGTATTC

2.1.3. Plasmids used in this study

Table 2.3. Table of plasmids

Plasmid	Description	Source
pK18*mobsacB*	Suicide vector (encoding kanamycin resistance, *lacZ*α for blue-white colony selection, and s*acB* for sucrose counter-selection) used for homologous recombination into the *B. bacteriovorus* genome	Schafer *et al*. (1994)[159]
pAKF56	Template for the *mCherry* gene	Fenton *et al*. (2010)[149]
pK18 Bd3285-mCherry SXO	pK18 plasmid containing the *bd3285* gene (minus the start codon and signal peptide), with mCherry fused to the protein C-terminus, to generate a single-crossover fusion of Bd3285-mCherry	This study
pK18 Δ*bd3285*	pK18 plasmid containing 1 kb of DNA upstream and downstream from *bd3285* to generate a deletion of *bd3285*	This study
pK18 Bd0064-mCherry SXO	pK18 plasmid containing the *bd0064* gene, with mCherry fused to the protein C-terminus, to generate a single-crossover fusion of Bd0064-mCherry	Our laboratory, Willis *et al*. (2016)[47]
pK18 Bd3285 WT comp DXO	pK18 plasmid containing the wild-type *bd3285* gene with 1 kb of upstream and downstream flanking DNA to generate a double-crossover complementation of Δ*bd3285*	This study
pK18 Bd3285 D321A comp DXO	pK18 plasmid containing the *bd3285* gene (with a mutation of D321A) with 1 kb of upstream and downstream flanking DNA to generate a double-crossover complementation of Δ*bd3285*	This study
pBAD HisA	pBAD HisA vector, *ara*BAD promoter, *ara*C, ampicillin resistance (swapped for kanamycin resistance in our laboratory)	Guzman *et al*. (1995)[160]
pBAD Bd3285 (WT)-mCherry	pBAD plasmid containing the wild-type *bd3285* gene fused to mCherry under the control of an arabinose-inducible promoter	This study
pBAD Bd3285 (D321A)-mCherry	pBAD plasmid containing the *bd3285* gene (with a point mutation of D321A) fused to mCherry under the control of an arabinose-inducible promoter	This study

pK18 Bd0599-mCherry SXO	pK18 plasmid containing the *bd0599* gene with 300 bp of upstream DNA and mCherry fused to the protein C-terminus, to generate a single-crossover fusion of Bd0599-mCherry	This study
pK18 Δ*bd0599*	pK18 plasmid containing 500 bp of DNA upstream and downstream from *bd0599* to generate a deletion of *bd0599*	This study
pBAD Bd0599-mCherry	pBAD plasmid containing the *bd0599* gene fused to mCherry under the control of an arabinose-inducible promoter	This study
pK18 Δ*bd1075*	pK18 plasmid containing 1 kb of DNA upstream and downstream from *bd1075* to generate a genetic deletion of *bd1075*	Banks (2018)[158]
pMQBAD	pMQBAD plasmid, gentamicin resistance, tdTomato gene, capable of autonomous replication within *B. bacteriovorus*	Our laboratory, derived from Mukherjee *et al*. (2015) [161]
pMQBAD *bd1075*$_{HD100}$	pMQBAD plasmid containing the *bd1075* gene and 100 bp of flanking DNA from *B. bacteriovorus* HD100	This study
pMQBAD *bd1075*$_{109J}$	pMQBAD plasmid containing the *bd1075* gene and 100 bp of flanking DNA from *B. bacteriovorus* 109J	This study
pET41 Bd1075	pET41 plasmid containing the *bd1075* gene (minus the signal peptide and stop codon) in-frame with a C-terminal hexahistidine tag	This study (Dr Ian Cady)
pK18 Bd1075-mCherry DXO	pK18 plasmid containing the *bd1075* gene with 1 kb of upstream and downstream flanking DNA, and with mCherry fused to the protein C-terminus, to generate a double-crossover fluorescent fusion	Banks (2018)[158]
pmCerulean3-N1	Template for the *mCerulean3* gene, kanamycin resistance, high copy number	Addgene (#54730)
pK18 Bd0064-mCerulean3 SXO	pK18 plasmid containing the *bd0064* gene with a C-terminal fusion of mCerulean3 to generate a single-crossover fluorescent fusion	This study
pET LIC mCitrine cloning vector	Template for the *mCitrine* gene, ampicillin resistance, low copy number	Addgene (#29771)

pK18 Bd1075-mCitrine SXO	pK18 plasmid containing the *bd1075* gene with 1 kb of upstream DNA and mCitrine fused to the protein C-terminus to generate a single-crossover fluorescent fusion	This study
pK18 Bd0064-mCitrine	pK18 plasmid containing the *bd0064* gene with 1 kb of upstream and downstream flanking DNA and with mCitrine fused to the protein C-terminus to generate a either a double-crossover or single-crossover merodiploid fluorescent fusion	This study
pK18 Bd1075-mCherry (Full) SXO	pK18 plasmid containing the wild-type full length *bd1075* gene with 1 kb of upstream DNA and mCherry fused to the protein C-terminus to generate a single-crossover fluorescent fusion	This study
pK18 Bd1075-mCherry (A304) SXO	pK18 plasmid containing the *bd1075* gene (which terminates at the residue A304) with 1 kb of upstream DNA and mCherry fused to the protein C-terminus to generate a single-crossover fluorescent fusion	This study
pK18 Bd1075-mCherry (E302) SXO	pK18 plasmid containing the *bd1075* gene (which terminates at the residue E302) with 1 kb of upstream DNA and mCherry fused to the protein C-terminus to generate a single-crossover fluorescent fusion	This study
pK18 Bd1075-mCherry (C156A) SXO	pK18 plasmid containing the full length *bd1075* gene (with a point mutation of C156A) with 1 kb of upstream DNA and mCherry fused to the protein C-terminus to generate a single-crossover fluorescent fusion	This study
pK18 Bd1075-mCherry (Y274A) SXO	pK18 plasmid containing the full length *bd1075* gene (with a point mutation of Y274A) with 1 kb of upstream DNA and mCherry fused to the protein C-terminus to generate a single-crossover fluorescent fusion	This study
pK18 Bd1075 comp SXO	pK18 plasmid containing the *bd1075* gene and 1 kb of flanking DNA to generate a single-crossover complementation of Δ*bd1075*	This study

2.2. Bacterial culture

2.2.1. Bacterial growth media

YT broth and agar

5 g/l NaCl, 5 g/l Difco-Bacto yeast extract, and 8 g/l Difco Bacto-tryptone, adjusted to pH 7.5 with 2 M NaOH and sterilised by autoclaving. For YT agar, 10 g/l of Sigma Select agar was added prior to sterilisation.

YPSC double layer overlay plates

0.25 g/l $MgSO_4.7H_2O$, 0.5 g/l anhydrous sodium acetate, 1 g/l broad bean peptone (Sigma), and 1 g/l Difco-Bacto yeast extract, adjusted to pH 7.6 with 2 M NaOH and sterilised by autoclaving. Following sterilisation, 0.25 g/l $CaCl_2.2H_2O$ was added. For YPSC bottom and top agar, either 10 g/l or 6 g/l of Sigma Select agar was added, respectively, prior to sterilisation.

Calcium HEPES (Ca/HEPES) buffer

5.94 g/l HEPES free acid and 0.294 g/l $CaCl_2.2H_2O$, adjusted to pH 7.6 with 2 M NaOH and sterilised by autoclaving.

PY broth and agar

10 g/l peptone (broad bean for broth and Difco-Bacto for agar) and 3 g/l Difco yeast extract, adjusted to pH 6.8 with 2 M NaOH and sterilised by autoclaving. For PY agar, 10 g of Sigma Select agar was added prior to sterilisation.

2.2.2. Routine culture of *E. coli* strains

E. coli strains were cultured in either YT liquid medium at 37 °C for 16 h with orbital shaking at 200 rpm, or on YT agar plates for 16 h at 37 °C. Where appropriate, kanamycin (25-50 µg/ml), gentamicin (5 µg/ml), ampicillin (100 µg/ml), X-Gal (40 µg/ml) or IPTG (40 µg/ml) were added to the medium. *E. coli* strains were regularly re-streaked from frozen glycerol stocks to maintain fresh cultures. Details of *E. coli* culture for specific purposes – for example conjugation - are described in later sections. Generally, stationary phase (cultured for ~ 16 h) *E. coli* S17-1 cells were used as prey for *B. bacteriovorus*.

2.2.3. Routine culture of *B. bacteriovorus* strains

Prey-dependent strains of *B. bacteriovorus* were cultured predatorily in either liquid buffer or on double-layer agar overlay plates containing the desired prey bacteria – usually stationary phase *E. coli* S17-1. For growth in liquid medium, a predatory culture typically consisted of either 2 ml calcium HEPES (Ca/HEPES) buffer containing 150 µl of prey and 50 µl of a previous *B. bacteriovorus* culture, or 10 ml Ca/HEPES containing 600 µl of prey and 200 µl of a previous *B. bacteriovorus* culture. Liquid cultures were incubated at 29 °C with orbital shaking at 200 rpm for 24 h or until complete prey lysis was observed by phase-contrast microscopy. Culture freshness was maintained by sub-culturing every 24 h.

For growth on solid medium, a double-layer overlay technique was used in which 100 µl of *B. bacteriovorus* was mixed with 100 µl of *E. coli* S17-1 prey and 5 ml of molten YPSC 0.6% top agar (at 55 °C) and then poured onto YPSC 1% bottom agar. Once set, plates were inverted and incubated at 29 °C until plaques of *B. bacteriovorus* developed (usually after 3-7 days). Kanamycin-resistant (kan^R) strains of *B. bacteriovorus* were cultured on *E. coli* S17-1 (pZMR100) (kan^R) in the presence of kanamycin (50 µg/ml).

B. bacteriovorus strains were revived from frozen stocks (21% glycerol) approximately every 2 weeks. For revival, 50 µl of a minimally-thawed glycerol stock was pipetted onto a double-layer overlay plate containing 100 µl of prey bacteria within the top agar layer. The glycerol stock was snap-frozen in liquid nitrogen and the overlay plate was incubated at 29 °C (with inversion once dry) until a *B. bacteriovorus* zone of lysis appeared after 2 days. A pipette tip was used to pick from the zone of lysis and inoculate 2 ml Ca/HEPES containing 150 µl of prey. The culture was incubated at 29 °C, shaking at 200 rpm, for 48 h until prey were fully lysed, giving free-swimming attack-phase *B. bacteriovorus* cells.

2.3. Quantification of *B. bacteriovorus* cell numbers

2.3.1. Plaque counts

Host-dependent *B. bacteriovorus* strains cannot be quantified by optical density readings at OD_{600} due to their small size and must instead be quantified using plaque counts. To do this, *B. bacteriovorus* strains were diluted (typically 10^{-4}, 10^{-5} and 10^{-6} dilutions) and 100 µl of each dilution was mixed with 100 µl of stationary phase *E. coli* S17-1 (S17-1 pZMR100 if the predator strain was kanamycin-resistant) and 5 ml of YSPC top agar in a bijou tube. The top agar containing predators and prey was carefully poured onto a YPSC bottom agar plate to create a double-layer overlay. After the overlays had set, plates were inverted and incubated at 29 °C until countable plaques had appeared (generally 5-7 days). From the plaque counts (carried out in triplicate due to inherent variability), the original concentration of predator cells that had been used in the experiment could be determined and expressed in PFU/ml.

Unfortunately, plaque counts can only retrospectively inform on the concentration of predator strains used in an experiment. It is therefore important to match the concentration of predator strains at the time of the experiment. It is important that an approximately equal concentration of wild-type and mutant strains are added to prey to compare predation efficiency, for example. In my PhD, I attempted to match *B. bacteriovorus* strains using three different techniques which are described below.

2.3.2. Lowry assay

The standard method that had been used previously in the lab to match predator concentrations was a Lowry assay[162] with Markwell's modification[163] which uses total protein content to match samples. The Lowry assay uses Folin's phenol reagent in the presence of copper-

bound proteins to measure a colour change that can be detected at OD_{750} in a spectrophotometer.

Attack-phase *B. bacteriovorus* cultures were filtered through a 0.45 µm filter to remove any remaining debris and 20 ml were centrifuged at 5,000 x *g* for 20 min, and 15 ml of supernatant was removed. The culture was re-centrifuged for 5 min and 4 ml of supernatant was removed. The pellet was resuspended in the remaining 1 ml and transferred to a microcentrifuge tube. The culture was microcentrifuged at 17,000 x *g* for 2 min and the pellet was resuspended in 1 ml of H_2O and aliquoted into cuvettes for quantification by Lowry assay. To make a standard protein concentration curve, 1 mg/ml of bovine serum albumin (BSA) was serially diluted (10-100 µg/ml) and aliquoted into cuvettes.

To each cuvette sample, 1.5 ml of Lowry Solution C (Solution A: Solution B in a ratio of 99:1) was added and the samples were then incubated in the dark for 20 min. After 20 min, 150 µl of Folin's mix (a 1:1 ratio of Folin's reagent and H_2O) was added to each cuvette, mixed, and incubated for a further 45 min in the dark. The OD_{750} of each sample was measured in a spectrophotometer and a standard curve was generated. From the standard curve, the OD_{750} readings of *B. bacteriovorus* strains were converted to protein concentration and used to match the strains.

The assay has several limitations including the lengthy duration (approximately 2 h), the indirect measurement of cell number using protein content, it not being a viable cell count, and a large discrepancy between the Lowry values and the ultimate, true *B. bacteriovorus* concentrations as determined by plaque counts. For this reason, two alternative assays were trialled as described below.

Solution A

2% (w/v) Na_2CO_3, 0.4% (w/v) NaOH, 0.16% (w/v) $Na_4C_4H_4O_6$ (sodium tartrate), 1% (w/v) SDS, all made up with distilled water.

Solution B

4% (w/v) $CuSO_4.5H_2O$, made up with distilled water.

2.3.3. NanoOrange assay

The first alternative assay to be trialled also used the indirect measure of total protein content to try and match *B. bacteriovorus* concentrations. The assay used the fluorescence-based NanoOrange™Protein Quantification Kit (Invitrogen) which contains a NanoOrange® protein quantitation reagent, NanoOrange® protein quantitation diluent and a BSA standard. NanoOrange does not fluoresce in aqueous solution but upon binding to proteins, the reagent emits strong fluorescence. The assay has a higher degree of sensitivity than other protein quantification assays including the Lowry assay. *B. bacteriovorus* samples were added to diluted NanoOrange® reagent (prepared according to the manufacturer's instructions) and heated at 95 °C for 10 min in the dark. Samples were cooled to room temperature in the dark and fluorescence readings were acquired at 590 nm in a spectrophotometer. The protein concentration of *B. bacteriovorus* strains was calculated using a BSA standard curve.

The primary advantage of the NanoOrange assay over the Lowry assay was that it is a less time-intensive assay (approximately 50% time duration), however, there were still limitations as it is an indirect measurement of cell number and there was variation between the assay-determined predator concentration and the true concentration determined by plaque count (although this was slightly improved in the NanoOrange assay – most probably due to the higher sensitivity of the NanoOrange reagent (50-100-fold greater than Lowry)).

2.3.4. Petroff-Hausser counting chamber

Due to the limitations of the protein content-based matching assays, a new method developed by Williams *et al*. (2019)[164] for *B. bacteriovorus* strains was trialled. The assay uses a Petroff-Hausser counting chamber (haemocytometer) to directly count *B. bacteriovorus* predator cells. To prepare *B. bacteriovorus* strains for counting, predatory cultures were filtered through a 0.45 µm membrane and 20 µl were mixed with 20 µl of 1 M sodium acetate buffer (pH 4.0) and vortexed to immobilise the predator cells and facilitate counting. 5 µl of predatory culture was pipetted onto the counting chamber and placed under the 100X oil immersion lens of a Nikon Eclipse upright microscope. The number of bacteria in each of 15 randomly selected squares was counted and averaged, and from this, the concentration of each *B. bacteriovorus* strain (cells/ml) was calculated. The primary advantage of this assay was that cells are counted directly rather than quantified indirectly, however, the method cannot distinguish between live and dead cells. The method was also very time-consuming, particularly when quantifying multiple *B. bacteriovorus* strains since each strain must be counted sequentially and this could take approximately 2-4 before setting up long experiments.

The NanoOrange assay appeared to be best of the three tested methods, however a new assay has been since been developed for *B. bacteriovorus* cell matching which is based on the reagent SYBR Green that binds to DNA[165]. It would therefore be worth validating this method in the future.

2.4. Predation efficiency assays

2.4.1. Predation efficiency in liquid culture

The predation efficiency of *B. bacteriovorus* wild-type and ∆*bd1075* strains in liquid culture was measured using prey luminescence as a reporter for predation. This luminescent prey assay was developed by Lambert *et al*. (2003)[166] and utilises the *E. coli* S17-1 strain strawberry lux which emits luminescence. *B. bacteriovorus* strains were cultured for 24 h and then matched by Lowry assay (**Section 2.3.2**). The matched strains were enumerated on double-layer overlay plates on which plaques developed after approximately 5-7 days. *E. coli* S17-1 strawberry lux was grown for 16 h and then adjusted to an OD_{600} = 0.2 in a 1:1 mixture of Ca/HEPES and PY medium. The prey was then aliquoted (200 µl) into each well of a 96-well microtiter optiplate. The *E. coli* prey was also enumerated on YT agar plates incubated at 37 °C for 16 h and generally had a concentration of 10^7 CFU/ml. A sample of each *B. bacteriovorus* strain was incubated at 105 °C for 5 min to heat-kill the cells. In the 96-well microtiter plate, a dilution series of *B. bacteriovorus* was created by aliquoting 0, 1, 2, 4, 8, 16, 32, and 64 µl of live predator cells into each well containing *E. coli* prey and making this up to a total of 64 µl using the heat-killed predator cells. The microtiter plate was covered with a Breathe-Easy® membrane and incubated in a BMG FLUOstar microplate reader at 29 °C with double orbital shaking at 200 rpm. The reduction in *E. coli* luminescence was measured every 30 min for 21 h. To compare the rates of predation, the area under each luminescence curve was measured and then normalised to the maximum luminescence value reached (as this differed between samples) for each dilution. These values were then plotted against *B. bacteriovorus* concentrations determined by plaque count. Data were analysed using BMG LABTECH MARS analysis software.

2.4.2. Predation efficiency on pre-formed prey biofilms

The predation efficiency of *B. bacteriovorus* wild-type and ∆*bd1075* strains on pre-formed *E. coli* prey biofilms was measured using an assay that was adapted from Lambert & Sockett (2013)[167] and Medina *et al*. (2008)[168]. 50 ml cultures of *B. bacteriovorus* and *E. coli* S17-1 strains were grown for 24 h and 16 h, respectively. *E. coli* S17-1 was adjusted to an OD_{600} = 0.1 and 200 µl were aliquoted into each well of a PVC microtiter plate. The plate was then incubated at 29 °C in a static incubator for 24 to allow biofilm development. The *E. coli* culture was also enumerated on YT plates as described before. Each *B. bacteriovorus* culture was split into two tubes and then filtered through either a 0.45 µm filter or a 0.22 µm filter (a negative no-predator control). Predator strains were matched using the NanoOrange assay (**Section 2.3.3**) and enumerated by plaque counts. Following 24 h of *E. coli* biofilm incubation, the microtiter plate was washed three times with Ca/HEPES, then 200 µl of *B. bacteriovorus* strains (in dilutions of 10^0, 10^{-1}, 10^{-2} and 10^{-3}) were added to the wells. The plate was incubated at 29 °C in a static incubator for 24 h. The microtiter plate was then stained by addition of 200 µl of 1% crystal violent to each well for 15 min. The plate was then washed with sterile distilled water and de-stained with 33% acetic acid for 15 min. The samples were mixed and 150 µl from each well was transferred to a black optiplate. The OD_{600} of each well was measured in a spectrophotometer and used to quantify the levels of remaining biofilm.

2.5. Bdelloplast damage assay

Potential bdelloplast damage caused by rod-shaped Δ*bd1075 B. bacteriovorus* predator cells growing inside prey bdelloplasts was tested using a bdelloplast damage assay developed by Kuru, Lambert *et al*. (2017)[33]. The assay measures leakage of β-galactosidase from prey bdelloplasts upon osmotic upshock, downshock or no shock. β-galactosidase converts the substrate chlorophenol red-β-D-galactopyranoside (CPRG) to the product chlorophenol red, causing a colour change from yellow to red. The colour change is detected at OD_{574} and is used to quantify bdelloplast leakage of β-galactosidase into the surrounding medium and thus report on bdelloplast stability. The CPRG assay method is illustrated in Figure 5.12 in **Chapter 5**, where it is placed to describe the experiment within the context of the results.

B. bacteriovorus strains were cultured for 24 h, then concentrated 50X by centrifugation at 5,000 x *g* for 20 min. *B. bacteriovorus* strains were matched to a starting cell count of $5x10^9$ cells using the Petroff-Hausser counting chamber method (**Section 2.3.4**). *E. coli* S17-1 was cultured for 16 h to stationary phase and then incubated with IPTG at 37 °C shaking for 2 h to stimulate the production of β-galactosidase, then washed and adjusted to an OD_{600} = 1.0 in Ca/HEPES. *B. bacteriovorus* strains and *E. coli* prey were mixed in microcentrifuge tubes (one sample per osmotic shock treatment) and incubated for 2.5 h at 29 °C shaking. Control samples did not contain *E. coli* prey. Predatory cultures were observed under the microscope after 30 min to ensure that the cultures were synchronous (>95% of bdelloplasts rounded). *E. coli* and *B. bacteriovorus* strains were enumerated on either YT plates or YPSC double-layer overlays, respectively.

After 2.5 h, all predatory cultures were removed from the incubator and microcentrifuged at 17,000 x *g* for 2 min and the supernatant was removed. Samples for osmotic downshock were resuspended in 1.2 ml

of Ca/HEPES containing 750 mM NaCl (initial upshock) and incubated at 29 °C in a static incubator for 30 min. During this time, the remaining cultures were either resuspended in 1.2 ml Ca/HEPES + 20 µg/ml CPRG (no shock treatment) or 1.2 ml Ca/HEPES containing 750 mM NaCl (osmotic upshock) and incubated at room temperature. The downshock treatment tubes were removed from the incubator and microcentrifuged again at 17,000 x *g* for 2 min. The pellets were resuspended in 1.2 ml Analar H2O + 20 µg/ml CPRG (final downshock treatment). Tubes from all treatments were incubated at 29 °C in a static incubator for 30 min. All tubes were microcentrifuged at 17,000 x *g* for 2 min to pellet the cells and the supernatant was filtered through a 0.22 µm membrane into a fresh microcentrifuge tube to isolate the bdelloplast leakage products. All samples were finally incubated at 29 °C in a static incubator for 21 h during which a colour change reaction occurs. Following incubation, 500 µl of each sample was transferred to a cuvette and absorbance was measured at OD_{574} in a spectrophotometer. Higher absorbance values corresponded with a stronger colour change, representing greater leakage of β-galactosidase from prey bdelloplasts.

2.6. RNA isolation and reverse-transcriptase PCR

2.6.1. Isolation of RNA samples from *B. bacteriovorus*

2.6.1.1. Isolation of RNA samples from *B. bacteriovorus* attack-phase cells

B. bacteriovorus was cultured in 50 ml Ca/HEPES containing 3 ml of *E. coli* S17-1 prey and 1 ml of a previous predatory culture for 24 h at 29 °C with shaking at 200 rpm. The lysed culture was filtered through a 0.45 µm membrane to remove residual prey debris and then centrifuged at 5,000 x *g* for 20 min at 29 °C. The cell pellet was resuspended in 4 ml of Ca/HEPES and 1 ml of 5% phenol: 95% ethanol, and incubated on ice for 45 min. The sample was then centrifuged at 5,000 x *g* for 10 min at 4 °C and the supernatant removed. The sample was centrifuged for an additional 2 min, the residual supernatant was removed, and the pellet was stored at -20 °C until RNA extraction.

2.6.1.2. Isolation of RNA samples from timepoints during the predatory cycle of *B. bacteriovorus* on *E. coli* S17-1 prey

In my PhD, it was important to analyse the transcriptional patterns of certain *B. bacteriovorus* genes throughout the predatory cycle. This required the isolation of total RNA across important timepoints in the predatory cycle.

To do this, *B. bacteriovorus* HD100 was cultured in 1 L Ca/HEPES containing 60 ml of stationary phase *E. coli* S17-1 and 50 ml of a previous predatory culture for 24 h at 29 °C with shaking at 200 rpm. Following complete prey lysis, the culture was dispensed into sterile tubes and centrifuged at 15,000 x *g* for 30 min at 29 °C. Concurrently, a stationary phase culture of *E. coli* S17-1 (100 ml) was centrifuged at 5,000 x *g* for 10 min at 29 °C then back-diluted in Ca/HEPES to an OD_{600} of 1.0. The *E. coli* culture was incubated at 29 °C for 1 h with shaking at 200 rpm to stabilise gene expression. Centrifuged pellets of *B. bacteriovorus* were

rapidly but gently resuspended in Ca/HEPES to a total volume of 100 ml. The culture was incubated at 29 °C for 1 h with shaking at 200 rpm to stabilise gene expression along with 3 flasks containing either 80 ml, 70 ml or 30 ml of Ca/HEPES.

After 1 h, each of the 3 flasks was inoculated with either: 1) 40 ml of *E. coli* (to the flask containing 80 ml of Ca/HEPES) to generate an *E. coli* only control, 2) 50 ml of *B. bacteriovorus* (to the flask containing 70 ml of Ca/HEPES) to generate a *B. bacteriovorus* only control, or 3) 40 ml of *E. coli* and 50 ml of *B. bacteriovorus* (to the flask containing 30 ml of Ca/HEPES) to generate the predatory test condition. Flasks were rapidly transferred to the 29 °C incubator shaking at 200 rpm. After 5 min, 4 ml samples in triplicate were removed from the *E. coli* control flask and transferred to 15 ml tubes containing 1 ml of 5% phenol: 95% ethanol, mixed well by inversion and incubated on ice for a minimum of 45 min. The process was repeated for the *B. bacteriovorus* control after 10 min. For the predatory test flask, samples were rapidly removed and processed in the same manner at the timepoints of 15 min, 30 min, 45 min, 1 h, 2 h, 3 h and 4 h.

Synchronicity of the predatory culture was assessed at 30 min using phase-contrast microscopy to confirm that >95% of *E. coli* prey had been rounded up and invaded, and the remainder of prey had an attached *B. bacteriovorus* predator. The multiplicity of infection (MOI) was determined by predator and prey PFU and CFU counts, respectively, with *B. bacteriovorus* usually in being excess of about 2-5X.

Following incubation in phenol/ethanol on ice, samples were centrifuged at 5,000 x *g* for 10 min at 4 °C and the supernatant removed. Samples were centrifuged for a further 30 s and the residual supernatant removed. Sample pellets were then frozen and maintained at -80 °C until RNA extraction.

2.6.2. RNA extraction and quality assessment

Bacterial cell pellets were thawed on ice and RNA was extracted using the SV Total RNA Isolation System (Promega) kit according to the manufacturer's instructions. Eluted RNA was stored in RNase-free tubes at -20 °C.

To confirm the absence of any contaminating DNA in RNA samples, a PCR was set up using universal 16S rDNA forward and reverse primers and an additional *Bdellovibrio*-specific forward primer. Each 25 µl reaction contained 2.5 µl of DreamTaq™ Green Buffer (10X), 2.5 µl of dNTPs (10 mM), 0.5 µl of each primer (100 µM), 0.2 µl of DreamTaq DNA polymerase, 17.8 µl of water, and 0.5 µl of PCR template (either RNA sample, *E. coli* gDNA or *B. bacteriovorus* gDNA positive controls or water negative control). The thermocycling conditions were as follows: initial denaturation at 95 °C for 5 min, followed by 30 cycles of denaturation at 95 °C for 30 s, annealing at 58 °C for 30 s, and extension at 72 °C for 1 min 30 s. There was a final extension at 72 °C for 10 min and PCR products were run on a 0.8% agarose gel for 1 h. The presence of 1.5 kb products for the gDNA positive controls and absence of bands in RNA samples confirmed that the RNA samples were not contaminated with DNA. If DNA was detected in RNA samples then the RNA was cleaned up using the RNeasy Mini Kit (Qiagen), according to the manufacturer's instructions, and tested again by PCR.

DNA-free RNA samples were subjected to a final quality control check on an Agilent 2100 Bioanalyzer using the Agilent RNA 6000 Nano Kit according to the manufacturer's instructions.

2.6.3. Reverse-transcriptase PCR (RT-PCR)

RT-PCR primers were designed to amplify a small product (~100 bp) internal to the transcript of the gene of interest. Primers were checked for specificity to only the *B. bacteriovorus* genome with Primer-BLAST[169]. RT-PCRs used components from the Qiagen OneStep RT-PCR kit. Each 25 µl reaction contained 5 µl of buffer (5X), 5 µl of Q-solution (5X), 1 µl of dNTP mix, 0.15 µl each primer (100 µM), 1 µl of Enzyme Mix, 12.2 µl of RNase-free water, and 0.5 µl of PCR template (either RNA sample, *B. bacteriovorus* gDNA positive control or water negative control). The following thermocycling parameters were used: Reverse transcription of RNA into cDNA (50 °C for 30 min), followed by inactivation of reverse transcriptase enzyme and activation of DNA polymerase (94 °C for 15 min). There followed 30 cycles of denaturation at 94 °C for 1 min, annealing at 50 °C for 1 min, and extension at 72 °C for 1 min. There was a final extension of 72 °C for 10 min. RT-PCR products were visualised on a 2% agarose gel run for 30 min at 100 V and band sizes were measured against a 100 bp DNA ladder (NEB). The *B. bacteriovorus* gene *dnaK* was used as a positive control for the confirmation of the presence/absence of another gene transcript. *B. bacteriovorus dnaK* is constitutively transcribed at a constant expression level during predation and therefore also served as a control gene for RT-PCR carried out on a gene of interest during the predatory cycle.

2.7. Standard molecular cloning techniques

2.7.1. Preparation of chemically-competent *E. coli*

To prepare competent cells, the desired *E. coli* strain was cultured in 10 ml of YT at 37 °C for 16 h with shaking at 200 rpm. The overnight culture was diluted 1:100 in fresh YT and grown to an OD_{600} of 0.4-0.6. The *E. coli* cells were then centrifuged in 50 ml aliquots at 5,000 x *g* for 5 min at 4 °C, resuspended in 20 ml of ice-cold TFB1 and incubated on ice for 5 min. The cell suspension was centrifuged again under the same conditions then the pellet was resuspended in 2 ml of ice-cold TFB2 and incubated on ice for 1 h. Aliquots of 200 µl were snap-frozen in liquid nitrogen and stored at -80 °C.

TFB1

2.94 g/l potassium acetate (30 mM), 1.47 g/l $CaCl_2.2H_2O$ (10 mM), 9.9 g/l $MnCl_2.4H_2O$ (50 mM), 12.08 g/l RbCl (100 mM), and 15% (v/v) glycerol, adjusted to pH 5.8 with 1 M acetic acid and sterilised through a 0.22 µm filter.

TFB2

2.1 g/l MOPS (10 mM), 11.02 g/l $CaCl_2.2H_2O$ (75 mM), 1.2 g/l RbCl (10 mM), and 15% (v/v) glycerol, adjusted to pH 6.5 with 1 M KOH and sterilised through a 0.22 µm filter.

2.7.2. Genomic DNA extraction from *B. bacteriovorus*

To extract genomic DNA (gDNA), 10 ml of *B. bacteriovorus* culture (in which prey had been fully cleared by the predator) was centrifuged at 5,000 x *g* for 20 min at 29 °C and the supernatant removed. gDNA was extracted using the GenElute™ Bacterial Genomic DNA Kit (Sigma) according to the manufacturer's instructions for Gram-negative bacteria and stored at 4 °C.

2.7.3. Standard PCR for Gibson cloning

To generate plasmid constructs in my PhD, I used the Gibson cloning strategy[170]. Gibson cloning involves the design of long primers that allow the amplification of multiple overlapping fragments. These are seamlessly ligated together into the cut recipient plasmid vector using a Gibson assembly enzyme mix.

To amplify each DNA fragment, 100 µl PCR reactions contained 20 µl of Phusion HF buffer (5X), 20 µl of Q-Solution (5X), 2 µl of dNTPs (10 mM), 1 µl of Phusion DNA polymerase, 0.5 µl of each primer (100 µM), 55 µl of water, and 1 µl of DNA template (plasmid or gDNA). The thermocycling conditions were as follows: initial denaturation at 98 °C for 3 min, followed by 30 cycles of denaturation at 98 °C for 30 s, annealing at 60 °C for 30 s, and extension at 72 °C for 1 min/kb of amplified product. The final extension was at 72 °C for 5 min.

2.7.4. Purification of DNA fragments for cloning

Gibson PCR products were mixed with 30 µl of Orange G DNA loading dye (3X) and run on a 0.8% agarose gel at 100V for 1 h. Product bands were excised and DNA was extracted from agarose band slices using the GenElute™ Gel Extraction Kit (Sigma) according to the manufacturer's instructions.

2.7.5. Gibson assembly and transformation into *E. coli* NEB 5-alpha

Purified PCR products were assembled into the desired plasmid vector using the NEBuilder® HiFi DNA Assembly Cloning Kit (NEB). Gibson assembly reactions consisted of a 3:1 ratio of PCR product to pre-digested plasmid vector mixed with 10 µl of Gibson Assembly Master Mix (2X) and made up to 20 µl with water. The Gibson reactions were

incubated at 50 °C for 60 min and stored on ice for subsequent transformation. Gibson reactions were transformed into chemically-competent *E. coli* NEB 5-alpha cells (NEB) according to the protocol of the NEBuilder® HiFi DNA Assembly Cloning Kit (NEB). Cell transformation mixtures were concentrated 10X and spread onto selection plates supplemented with the appropriate antibiotic marker. X-Gal (40 µg/ml) and IPTG (40 µg/ml) were additionally added to the selection plates if blue-white colony selection was possible.

2.7.6. Plasmid purification and verification

Single colonies of *E. coli* NEB 5-alpha were inoculated into 5 ml of YT and patched onto YT agar plates, both supplemented with the appropriate antibiotic. If blue-white selection was feasible then only white colonies were selected as these clones are likely to contain a plasmid with a disrupted *lacZ*-alpha fragment which indicates probable insertion of the Gibson fragments. *E. coli* clones were grown under standard conditions and the liquid cultures were then centrifuged at 5,000 x *g* for 5 min at 29 °C. The supernatant was removed, and the plasmid DNA purified with the GenElute^{TM} Plasmid Miniprep Kit (Sigma) according to the manufacturer's instructions and stored at -20°C. If purification of many plasmids was required, then an alternative kit-free purification protocol was used. In this method, 200 µl of *E. coli* culture was mixed with 200 µl of alkaline SDS (1% SDS, 0.2 M NaOH) and subsequently with 200 µl of 3 M potassium acetate (pH 5.5). The mixture was microcentrifuged at 17,000 x *g* for 5 min at 29 °C and the supernatant transferred to a new microcentrifuge tube containing 500 µl of 100% isopropanol. The contents were mixed, microcentrifuged again under the same conditions and the supernatant removed. The process was repeated to remove residual supernatant. The pellet was washed with 100 µl of 75% ethanol, microcentrifuged for 1 min and the supernatant removed. The pellet of purified plasmid was dried in a SpeedVac

concentrator for 10 min, resuspended in 25 µl of TE + RNase (10 µg/ml) and stored at -20 °C.

Plasmids were initially screened by diagnostic restriction digests using appropriate restriction enzymes. Each 10 µl digest contained 5 µl of plasmid, 1 µl of FastDigest Green Buffer (10X) (Thermo Scientific™), 0.5 µl of FastDigest Restriction Enzyme(s) (Thermo Scientific™) and 3-3.5 µl of water. Digests were incubated at 37 °C for 15 min and run on 0.8% agarose gel at 100 V for 1 h. DNA products were compared against expected band sizes to identify potentially correct plasmid clones. Plasmid constructs were finally verified by Sanger sequencing (provided by Source Bioscience) and glycerol stocks of correct *E. coli* clones were made and stored at -80 °C.

2.7.7. Generation of site-directed point mutations in plasmids

To change the DNA encoding one amino acid to a different amino acid within a plasmid, one of two different site-directed mutagenesis techniques was used. To change a codon within an existing plasmid, mutagenic primers were designed using NEBase Change (NEB) and then mutagenesis was carried out using the Q5® Site-Directed Mutagenesis Kit (NEB) according to the manufacturer's instructions. To construct a new plasmid and simultaneously change a codon of interest, Gibson assembly was carried out with an additional primer pair containing the desired mutation. For both methods, plasmid products were sequenced to verify that the codon had been successfully changed.

2.7.8. Transformation of plasmids into the donor strain *E. coli* S17-1

A 200 µl aliquot of chemically-competent *E. coli* S17-1 was thawed, then 1 µl of plasmid was added to the *E. coli* aliquot and incubated on ice for

2 min. The mixture was heat-shocked at 42 °C for 1 min, placed back on ice for 2 min and then mixed with 1 ml of SOC. Cells were incubated at 37 °C with shaking for 30 min then microcentrifuged at 17,000 x *g* for 2 min at 29 °C. The cell pellet was resuspended in 100 µl of SOC, spread onto YT plates containing the appropriate antibiotic and incubated at 37 °C for 16 h.

2.7.9. Conjugation of plasmids into *B. bacteriovorus*

While *E. coli* S17-1 are preyed upon by *B. bacteriovorus* predators attaching and invading the *E. coli*, it is nonetheless possible for *E. coli* S17-1 cells to attach to the lateral walls of *B. bacteriovorus* predators and deliver plasmids via rolling circle replication. This allows the conjugation of desired plasmid constructs into *B. bacteriovorus*.

To conjugate plasmids into *B. bacteriovorus*, a 10 ml culture of the *E. coli* S17-1 donor strain containing the desired plasmid and a 10 ml culture of the *B. bacteriovorus* host strain recipient were grown under standard conditions. The *B. bacteriovorus* culture was centrifuged at 5,000 x *g* for 20 min at 29 °C, resuspended in ~ 100 µl of residual supernatant and pipetted onto a sterile nylon membrane placed on an antibiotic-free PY plate. The *E. coli* S17-1 donor was centrifuged at 5,000 x *g* for 5 min at 29 °C, resuspended in 100 µl of fresh YT to remove the antibiotic-containing growth medium, and then pipetted onto the nylon membrane containing *B. bacteriovorus*. The PY plate was then incubated at 29 °C for 16 h. The nylon membrane was transferred from the plate to a 20 ml universal tube and the cells washed off the membrane with 1 ml of Ca/HEPES. Double-layer overlay YPSC plates supplemented with the appropriate antibiotic were prepared with 100 µl of antibiotic-resistant S17-1 prey and either 100 µl or 900 µl of the conjugation mixture. YPSC plates were incubated at 29 °C until plaques developed after 3-7 days. The plaques were picked into 2 ml Ca/HEPES containing 150 µl of antibiotic-resistant prey and cultured for 48 h until prey lysis. The

resulting *B. bacteriovorus* strain was either a single-crossover merodiploid strain (pK18*mobsacB* suicide plasmid conjugations) or a strain expressing a protein from a plasmid *in trans* (pMQBAD replicative plasmid conjugations).

2.8. Generation of silent gene deletions

To generate a markerless gene deletion, Gibson assembly was used to generate and seamless ligate overlapping DNA fragments into the non-replicative suicide vector pK18*mobsacB*. The suicide vector integrates into the *B. bacteriovorus* genome in a first genetic crossover event to generate a merodiploid strain. To encourage a second crossover event, the strain undergoes sucrose suicide counter-selection in which the suicide plasmid gene *sacB* (encoding the levansucrase enzyme) converts sucrose to a product that is toxic to *B. bacteriovorus*. This process selects for excision of the genomic plasmid via a second crossover event which results in either a wild-type revertant or genetic knockout exconjugant. The process is illustrated in Figure 2.1.

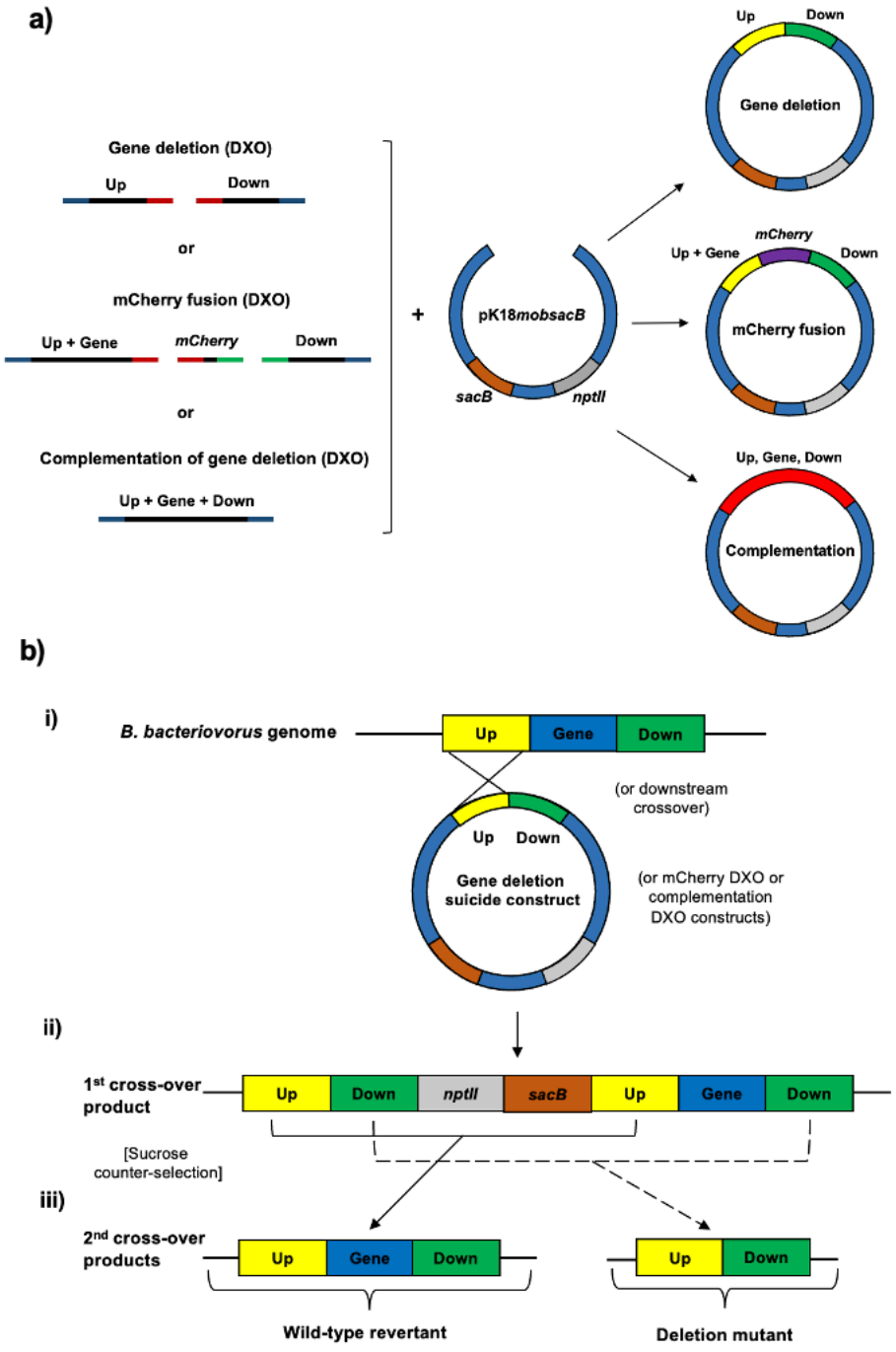

Figure 2.1. Construction of double-crossover *B. bacteriovorus* strains for gene deletions, fluorescent fusions and complementation

a) For gene deletions, generally 1 kb of upstream (Up) and downstream (Down) DNA flanking the gene to be deleted is cloned into the suicide plasmid pK18*mobsacB* by Gibson assembly. For an mCherry fusion, 3 fragments are assembled: 1 kb of upstream DNA and the gene of interest, the *mCherry* gene and 1 kb of downstream DNA. For complementation, 1 kb of upstream DNA, the gene of interest and 1 kb of downstream DNA are cloned into pK18*mobsacB*. DNA fragments are amplified using primers designed to generate fragments with overlapping ends (shown by coloured ends) which

seamlessly assemble into the plasmid vector by Gibson assembly. **b**) Each construct is conjugated into *B. bacteriovorus* (only the gene deletion construct is shown for simplicity but the process is the same). In the 1st crossover event by homologous recombination, the plasmid integrates into the genome. Sucrose counter-selection forces a 2nd crossover event (due to toxicity caused by the *sacB* gene product) where the plasmid is excised and either generates a wild-type revertant or the desired exconjugant (e.g. deletion mutant). Revertants and mutants are distinguished by PCR. *sacB*: levansucrase gene, *nptII:* kanamycin resistance marker.

2.8.1. Construction of the suicide plasmid vector

To construct the suicide plasmid, 1 kb of upstream DNA and 1 kb of downstream DNA flanking the gene of interest were amplified by PCR (**Section 2.7.3**) using overlapping primers designed with NEBuilder (NEB) (Figure 2.1a). The upstream and downstream flanking fragments additionally contained the first 6 bp or the last 9 bp of the gene to be deleted, respectively. If a neighbouring gene was in close proximity to and was convergently transcribed with the gene to be deleted, then the appropriate DNA flanking fragment was extended to include either 50 bp of the start (upstream fragment) or end (downstream fragment) of the gene of interest to avoid disruption to the promoter of the neighbouring gene. The recipient suicide vector pK18*mobsacB* was digested with the restriction enzymes HindIII and EcoRI and the DNA fragments were cloned into the vector using Gibson assembly (**Section 2.7.5**). The plasmid construct was isolated and verified (**Section 2.7.6**) and conjugated into the host *B. bacteriovorus* strain (**Section 2.7.9**).

2.8.2. Sucrose suicide counter-selection

The pK18*mobsacB* suicide plasmid contains a *sacB* gene which encodes the enzyme levansucrase. Levansucrase converts sucrose to products which are toxic to the cell. Addition of sucrose to the cell culture encourages excision of the plasmid which contains the levansucrase gene.

The merodiploid *B. bacteriovorus* strain was therefore subjected to sucrose suicide counter-selection to force a second genetic crossover event, removing genome-integrated plasmid and generating either a wild-type revertant or gene deletion mutant (Figure 2.1b). For sucrose suicide counter-selection, predatory cultures contained 2 ml Ca/HEPES (5% sucrose), 50 µl of the merodiploid *B. bacteriovorus* strain, and 150 µl of *E. coli* S17-1 prey which had been heat-killed at 105 °C for 3 min to prevent overgrowth in sucrose. Following at least 3 successful rounds of sub-culture in sucrose, the *B. bacteriovorus* culture was serially diluted and inoculated onto overlay plates to isolate single plaques. Single plaques were picked into 96-well round-bottomed plates containing Ca/HEPES and *E. coli* S17-1 and cultured in a static incubator at 29 °C for 24 h. Two 96-well plates containing either Ca/HEPES and *E. coli* S17-1, or Ca/HEPES (supplemented with 50 µg/ml kanamycin) and *E. coli* S17-1 (pZMR100) were each inoculated with 20 µl from the original plate and cultured in a static incubator at 29 °C for 48 h.

2.8.3. Isolation and verification of gene deletion mutants

Kanamycin-sensitive *B. bacteriovorus* clones were initially screened by colony PCR to identify potential deletion mutants. Primers were designed to flank the region of homologous recombination, annealing at a distance of at least 100 bp away. Each 25 µl PCR reaction contained 2.5 µl of DreamTaq™ Green Buffer (10X), 2.5 µl of dNTPs, 0.3 µl of each primer, 0.3 µl of DreamTaq DNA polymerase, 17.1 µl of water, and 2 µl of predatory lysate as template. Thermocycling conditions were as follows: initial denaturation at 95 °C for 5 min, followed by 35 cycles of denaturation at 95 °C for 10 s, annealing at 60 °C for 30 s and extension at 72 °C (1 min/kb). The final extension was at 72 °C for 10 min. PCR products were visualised on a 0.8 % agarose gen run at 100 V for 1 h. Wild-type revertants and deletion mutants were distinguished by their expected product sizes. gDNA was extracted from potential knockout clones and used as a PCR template. The PCR product was purified and

sequenced to verify successful gene deletion. Whole genome sequencing (provided by MicrobesNG) was additionally used to verify the mutant strains ∆*bd1075* and ∆*bd1075*∆*bd1176*∆*bd0886*, confirming that no genetic mutations had occurred because of the gene deletion.

2.9. Complementation of gene deletions in *B. bacteriovorus*

Complementation is still a relatively 'new' technique in *Bdellovibrio* research, having only been developed in the past few years. When I started my PhD, only plasmid-based complementation had been tested in *B. bacteriovorus*, therefore I initially complemented my ∆*bd1075* deletion mutant using this method (**Chapter 4 Section 4.3.3**). As my PhD progressed, I tested two different methods that were cis-based, using homologous recombination into the genome. This could be achieved by either single-crossover recombination, generating a strain containing the plasmid construct and gene of interest under antibiotic selection (**Chapter 4 Section 4.3.7.2** and **Chapter 5 Section 5.3.3**), or double-crossover recombination, generating a markerless strain in which the plasmid is excised and the gene has been silently re-introduced (**Chapter 3 3.3.7**). I discovered that double-crossover cis-complementation (which I show for my Bd3285 work in Chapter 3) was most effective, although the process was more time-consuming (~ 2 months). I outline the process for each type of complementation below.

2.9.1. Plasmid-based complementation

This was the original complementation method and used for initial complementation studies of *bd1075* (**Chapter 4 Section 4.3.3**). To generate plasmids for complementation *in trans*, the gene of interest plus 100 bp of flanking DNA (to include the native gene promoter) was cloned into the vector pMQBAD, a derivative of the original plasmid pMQ414

which was generated by Mukherjee *et al*. (2016) and shown to be capable of autonomous replication within *B. bacteriovorus*[161]. The plasmid constructs were conjugated into *B. bacteriovorus* (as described in **Section 2.7.9**) and maintained under a gentamicin selection pressure. It is important to note that plasmid expression in *B. bacteriovorus* is not optimal due to the nature of filamentous growth and septation into multiple progeny which makes plasmid segregation difficult. Former attempts by the lab to generate an over-expression system in *B. bacteriovorus* via either arabinose or IPTG induction were unsuccessful. Early in my PhD, plasmid-based complementation resulted in partial complementation. I therefore explored the alternative method of cis-complementation by homologous recombination into the genome of the deletion mutant.

2.9.2. Single-crossover homologous recombination-based complementation

To complement a deletion mutant by single-crossover cis-based homologous recombination, the gene of interest plus 1 kb of upstream DNA was cloned into the vector pK18*mobsacB* by Gibson assembly and verified by restriction digest and Sanger sequencing. The complementation construct was the conjugated in the genome of the *B. bacteriovorus* deletion mutant. The resulting single-crossover complementation strain verified by Sanger sequencing and maintained under a kanamycin selection pressure. This process is very similar to that of constructing single-crossover fluorescent fusions which is described later.

2.9.3. Double-crossover homologous recombination-based complementation

To complement a deletion mutant by double-crossover cis-based homologous recombination, the gene of interest plus 1 kb of upstream and 1 kb of downstream DNA was cloned in the vector pK18*mobsacB* by Gibson assembly and verified by restriction digest and Sanger sequencing. The construct was conjugated into the *B. bacteriovorus* deletion mutant (in this case Δ*bd3285*), resulting in the first genomic crossover event. The double-crossover complemented strain was then generated via sucrose suicide counter-selection as previously described for the generation of silent gene deletions (**Section 2.8.2** and **Section 2.8.3**). The final strain was verified by Sanger sequencing. The process is illustrated in Figure 2.1.

2.10. Generation of double-crossover fluorescent fusion proteins

To generate a markerless double-crossover C-terminal fluorescent fusion to a protein of interest, 3 fragments were assembled into the suicide vector pK18*mobsacB* by Gibson assembly: 1 kb of upstream DNA and the gene of interest minus the stop codon, the *mCherry* coding sequence, and 1 kb of downstream DNA. The final *B. bacteriovorus* fluorescent strain was constructed and verified analogously to markerless gene deletion mutants and double-crossover complementation (**Section 2.8**). I used this method to generate a Bd1075-mCherry double-crossover strain during in my MRes project[158] which is used as a recipient strain for a single-crossover introduction of Bd0064-mCerulean3 (described below).

2.11. Generation of single-crossover fluorescent fusion proteins

The process to generate single-crossover fusions is illustrated in Figure 2.2.

2.11.1. Bd0064 fusions to label the predator cytoplasm

The gene *bd0064* encodes a small PilZ domain-containing protein which is localised to the cytoplasm of *B. bacteriovorus*. Our laboratory has shown previously that a Bd0064-mCherry fluorescent fusion could illuminate the cytoplasm of *B. bacteriovorus* without detriment to the cell[47]. In Chapter 3, the existing *bd0064-mCherry* plasmid was conjugated into different gene deletion mutants and in Chapter 5, a newly constructed *bd0064-mCerulean3* plasmid (this study) was conjugated into the strain Bd1075-mCherry (generated during my MRes project[158]). Plasmids were constructed by assembling the *bd0064* gene (minus its stop codon) and the *mCherry*/*mCerulean3* coding sequence (in-frame with the C-terminus of *bd0064*) into pK18*mobsacB* by Gibson assembly. The strains were verified by Sanger sequencing and maintained under a kanamycin selection pressure. The cytoplasmic Bd0064 fluorescent tag subsequently allowed visualisation of predators inside bdelloplasts using fluorescence microscopy.

2.11.2. Bd3285-mCherry and Bd0599-mCherry single-crossover fusions to study localisation during predation

To construct a single-crossover fluorescent fusion of Bd3285-mCherry, the *bd3285* gene (minus its start codon, signal peptide and stop codon), and the *mCherry* gene (in-frame with the C-terminus of *bd3285*) were assembled into the vector pK18*mobsacB*. It was important to not include the start codon and signal peptide of *bd3285* as all cloning attempts which contained the entire gene sequence failed – most likely due to toxicity of the gene-product to *E. coli* cloning strains. To construct

Bd0599-mCherry, the entire gene (minus the stop codon) plus 300 bp of upstream DNA and the *mCherry* gene (in-frame with the C-terminus of *bd0599*) were assembled into pk18*mobsacB*. Upstream DNA was included here due to the shorter length of the *bd0599* gene (711 bp) to improve the potential efficiency of homologous recombination into the genome. Both fluorescent constructs were conjugated into *B. bacteriovorus* HD100, verified by Sanger sequencing and maintained under kanamycin selection.

2.11.3. Bd1075-mCherry truncation and point mutants used in targeting experiments

To test the subcellular localisation of different truncations or point mutants of Bd1075 (**Chapter 4 Section 4.3.7**), 1 kb of upstream DNA, the desired gene length minus the stop codon and the *mCherry* gene (in-frame with the C-terminus of *bd1075*) were cloned into pK18*mobsacB* using Gibson assembly. Point mutations, where appropriate, were subsequently generated through Q5® site-directed mutagenesis (**Section 2.7.7**). The suicide plasmids were then conjugated into wild-type *B. bacteriovorus* HD100 to generate a strain which, due to inclusion of the 1 kb upstream region, contained two copies of *bd1075*: the original wild-type copy and the new mCherry fusion copy. The suicide plasmids were also conjugated into *B. bacteriovorus* HD100 Δ*bd1075* to generate a strain which contained only the Bd1075-mCherry fluorescent fusion as the sole copy of *bd1075*. Single-crossover strains were verified by Sanger sequencing and maintained under a kanamycin selection pressure.

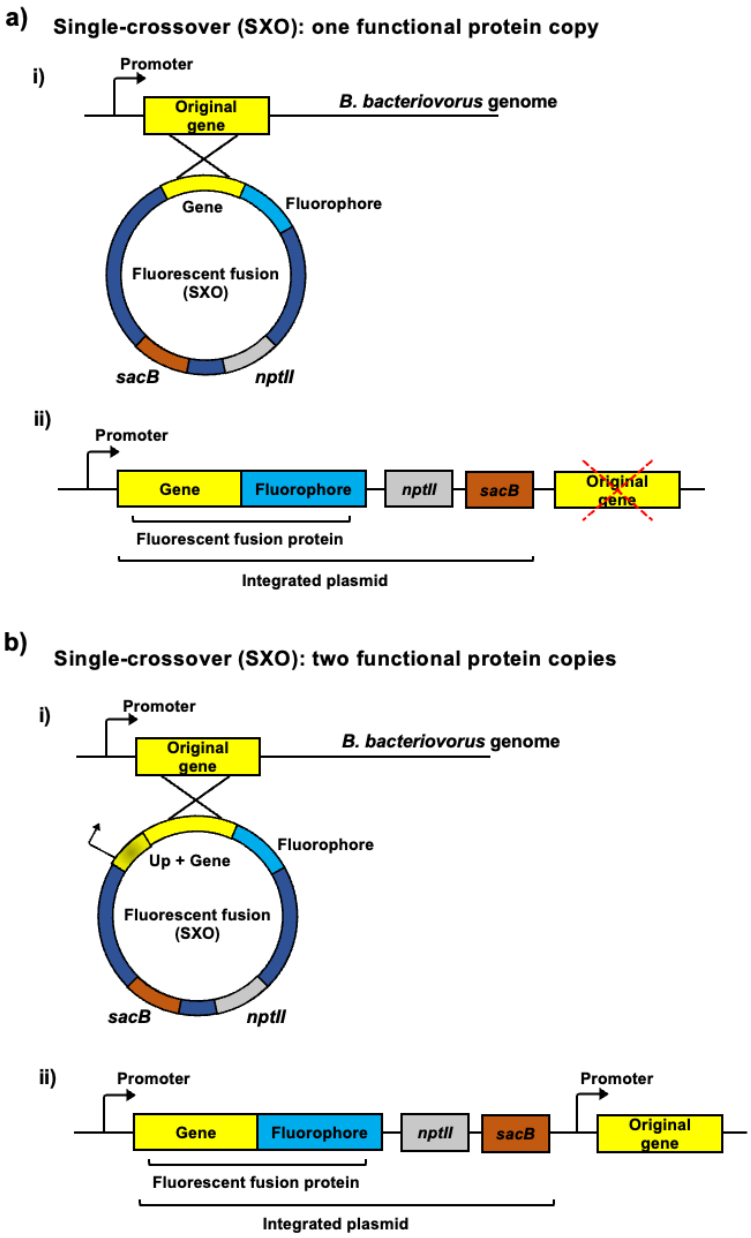

Figure 2.2. Construction of single-crossover fluorescent fusions in *B. bacteriovorus*

i) The gene of interest (minus its stop codon) and the desired fluorophore (in-frame with the gene C-terminus) are cloned into the plasmid pK18*mobsacB*. The plasmid is conjugated into *B. bacteriovorus* and integrates into the genome via homologous recombination, generating a strain in which the fluorescently-tagged gene is the sole copy of that gene. **ii**) The gene of interest plus upstream flanking DNA containing the native gene promoter (arrow) and the desired fluorophore (in-frame with the gene C-terminus) are cloned into pK18*mobsacB*. Homologous recombination into the *B. bacteriovorus* genome generates a strain containing two copies of the gene: the new fluorescent fusion and the original untagged gene. *sacB*: levansucrase gene; *nptII*: kanamycin resistance gene.

2.12. Generation of *E. coli* over-expression constructs

To heterologously over-express a protein (in this case Bd3285) from *B. bacteriovorus* in *E. coli*, the gene of interest was cloned into the plasmid pBAD HisA using Gibson assembly. The pBAD vector contains an arabinose-inducible *araBAD* promoter which drives protein over-expression. Site-directed point mutations were incorporated into PCR primers where appropriate (**Section 2.7.7**) to generate a catalytically-inactive protein variant. pBAD constructs were transformed into the *E. coli* strain TOP10 which contains the mutation *araD139* and is therefore incapable of arabinose metabolism, improving expression from the *araBAD* promoter. Strains were verified by Sanger sequencing and maintained under a kanamycin selection pressure. Over-expression microscopy was carried out as described (**Section 2.16.2**).

2.13. Western blot detection of Bd3285-mCherry during predation

Samples for western blots were prepared by me and the western blot was kindly carried out by Dr Carey Lambert.

To prepare samples for western blots, semi-synchronous predatory timecourses of *B. bacteriovorus* Bd3285-mCherry (and the control Bd0064-mCherry) upon *E. coli* S17-1 (pZMR100) were prepared. At each timepoint (0 min, 30 min, 1 h, 2 h and 3 h), a 100 µl sample was removed from the predatory culture, mixed with 40 µl of 4X SDS-PAGE loading buffer containing β-mercaptoethanol and placed at – 20 °C. For western blot detection, samples were removed from – 20 °C, boiled for 5 min and then loaded onto a 4-20% SDS-PAGE gel (Bio-Rad) alongside either a MagicMark™ XP Western protein standard ladder (ThermoFisher) (for the western blot gel) or a SeeBlue™ Plus2 Pre-stained Protein Standard ladder (ThermoFisher) (for the loading control gel). The gels were run for

1 h at 150 V. Loading control gels were stained and de-stained with QuickBlue Protein Stain (LubioScience). The blotting gel was transferred onto a nitrocellulose membrane for 2 h at 25 V. An anti-mCherry primary antibody was used to detect Bd3285-mCherry and Bd0064-mCherry using a WesternBreeze™ Chemiluminescent kit (ThermoFisher) according to the manufacturer's instructions. Images were captured by exposure to X-ray film.

2.14. Muropeptide cell wall sacculi analysis

2.14.1. Purification and characterisation of cell wall sacculi *in vivo*

To prepare *B. bacteriovorus* cell wall sacculi, 1 l of Ca/HEPES containing 60 ml of *E. coli* S17-1 was inoculated with 50 ml of a previous predatory culture from the previous 24 h. *B. bacteriovorus* complementation test strains containing the plasmid pMQBAD were cultured on *E. coli* S17-1 pUC19 ($gent^R$) in the presence of gentamicin. Following complete prey lysis, cultures were filtered through a 0.45 µm membrane to remove residual prey debris and then centrifuged at 15,000 x *g* for 30 min at 4 °C. The cell pellets were resuspended in 6 ml of ice-cold PBS and then boiled in 6 ml of 8% SDS for 30 min to liberate peptidoglycan sacculi.

The following steps were carried out by our collaborators Dr Jacob Biboy and Prof Waldemar Vollmer at Newcastle University.

For preparation of *E. coli* sacculi, the *E. coli* strain BW25113 was cultured at 37 °C for 16 h and then sacculi were isolated using an analogous method. PG was purified from the cell lysates and cell wall muropeptides were then reduced by sodium borohydride. HPLC analysis was performed as described by Glauner *et al*. (1988)[171].

2.14.2. Purification of Bd1075 and application to sacculi *in vitro*

Enzyme purification was carried out by the PhD student Ms Amber Wilson and Dr Ian Cadby in the laboratory of my co-supervisor/collaborator Prof Andrew Lovering at the University of Birmingham.

To purify the enzyme Bd1075 from *B. bacteriovorus* HD100, the *bd1075* gene (minus the DNA encoding the signal peptide and stop codon) was cloned in-frame with a C-terminal histidine tag into the plasmid pET41. The construct was transformed into *E. coli* BL21, cultured in TB media to an OD_{600} of 0.6-0.8, and then over-expressed via induction with 0.5 mM IPTG at 18 °C for 16 h. The $Bd1075_{HD100}$ protein was purified firstly by nickel Ni-NTA affinity and secondly by size-exclusion chromatography, resulting in near homogeneously pure protein, which was finally dialysed into 10 mM Na Citrate pH 6.0, 30 mM KCl and glycerol (2% w/v) buffer.

The application of purified $Bd1075_{HD100}$ enzyme to PG sacculi in vitro and the resulting analysis described below was performed by Dr Jacob Biboy at Newcastle University.

Cell wall sacculi of *B. bacteriovorus* Δ*bd1075*, WT 109J, or *E. coli* BW25113 was incubated with purified $Bd1075_{HD100}$ (10 μM) in 50 mM Tris-HCl, 50 mM NaCl pH 7.0 for 16 h at 37 °C on a Thermomixer at 900 rpm. For controls, sacculi received buffer which did not contain enzyme. Following enzyme activity, samples were boiled at 100 °C for 10 min and added to an equal volume of 80 mM NaP buffer pH 4.8. Samples were then incubated with 10 μg of cellosyl (Hoechst, Frankfurt am Main, Germany) at 37 °C on a Thermomixer at 900 rpm for an additional 16 h. The samples were then boiled for 10 min and centrifuged for at 16,000 x *g* for 15 min at room temperature. PG was purified from the cell lysates and muropeptides were then reduced by sodium borohydride. Finally, HPLC analysis was performed as previously described by Glauner *et al*. (1988)[171].

2.15. Crystallisation and structure of Bd1075

The crystal structure of Bd1075 was solved by the PhD student Mr Mauricio Valdivia-Delgado in Prof Andrew Lovering's lab at the University of Birmingham.

Crystal screening was performed using ~ 25 mg/ml of purified Bd1075 protein. Bd1075 crystals were grown at 18 °C using the sitting drop technique with 4 µl drops composed of equal volumes of protein and reservoir solution. Crystals were identified in condition 2-44 of the BCS screen (Molecular Dimensions) which contained 0.1 M Tris pH 7.8, 0.1 M KSCN, 0.1 M NaBr and 25% PEG Smear broad range. The crystals were cryo-protected in mother liquor with 25% (v/v) ethylene glycol and flash-cooled in liquid nitrogen. The diffraction data were acquired at the Diamond Light Source (Oxford, UK) and data reduction and processing were completed using XDS[172] and the xia2 suite[173]. Phasing of Bd1075 was achieved using a merged SAD data set (9000 frames, 0.1° oscillations) collected at a wavelength of 0.91 A, corresponding to the bromide anomalous scattering peak. The data were input into CCP4 online CRANK2[174] which identified 6 bromide sites with an initial FOM of 0.14, followed by iterative cycles of building and model-based phasing improvement. The model was build further and modified using COOT[175], with refinement cycles in PHENIX[176].

2.16. Microscopy

2.16.1. Electron microscopy

To acquire transmission electron micrographs, *B. bacteriovorus* cells were firstly cultured for 24 h until prey had completely lysed. Predator cells were then microcentrifuged for 10 min at 5,000 x *g* and carefully resuspended in fresh Ca/HEPES. *B. bacteriovorus* cells were applied to Formvar/Carbon-coated 200-mesh copper grids (EM Resolutions) which had first been glow-discharged. Cells were stained with 0.5% uranyl acetate for 1 min and then de-stained with Tris-EDTA pH 7.6 for 30 s. An FEI Tecnai G2 12 Biotwin transmission electron microscope was used to image samples at 100 kV.

2.16.2. Phase contrast and fluorescence microscopy

2.16.2.1. Sample preparation and imaging conditions

Bacterial cells were generally immobilised on a 1% agarose Ca/HEPES pad and visualised with a Plan Apo 100x Ph3 oil objective lens (NA 1.45) of a Nikon Ti-E inverted wide-field fluorescence microscope. A phase exposure time of 250 ms was used along with Gain 1. For fluorescence imaging various filter sets were used including: mCherry (excitation: 555 nm, emission: 620/60 nm); DAPI for HADA stain (excitation: 395 nm, emission: 435-485 nm); CFP for mCerulean3 (excitation: 440 nm, emission: 470-490 nm); and YFP for mCitrine (excitation: 508 nm, emission: 540/25 nm). Generally, 10 s exposure times were used for each fluorophore with the exception of HADA visualisation which used a 1 s exposure due to the absence of agarose pad mounting. Images were acquired using Nikon NIS software and an Andor Neo sCMOS camera.

2.16.2.2. Semi-synchronous predatory timecourses

To prepare for a semi-synchronous predatory timecourse, a 50 ml culture of *E. coli* S17-1 (or S17-1 pZMR100 if using kanamycin-resistant predator strains) was grown for ~ 16 h, therefore cells were in stationary phase. *B. bacteriovorus* strains (10 ml predatory cultures) were also grown for 24 h and examined under the microscope to ensure that prey had completely lysed. *B. bacteriovorus* cultures were then concentrated by centrifuging 5 ml at 5,000 x *g* for 20 min followed by removing 4.5 ml of supernatant and resuspending in the remaining 500 µl. To initiate a semi-synchronous culture, the following ratio was used: 5 of 10X concentrated *B. bacteriovorus* strain, 4 of *E. coli* prey at OD_{600} = 1.0, and 3 of Ca/HEPES. Kanamycin (50 µg/ml) was supplemented to the final 1.2 ml predatory culture when appropriate. Following predator-prey mixing, the timecourse was started immediately and the culture was incubated at 29 °C, shaking. At each timepoint (generally 0 min, 15 min, 30 min, 45 min, 1 h, 2 h, 3 h and 4 h), a 10 µl sample was transferred from the predatory culture onto a pre-prepared 1% agarose Ca/HEPES slide. If, at 30 min, >95% of bdelloplasts had not rounded (an asynchronous timecourse), then the experiment was aborted and re-started (exceptions to this were for the *B. bacteriovorus* Δ*DacB* and Δ*bd3285* deletion strains which do not round up bdelloplasts).

2.16.2.3. HADA pre-labelling of the prey cell wall

To visualise the prey cell wall and septum (if present) during predation, the *E. coli* prey strain was pre-labelled with the fluorescent D-amino acid cell wall stain HADA (gift to the lab from Dr Erkin Kuru and Prof Michael VanNieuwenhze) prior to predation. *E. coli* S17-1 (pZMR100) was cultured for ~ 16 h, adjusted to an OD_{600} = 1.0 in fresh YT, and mixed with 500 µm of HADA (from a 50 mM stock in DMSO) and incubated at 29 °C in a static incubator for 30 min. *B. bacteriovorus* predatory cultures that had been grown for 24 h were concentrated 10X as described above. Following 30 min of HADA-labelling, the *E. coli* culture was microcentrifuged at 17,000 x *g* for 5 min and the pellet resuspended in

Ca/HEPES. The process was repeated to remove any unincorporated free HADA stain. Predatory cultures for a semi-synchronous timecourse were then set up in a 5:4:3 ratio of concentrated predator cells: pre-labelled *E. coli*: Ca/HEPES. At each desired timepoint, 120 µl was removed from the predatory timecourse culture and transferred to a microcentrifuge tube containing 175 µl of pre-cooled 100% ethanol. The tube contents were mixed by inversion and transferred to a -20 °C freezer for a minimum of 15 min. At completion of the timecourse, the -20 °C samples were microcentrifuged at 17,000 x *g* for 5 min and the pellet was resuspended in 500 µl of 1X PBS. The tubes were microcentrifuged again and the faint pellet was carefully resuspended in 5 µl of Slow-Fade™ (Molecular Dimensions) to preserve the sample and stored at -20 °C. To take images of each timepoint, 2 µl of each sample were transferred to a microscope slide. A cover slip was placed on top of the sample and pressure was carefully applied to the coverslip to fix cells and facilitate imaging of the wet mount.

2.16.3. Time-lapse microscopy to visualise *B. bacteriovorus* invasion into prey

Time-lapse microscopy videos were captured on a Nikon Eclipse E600 upright microscope with a 100X oil objective lens (NA: 1.25). To prepare a predatory culture for time-lapse microscopy, 1 ml of attack-phase *B. bacteriovorus* and 50 µl of *E. coli* S17-1 were separately microcentrifuged at 17,000 x *g* for 2 min and resuspended in 50 µl of Ca/HEPES. A 0.3% agarose Ca/HEPES slide was prepared, with two wells created at each end (to allow hydration of the slide with H_2O during the video) using weighted bijoux tubes that were removed after the agarose had set. *B. bacteriovorus* and *E. coli* strains were mixed and 10 µl was immediately transferred onto the centre of the agarose slide and a cover slip placed on top of the sample. The slide was then placed under the Nikon Eclipse microscope which was configured to revisit 6 different field of view coordinates every 1 min for ~ 2 h using its Prior Scientific H101A XYZ

stage. Images were captured on a Hammamatsu Orca ER Camera with Simple PCI software.

2.17. Microscopy image analysis

2.17.1. Standard Fiji analysis

Images were processed in the Fiji distribution of ImageJ[177]. Images were minimally processed with the sharpen and smooth tools and adjustments to brightness and contrast.

2.17.2. Time-lapse analysis

Time-lapse videos of predator invasions into prey were analysed in Fiji. Approximately 5 predatory invasions were analysed per field of view (6 in total) to give 30 invasions per biological repeat. Two parameters were measured: predator attachment time and predator entry time. Predator attachment time was defined as the number of frames (1 frame = 1 min) between initial attachment of the predator to the prey cell and the frame at which the predator begins to move into its prey. Predator entry time was defined as the number of frames between initial movement into the prey cell and completion of entry (when the tail of the predator is no longer visible outside the bdelloplast).

2.17.3. MicrobeJ measurements of cell shape

The MicrobeJ plug-in[178] (version 5.11z) for Fiji was used to detect bacterial cells and measure different cell shape morphologies. *B. bacteriovorus* cells were generally defined by the parameters of area: 0.2-1.5 μm^2, length: 0.5-2.5 µm, width: 0.2-0.8 µm, circularity 0-0.9 A.U, and curvature: 0-max. The curvature of *B. bacteriovorus* strains was defined by MicrobeJ as the “reciprocal of the radius of curvature

measured between the end points and the centre of the medial axis of the cell, described in arbitrary units". Bdelloplasts were generally defined by the parameters of area: 1.0-max μm^2, length: 0.5-max μm, width: 0.5-max μm, curvature: 0-0.35 A.U., and circularity: 0.6-1.0 A.U. Circularity was defined by MicrobeJ as "4πr x area/perimeter^2, with a value of 1.0 indicating a perfect circle". Bdelloplasts that had a circularity value of <0.96 A.U. were classified as non-circular based on visual observations and the fact that ~ 0% of wild-type bdelloplasts had a circularity score of >0.96 A.U. The classification of non-circular bdelloplasts allowed the proportion of spherical bdelloplasts to be quantified. All images were manually inspected to ensure that predator or prey cells had been correctly detected. Bdelloplasts that had *B. bacteriovorus* cells attached to the outside (distorting shape measurements) were removed prior to analysis.

2.17.4. MicrobeJ fluorescent foci detection

MicrobeJ (version 5.13j) was used to detect the fluorescent signal of Bd1075-mCherry for analysis of subcellular localisation. Bd1075-mCherry signal was detected within attack-phase *B. bacteriovorus* cells using the foci method with default maxima settings and an association with parent bacteria of 0.1 μm. This allowed the generation of heatmaps which both measured the cell contour of all bacteria to generate a shape outline and detected the maxima in each cell to show the distribution of fluorescence signal across the bacterial population. To detect Bd1075-mCherry fluorescent fusions in a curved, wild-type genetic background, only cells with a curvature of >0.6 A.U. were analysed so as to only analyse cells with a definitively curved shape. To detect the fluorescent fusions in the rod-shaped Δ*bd1075* genetic background, curvature parameters were re-set to 0-max to also allow the degree of shape complementation to be measured. To detect *B. bacteriovorus* cells within bdelloplasts, the predator cells were detected in the maxima channel with the bacteria method using a tolerance of 0.1 μm. All images were

manually inspected to ensure that predator or prey cells had been correctly detected. Bdelloplasts that had *B. bacteriovorus* cells attached to the outside (distorting shape measurements) were removed prior to analysis.

2.18. Bioinformatics

2.18.1. DNA and protein sequences

DNA and protein sequences for *B. bacteriovorus* genes were acquired from the NCBI database using either the xBASE server[179, 180] or EnsemblBacteria[181] . The NCBI BLAST tool[182] was used to identify protein homologues in other strains and species.

2.18.2. Prediction of protein features and domains

Signal sequences were identified using the prediction tool SignalP 5.0[183]. Protein domains were predicted using tools including the Pfam[184] and InterPro[185] databases.

2.18.3. DNA and protein alignments

DNA and protein sequence alignments were created using the EMBL-EBI tools EMBOSS NEEDLE[186] (pairwise alignments) and Clustal Omega[187] (multiple alignments). Alignments were presented using ESPript[188].

2.18.4. Generation of a phylogenetic tree

Protein sequences were aligned with ClustalW[189] and a maximum-likelihood phylogenetic tree was generated in MEGA-X[190] with the Jones-Taylor-Thornton substitution model[191] and using 500 bootstrap replications. The tree was visualised and edited in FigTree.

2.18.5. RNA-Seq data set analysis

To confirm the transcriptional start site of each gene, the RNA-Seq dataset previously acquired the host-independent strain HID13 was aligned against the genome of *B. bacteriovorus* using the programme Rockhopper[192, 193].

To visualise the transcriptional pattern and possible differential regulation of *B. bacteriovorus* genes at different timepoints during a predatory cycle, an unpublished RNA-Seq data set (acquired by Dr Simona Huwiler during her postdoctoral time in our laboratory) was used. The RNA-Seq measured transcription of all *B. bacteriovorus* HD100 genes during predation on *E. coli* K12 across the predatory cycle. Reads per kb per million reads (RPKM) values were acquired by Dr Simona Huwiler in Rockhopper and compared to attack-phase transcription values to visualise differentially-regulated genes.

2.19. Statistical analysis

Statistical analysis was carried out in GraphPad Prism 9.0. All experimental data were first tested for normality to determine whether the data sets followed a normal (Gaussian) distribution or a non-normal (non-Gaussian) distribution. Data were then analysed using the appropriate statistical test depending on the type of distribution. For example, an unpaired t-test would be used to compare two groups of normally distributed data whereas a Mann-Whitney test would be used to compare two groups of non-normally distributed data. The type of statistical test applied to each dataset, the number of cells analysed (n number) and the number of biological repeats performed is described in every figure legend.

Chapter 3. Role of a lytic transglycosylase in prey cell rounding

3.1. Chapter introduction

The role of several *B. bacteriovorus* PG-modifying enzymes during predation has been studied previously. The DD-endopeptidase DacB enzymes Bd0816 and Bd3459 are secreted into the prey periplasm during invasion, cutting 4-3 muropeptide crosslinks and facilitating prey cell rounding[115]. Following prey invasion by *B. bacteriovorus*, two LD-transpeptidases Bd0886 and Bd1176 are secreted into prey, utilising substrates from DacB action and creating 3-3 crosslinks in the prey wall, thereby strengthening the structure of the bdelloplast and providing a more osmotically-stable niche for predator replication[33]. The deacetylase enzymes Bd0468 and Bd3279 are also secreted into the prey during early invasion, deacetylating N-acetylglucosamine residues in the prey PG and thus demarcating predator PG from prey PG[139]. Prior to prey lysis, a novel lysozyme Bd0314 (DslA) (which is specific for N-deacetylated PG) then cleaves the prey PG wall, assisting the escape of predator progeny cells[38].

Despite the characterisation of these enzymes, *B. bacteriovorus* contains many more putative PG-active enzymes that have not been investigated. The identity of the enzymes involved in the creation and then resealing of the entry porthole - through which *B. bacteriovorus* traverses the prey cell wall - are unknown. One potential protein is the lytic transglycosylase Bd3575 - deletion of which resulted in 3-fold slower entry into prey[123]. Enzymes that cut the PG sugar backbone such as lytic transglycosylases and lysozymes are excellent candidates for proteins that create the entry porthole.

This chapter aims to identify further proteins that are important for *B. bacteriovorus* prey invasion, focussing on the lytic transglycosylase family.

3.1.1. Bacterial lytic transglycosylases

Lytic transglycosylases (LTs) cut β-1,4-glycosidic bonds between Glc*N*Ac and Mur*N*Ac residues in the PG sugar backbone, yielding 1,6-anhydroMur*N*Ac[105] (Figure 3.1).

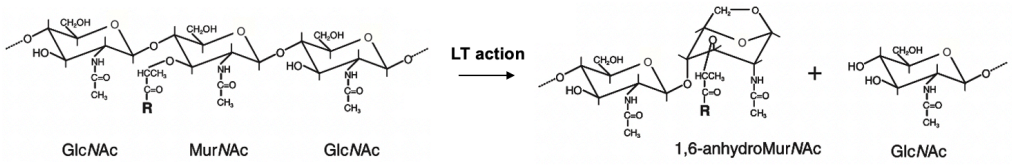

Figure 3.1. Mechanism of lytic transglycosylase action on PG

Cleavage of the β-1,4-glycosidic bond between Mur*N*Ac and Glc*N*Ac in the PG cell wall by lytic transglycosylases (LTs). An intramolecular transglycosylation reaction produces the products 1,6-anhydroMur*N*Ac and Glc*N*Ac. R: stem peptide attached to Mur*N*Ac. Figure adapted from Vollmer (2008)[105].

LTs have a wide range of roles in different bacteria including general cell elongation via facilitating the insertion of new PG into the cell wall, recycling of PG subunits back to the cytoplasm, sporulation, and the insertion of bacterial appendages such as flagella, pili, conjugation and secretion machinery through the PG wall[105]. LTs could also be classified as virulence factors as they are upregulated in and important for the pathogenesis of several pathogens such as *N. gonorrhoeae* and *Bordetella pertussis*[194, 195]. In infection caused by these pathogens, PG products released by LT activity are immunogenic, stimulating human Nod receptor activation and causing inflammation[196]. The LT product Glc*N*Ac-anhMur*N*Ac-tetrapeptide is more commonly known as the tracheal cytotoxin TCT which is important for *B. pertussis* pathology[195]. LTs can also have a role in bacterial cell division alongside amidases[105] and it is this particular function which is critically important in this chapter.

LTs have generally been most characterised in *E. coli*, *Pseudomonas* and *Neisseria* species[114] which are summarised in Table 3.1. Although LTs also exist in Gram-positive bacteria, this chapter will focus on Gram-

negative proteins since these are most relevant to the Gram-negative *B. bacteriovorus*.

Table 3.1. Characteristics of common lytic transglycosylases

Description of *E. coli* lytic transglycosylase (LT) enzymes with corresponding homologues in other bacteria also listed. *B. bacteriovorus* HD100 homologues (*Bb*) are shown in bold. The domain structure, localisation, genetic knockout (KO) phenotype and cellular function (if known) of each LT are detailed.

E. coli LT	Homologues	Domains	Localisation	KO phenotype	Function(s)
Slt70	LtgA (*Neisseria*) **Bd3575** (*Bb*) **Bd1285** (*Bb*) **Bd2711** (*Bb*) **Bd2462** (*Bb*)	Slt	Periplasm (soluble)	Unclear	Maintains PG integrity, repairs β-lactam damage
MltA	LtgC (*Neisseria*), MltA (*P. aeruginosa*), MltA (*S. maltophilia*) **Bd3285** (*Bb*) **Bd0599** (*Bb*) **Bd0519** (*Bb*)	"A" and "B" with 3D catalytic domain	OM	*E. coli* MltA: unclear. *Neisseria* LtgC: daughter cells unable to separate	Cell division in *Neisseria*. Unclear in *E. coli*.
MltB	LtgD (*Neisseria*)	SLT_2	OM (as MltB) and periplasm (as soluble truncate Slt35)	Unclear	Unknown
MltC	LtgB (*Neisseria*)	DUF3393, Slt	OM	Unclear	Unknown
MltD	LtgE (*Neisseria*) **Bd1125** (*Bb*) **Bd0529** (*Bb*) **Bd3243** (*Bb*)	Slt, 2x LysM	OM	Unclear	Unknown
MltE	**Bd1124** (*Bb*)	Slt	OM	Unclear	Insertion of T6SS in enteroaggregative *E. coli*.
MltF	**Bd3421** (*Bb*)	SBP_bac 3, Slt	OM	Unclear	Unclear
MltG	**Bd0132** (*Bb*)	YceG	IM	Longer glycan chains	Generates short glycan strands in PG synthesis
RlpA	RlpA (*P. aeruginosa*)	DPBP_1, SPOR	Septal ring (*P. aeruginosa*)	Cell chaining, cells cannot separate, longer naked glycan chains (*P. aeruginosa*)	Cell separation during division (*P. aeruginosa*)

Nine different LTs exist in *E. coli* K12: the soluble protein Slt70 and the membrane-bound proteins MltA, MltB, MltC, MltD, MltE, MltF, MltG and RlpA[114] (Table 3.1). LTs are generally classified into 6 different families based on their consensus sequence and folds.

Family 1 comprises Slt70, MltC, MltD, MltE and MltF. Slt70 is the only LT which is soluble in its native form. Slt70 contains a C-terminal Slt domain with the catalytic residue E478[197, 198]. Deletion of *slt70* did not cause any growth defect in *E. coli*[199]. Under β-lactam stress, however, Slt70 degraded potentially damaging PG by-products and may therefore have a role in maintain PG quality[200]. Slt70 also interacts with the PBPs 1b, c, 2, 3 and 7/8[201, 202].

Membrane-bound MltC has a lipobox signal peptide, a DUF3393 domain at the N-terminus and a C-terminal catalytic Slt domain containing the catalytic residue E218[203].

The protein MltD contains lipobox signal peptide and an Slt domain at the N-terminus which is followed by 2 LysM domains (the number of which can vary between species) that may bind PG[184].

The small protein MltE (203 amino acids) simply contains a lipobox signal peptide and an Slt domain with the catalytic residue E64[204, 205]. In enteroaggregative *E. coli*, MltE enables the insertion of the T6SS machinery into the cell wall[206].

The final protein in family 1 is MltF. MltF contains a lipobox signal peptide, an N-terminal SBP_bac3 domain (bacterial extracellular solute-binding family 3) and a C-terminal Slt domain with the catalytic residue E316 in *P. aeruginosa*[207]. MltF is predicted to function in the insertion of bacterial appendages and machinery into the cell wall[207].

Family 2 comprises only MltA which has homologues in *P. aeruginosa* and *S. maltophilia* (also called MltA) and *N. gonorrhoeae* (LtgC)[114]. LtgC differs from MltA in containing an amino acid insertion of unknown function[184]. Most LTs have a helical lysozyme-like fold but MltA proteins differ in containing an alternative β-barrel endoglucanase V-like fold[208]. MltA contains a lipobox signal peptide and the two domains ‘A’ and ‘B’

which are described in more detail in **Section 3.3.2.5**. Importantly, Domain A contains three aspartate residues (3D domain), of which D328 is essential for PG catalysis[208]. Interestingly, MltA is the only *E. coli* LT which swaps a catalytic glutamate for an aspartate residue. MltA can cleave both crosslinked and non-crosslinked PG and possesses solely exolytic activity[209]. The protein interacts with PBP1b via the scaffold protein MipA[210]. In *N. gonorrhoeae*, however, LtgC only interacts with PBP2 and not a MipA homologue[211]. Deletion of MltA in *E. coli* did not cause any obvious phenotype[212] but deletion of LtgC resulted in daughter cells that were defective for cell separation[213, 214].

LT Family 3 comprises just MltB. MltB contains a lipobox signal peptide and the single domain SLT_2 which contains the catalytic residue E162[215]. Interestingly, MltB is not a lipoprotein as it is truncated in the periplasm, resulting in the soluble protein product Slt35[216].

Family 4 contains the bacteriophage LTs but these are not discussed here. Family 5 contains the most recently discovered LT: MltG. MltG contains a lipobox signal peptide and the domain YceG (the original name of the protein) which contains the catalytic amino acid E218[114]. MltG is widely conserved and located in the inner membrane where it interacts with PBP1b and is involved in generating short glycan chains during PG synthesis[217, 218].

The final family, Family 6, is most similar to MltA as the proteins contain 3 conserved aspartate residues[114]. Family 6 LTs often contain a catalytic DPBP_1 domain prediction which is similar to the 3D domain[114]. RlpA from *P. aeruginosa* is the best characterised member of Family 6 LTs. RlpA contains a DPBP_1 domain and a SPOR domain at the protein C-terminus[112]. Bacterial SPOR domains to bind PG[219, 220] . RlpA localises to the outer membrane and to the septal ring of dividing cells where it is involved in cell division[112]. RlpA preferentially cleaves glycan chains that are not attached to a stem peptide (‘naked glycans’)[112, 220]. In a *P. aeruginosa* RlpA deletion strain, longer naked glycan chains are present

and cells grew slowly as a long chain which could form septa but not separate[112]. Cells in these chains were 50% shorter and 20% wider than the wild-type[112]. This chaining phenotype was only observed under osmotic stress conditions, however, with no phenotype apparent under standard laboratory culture conditions[112]. Interestingly, *E. coli* encodes 4 proteins that contain a SPOR domain – 3 of these are essential but the fourth protein, RlpA, is not[104, 221]. Deletion of RlpA from *E. coli* did not result in a phenotype and the protein did not exert LT activity[112]. It is possible that the inactivity of *E. coli* RlpA may result from a replacement of D168 in *P. aeruginosa* to S147 in *E. coli* but this has not been confirmed[114].

A large degree of functional redundancy exists for lytic transglycosylases since each can be individually deleted without any obvious growth defects, however a Δ7*ldt* deletion of Δ*slt70*Δ*mltA-F* was not tolerated in *E. coli*[114]. Moreover a Δ6*ldt* deletion of Slt70 and MltA-E resulted in an *E. coli* chaining phenotype similar to that observed for a triple amidase deletion mutant Δ*amiA-C*[105]. The role of most LTs remains unclear, however, and more work is required to elucidate the function of each LT.

3.1.2. Lytic transglycosylases in *B. bacteriovorus*

The genome of *B. bacteriovorus* HD100 encodes 13 LTs. Of these, 12 had been identified previously by Dr Thomas Lerner[123]. The additional LT, Bd0132, was identified during my PhD from BLAST analysis of *E. coli* MltG (which was only discovered in 2016[217]). The four LTs Bd3575, Bd1285, Bd2711 and Bd2462 have homology to *E. coli* Slt70. Three LTs Bd3285, Bd0599 and Bd0519 are homologous to *E. coli* MltA. Three further LTs Bd1125, Bd0529 and Bd3243 share homology with *E. coli* MltD. There do not appear to be homologues of *E. coli* MltB or MltC in *B. bacteriovorus* HD100. Bd1124 is homologous to MltE, Bd3421 to MltF and Bd0132 to MltG.

LTs may fulfil several different roles during both the host-dependent (HD) and host-independent (HI) life cycles of *B. bacteriovorus*. These could include:

1. Remodelling of *B. bacteriovorus* PG to aid invasion

During prey invasion, *B. bacteriovorus* must squeeze through an entry porthole that is narrower than the width of a predator cell[15, 122]. Early electron micrographs appear to show a narrowing of the *B. bacteriovorus* invasive nose to facilitate entry[15, 122]. It is possible that this self-modification may involve localised LT activity.

2. Conventional cell wall elongation and division of *B. bacteriovorus*

LTs could be involved in the insertion of new PG material into the predator cell wall to allow elongation of HD and/or HI *B. bacteriovorus* cells. Previous work suggested that the LT Bd1285 may be involved in the filamentous growth of HI *B. bacteriovorus*[222]. LTs may also contribute towards the cell division of HD and/or HI *B. bacteriovorus* cells.

3. Remodelling of prey PG for invasion into and/or exit from prey

LTs may be involved in the creation of the entry porthole during prey invasion. Previous work showed that the LT Bd3575 has a role in

predatory invasion[123]. LTs may also work in concert with the lysozyme DslA to facilitate exit from prey.

The DD-endopeptidase DacB proteins which modify prey PG wall during invasion are upregulated at 15-30 min during a predatory timecourse[115]. Transcription of the LT Bd3575 which is involved in prey invasion also peaks at 15 min[123]. It would therefore be expected that additional LTs which are involved in prey invasion and creation of the entry porthole are also transcriptionally upregulated at approximately 15-30 min. An unpublished RNA-Seq data set (kindly shared by Dr Simona Huwiler during her postdoctoral time in our group) can be used to visualise the transcriptional patterns of all *B. bacteriovorus* HD100 genes at different timepoints during a predatory cycle upon *E. coli* K12 prey.

Table 3.2 shows the transcriptional pattern of the 13 *B. bacteriovorus* LTs (compared to attack-phase cells) during predation on *E. coli* K12. The green boxes highlight timepoints where a particular gene is upregulated compared to expression levels in attack-phase cells outside of prey. Only 4 LTs appear to be upregulated during predation: Bd3575, Bd3285, Bd0599 and Bd3421. Bd3421 (MltF) is upregulated from 30 min – 4 h, with transcription peaking at 1 h.

Considering this transcriptional pattern, it is possible that Bd3421 is involved in general growth and elongation of *B. bacteriovorus* within prey which occurs between 1 – 3.5 h or cell division at 3.5 h. The two LTs Bd3285 and Bd0599 are upregulated at 15-30 min and are both homologues of MltA along with a third protein: Bd0519. Although Bd0519 is not upregulated in this data set, later validation of transcriptional patterns by RT-PCR in **Section 3.3.3** revealed that Bd0519 is also upregulated at 15 min.

Due to upregulation of Bd3285 and Bd0599 at 15-30 min, this family of MltA homologues was chosen as a set of candidates for LTs that may be involved in prey invasion. During my PhD, I primarily investigated the

proteins Bd3285 and Bd0599. The third protein, Bd0519, will be the subject of future work by an MSci project student.

Table 3.2. Transcription of *B. bacteriovorus* HD100 lytic transglycosylases during predation on *E. coli* K12, determined by RNA-Seq

Transcriptional pattern of the 13 lytic transglycosylases from *B. bacteriovorus* HD100 during predation on *E. coli* K12 prey. Each timepoint (15 min – 4 h) is compared to the transcription of attack-phase cells to determine timepoints at which each gene is upregulated. Upregulated timepoints are indicated in green. Numbers represent the number of reads per kb per million reads (RPKM) normalised to attack-phase values. Lytic transglycosylases are grouped according to their closest *E. coli* homologue. The table was generated from an RNA-Seq data set acquired by Dr Simona Huwiler.

	Gene	Transcription at predatory cycle timepoints compared to attack-phase (AP)						
		15 min/AP	30 min/AP	45 min/AP	1 h/AP	2 h/AP	3 h/AP	4 h/AP
Slt70 family	Bd3575	**16.621**	**4.828**	**2.483**	1.121	0.276	0.672	0.776
	Bd1285	0.196	0.098	0.109	0.272	0.152	0.435	0.457
	Bd2711	0.487	0.259	0.289	0.264	0.197	0.179	0.214
	Bd2462	0.618	0.328	0.318	0.217	0.243	0.097	0.115
MltA family	Bd3285	**33.609**	**39.652**	**18.261**	**4.826**	1.391	**2.043**	**2.130**
	Bd0599	**2.250**	**4.346**	0.923	0.692	0.154	0.231	0.250
	Bd0519	1.333	0.333	0.333	0.333	1.000	1.000	1.333
MltD family	Bd1125	0.638	0.385	0.412	0.481	0.385	0.528	0.564
	Bd0529	0.248	0.124	0.131	0.203	0.077	0.311	0.418
	Bd3243	0.564	0.350	0.390	0.299	0.345	0.173	0.216
MltE	Bd1124	1.000	1.000	2.000	3.000	13.000	19.000	15.000
MltF	Bd3421	0.333	**19.667**	**59.667**	**108.667**	**53.000**	**14.000**	**10.333**
MltG	Bd0132	0.531	0.222	0.210	0.309	0.642	0.889	0.951

3.2. Research aims

I designed and supervised a 3-month MSci project carried out by Mr Samuel Mason which included constructing a deletion mutant of *bd3285*, thereby generating preliminary data for this project. I then continued extensive experimentation myself in the third and final year of my PhD which included the following aims:

- To examine the conservation of the MltA family proteins Bd3285, Bd0599 and Bd0519 across different *Bdellovibrio* strains.

- To compare the predicted domains and important residues of the three MltA homologues with each other and with *E. coli* MltA.

- To confirm the RNA-Seq transcriptional patterns for genes encoding the three *B. bacteriovorus* MltA homologues across the predatory cycle using RT-PCR.

- To determine the natural localisation of Bd3285 and Bd0599 fusing each protein to mCherry and visualising the fluorescent proteins during *B. bacteriovorus* predation on *E. coli*.

- To determine the subcellular localisation of Bd3285 and Bd0599 when heterologously over-expressed in *E. coli* TOP10.

- To delete *bd3285* from the genome of *B. bacteriovorus* (achieved with Mr Samuel Mason) and determine any phenotype caused by loss of the gene.

- To delete *bd0599* from the genome of *B. bacteriovorus* (as both a single mutant and a double mutant in combination with Δ*bd3285*) and examine any phenotypic changes in the deletion mutants during predation.

3.3. Chapter results

3.3.1. MltA homologues are largely conserved in *Bdellovibrio bacteriovorus* but differ in epibiotic strains

While *E. coli* K12 contains just one copy of the protein MltA, the genome of *B. bacteriovorus* HD100 encodes three copies. To determine whether this gene duplication is specific to strain HD100 or more widely observed in other strains of *Bdellovibrio*, the protein sequences of Bd3285, Bd0599 and Bd0519 were entered into BLAST, searching against the taxid *Bdellovibrio*. Table 3.3 shows the presence (including number of copies) and absence of each gene across the 14 available *Bdellovibrio* genomes. 57% of *Bdellovibrio* genomes encode at least one copy of each MltA family protein. Bd3285 is the most conserved MltA protein; only the strains *Bdellovibrio* sp. ArHS, *Bdellovibrio* sp. Qaytius and *Bdellovibrio exovorus* do not encode a homologue of Bd3285. *Bdellovibrio exovorus* is notably the only strain of *Bdellovibrio* that does not contain a copy of any of the three MltA homologues. As *Bdellovibrio* sp. Qaytius and *Bdellovibrio exovorus* are confirmed epibiotic predators that do not physically invade their prey, this may suggest an intraperiplasmic-related role for Bd3285 in predation.

Table 3.3. Conservation of MltA homologues in *Bdellovibrio* strains

Table showing the number of MltA-family homologues of Bd3285, Bd0599 and Bd0519 in each sequenced strain of *Bdellovibrio*. The predatory lifestyle (intraperiplasmic or epibiotic) of each *Bdellovibrio* strains is also indicated.

	Bdellovibrio strain	Number of homologues		
		Bd3285	Bd0599	Bd0519
Intraperiplasmic	***B. bacteriovorus* HD100**	x1	x1	x1
	***B. bacteriovorus* 109J**	x1	x1	x1
	***B. bacteriovorus* Tiberius**	x2	x2	x2
	***B. bacteriovorus* W**	x1	x1	None
	***B. bacteriovorus* ArHS**	None	x1	None
	***Bdellovibrio* sp. SKB1291214**	x1	x1	x1
	***Bdellovibrio* sp. SSB218315**	x1	None	x1
	***Bdellovibrio* sp. ZAP7**	x1	x1	x1
	***Bdellovibrio* sp. BER2**	x2	x1	x1
	***Bdellovibrio* sp. EC13**	x2	x1	x1
	***Bdellovibrio* sp. R0**	x2	x1	x2
	***Bdellovibrio* sp. NC01**	x1	x1	None
	***Bdellovibrio* sp. KM01**	x1	x2	None
Epibiotic	***Bdellovibrio* sp. Qaytius**	None	None	x2
	Bdellovibrio exovorus	None	None	None

3.3.2. Genomic introduction to the MltA family

3.3.2.1. Genomic location of genes encoding the MltA family in *B. bacteriovorus* HD100

In *B. bacteriovorus* HD100, the three MltA protein homologues are encoded separately from one another in the genome. Bd3285 is a 1,263 bp gene predicted to encode a 421 amino acid protein (however these numbers are adjusted in **Section 3.3.2.4** to account for a mis-annotated start codon). The gene *bd3285* is flanked by *bd3284* (a predicted hypothetical protein) and the heat shock chaperone *bd3286* and both are transcribed divergently from *bd3285* (Figure 3.2).

The *mltA* homologue *bd0599* is a 711 bp gene which encodes a 237 amino acid protein. The gene is flanked by the ABC transporter gene *bd0597* and *bd0600* (hypothetical gene but with a possible α/β-hydrolase fold).

The third *mltA* gene *bd0519* is 741 bp in length and encodes a 247 amino acid protein. The upstream gene *bd0518* is a predicted CDP-diacylglycerol phosphotidylhydrolase (Cdh) and the downstream gene *bd0520* encodes a hypothetical protein.

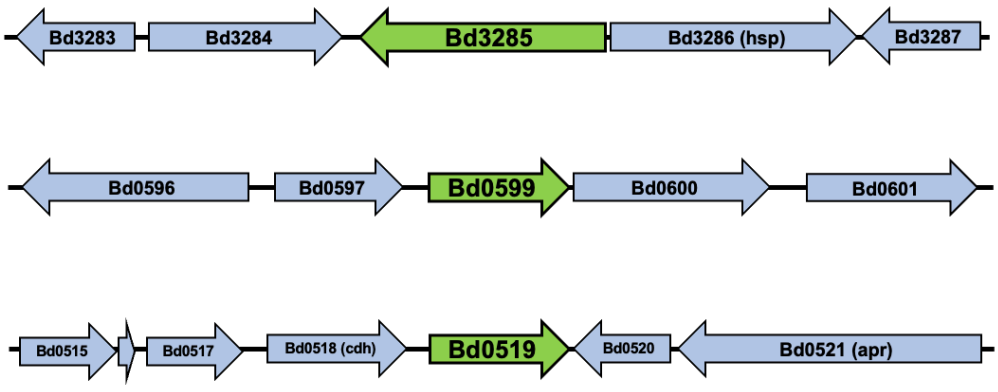

Figure 3.2. Genomic context of Bd3285, Bd0599 and Bd0519

5 kb genomic regions of the *B. bacteriovorus* HD100 genome showing the location of the *mltA* family genes *bd3285*, *bd0599* and *bd0519*. Images were acquired and re-drawn from the xBASE server[179, 180].

3.3.2.2. Gene *bd0599* is not co-transcribed with its neighbour *bd0600*

Since the gene *bd0600* is located just 25 bp downstream from *bd0599* and transcribed in the same direction as *bd0599*, it is possible that the two genes are co-transcribed. Moreover, *bd0600* has a predicted α/β-hydrolase fold and therefore may have a similar function to the lytic transglycosylase *bd0599*. Before any further genetic work (such as a gene knockout) was carried out on *bd0599*, it was considered useful to assess whether the two genes are co-transcribed together or not.

To test this, a pair of RT-PCR primers were designed with the forward primer annealing within the *bd0519* gene and the reverse primer annealing within the *bd0600* gene. If the two genes are co-transcribed on the same mRNA transcript then a 1,092 bp RT-PCR product should be generated, however no product was detected, indicating that the two genes are not transcribed together (Figure 3.3).

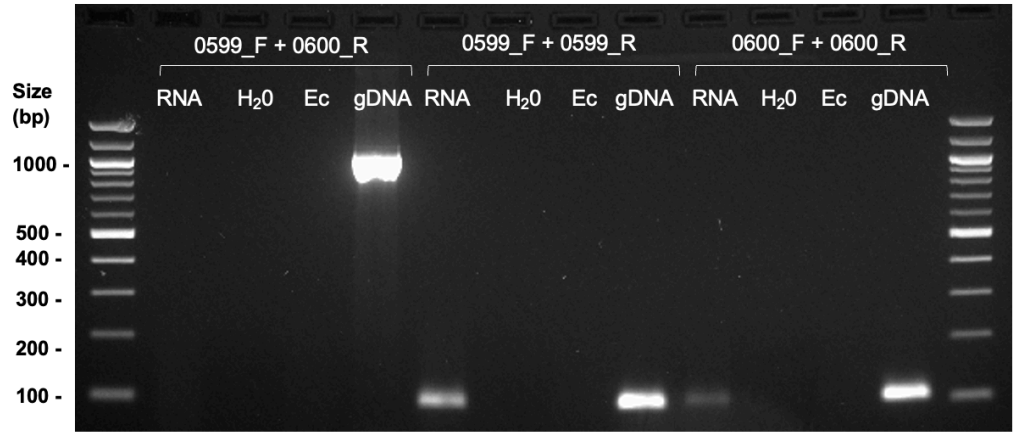

Figure 3.3. Reverse-transcriptase PCR showing no co-transcription of *bd0599* and *bd0600*

RT-PCR designed to test whether the genes *bd0599* and *bd0600* are co-transcribed. The absence of a 1,092 bp product for the primer pair 0599_F + 0600_R indicates that the genes are not co-transcribed. The control primer pairs 0599_F + 0599_R and 0600_F + 0600_R amplify a 108 bp product internal to each gene. RNA: *B. bacteriovorus* HD100 RNA isolated 15 min into the predatory lifecycle, H_20: negative water control, Ec: *E. coli* S17-1 negative control, gDNA: *B. bacteriovorus* HD100 genomic DNA positive control. The RT-PCR is representative of two biological repeats.

3.3.2.3. Bd0599 and Bd0519 contain predicted signal peptides

Entering the protein sequence of Bd0599 and Bd0519 into a signal peptide prediction server SignalP 5.0 reveals that both proteins contain a predicted N-terminal signal peptide. The presence of a signal peptide suggests that both proteins are translocated into the bacterial periplasm and possibly additionally secreted from the cell (although this is not possible to predict). While Bd0599 (and also Bd3285 as described in **Section 3.3.2.4**) contain lipoprotein signal peptides, the third homologue Bd0519 instead contains a more classical sec signal peptide and therefore may not be membrane-bound (Figure 3.4).

The lipoprotein signal peptide prediction for Bd0599 indicates that the protein is probably inserted into either the inner or outer cell membrane. The signal peptide of Bd0599 contains a lipobox motif (which are generally characterised by the amino acids [LVI]-[ASTVI]-[GAS]-C at the C-terminus). The lipobox contains the critically important cysteine residue at position +1 (residue C20 of Bd0599) which becomes the first amino acid following cleavage of the N-terminal signal peptide and is the residue to which a diacylglycerol moiety is added, lipidating the protein[223]. In many (but not all) bacteria, the presence of an aspartate residue immediately after the lipobox cysteine (position +2) results in the protein being retained at the inner cell membrane instead of being transported by the Lol (localisation of lipoprotein) machinery to the outer membrane[223]. This +2 rule is also called a 'lol avoidance motif'. Since there is an alanine at position +2 of Bd0599, it is most likely that the protein is transported and inserted into the outer membrane. Due to the proximity and physical interaction between predator and prey cell membranes during predation, it is also possible that the lipoprotein is inserted into the outer membrane of the prey. This might occur through blebbing of outer membrane vesicles (containing enzymes like Bd0599) from the *B. bacteriovorus* outer membrane that then fuse with the prey outer membrane.

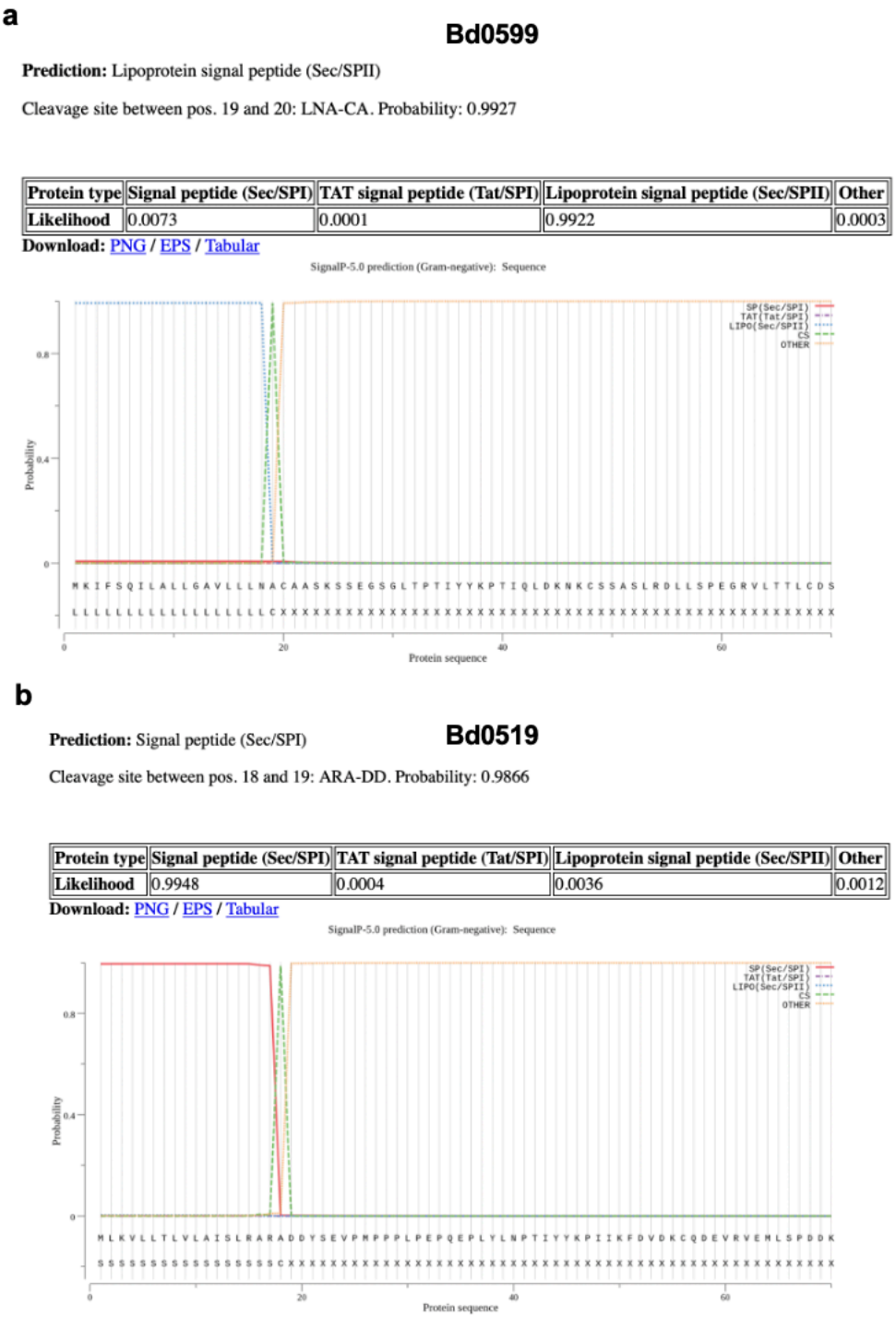

Figure 3.4. Signal peptide predictions for Bd0599 and Bd0519

a) Lipoprotein signal peptide prediction for Bd0599 (probability of 0.99) which is cleaved between the residues Ala-19 and Cys-20. **b)** Sec signal peptide prediction for Bd0519 (probability of 0.99) which is cleaved between the residues Ala-18 and Asp-19 Predictions were obtained from the SignalP 5.0 server[183] .

3.3.2.4. The start codon of Bd3285 was mis-annotated; correction reveals a predicted lipoprotein signal peptide

Entering the protein sequence of Bd3285 into a signal peptide prediction server gave an initially surprising result: no signal peptide was detected (Figure 3.5).

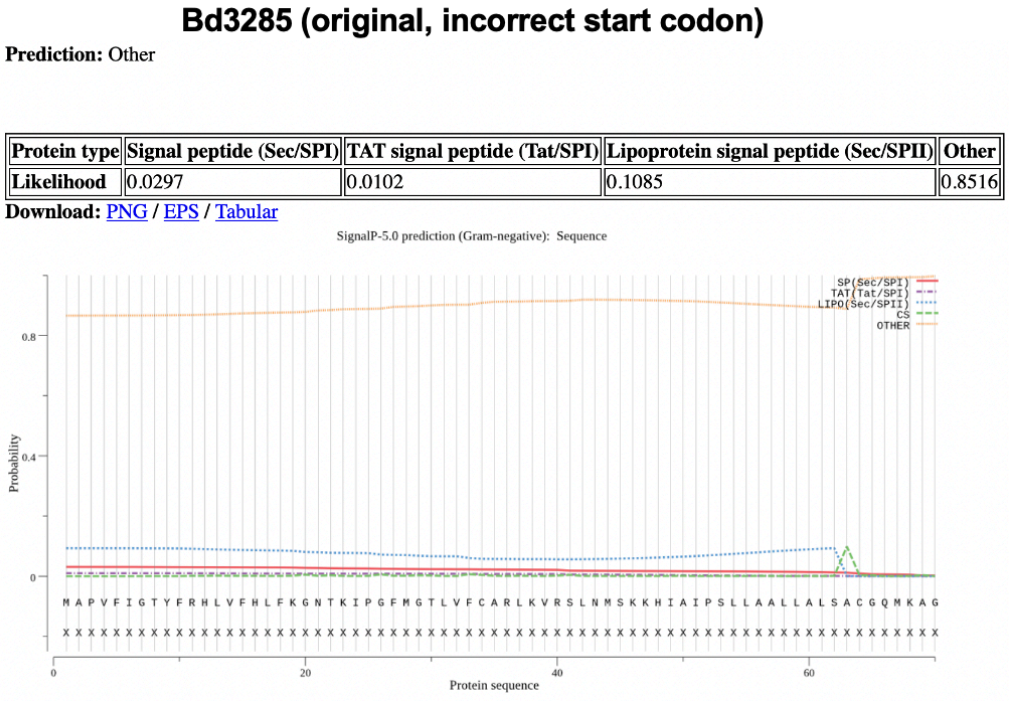

Figure 3.5. The original Bd3285 protein sequence does not contain a signal peptide

The original Bd3285 protein sequence (amino acids 1-421) does not contain any prediction of a signal peptide (prediction = “other” with a probability of 0.85). Prediction was obtained from the SignalP 5.0 server[183] .

Considering that the start codons of *B. bacteriovorus* HD100 genes are occasionally mis-annotated by software used to find the most likely opening reading frame (observed most recently by Lowry *et al*., 2019[224]), RNA-Seq reads from *B. bacteriovorus* HD100 (generated by Dr Simona Huwiler) were aligned to the HD100 genome sequence, allowing mRNA transcription of each gene to be visualised. The mRNA transcript should begin several bases upstream from a gene, and the Shine-Dalgarno (ribosome binding site) sequence (usually characterised by a very short run of As and Gs) is typically found approximately 8 bp upstream from the gene start codon. This was not the case for *bd3285* (Figure 3.6). The mRNA transcript (shown in red) begins approximately 106 bp into the gene itself and since the Shine-Dalgarno sequence and start codon of a gene must follow the start of mRNA transcription, this indicates that the original ATG start codon predicted for *bd3285* was mis-annotated. Examining the gene sequence, a probable true Shine-Dalgarno site (AGGAG) and an alternative ATG start codon 8 bp downstream from this site were identified (Figure 3.6).

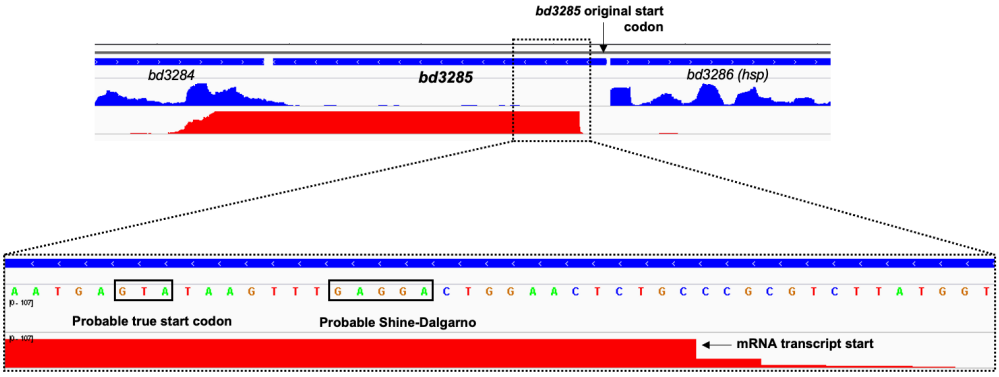

Figure 3.6. Prediction that the start codon of *bd3285* was mis-annotated

B. bacteriovorus HD100 RNA-Seq reads (kindly provided by Dr Simona Huwiler) from a 15 min predatory cycle timepoint aligned to the genome of *B. bacteriovorus* HD100 with Rockhopper[192, 193]. Reads (red block) show the transcriptional initiation site of *bd3285* (blue) which is encoded on the reverse strand. Transcription begins 106 bp into the gene sequence, indicating that the start codon was mis-annotated. The probable true Shine-Dalgarno site (AGGAG) and start codon (ATG) are annotated. The DNA sequence was reverse-complemented for ease of viewing. Data were visualised in Integrative Genomics Viewer[225].

This prediction could be further validated experimentally by using RT-PCR. Two sets of RT-PCR primers were designed: 3285_F2 and 3285_F3 which were each paired with the same reverse primer 3285_R (Figure 3.7a). 3285_F2 anneals 19 bp downstream from the originally predicted start codon but before the initiation of mRNA transcription, while 3285_F3 anneals at the initiation site of mRNA transcription. If the original start codon prediction is correct, then a 566 bp product should generated by 3285_F2 and 3285_R. If, however, the start was mis-annotated, then no product would be detected using this primer pair but a 481 bp product would be generated by 3285_F3 and 3285_R. RT-PCR showed no product using the 3285_F2 primer and a 481 bp product using the 3285_F3 primer (Figure 3.7) confirming that the start codon was indeed mis-annotated.

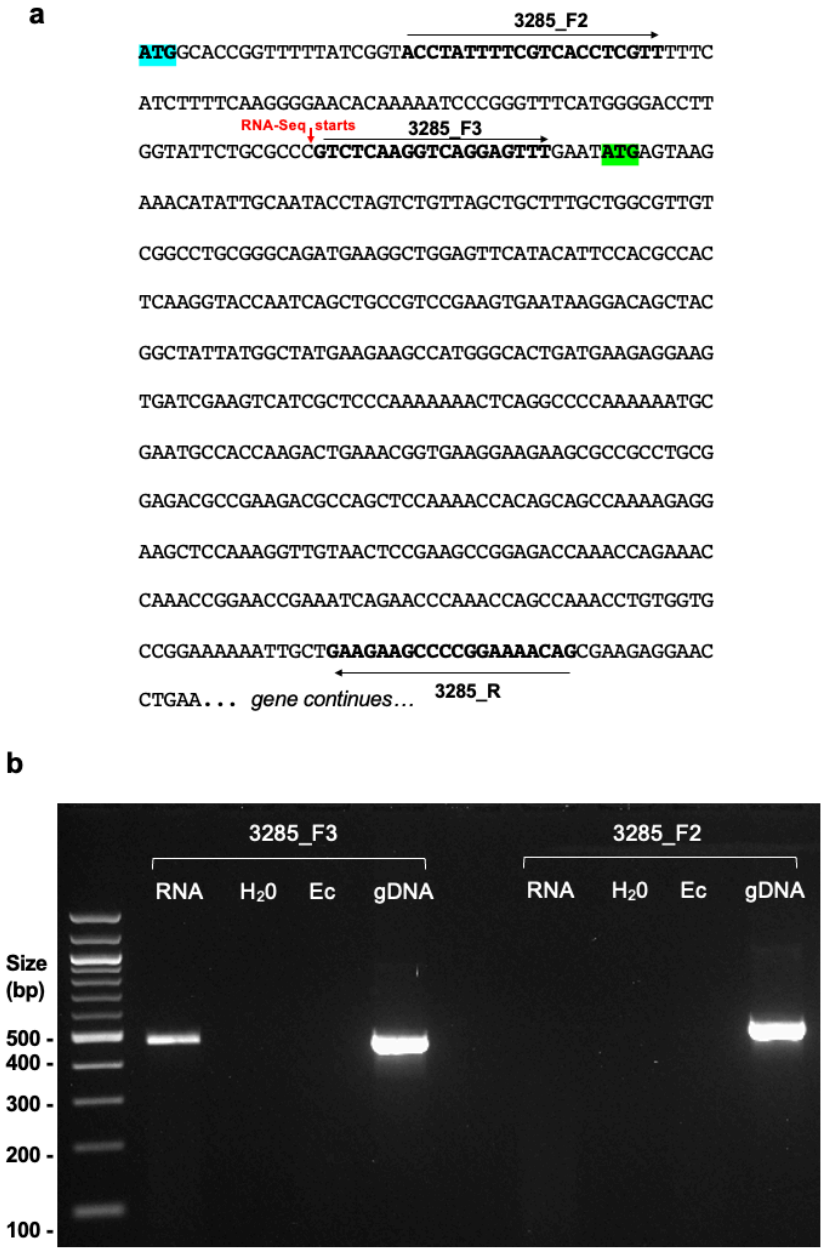

Figure 3.7. Confirmation that the start codon of *bd3285* was mis-annotated

a) 5' end of the *bd3285* gene. The originally annotated ATG start codon is highlighted in blue, the more probably true ATG start codon is highlighted in green and the RNA-Seq transcription start site is indicated by a red arrow. **b)** RT-PCR to test if the start codon of *bd3285* was mis-annotated using the primers 3285_F3 with 3285_R or 3285_F2 with 3285_R. The annealing site of each primer is indicated in **a**. No product was detected using the 3285_F2 primer but a 481 bp product was detected using 3285_F3, indicating that the RNA-Seq data is correct and that the original ATG start codon was mis-annotated. RNA: *B. bacteriovorus* HD100 15 min RNA, H_20: negative water control, Ec: *E. coli* S17-1 negative control, gDNA: *B. bacteriovorus* HD100 genomic DNA positive control. The RT-PCR is representative of two biological repeats.

Assigning the new ATG start codon to *bd3285* results in the protein sequence beginning at the amino acid M44 (which now becomes M1) and the protein reducing in size from 421 amino acids to 377 amino acids.

Importantly, entering the new protein sequence into the signal peptide prediction server results in the output of a lipoprotein signal peptide prediction (residues 1-20), with the lipobox cysteine at position 21 and a glycine at position 22, suggestive of insertion into the outer membrane (Figure 3.8).

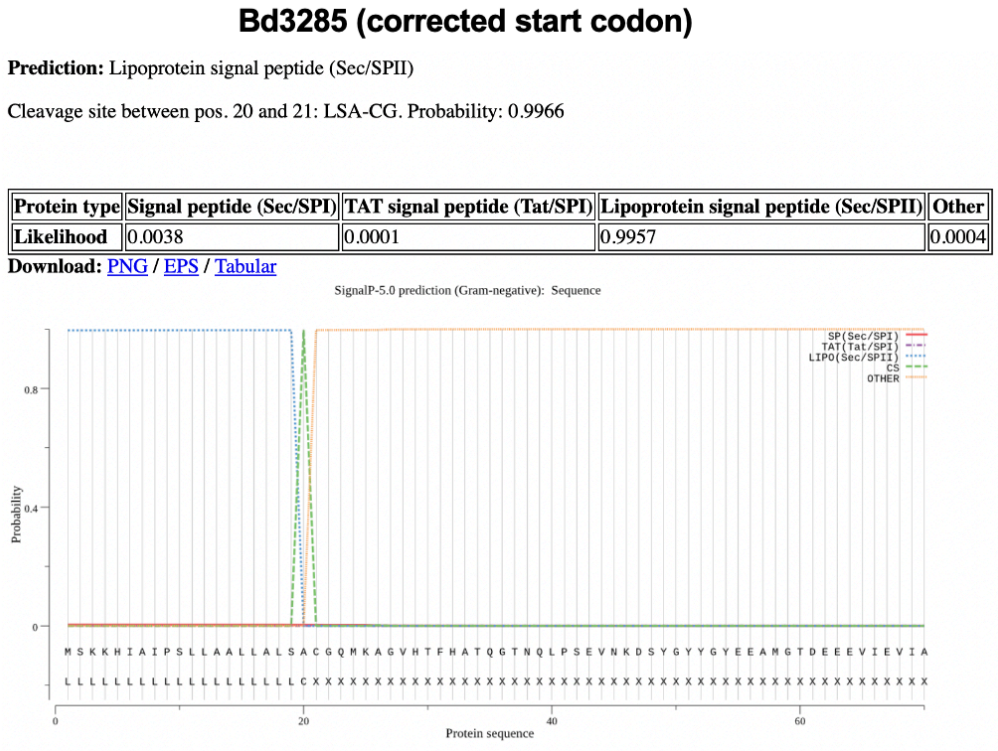

Figure 3.8. The corrected Bd3285 protein sequence contains a lipoprotein signal peptide

The corrected Bd3285 protein sequence (amino acids 1-377) now contains a lipoprotein signal peptide prediction (probability of 0.996). Prediction was obtained from the SignalP 5.0 server[183] .

3.3.2.5. Protein domains and residue predictions for the *B. bacteriovorus* MltA family

To further characterise the three *B. bacteriovorus* MltA family proteins at a bioinformatic level, protein domains (that could be predicted using online tools such as the Pfam server[184]) were annotated and compared to the domain structure of *E. coli* MltA (Figure 3.9).

E. coli MltA comprises a lipoprotein signal peptide (residues 1-20) and two domains: Domain A and Domain B[208, 226]. The domains are separated by a large groove, forming the characteristic 'kidney bean' shape of the monomeric protein[208, 226]. Domain A is separated into two discontinuous parts which are referred to in this thesis as Domain A1 (residues 23-124) and Domain A2 (3D) (residues 264-357)[208, 226]. Domain A2 (3D) consists of a large double-psi β-barrel fold and contains three conserved aspartate residues (3Ds): D281, D317 and D328[208, 226]. Domain B (residues 125-263) is an insertion within Domain A and comprises a smaller β-barrel fold[208, 226]. The wide grove dividing the two domains forms the active site of the protein, accommodating a peptidoglycan backbone strand which is subsequently cleaved[227].

The contribution of the 3 conserved aspartate residues towards PG catalysis was assessed by van Straaten *et al*. (2005)[208] by mutating each aspartate to an alanine and comparing the activity of each mutant protein on PG sacculi relative to wild-type MltA[208]. The D281A mutant retained 91 ± 6% activity on PG, suggesting that this residue is not important for catalysis. D281 also points away from the active site groove, indicating that it may not bind PG either. In contrast, the D317A had diminished activity on PG (24 ± 2%). The authors hypothesised - and later confirmed[227] - that D317 does not have a catalytic role but instead participates in PG-binding. Mutation of the final aspartate residue D328 to alanine completely abolished activity on PG (<1 % activity), indicating that this residue is the only essential aspartate for PG catalysis[208]; this

was confirmed by a subsequent study showing that D328 acts as a proton donor and acid catalyst to facilitate cleavage of PG strands[227].

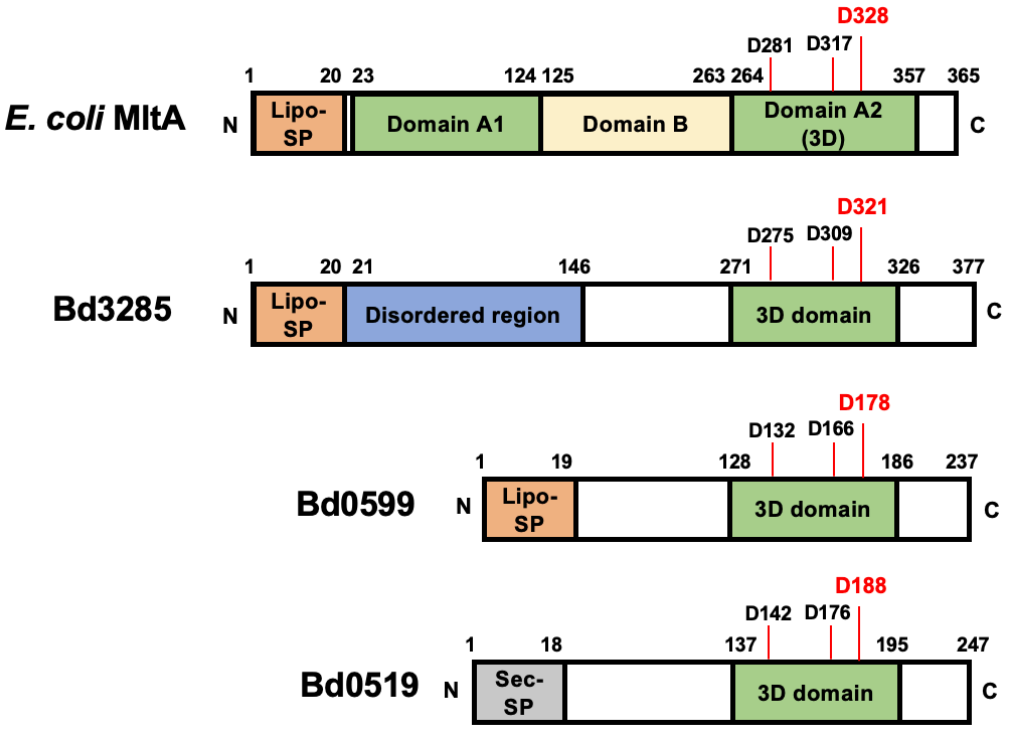

Figure 3.9. Predicted protein domains and conserved aspartate residues for *B. bacteriovorus* HD100 homologues of MltA

Schematics of predicted domains and catalytic residues for *E. coli* MltA and the three *B. bacteriovorus* HD100 homologues: Bd3285, Bd0599 and Bd0519. Numbers indicate amino acid position. Lipo-SP: lipoprotein signal peptide, Sec-SP: sec signal peptide. Domain and disordered region predictions are shown. The three conserved aspartate residues within the 3D domain are labelled, with the catalytic residue coloured in red. Schematics were drawn using information from the SignalP 5.0 prediction server[183], Phyre2 server[228] (for disordered region) and Pfam server[184] (for MltA and 3D domains).

The three *B. bacteriovorus* MltA homologues have some key similarities to the structure of *E. coli* MltA but also some clear differences. All three contain a well-conserved C-terminal catalytic 3D domain with complete conservation of the three aspartate residues (Figure 3.9 and Figure 3.10). The predicted catalytic aspartate residue (shown in red in Figure 3.9) is D321 in Bd3285, D178 in Bd0599 and D188 in Bd0519. The three homologues are also similar to *E. coli* MltA in that they contain N-terminal signal peptide sequences, although Bd0519 differs from the other proteins, containing a sec signal peptide instead of a lipoprotein signal.

B. bacteriovorus encodes machinery for the twin-arginine translocation (Tat) export pathway which, like sec, transports proteins into the periplasm, however none of the proteins studied in my PhD are candidates for Tat translocation as they do not contain a Tat motif. A Tat motif is characterised by a positively-charged N-terminus, a hydrophobic region and a C-terminus with the consensus sequence S/TRRXFLK.

In contrast to *E. coli* MltA, none of the three *B. bacteriovorus* proteins contain predictions for Domain A1 or Domain B, however, it is important to note that the organisation of these domains was only revealed following determination of the *E. coli* MltA crystal structure. However, while Bd3285 is of a similar length (377 amino acids) to *E. coli* MltA (365 amino acids), the N-terminus of Bd3285 (approximate residues 21-146) is predicted to be disordered and therefore unlikely to form a structural domain equivalent to Domain A1 in *E. coli* MltA. It is possible that the disordered region may still play a role in the function of Bd3285 although this is not possible to predict.

Bd0599 and Bd0519 are noticeably much shorter in length (237 and 247 amino acids, respectively) than both *E. coli* MltA and Bd3285 and it is therefore possible that these two homologues have a different physiological role.

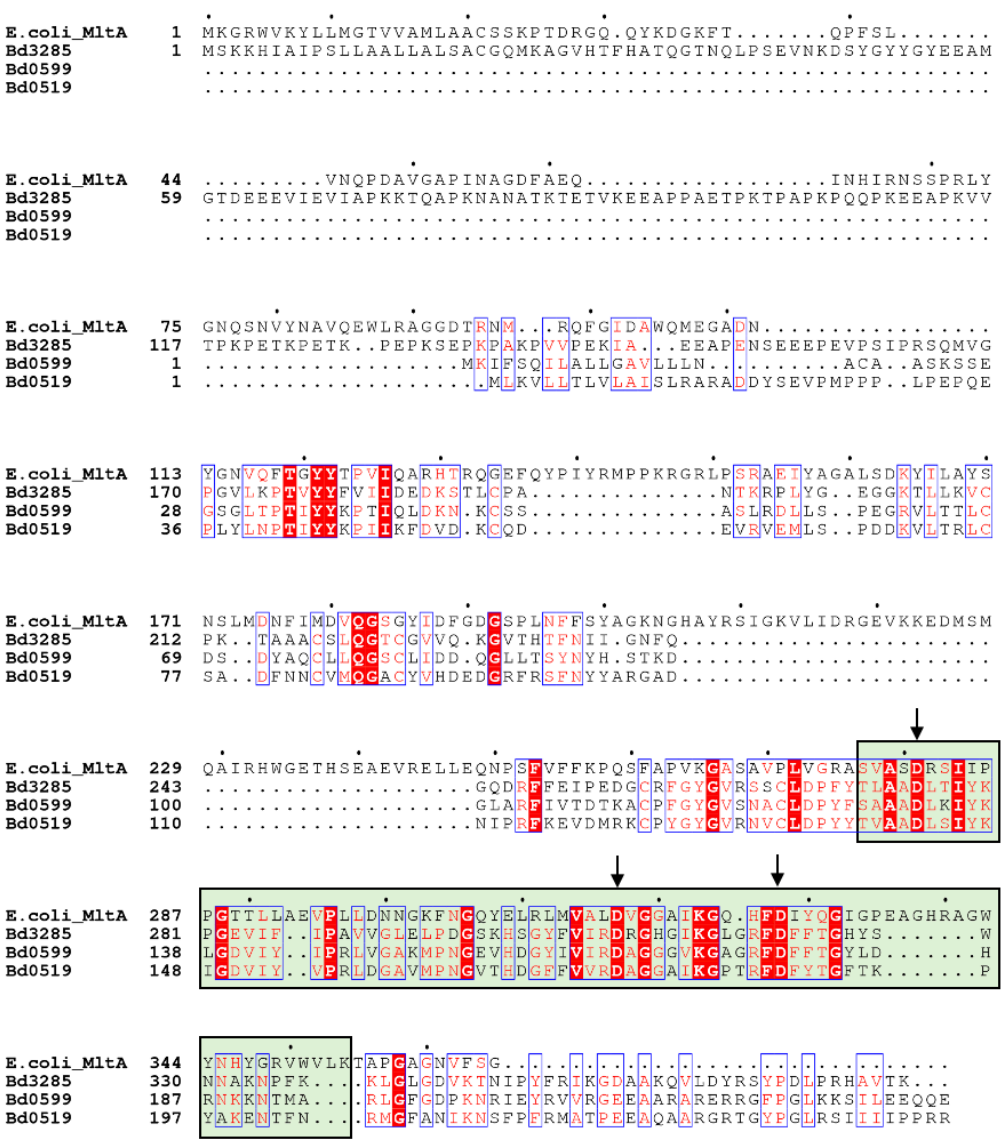

Figure 3.10. Protein sequence alignment of *B. bacteriovorus* HD100 MltA family proteins with MltA from *E. coli*

Sequence alignment of MltA from *E. coli* K12 with the MltA family proteins of *B. bacteriovorus* HD100: Bd3285, Bd0599 and Bd0519. Green boxed region: the predicted catalytic 3D domain of MltA from *E. coli*. Black arrows: the three conserved aspartate residues of the 3D domain. Red character: similarity across some proteins. Blue frame: similarity across all proteins. White character within a red box: strict identity conserved across all proteins. The sequence alignment was generated with Clustal Omega[229] and visualised with ESPript 3.0[188]

3.3.3. The genes encoding *B. bacteriovorus* MltA family proteins are all upregulated at 15-30 min during predation

The RNA-Seq dataset detailing the transcription of the MltA family genes across the predatory cycle indicated that Bd3285 and Bd0599 were upregulated at 15-30 min but Bd0519 was not (Table 3.2). It was on this basis that only the genes Bd3285 and Bd0599 were selected for investigation during this project. However, towards the end of my PhD, RT-PCR was performed for each gene across the predatory cycle to generate a manuscript figure (Figure 3.11). The RT-PCR confirmed that both Bd3285 and Bd0599 were upregulated at 15-30 min. Somewhat surprisingly, Bd0519 was also upregulated at 15 min and this result was consistently observed across three independent repeats. Although RNA-Seq is now a gold-standard technique to measure genetic transcription and assess differential gene expression, particularly for large datasets, it is not 100% accurate[230]. One study found that for 7 genes determined by RNA-Seq to be differentially expressed, 6/7 could be corroborated by RT-qPCR[192]. Moreover, for 3 out of 10 genes, the direction of differential gene expression as determined by RNA-Seq disagreed with RT-qPCR data[192]. Another study found that between 15-20% of genes in an RNA-Seq dataset could disagree with RT-qPCR results[231]. The authors also noted that the genes with a large degree of non-concordance between the two techniques were often expressed at very low levels, having a low number of reads per kb per million mapped reads (RPKM values)[231]. Bd0519 has very low RPKM values (varying from 1-8) compared to Bd3285 (12-1079) and Bd0599 (12-267) (Figure 3.12), therefore it is possible that the RNA-Seq struggled to identify differential expression for Bd0519.

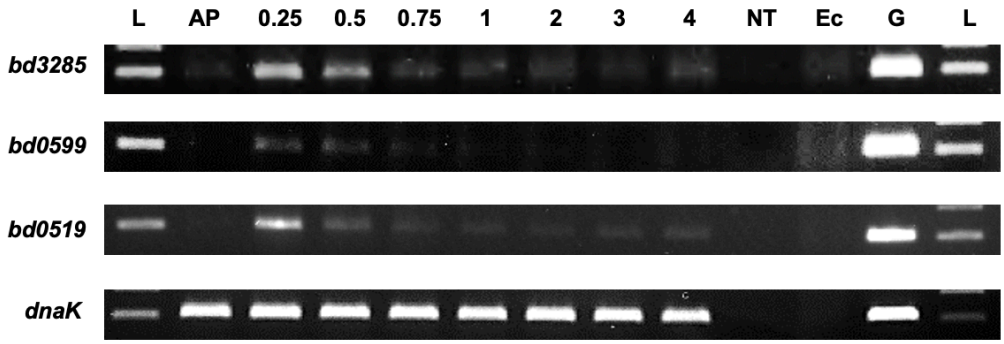

Figure 3.11. *B. bacteriovorus* HD100 MltA genes are upregulated during prey invasion

Reverse-transcriptase PCR (RT-PCR) performed on RNA isolated from different timepoints across the life cycle of *B. bacteriovorus* HD100. Primers were designed to amplify an approximately 100 bp product internal to *bd3285*, *bd0599*, *bd0519* or *dnaK* (known constitutively transcribed control gene). L: 100 bp DNA ladder, AP: attack-phase, 0.25-4: h since predators and prey were mixed, NT: no-template control, Ec: *E. coli* S17-1 RNA, G: *B. bacteriovorus* HD100 genomic DNA. Image is representative of at least two biological repeats for each gene.

Gene	Reads per kb per million mapped reads (RPKM) values							
	AP	15 min	30 min	45 min	1 h	2 h	3 h	4 h
Bd3285	12	580	1079	476	159	50	40	84
Bd0599	27	88	267	54	48	12	17	23
Bd0519	1	3	1	2	2	4	8	6

Figure 3.12. RPKM RNA-Seq values for *B. bacteriovorus* HD100 MltA family genes

RNA-Seq data was generated from total RNA isolated across different timepoints in the lifecycle of *B. bacteriovorus* HD100 preying upon *E. coli* K12 (data obtained by Dr Simona Huwiler). The RPKM values (reads per kb per million mapped reads) for all *B. bacteriovorus* genes were obtained by Dr Simona Huwiler from Rockhopper[192, 193] following the input of raw RNA-Seq fastq files.

3.3.4. Bd3285-mCherry is secreted into the prey bdelloplast

Bd3285 was selected as the first MltA homologue to be characterised experimentally. As previously stated, the third homologue Bd0519 was not investigated during my PhD.

The proteins encoded by *B. bacteriovorus* genes that are upregulated at prey invasion (15-30 min) may be secreted from the *B. bacteriovorus* predator cell into the dying prey cell to facilitate invasion. For example, the DD-endopeptidase (DacB enzymes) Bd0816 and Bd3459 are secreted into the prey periplasm to cut PG crosslinks, relaxing the prey cell wall and resulting in the transformation of rod-shaped prey into spherical prey bdelloplasts[115]. The signal peptide prediction and upregulation of the transcript for *bd3285* at prey invasion suggested that it may also be secreted into prey.

To determine whether Bd3285 localises to *B. bacteriovorus* predator cells during predation or is secreted into the prey bdelloplast, Bd3285 was fluorescently tagged with the fluorophore mCherry. Although mCherry is not the brightest fluorophore, it was selected here as it is one of few fluorophores that can fluoresce within the bacterial periplasm (mNeonGreen is an exception but often results in autofluorescence within bdelloplasts if the protein of interest is expressed at low levels).

The fluorescent fusion protein Bd3285-mCherry was constructed and introduced into the genome of *B. bacteriovorus* HD100 via single-crossover homologous recombination (as described in **Chapter 2 Section 2.11**). The resulting *B. bacteriovorus* strain (maintained under a kanamycin selection pressure) was verified by Sanger sequencing. *B. bacteriovorus* Bd3285-mCherry was then mixed with *E. coli* S17-1 (pZMR100) (a strain of S17-1 containing the plasmid pZMR100 which expresses a kanamycin-resistance gene) to set up a synchronous predatory cycle (as described in **Chapter 2 Section 2.16.2.2**). Samples

were then removed at different timepoints throughout predation to acquire fluorescence microscopy images.

There was no detectable Bd3285-mCherry fluorescence within free-swimming *B. bacteriovorus* attack-phase cells, nor was any fluorescence detected at 15 min or 30 min during predator-prey attachment and invasion (Figure 3.13). At approximately 1.5 h, however, faint Bd3285-mCherry fluorescence was visible within prey bdelloplasts and could be observed until prey lysis at 4 h (Figure 3.13).

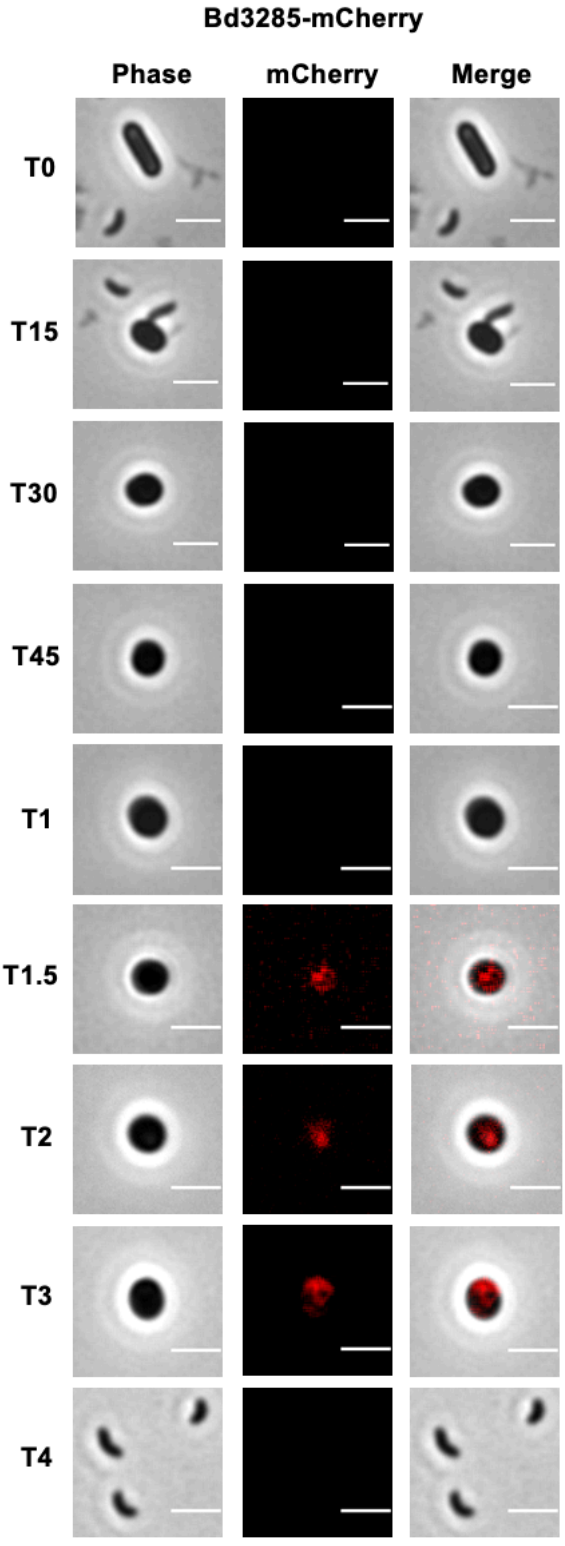

Figure 3.13. Bd3285-mCherry fluorescence inside *E. coli* prey bdelloplasts
Fluorescence microscopy images of *B. bacteriovorus* HD100 containing the single-crossover fusion Bd3285-mCherry during predation on *E. coli* S17-1 (pZMR100). T0-T4: hours elapsed since predators and prey were first mixed. Scale bars = 2 μm and images are representative of three biological repeats.

To verify that the fluorescent signal was secreted into the periplasm of the prey bdelloplast and not retained within the *B. bacteriovorus* predator, the Bd3285-mCherry construct was introduced into a strain of *B. bacteriovorus* HD100 that contained an existing fusion of Bd0064-mCerulean3. Bd0064 is one of many PilZ domain-containing proteins in *B. bacteriovorus* and PilZ domains are common receptors for binding cyclic-di-GMP[232, 233, 234, 235, 236]. Bd0064 is cytoplasmic and a previous fusion of Bd0064-mCherry labelled the cytoplasm of *B. bacteriovorus* effectively without any detrimental effects[47]. Bd0064 fluorescent fusions are therefore incredibly useful as a label for the *B. bacteriovorus* cell during predation, thus allowing the visualisation of predators inside prey bdelloplasts. Imaging *B. bacteriovorus* Bd3285-mCherry + Bd0064-mCerulean3 during a predatory timecourse revealed that the Bd3285-mCherry signal did not co-localise with the blue *B. bacteriovorus* predator cell, confirming that the protein is secreted into the prey cell (Figure 3.14).

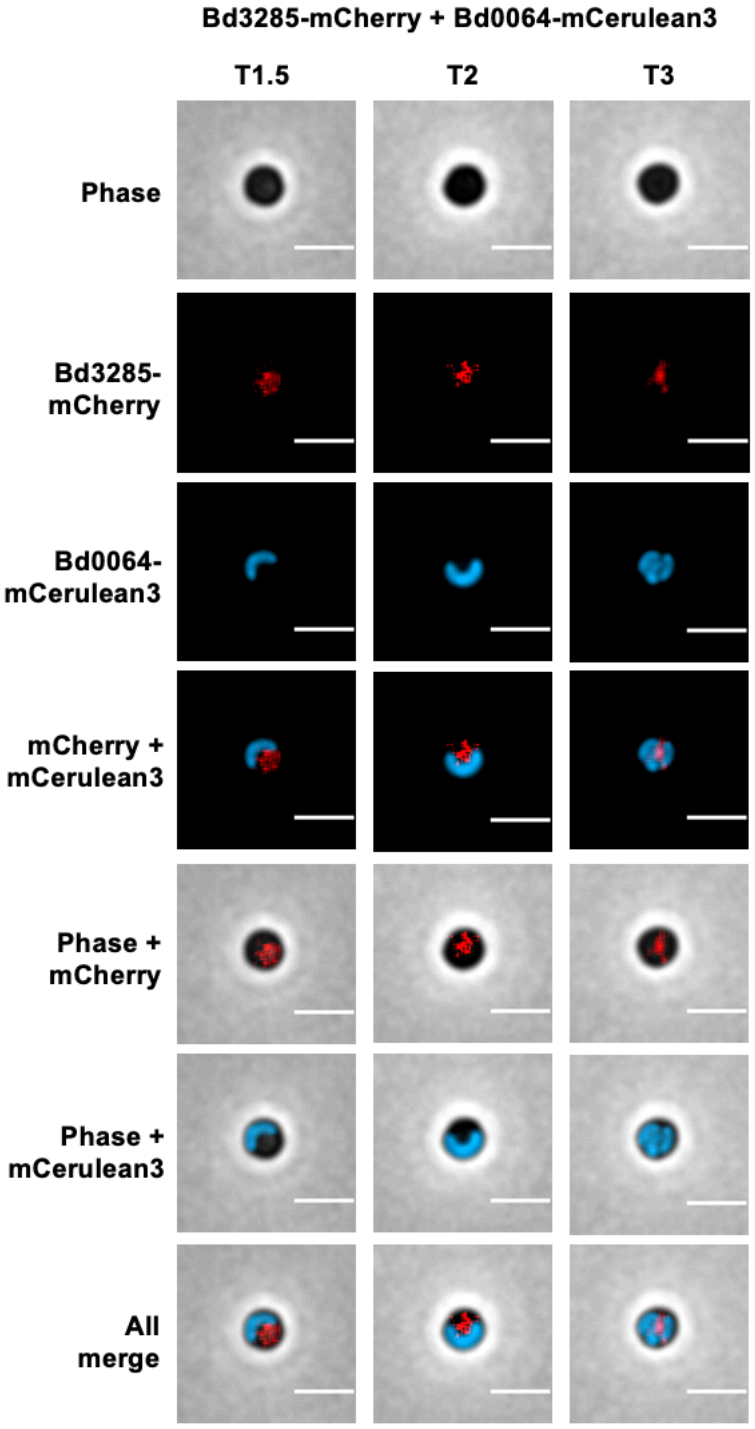

Figure 3.14. Bd3285-mCherry fluorescence does not co-localise with *B. bacteriovorus* predators and is thus secreted inside prey bdelloplasts

Fluorescence microscopy images of *B. bacteriovorus* HD100 containing both a single-crossover fusion of Bd3285-mCherry and a double-crossover fusion of Bd0064-mCerulean3 during predation on *E. coli* S17-1 (pZMR100). T1.5-3: hours elapsed since predators and prey were first mixed. Scale bars = 2 μm and images are representative of three biological repeats.

Although Bd3285 is secreted into the prey bdelloplast, the time at which fluorescence appeared (1.5 h) does not agree with transcriptional upregulation of the gene at 15-30 min. This discrepancy between the transcriptional peak and visualisation of mCherry fluorescence within prey has, however, been previously noted in our laboratory (pers. comm. from Dr Carey Lambert). The gene *bd1904* which is strongly upregulated at 15 min was not visible inside prey bdelloplasts (detected as a Bd1904-mCherry fusion) until approximately 1.5 h. Indeed, no *B. bacteriovorus* protein (which is secreted into the prey bdelloplast) has been detected before 45 min.

Considering this, I hypothesised that the oxidising conditions, oxygenation levels and/or pH of the *E. coli* periplasm may change during predation. Following initial prey invasion, the *E. coli* periplasmic environment may be different to that of the *E. coli* periplasm >1h into predation. *B. bacteriovorus* secretes many degradative proteins into the *E. coli* periplasm and cytoplasm in order to assimilate nucleic acids and proteins and facilitate growth[34, 35]. This molecular secretion may be sufficient to alter the physico-chemical environment of the *E. coli* periplasm. Successful fluorophore folding is dependent on multiple factors including the oxidative state and pH of the environment[237]. It is therefore possible that the conditions of the 'early' *E. coli* periplasm may not be conducive to the folding of the mCherry fluorophore (for example, mCherry may not be visible below a pH of 4.5 as this is its pKa value[237]). Over time, however, the conditions of the *E. coli* periplasm may alter and reach a more optimal environment for mCherry folding, resulting in visualisation of the fluorescent protein of interest.

To test this hypothesis, I collaborated with Dr Carey Lambert to try and detect Bd3285 and Bd1904 by western blot using an anti-mCherry antibody as this would report on the production of the fusion protein even if it is unable to fold correctly. This western blot analysis was kindly performed by Dr Carey Lambert. Figure 3.15 shows the detection of both Bd0064-mCherry (a constitutive control) and Bd3285-mCherry in either

attack-phase (AP) *B. bacteriovorus* cells or at the timepoints of 30 min, 1 h, 2 h and 3 h during predation on *E. coli* S17-1 (pZMR100). Bd0064-mCherry is retained within *B. bacteriovorus* predator cells and not secreted into the bdelloplast. As expected Bd0064-mCherry was detected across all timepoints, however, two bands (31 kDa and 41 kDa) were observed instead of a predicted single band of 39 kDa. This could suggest that the Bd0064-mCherry undergoes cleavage. Bd3285-mCherry was detected by western blot at only 30 min. A protein band of the expected size (66 kDa) was observed but a second band at approximately 76 kDa was also detected. This could indicate that the Bd3285-mCherry protein is post-translationally modified in some way. Bd1904-mCherry - for which fluorescence is also only visible from 1.5 h onwards - was also detected by western blot as early as 30 min (data not shown).

This analysis confirms that the Bd3285 protein is produced at or before 30 min during predation, supporting transcriptional upregulation at 15-30 min, and suggests that an inability of the mCherry fluorophore to fold in ‘early’ periplasmic conditions (<1-1.5 h) may explain the absence of Bd3285-mCherry (and Bd1904-mCherry) fluorescence inside prey until 1.5 h.

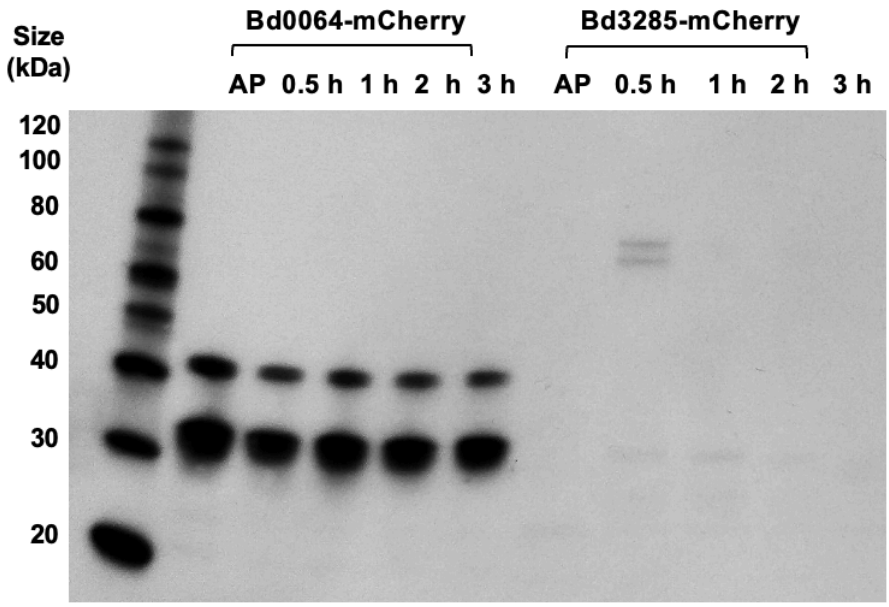

Figure 3.15. Bd3285-mCherry is only detected at 0.5 h during predation by western blot

Western blot **(performed by Dr Carey Lambert)** to detect Bd3285-mCherry during predation by *B. bacteriovorus* on *E. coli* S17-1 (pZMR100) prey. Samples were removed prior to predation (attack-phase: AP) and at timepoints throughout predation (0.5 h – 3 h). Samples were mixed with 4X SDS-PAGE loading buffer containing β-mercaptoethanol, frozen, boiled for 5 min and then loaded onto a 4-20% SDS-PAGE gel. Proteins were detected with an anti-mCherry antibody. Bd0064-mCherry (which is retained inside the *B. bacteriovorus* predator cell cytoplasm) is a continuously expressed control for mCherry detection during predation. Bd0064-mCherry (39 kDa) was detected as two products approximately 41 kDa and 31 kDa in size. Bd3285-mCherry (66 kDa) was detected only at 0.5 h alongside a slightly larger band of approximately 76 kDa. The blot is representative of one independent repeat.

3.3.5. Deletion of *bd3285* from *B. bacteriovorus* HD100

Visualisation of Bd3285-mCherry inside *E. coli* prey bdelloplasts indicates that the protein is secreted by *B. bacteriovorus* into prey. To determine the function of Bd3285, an in-frame markerless deletion of the *bd3285* gene was constructed in *B. bacteriovorus* HD100. This genetic knockout was generated by Mr Samuel Mason, an MSci project student in our lab under my supervision. In brief, 1 kb of DNA flanking the *bd3285* was cloned into the suicide vector pK18*mobsacB* and conjugated into *B. bacteriovorus* HD100 via an *E. coli* S17-1 donor strain containing the suicide plasmid. The resulting single-crossover merodiploid strain underwent multiple rounds of sucrose suicide counter-selection to force a second crossover event whereby the plasmid is excised and either a wild-type revertant or genetic deletion is generated. Gene *bd3285* was successfully deleted from the genome of *B. bacteriovorus* HD100 (Figure 3.16) and confirmed by Sanger sequencing. Successful deletion of *bd3285* within a prey-dependent culture of *B. bacteriovorus* HD100 indicates that the gene is not essential for predation, however the deletion did result in a predation-related phenotype which is described in the following sections.

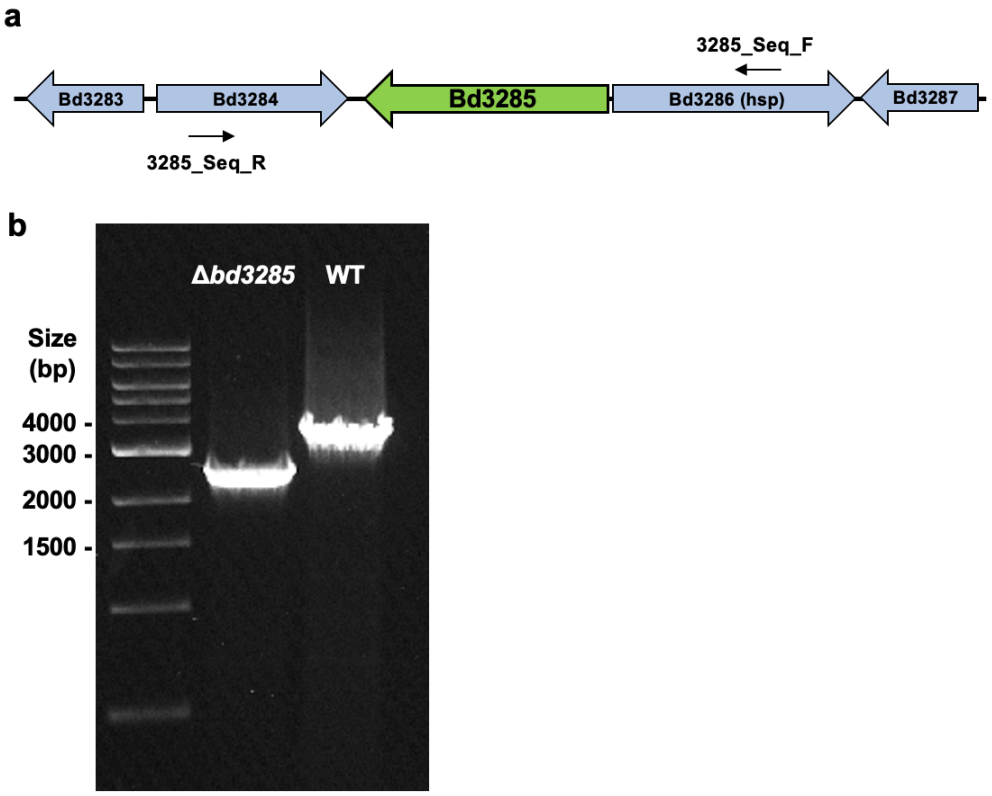

Figure 3.16. Genetic deletion of *bd3285* from *B. bacteriovorus* HD100

a) Amplification across the chromosomal region containing the *bd3285* gene showing the primers 3285_Seq_F and 3285_Seq_R used to confirm the deletion of *bd3285*. **b)** Agarose gel confirming the successful deletion of *bd3285* from the genome of *B. bacteriovorus* HD100. Bands show PCR products amplified from the genomic DNA of the Δ*bd3285* mutant and wild-type (WT) *B. bacteriovorus* HD100. Primers (annotated in **a**) were designed to anneal approximately 200 bp either side of the site of homologous recombination. The Δ*bd3285* band (2,590 bp) was 1,118 bp smaller than the wild-type (3,708 bp), indicating successful deletion of *bd3285*. The deletion mutant was obtained by MSci project student Mr Samuel Mason under my supervision.

3.3.6. Deletion of *bd3285* alters the morphology of *E. coli* prey bdelloplasts

To visualise Δ*bd3285 B. bacteriovorus* predators inside prey, a C-terminal fusion of mCherry to the cytoplasmic protein Bd0064 (generating Bd0064-mCherry) was introduced into Δ*bd3285* via single-crossover homologous recombination, thus labelling the cytoplasm of *B. bacteriovorus* cells red. Wild-type and Δ*bd3285* strains were then mixed with *E. coli* S17-1 (pZMR100) prey to begin a synchronous predatory timecourse during which fluorescent microscopy images were acquired.

Wild-type *B. bacteriovorus* predators round up all rod-shaped *E. coli* cells into spherical bdelloplasts during prey invasion, however, this did not occur during prey invasion by the Δ*bd3285* mutant (Figure 3.17a). Bdelloplasts invaded by Δ*bd3285* predators could be classified into three distinct shapes: spheres, rods, and rods that narrowed in width at the mid-cell (hereafter referred to as 'dumbbells'). Dumbbells were identified by eye and rods were classified as bdelloplasts that had a circularity value of ≤0.96 A.U. as all wild-type round bdelloplasts had a circularity value above this threshold.

While 100% of bdelloplasts invaded by wild-type predators were spherical, for bdelloplasts invaded by Δ*bd3285*, only 62.7% were spherical, 33.0% were rod-shaped, and 4.3% were dumbbell-shaped (Figure 3.17b). Quantifying the proportion of spherical bdelloplasts for wild-type HD1000 and Δ*bd3285* predation showed that there was a statistically significant difference in *E. coli* bdelloplast shape between the two strains ($p<0.01$; Figure 3.17c). Moreover, the median circularity of bdelloplasts invaded by Δ*bd3285* was significantly lower than those invaded by the wild-type ($p<0.0001$; Figure 3.17d). In comparison to the wild-type, *E. coli* prey invaded by Δ*bd3285* predators also had a significantly longer length ($p<0.0001$; Figure 3.18a), accompanied by a significantly shorter width ($p<0.0001$; Figure 3.18b). The lower circularity,

longer length and shorter width of Δ*bd3285*-invaded *E. coli* prey reflects the presence of rod-shaped and dumbbell-shaped prey bdelloplasts which are absent during wild-type predation.

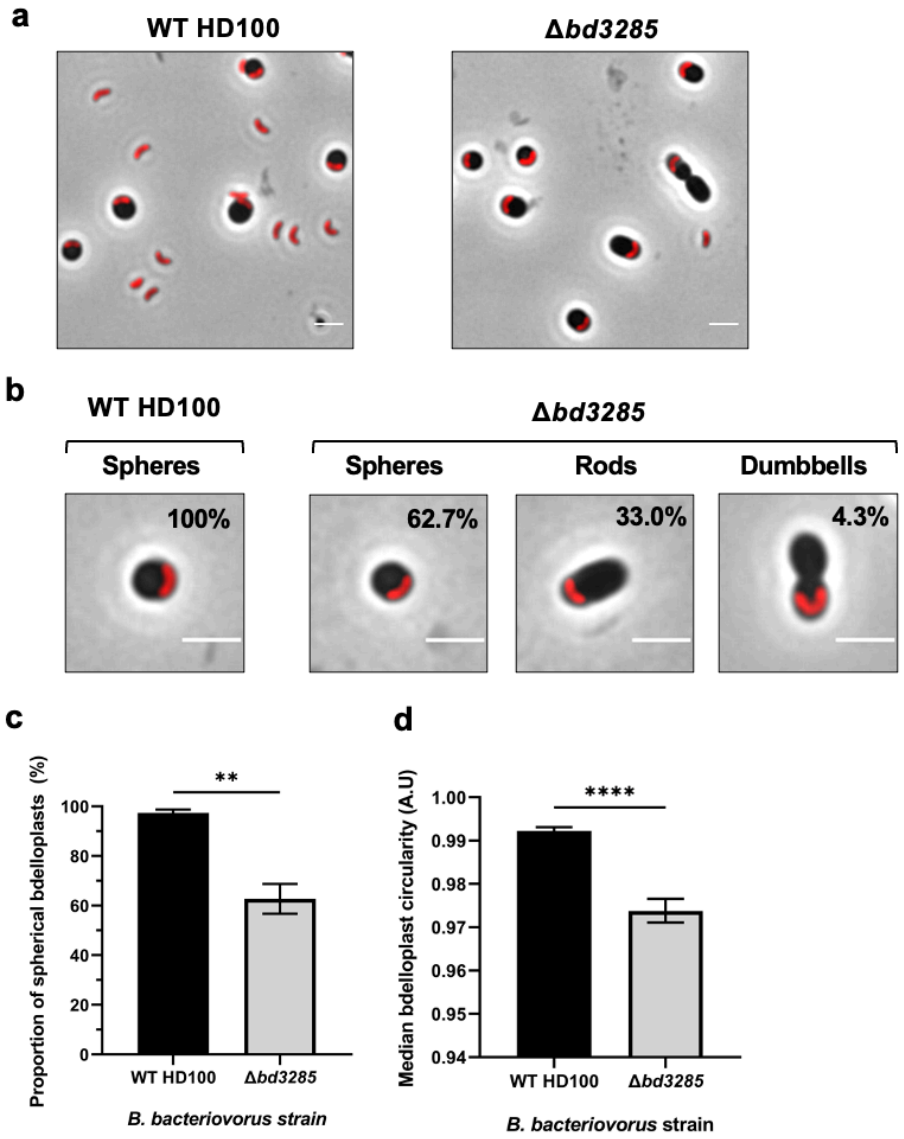

Figure 3.17. Deletion of *bd3285* results in three different prey bdelloplast shapes, compared to just one observed for wild-type *B. bacteriovorus*

Predation of *B. bacteriovorus* HD100 wild-type and Δ*bd3285* (both containing a cytoplasmic fusion of Bd0064-mCherry) on *E. coli* S17-1 (pZMR100). **a)** Images of wild-type (left) and Δ*bd3285* (right) predators inside prey, showing the different morphologies of prey invaded by Δ*bd3285*. **b)** The three different bdelloplast shapes for prey invaded by Δ*bd3285*. The proportion of bdelloplasts represented by each shape is noted in the top right of each image. For **a** and **b**, scale bars = 2 μm and images are representative

of three biological repeats. **c)** Proportion of spherical bdelloplasts (spherical bdelloplasts classified by a circularity value of >0.96 A.U.) and **d)** median circularity of bdelloplasts invaded by wild-type or Δ*bd3285* predators. Error bars represent either standard error of the mean (**c**) or 95% confidence intervals of the median (**d**). n = 234-670 total cells analysed at the 1 h timepoint across three biological repeats. ** = $p<0.01$ (unpaired t-test), **** = $p<0.0001$ (Mann-Whitney test).

Deletion of Δ*bd3285* results in aberrant prey bdelloplast morphologies, suggesting that Bd3285 is secreted into *E. coli* prey bdelloplasts during invasion, facilitating the conversion of rod-shaped prey into spherical prey cells.

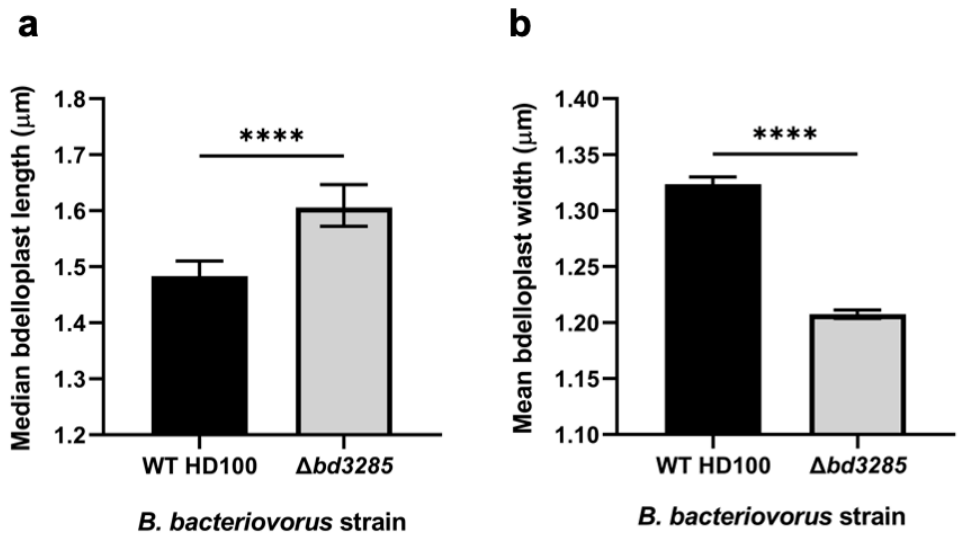

Figure 3.18. Length and width of *E. coli* bdelloplasts invaded by *B. bacteriovorus* wild-type and Δ*bd3285* strains

MicrobeJ measurements of median length (**a**) and mean width (**b**) of prey bdelloplasts invaded by *B. bacteriovorus* HD100 wild-type or Δ*bd3285* predators – each containing a cytoplasmic fusion of Bd0064-mCherry. Error bars represent either 95% confidence intervals of the median (**a**) or standard error of the mean (**b**). n = 234-670 cells analysed at the 1 h timepoint across three biological repeats. **** = p<0.0001 (Mann-Whitney test (**a**) and unpaired t-test (**b**)).

3.3.7. Prey bdelloplast shape is complemented by a wild-type copy of *bd3285* but not the predicted catalytic-null point mutant D321A

To verify that the phenotype of prey cell shape could be solely attributed to Bd3285, it was important to complement the genetic deletion of Δ*bd3285*. Complementation can be achieved by one of three methods: 1) Introduction of a plasmid containing the gene of interest into the mutant, 2) Re-introduction of the gene into the genome via single-crossover homologous recombination, or 3) Re-introduction of the gene into the genome via double-crossover homologous recombination (all described in **Chapter 2 Section 2.9**). The first two methods are the simplest and most rapid. These are explored later in **Chapter 4** and **Chapter 5**. The third method: re-introduction of the gene via double-crossover recombination is more time-consuming as the work-flow process is similar to the creation of the original genetic knockout.

To measure the prey shape phenotype of Δ*bd3285*, it was important to introduce the Bd0064-mCherry fusion protein into Δ*bd3285* to verify that all bdelloplasts which were analysed contained a *B. bacteriovorus* predator cell and were not empty. It was therefore also necessary to introduce Bd0064-mCherry into Δ*bd3285* complementation strains. Bd0064-mCherry is introduced via single-crossover recombination (generating a kanamycin-resistant strain). It was therefore essential to first construct complementation strains via double-crossover recombination to generate a markerless recipient strain into which Bd0064-mCherry could subsequently be introduced.

Two different complementation constructs were designed: 1) a wild-type copy of *bd3285*, and 2) a copy of *bd3285* containing the point mutation D321A within the 3D catalytic domain (Figure 3.19). The wild-type copy should successfully complement the gene deletion, while the D321A copy should be incapable of complementation if D321 is the critical

catalytic residue of Bd3285 - as previously predicted due to conservation with *E. coli* MltA (Figure 3.9 and Figure 3.10).

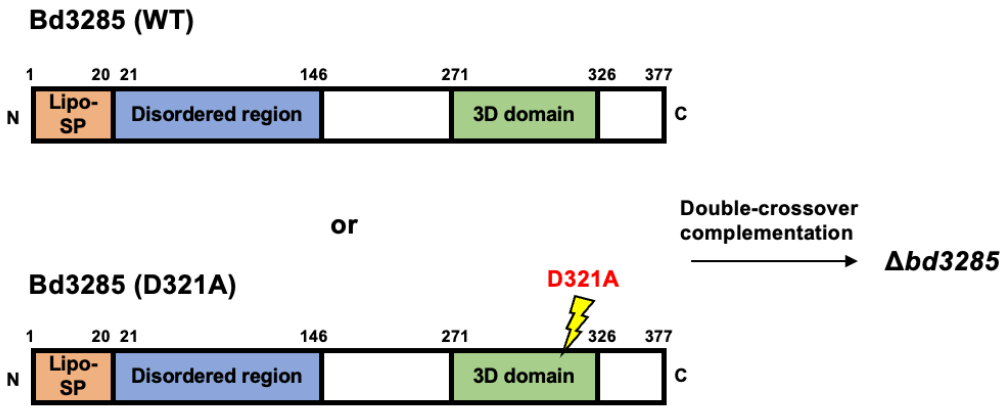

Figure 3.19. Bd3285 constructs designed for complementation of Δ*bd3285* via double-crossover homologous recombination

Schematics of either a wild-type copy of *bd3285* (top) or a copy of *bd3285* containing a catalytic point mutation of D321A in the predicted 3D domain (bottom). Numbers above schematics indicate amino acid position. The D321A mutation is shown in bold red characters and the location is indicated by a yellow lightning strike symbol. The complementation constructs were separately introduced into the genome of the *B. bacteriovorus* Δ*bd3285* mutant via double-crossover homologous recombination and confirmed by Sanger sequencing.

Each complementation construct was separately introduced into the ∆*bd3285* chromosome via double-crossover complementation to generate the two new strains ∆*bd3285* (WT comp) and ∆*bd3285* (D321A comp) which were confirmed by Sanger sequencing. Finally, Bd0064-mCherry was introduced into the two strains via a single-crossover to label the *B. bacteriovorus* cytoplasm red. Each *B. bacteriovorus* complementation strain was then mixed with *E. coli* S17-1 (pZMR100) and images were taken throughout the predatory cycle as described previously. *E. coli* prey bdelloplasts invaded by the *B. bacteriovorus* ∆*bd3285* complementation strain containing the wild-type copy of *bd3285* were spherical and did not significantly differ in circularity, length, or width from the wild-type strain (Figure 3.20). In contrast, *E. coli* prey bdelloplasts invaded by the *B. bacteriovorus* ∆*bd3285* complementation strain containing the D321A mutated copy of *bd3285* had a very similar distribution of morphological phenotypes to the original ∆*bd3285* mutant. Spheres, rods and dumbbell bdelloplasts were observed, with the overall population of prey bdelloplasts having a significantly lower circularity, longer length and shorter width compared to the wild-type (Figure 3.20).

The construction of these two different complementation strains confirmed that 1) the *bd3285* gene is responsible for the phenotypic difference in bdelloplast morphology and that 2) the aspartate residue D321 within the predicted C-terminal 3D domain is a critical residue for the bdelloplast remodelling function of Bd3285.

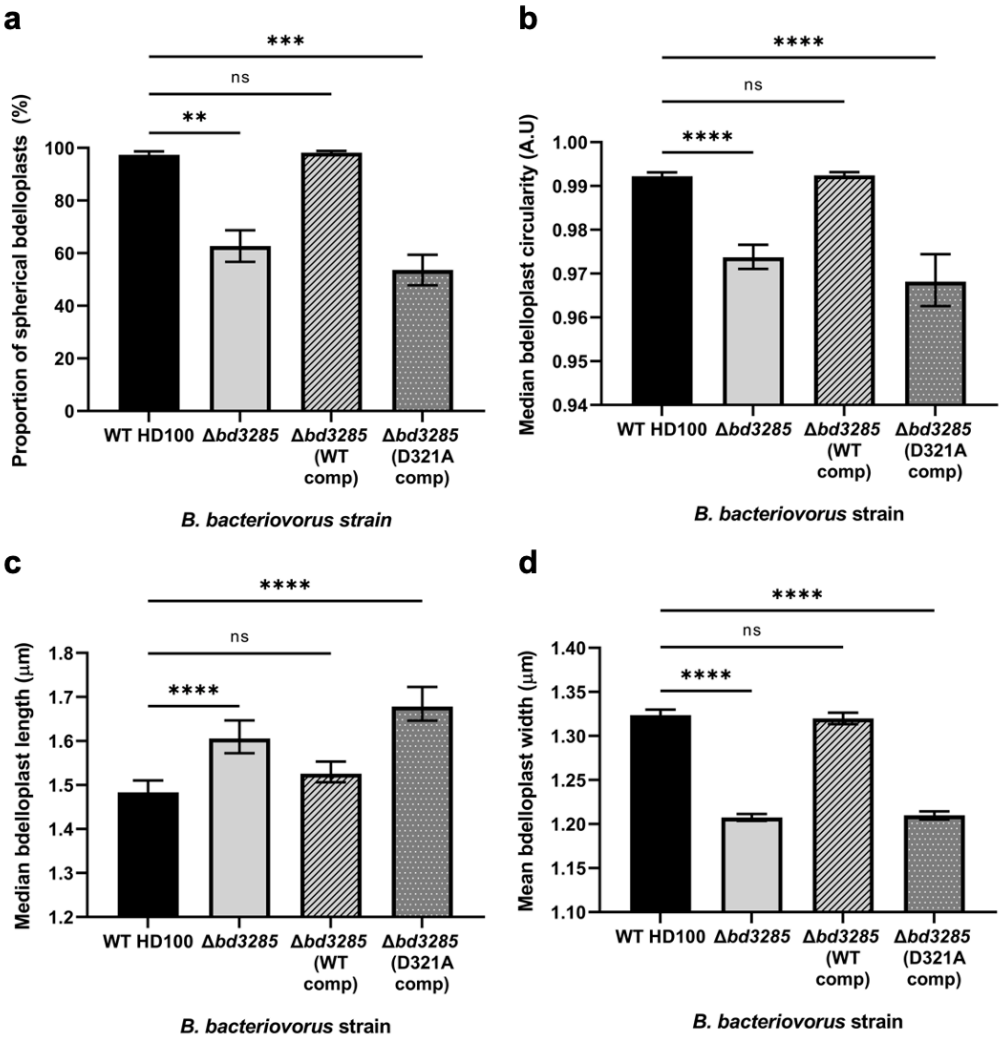

Figure 3.20. Morphology of *E. coli* bdelloplasts invaded by different *B. bacteriovorus bd3285* complementation strains

Measurements of *E. coli* S17-1 (pZMR100) prey bdelloplast morphologies invaded by by *B. bacteriovorus* Δ*bd3285* (WT comp) – a strain of Δ*bd3285* containing a wild-type copy of *bd3285* – and Δ*bd3285* (D321A comp) – a strain of Δ*bd3285* containing a copy of *bd3285* which has a catalytic point mutation of D321A. Wild-type and Δ*bd3285* strain values are reproduced from Figure 3.17 and Figure 3.18 for comparison. Each *B. bacteriovorus* strain also contains a cytoplasmic fusion of Bd0064-mCherry. **a)** proportion of spherical bdelloplasts (spherical bdelloplasts classified by a circularity value of >0.96 A.U.), **b)** median bdelloplast circularity, **c)** median bdelloplast length, and **d)** Mean bdelloplast width. n = 234-670 total cells analysed at the 1 h timepoint across three biological repeats. Error bars represent either standard error of the mean (**a, d**) or 95% confidence intervals of the median (**b-c**). For **a** and **d**, ns: non-significant, **: p<0.01, ***: p<0.001, ****: p<0.0001 (one-way ANOVA). For **b** and **c**, ns: non-significant, **: p<0.01, ***: p<0.001, ****: p<0.0001 (Kruskal-Wallis test).

3.3.8. Dumbbell-shaped bdelloplasts derive from dividing *E. coli* invaded by *B. bacteriovorus* Δ*bd3285* predators

Invasion of *E. coli* prey by the *B. bacteriovorus* Δ*bd3285* mutant results in spherical, rod and dumbbell-shaped bdelloplasts. Both spherical and rod-shaped bdelloplasts have been observed previously: spheres for prey invaded by wild-type *B. bacteriovorus* and rods for prey invaded by *B. bacteriovorus* lacking the DD-endopeptidases Bd0816 and Bd3459[115]. The presence of dumbbells was striking, however, since this shape of prey bdelloplast had not been observed before.

Dumbbell bdelloplasts appeared narrowed and 'pinched in' at the mid-cell, reminiscent of bacteria in the process of cell division and separation into two daughter cells. Due to this resemblance, I hypothesised that dumbbell bdelloplasts may have originated from an *E. coli* prey cell that was undergoing cell division at the point of invasion by *B. bacteriovorus* Δ*bd3285*. Invasion by Δ*bd3285* (concurrent with the death of the dividing prey cell) would result in 'fixation' of the dividing *E. coli* shape, forming a dumbbell bdelloplast.

In support of this possibility, there was no significant difference between the proportion of *E. coli* (pZMR100) prey cells that were dividing prior to predation (approximately 6.76%) and the proportion of dumbbell bdelloplasts observed during predation by Δ*bd3285* (approximately 4.26%) (Figure 3.21), suggesting that dividing *E. coli* invaded by *B. bacteriovorus* may transform into dumbbell-shaped bdelloplasts.

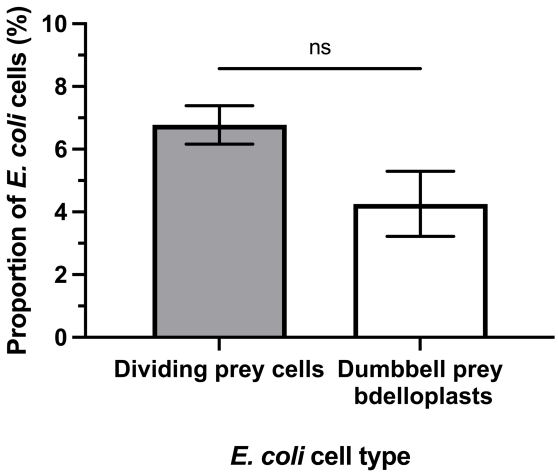

Figure 3.21. Proportion of dividing *E. coli* compared to the proportion of dumbbell bdelloplasts

Proportion of *E. coli* (pZMR100) cells in the process of cell division prior to predation by *B. bacteriovorus* Δ*bd3285* compared to the proportion of *E. coli* (pZMR100) dumbbell-shaped prey bdelloplasts observed 1 h into predation with *B. bacteriovorus* Δ*bd3285*. Dividing cells and dumbbell-shaped bdelloplasts were manually identified by the presence of a constriction in width at the mid-cell. ns: p>0.05 (Mann-Whitney test). Data are from three biological repeats.

To test this hypothesis further, time-lapse videos of *B. bacteriovorus* wild-type and Δ*bd3285* predators invading stationary phase *E. coli* S17-1 were captured. In comparison to exponential phase, most *E. coli* cells in stationary phase are less metabolically-active and are growing much more slowly, however a small proportion of cells are still undergoing cell division.

E. coli cells invaded by the wild-type strain rounded up into spherical bdelloplasts (Figure 3.22a). Upon invasion by Δ*bd3285*, non-dividing *E. coli* either completely rounded up into spheres or shortened in cell length but remained rod-shaped (Figure 3.22b). *E. coli* in the process of cell division (a low percentage of stationary phase *E. coli*) were visually identified by a narrowing and constriction at the mid-cell. Prior to the invasion of a dividing *E. coli* cell by an attached Δ*bd3285* predator, the poles of each compartment rounded slightly and started to shorten,

‘shrinking’ towards the middle and reducing the cell length slightly (Figure 3.22b). The ∆*bd3285* predator then entered one of the compartments, completing prey invasion and resulting in the unique dumbbell-shaped bdelloplast. This confirmed the hypothesis that dividing *E. coli* form dumbbell bdelloplasts upon invasion by the ∆*bd3285* mutant.

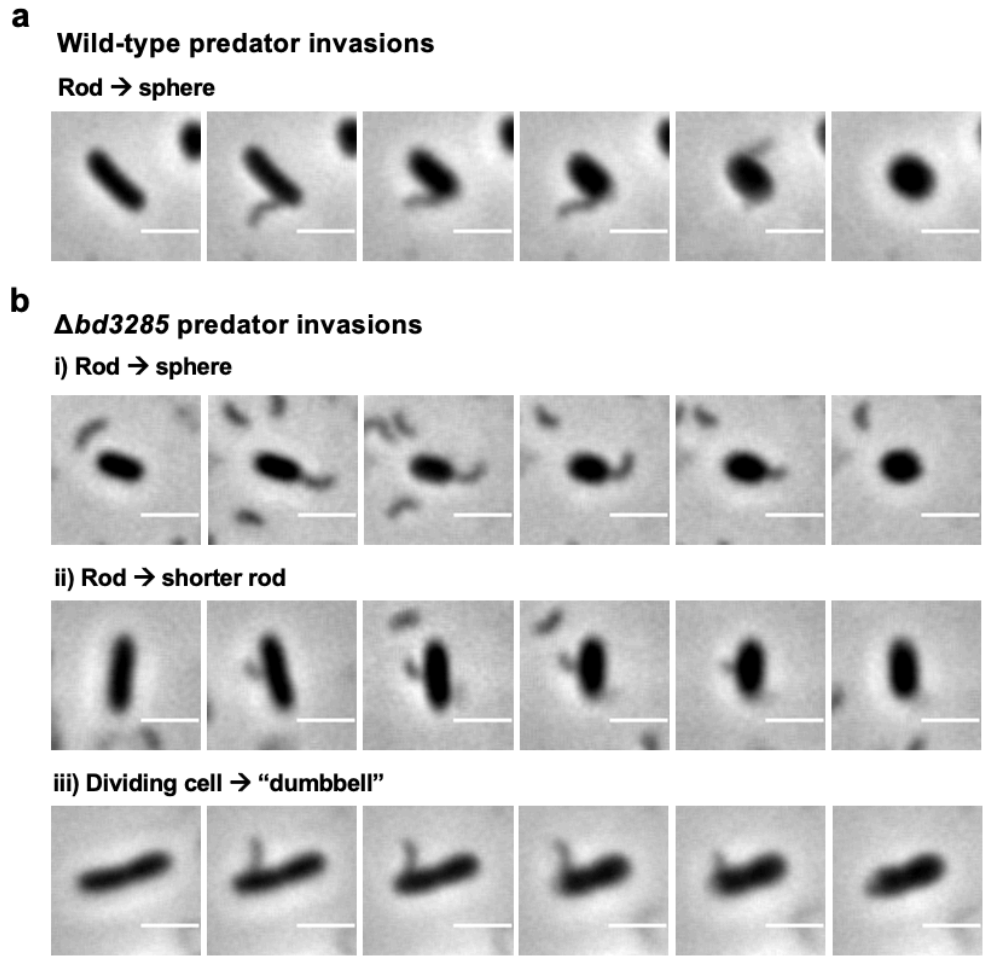

Figure 3.22. Time-lapse microscopy of *B. bacteriovorus* HD100 wild-type and Δ*bd3285* into *E. coli* prey

Time-lapse microscopy stills of invasion by either *B. bacteriovorus* HD100 wild-type (**a**) or Δ*bd3285* (**b**) into *E. coli* S17-1 prey. Three examples of prey invasion for Δ*bd3285* are shown: i) a rod rounding up into a spherical bdelloplast, ii) a rod shortening in length but remaining rod-shaped (middle) and iii) a dividing *E. coli* that shortens in length and becomes a dumbbell bdelloplast (bottom). Scale bars = 2 μm and examples are representative of three biological repeats.

3.3.9. Bd3285-mCherry localises to the septum of dividing *E. coli* prey

It was previously observed that Bd3285-mCherry is secreted into *E. coli* prey bdelloplasts during predation (Figure 3.13). This is a dynamically changing and heterogenous environment to visualise. To study the subcellular localisation of Bd3285 more directly within *E. coli* further, Bd3285-mCherry was heterologously-expressed in *E. coli* cells. *bd3285* could only be cloned into *E. coli* when the signal peptide of the gene was absent (most likely due to toxicity of the gene-product), therefore the gene (fused to mCherry) was cloned into the plasmid vector pBAD HisA under the control of an arabinose-inducible promoter. The construct was transformed into *E. coli* TOP10 – a strain which is often used for controlled overexpression as it cannot naturally metabolise L-arabinose. Addition of L-arabinose to the *E. coli* growth medium causes overexpression of the gene, while addition of D-glucose results in repression of gene expression. The pBAD Bd3285-mCherry TOP10 strain was incubated with either 0.5% D-glucose or 0.2% L-arabinose for 20 h and then fluorescent microscopy images were acquired. As expected, there was no detectable Bd3285-mCherry fluorescence for the culture incubated with D-glucose (negative control). In the arabinose-induced culture, however, Bd3285-mCherry localised most strongly to the outer edge of the *E. coli* cell, suggesting that the protein is periplasmic. (Figure 3.23a). Most strikingly, in dividing cells, the Bd3285-mCherry signal was strongest at the cell septum (Figure 3.23b). Bd3285 (D321A)-mCherry also showed a similar localisation pattern to the wild-type protein, suggesting that the catalytic residue D321 is not required for localisation (data not shown).

These heterologous expression results provide further support for the conclusion that Bd3285 is secreted into the *E. coli* periplasm during natural predation and demonstrate that Bd3285 can localise to the septum of dividing *E. coli*.

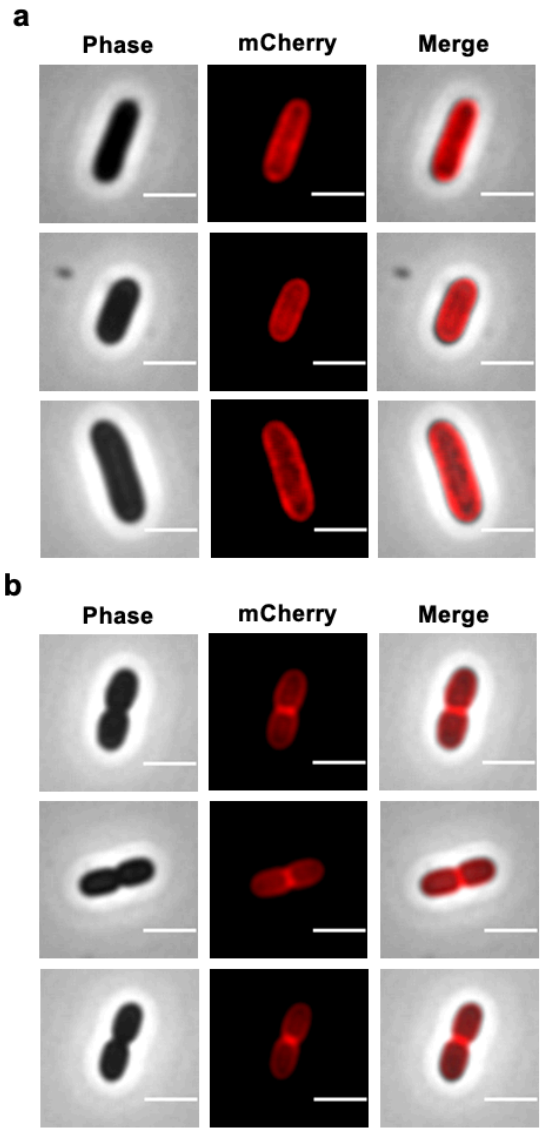

Figure 3.23. Bd3285-mCherry localises to the mature septum of *E. coli*

Fluorescence microscopy images of *E. coli* TOP10 containing the fusion of Bd3285-mCherry within the vector pBAD. Cells were induced with 0.2% arabinose for 20 h and then images were acquired of both non-dividing cells (**a**) and dividing cells with a visible constriction at the mid-cell (**b**). Scale bars = 2 μm and images are representative of three biological repeats.

3.3.10. Bd3285 acts on the septum of *E. coli* prey

Since dumbbell-shaped bdelloplasts derive from dividing *E. coli* prey and Bd3285-mCherry can localise to the *E. coli* septum, I hypothesised that Bd3285 is secreted into the prey periplasm to cleave the septum of dividing prey bacteria.

If Bd3285 cleaves the septum of prey bacteria which are in the process of dividing, then the prey septum should still be visible in a proportion of bdelloplasts invaded by the Δ*bd3285* mutant. Dumbbell bdelloplasts would be expected to contain a septum and possibly also some rod-shaped bdelloplasts (but only if the cell had started to construct septal PG at the point of death by predator invasion).

To test this hypothesis, a new experiment was devised utilising the fluorescent synthetic D-amino acid HADA which is incorporated into the bacterial cell wall and is enriched by muropeptide modifications[238]. HADA is a very useful dye to either visualise the sites of new PG incorporation (using HADA pulse-chases) or more simply to uniformly label the PG cell wall (using longer HADA pulses)[238].

B. bacteriovorus wild-type and Δ*bd3285* strains (each also containing a single-crossover fusion of Bd0064-mCherry to label the predator cell cytoplasm) were mixed with *E. coli* S17-1 (pZMR100) that had been incubated with HADA dye for 30 min to uniformly label the PG cell wall. At the timepoint of 30 min post predator-prey mixing when all *E. coli* prey should have been invaded by predators, samples were taken and fixed for imaging.

Bdelloplasts invaded by wild-type *B. bacteriovorus* were spherical in shape and the blue HADA signal could be observed throughout the bdelloplast sphere, uniformly labelling all PG as expected (Figure 3.24a). Prey invaded by Δ*bd3285* that formed spheres showed an identical pattern of HADA incorporation (Figure 3.24a). The majority of rod-shaped

bdelloplasts formed by Δ*bd3285* showed uniform HADA incorporation across the rod-shaped cell (Figure 3.24a). Importantly, however, all dumbbell-shaped bdelloplasts (alongside a few rods) showed HADA fluorescence additionally across the mid-cell, labelling septal PG (Figure 3.24b).

Repeating the experiment with the *B. bacteriovorus* complementation strain Δ*bd3285* (WTcomp) resulted in solely spherical bdelloplasts with a uniform HADA signal (Figure 3.25a). In contrast, complementation of Δ*bd3285* with the catalytic point mutant D321A comp resulted in a mixture of spheres, rods and dumbbell bdelloplasts, with an intact prey septum visible within dumbbell bdelloplasts (Figure 3.25b).

These data confirmed that the septum of dividing *E. coli* prey is not cleaved by *B. bacteriovorus* strain Δ*bd3285*, providing evidence that Bd3285 is involved in the cleavage of *E. coli* septal PG by wild-type *B. bacteriovorus*. Moreover, when the septum is not cleaved, dividing prey bacteria fail to be sculpted into spherical bdelloplasts.

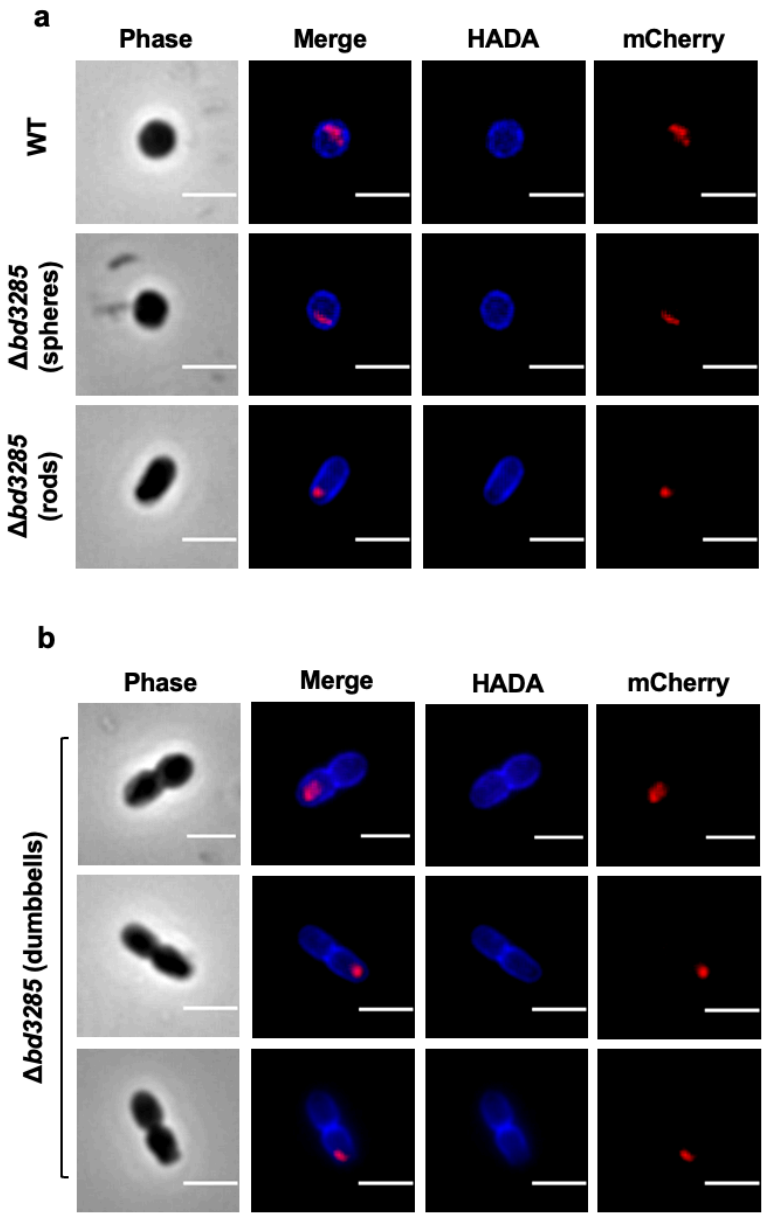

Figure 3.24. The septum of dividing *E. coli* is not cleaved in prey invaded by *B. bacteriovorus* Δ*bd3285*

Fluorescence microscopy images of *E. coli* S17-1 (pZMR100) prey invaded by either *B. bacteriovorus* wild-type or Δ*bd3285*. The *E. coli* PG cell wall was pre-labelled with the blue D-amino acid HADA prior to predation. *B. bacteriovorus* predator strains contain a Bd0064-mCherry fusion to label the predator cytoplasm and allow visualisation of predators inside prey. Samples were fixed for imaging 30 min after predator-prey mixing. **a)** Spherical bdelloplast invaded by a wild-type predator (top row), and spherical and rod-shaped bdelloplasts invaded by Δ*bd3285* (middle and bottom rows, respectively). **b)** Examples of dumbbell-shaped bdelloplasts invaded by Δ*bd3285* which still contain a septum. Scale bars = 2 μm and images are representative of three biological repeats.

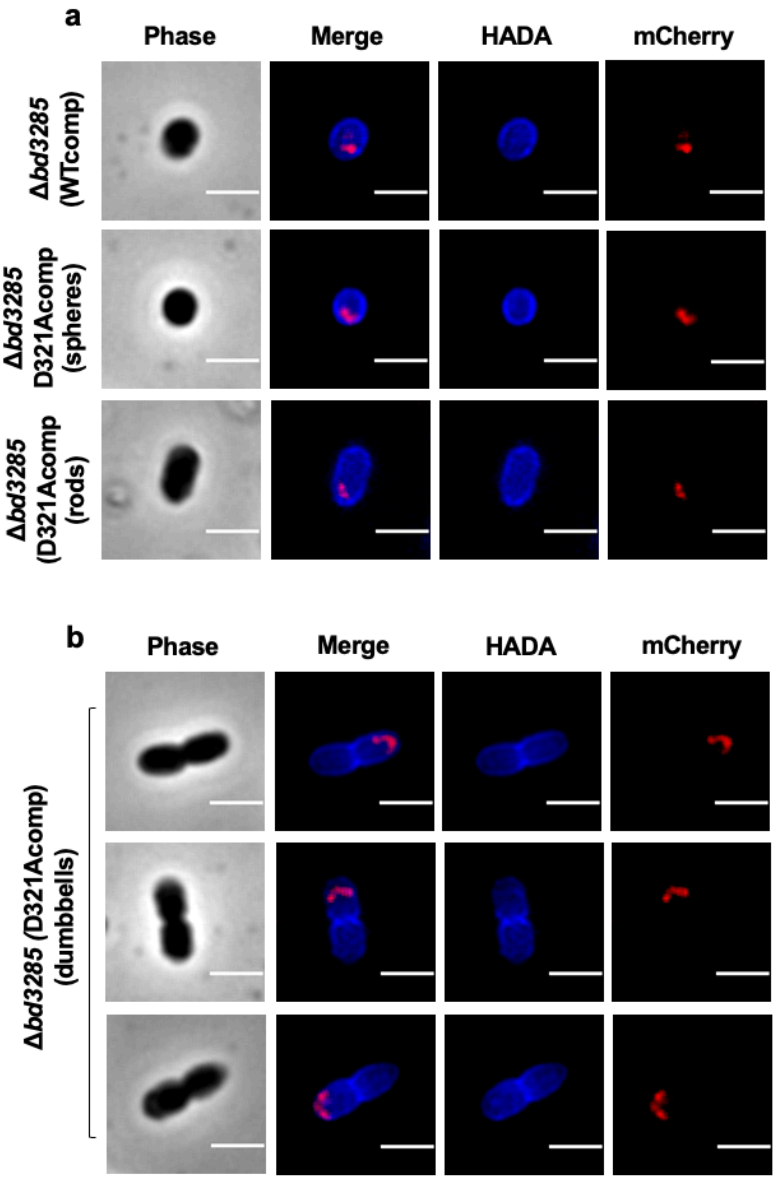

Figure 3.25. Complementation of Δ*bd3285* with a WT copy of *bd3285* restores prey septum cleavage but a D321A catalytic point mutant copy does not

Fluorescence microscopy images of *E. coli* S17-1 (pZMR100) prey invaded by either *B. bacteriovorus* Δ*bd3285* (WTcomp) or Δ*bd3285* (D321Acomp). The *E. coli* PG wall was pre-labelled with the blue D-amino acid HADA prior to predation. *B. bacteriovorus* predator strains contain a Bd0064-mCherry fusion to label the predator cytoplasm and allow visualisation of predators inside prey. Samples were fixed for imaging 30 min after predator-prey mixing. **a)** Spherical bdelloplast invaded by a Δ*bd3285* (WTcomp) predator (top row), and spherical and rod-shaped bdelloplasts invaded by Δ*bd3285* (D321Acomp) (middle and bottom rows, respectively). **b)** Examples of dumbbell-shaped bdelloplasts invaded by Δ*bd3285* (D321Acomp) which still contain a septum. Scale bars = 2 μm and images are representative of three biological repeats.

3.3.11. The MltA LT homologue Bd0599-mCherry is also secreted into the prey bdelloplast

The evidence thus far suggests that the function of Bd3285 is to cut the septum of dividing prey cells. As the MltA family protein Bd0599 is also upregulated at the timepoint of prey invasion (Figure 3.11) and contains conserved predicted catalytic residues (Figure 3.10), it was possible that Bd0599 may have a similar role.

To determine whether Bd0599 is secreted into the prey bdelloplast like Bd3285, a fluorescent C-terminal fusion of Bd0599-mCherry was constructed, introduced into the genome of *B. bacteriovorus* HD100 via single-crossover homologous recombination, and finally verified by Sanger sequencing. Attack-phase cells of *B. bacteriovorus* Bd0599-mCherry did not show any observable fluorescence, however during predation on *E. coli* S17-1 (pZMR100), a faint mCherry signal was visible inside *E. coli* bdelloplasts from approximately 1.5 h until prey lysis (Figure 3.26). This fluorescence – although weaker in intensity than Bd3285-mCherry – could still be detected above background levels, indicating that Bd0599-mCherry is also secreted into prey.

Microscopy during the predatory timecourse was repeated with a strain of *B. bacteriovorus* containing both Bd0599-mCherry and Bd0064-mCerulean3 which confirmed that the signal of Bd0599-mCherry was distinct from predator cells and secreted into the *E. coli* periplasm (Figure 3.27).

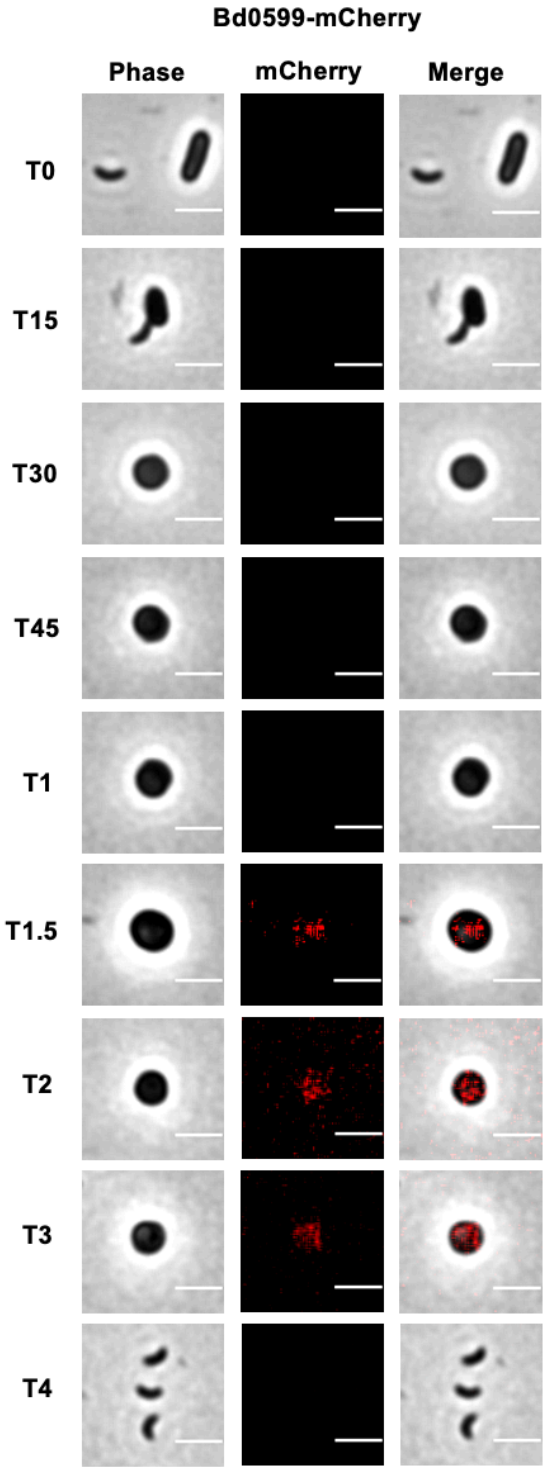

Figure 3.26. Bd0599-mCherry fluorescence inside *E. coli* prey bdelloplasts
Fluorescence microscopy images of *B. bacteriovorus* HD100 containing the single-crossover fusion Bd0599-mCherry during predation on *E. coli* S17-1 (pZMR100). T0-T4: hours elapsed since predators and prey were first mixed. Scale bars = 2 μm and images are representative of three biological repeats.

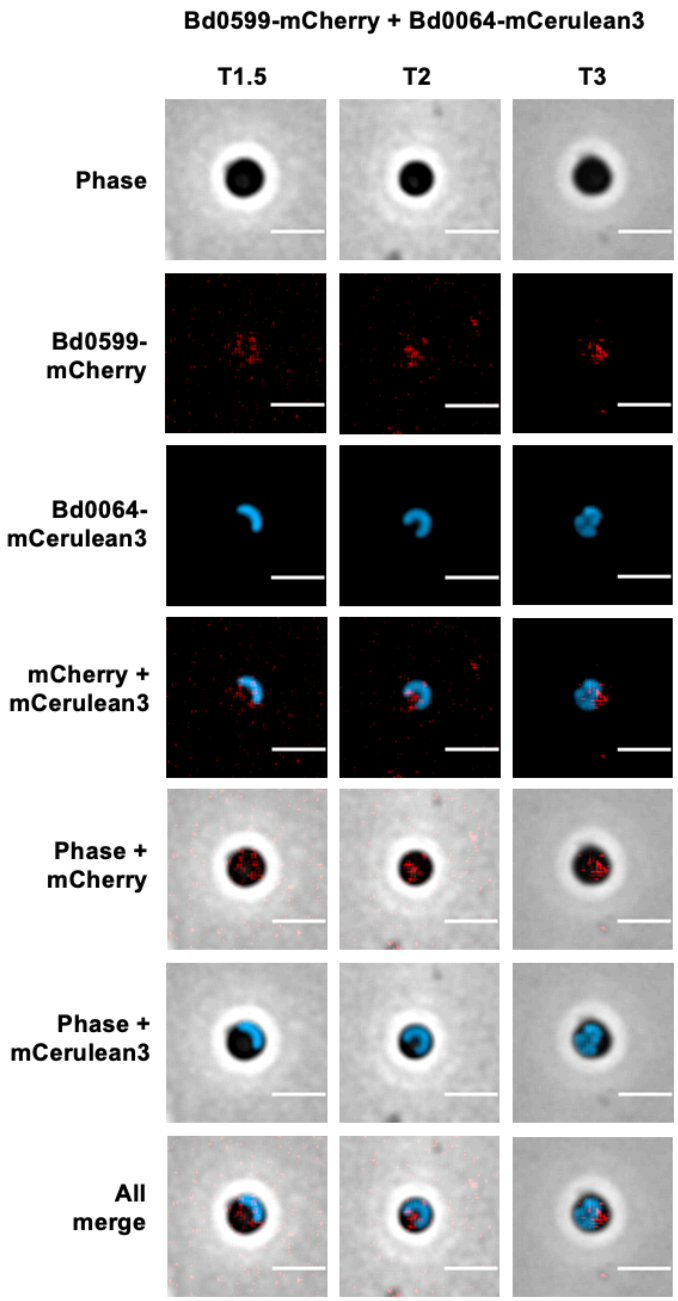

Figure 3.27. Bd0599-mCherry does not co-localise with *B. bacteriovorus* predators and is thus secreted inside prey bdelloplasts

Fluorescence microscopy images of *B. bacteriovorus* HD100 containing both a single-crossover fusion of Bd0599-mCherry and a double-crossover fusion of Bd0064-mCerulean3 during predation on *E. coli* S17-1 (pZMR100). T1.5-3: hours elapsed since predators and prey were first mixed. Scale bars = 2 μm and images are from one biological repeat.

3.3.12. Deletion of *bd0599* does not alter prey bdelloplast morphology

Since Bd0599 is secreted into the *E. coli* periplasm (Figure 3.26) and can localise to the septum of dividing *E. coli* (Figure 3.31) – which was also the case for Bd3285 – it was possible that Bd0599 may act in concert with Bd3285 to cleave the prey septum.

To test this possible function of Bd0599, an in-frame silent deletion of *bd0599* was constructed in the genome of wild-type *B. bacteriovorus* HD100 and verified by PCR and Sanger sequencing (Figure 3.28).

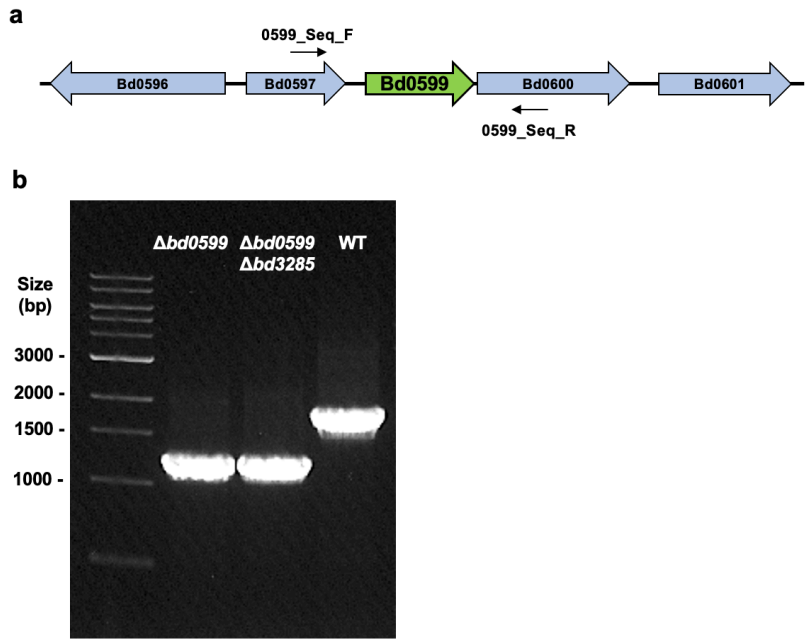

Figure 3.28. Single and double deletions of *bd0599* from the genome of *B. bacteriovorus* HD100

a) Amplification across the chromosomal region containing the *bd0599* gene showing the primers 0599_Seq_F and 0599_Seq_R used to confirm the deletion of *bd0599*. **b)** Agarose gel confirming the successful deletion of *bd0599* from the genomes of *B. bacteriovorus* HD100 wild-type (generating the single Δ*bd0599* knockout) and *B. bacteriovorus* HD100 Δ*bd3285* (generating the double knockout Δ*bd0599*Δ*bd3285*). Bands show PCR products amplified from the genomic DNA of Δ*bd0599,* Δ*bd0599*Δ*bd3285* and wild-type (WT) *B. bacteriovorus* HD100. Primers (annotated in **a**) were designed to anneal approximately 200 bp either side of the site of homologous

recombination. Δ*bd0599* and Δ*bd0599*Δ*bd3285* bands (1,297 bp) were 657 bp smaller than the wild-type (1,954 bp), indicating successful deletion of *bd0599*.

The fluorescent fusion Bd0064-mCherry was subsequently introduced into the genome of the Δ*bd0599* deletion mutant via single-crossover homologous recombination to label the cytoplasm of Δ*bd0599* predator cells red. *B. bacteriovorus* wild-type and Δ*bd0599* strains were then mixed with *E. coli* S17-1 (pZMR100) and images were taken throughout the predatory lifecycle.

In contrast to the Δ*bd3285* mutant, 100% of *E. coli* prey invaded by the single Δ*bd0599* mutant were transformed from rods into spheres (Figure 3.29a-b). There was also no significant difference in the length or width of bdelloplasts invaded by wild-type and Δ*bd0599* strains (Figure 3.29c-d).

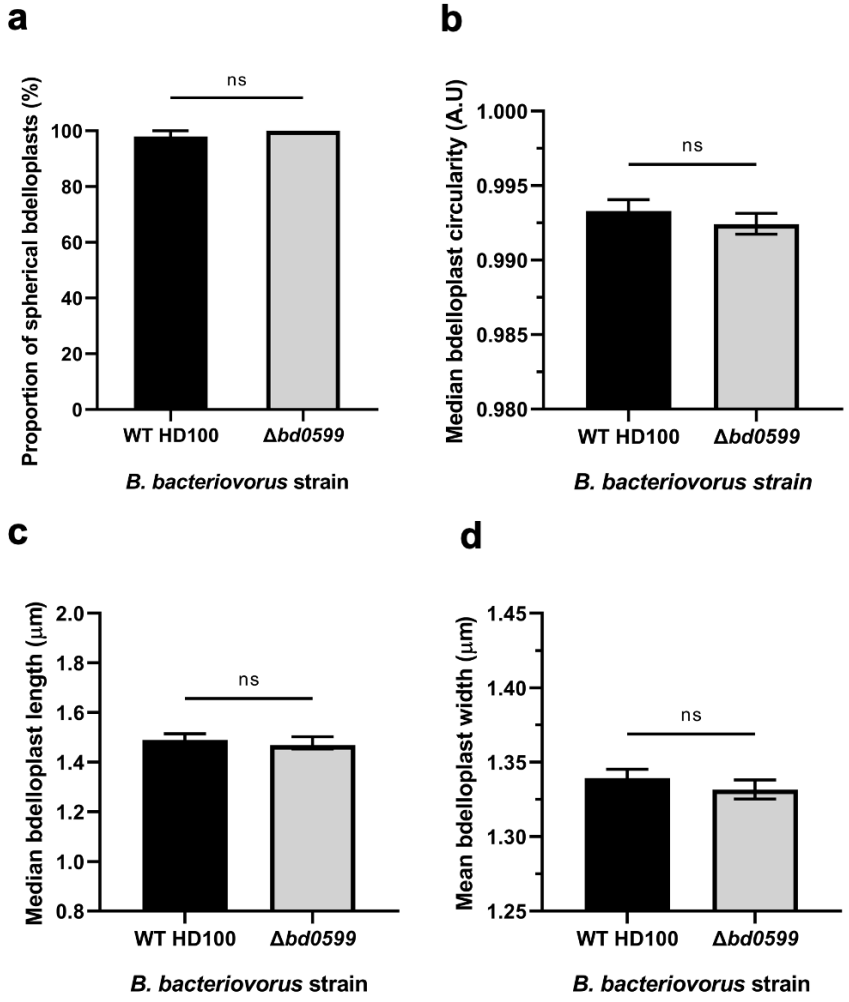

Figure 3.29. Morphology of *E. coli* prey bdelloplasts invaded by *B. bacteriovorus* WT and Δ*bd0599* strains do not significantly differ

Predation of *B. bacteriovorus* HD100 wild-type and Δ*b0599* (both containing a cytoplasmic fusion of Bd0064-mCherry) on *E. coli* S17-1 (pZMR100). **a)** Proportion of spherical bdelloplasts formed upon invasion by wild-type and Δ*bd0599* predators (spherical bdelloplasts classified by a circularity value of >0.96 A.U.) Median circularity (**b**), median length (**c**), and mean width (**d**) of prey bdelloplasts invaded by wild-type or Δ*bd0599* predators. n = 197-199 total cells analysed at the 1 h timepoint across three biological repeats. Error bars represent either standard error of the mean (**a, d**) or 95% confidence intervals of the median (**b-c**). ns: non-significant by unpaired-test test (**a, d**) or Mann-Whitney test (**b-c**).

It is not uncommon for single *B. bacteriovorus* gene deletions to not have an immediately discernible phenotype. Although a single deletion of the DD-endopeptidase *bd3459* reduced bdelloplast rounding from 100% to 75%, a single deletion of the second homologue *bd0816* did not have any effect on rounding[115]. However, construction of the double deletion mutant ∆*bd0816*∆*bd3459* resulted in almost complete elimination of bdelloplast rounding. This showed that a single deletion mutant with 'no phenotype' can contribute towards an additive phenotypic effect when combined with one or more existing gene deletions to form a multiple deletion mutant[115].

Considering this possibility, *bd0599* was deleted in the existing ∆*bd3285* strain background to generate the double deletion mutant ∆*bd0599*∆*bd3285* (Figure 3.28). The cytoplasmic fusion Bd0064-mCherry was then introduced into this new strain as described previously. *B. bacteriovorus* ∆*bd3285* and ∆*bd0599*∆*bd3285* strains were then mixed with *E. coli* S17-1 (pZMR100) and images were acquired during predation to determine bdelloplast morphology.

No significant differences were observed in the proportion of spherical bdelloplasts (Figure 3.30a), median bdelloplast circularity (Figure 3.30b), median bdelloplast length (Figure 3.30c) or mean bdelloplast width (Figure 3.30d) between the two strains.

This result suggests that Bd0599 does not have a discernible role in prey septum cleavage unlike Bd3285 which appears to be the more important enzyme of the two as determined in these experiments.

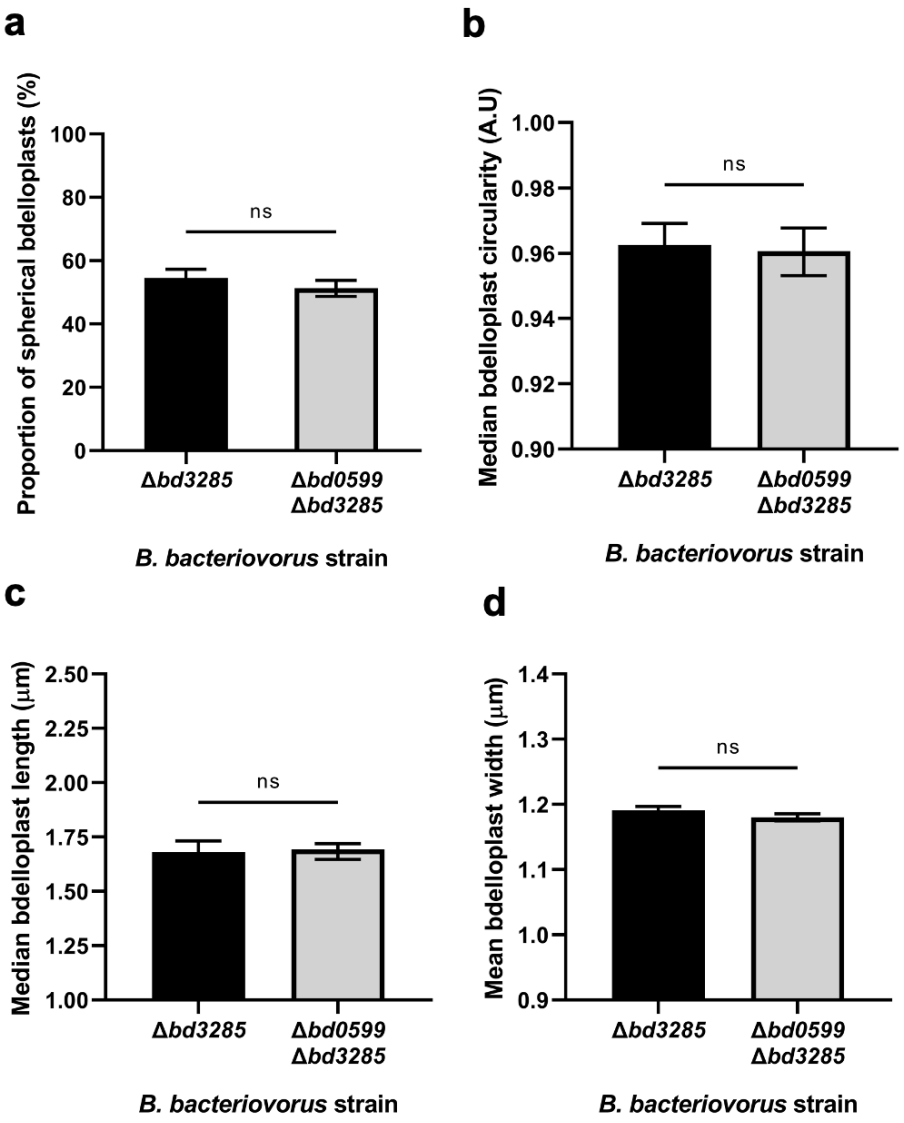

Figure 3.30. Morphology of *E. coli* prey bdelloplasts invaded by *B. bacteriovorus* Δ*bd3285* and Δ*bd0599*Δ*bd3285* strains

Predation of *B. bacteriovorus* HD100 Δ*bd0599* and Δ*bd0599*Δ*bd3285* (both containing a cytoplasmic fusion of Bd0064-mCherry) on *E. coli* S17-1 (pZMR100). **a)** Proportion of spherical bdelloplasts formed upon invasion by Δ*bd0599* and Δ*bd0599*Δ*bd3285* predators (spherical bdelloplasts classified by a circularity value of >0.96 A.U.). Median circularity (**b**), median length (**c**), and mean width (**d**) of prey bdelloplasts invaded by Δ*bd0599* or Δ*bd0599*Δ*bd3285* predators. n = 322-370 total cells analysed at the 1 h timepoint across three biological repeats. Error bars represent either standard error of the mean (**a, d**) or 95% confidence intervals of the median (**b-c**). ns: non-significant by unpaired-test test (**a, d**) or Mann-Whitney test (**b-c**).

3.3.13. Bd0599-mCherry localises to the septum of dividing *E. coli* prey

As deletion of *bd0599* – either singly or in combination with *bd3285* – did not appear to have a clear phenotype during predation, I considered whether this might be due to differences between the two proteins. While *E. coli* MltA and Bd3285 are approximately equal in length, Bd0599 is 140 amino acids shorter than Bd3285 and does not contain a disordered N-terminus like Bd3285 (Figure 3.9). It is therefore possible that the N-terminal region unique to Bd3285 may be important for its function and that the absence of this region from Bd0599 may explain the lack of phenotypic differences in the ∆*bd0599* mutants. One possibility is that the N-terminus of Bd3285 is required for protein localisation to the prey septum. To test this hypothesis, a fusion of Bd0599-mCherry was constructed within the arabinose-inducible pBAD vector and introduced into *E. coli* TOP10. Fluorescent microscopy images of the *E. coli* TOP10 Bd0599-mCherry strain were acquired following arabinose induction for 20 h and revealed that, like Bd3285-mCherry, Bd0599-mCherry can localise to the *E. coli* periplasm (Figure 3.31a) and also localises to the septum of diving cells (Figure 3.31b).

This result suggests that it is probably not the N-terminal region of Bd3285 (absent from Bd0599) which targets the protein to the *E. coli* septum, and that other factors are responsible for the absence of prey shape phenotype in ∆*bd0599*. These factors might include a possible lower protein concentration than Bd3285 (transcriptional read values are lower for Bd0599 - Figure 3.12) or differences within the Bd0599 protein which result in a less enzymatically-active enzyme.

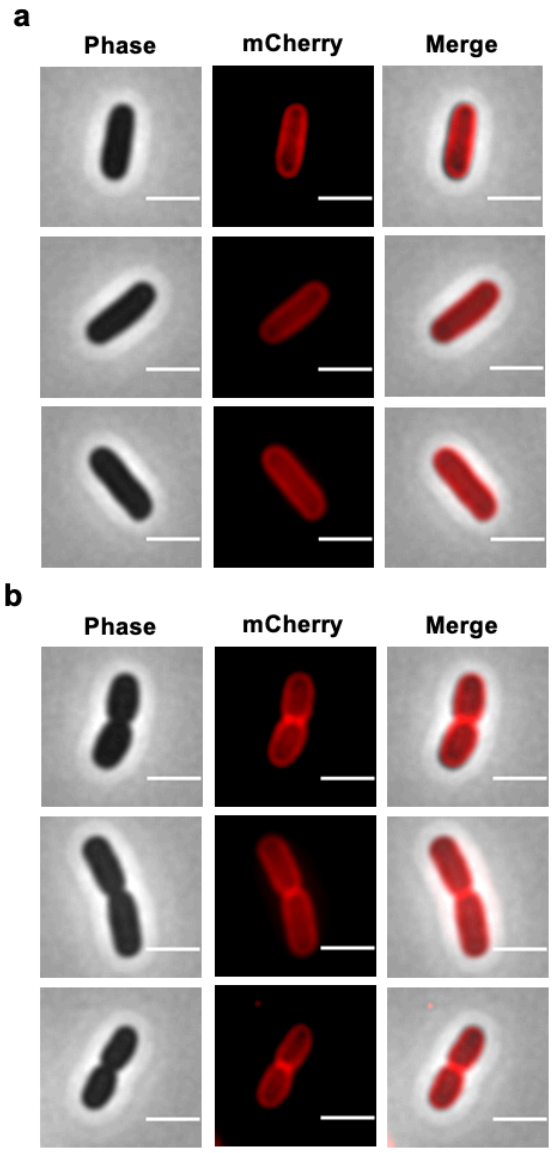

Figure 3.31. Bd0599-mCherry localises to the septum of *E. coli*

Fluorescence microscopy images of *E. coli* TOP10 containing the fusion of Bd0599-mCherry within the vector pBAD. Cells were induced with 0.2% arabinose for 20 h and then images were acquired of both non-dividing cells (**a**) and dividing cells with a visible constriction at the mid-cell (**b**). Scale bars = 2 μm and images are representative of three biological repeats.

3.4. Chapter discussion

During invasion into prey, the predator *B. bacteriovorus* secretes the DD-endopeptidase DacB enzymes Bd0816 and Bd3459 into the periplasm of the prey. The DD-endopeptidases cleave 4-3 crosslinks between PG stem peptides, weakening the cell wall and resulting in the conversion of rod-shaped prey into spherical prey. In this chapter, a new enzyme that is also important for prey shape transformation was identified: the lytic transglycosylase Bd3285. Bd3285 is required for cleavage of the PG septum that is present in prey cells undergoing cell division. In the absence of Bd3285, the septum remains intact (Figure 3.24) and while dividing cells shorten slightly, they do not round up into spheres, remaining as two distinct compartments (Figure 3.17 and Figure 3.22). The predicted catalytic aspartate residue of Bd3285, D321, (based on homology to *E. coli* MltA) was essential for protein activity (Figure 3.20 and Figure 3.25).

Based on the results in this chapter, a potential model for prey invasion is proposed, combining previous data on DacB DD-endopeptidase activity from Dr Thomas Lerner with my new findings on the lytic transglycosylase Bd3285 (Figure 3.32).

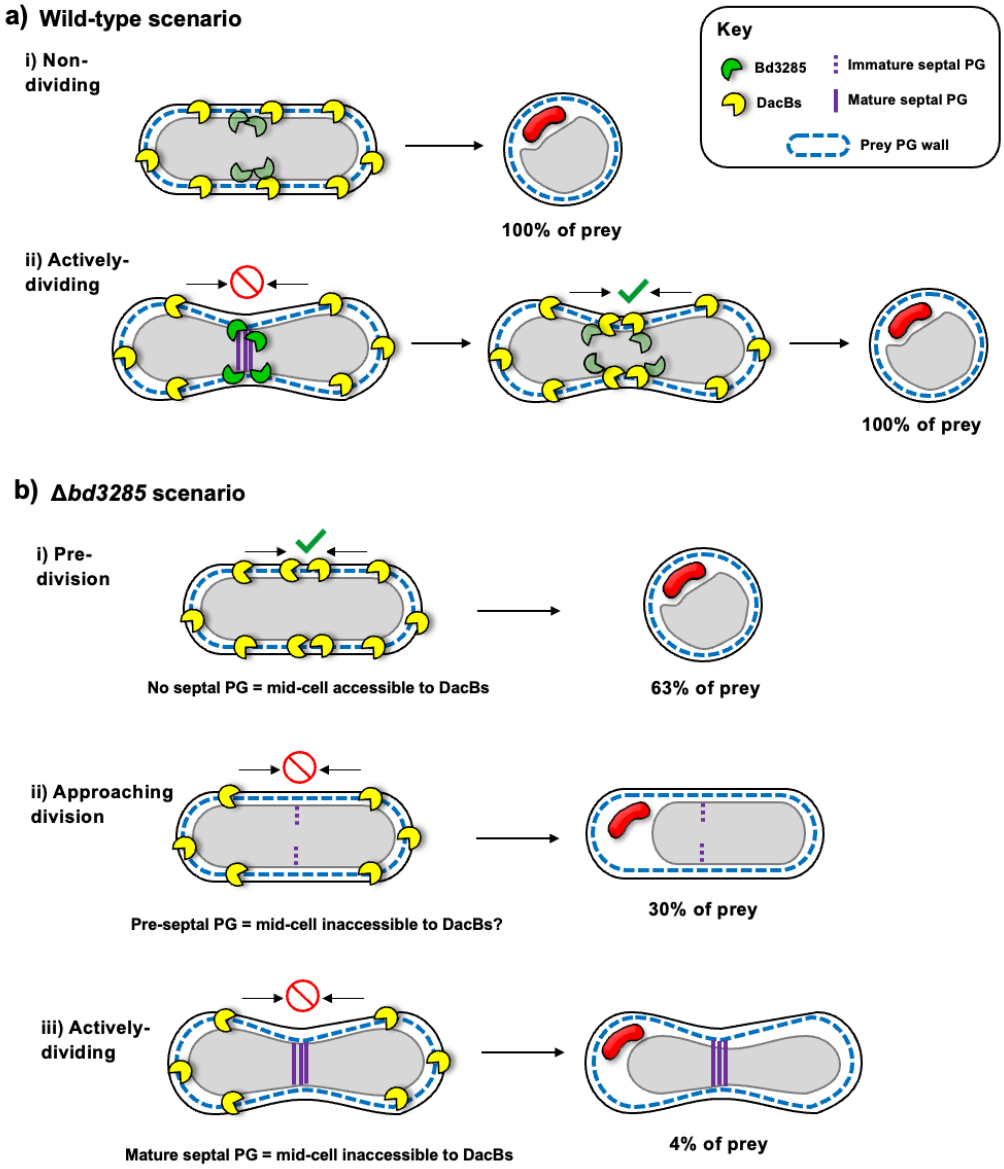

Figure 3.32. Proposed model for concerted DacB and Bd3285 action during prey invasion

a) In wild-type *B. bacteriovorus* strains, the DacB enzymes Bd0816 and Bd3459 (yellow proteins) are secreted into the prey periplasm and cut 4-3 PG crosslinks, resulting in malleable PG that is pushed outwards by internal turgor pressure to generate spherical prey. In non-dividing prey (**i**), this action may or may not require Bd3285 activity (green protein). However, in actively-dividing prey that have formed a mature septum, Bd3285 LT activity is required to cleave the septal PG and allow DacB access to peptide crosslinks at the mid-cell, converting prey into spheres (**ii**). In the Δ*bd3285* mutant, three shapes of bdelloplast are observed (**b**). **i)** For prey that are not dividing, PG crosslinks at the mid-cell are accessible to DacB enzymes, resulting transformation of rods into spheres. **ii)** In prey cells approaching division, perhaps with some pre-septal PG, the mid-cell is inaccessible to DacB enzymes, therefore rod-shaped prey remain rod-

shaped. i**ii)** In actively dividing prey with a mature PG septum that is not cut by Bd3285, the DacB enzymes cannot access mid-cell crosslinks, resulting in dumbbell-shaped bdelloplasts. Purple lines: septal PG (dashed: immature, whole line: mature).

In this model, Bd3285 acts upstream of DacB activity, and its most important role is to cut the PG septum of dividing prey (Figure 3.32aii). This hypothesis is supported by the bdelloplast shapes observed in the Δ*bd3285* mutant. For spherical Δ*bd3285* bdelloplasts (62.7%), the originally-rod shaped *E. coli* prey is rounded up by the efficient activity of DacB enzymes (Figure 3.32bi). In the case of dumbbell bdelloplasts (4.3%), the septum of these dividing prey was not cleaved by Bd3285. The DacB enzymes can only access the poles of the prey, explaining the slight shortening in length towards the mid-cell that was observed during invasion. Due to the presence of septal PG, however, the DacB enzymes cannot access peptide chains at the mid-cell, therefore the prey cell cannot be transformed into a spherical shape and the resulting bdelloplast consists of two compartments (Figure 3.32biii). The presence of rod-shaped bdelloplasts (33.0%) is less clear. It is possible that either: 1) some preliminary septal PG had been constructed in preparation for cell division, inhibiting DacB activity (this is supported by the observation of some rod-shaped bdelloplasts that contained faint HADA puncta either across the mid-cell or at each side-wall) or 2) the absence of Bd3285 PG backbone-cutting can (but not always) prevent DacB access to and therefore activity upon peptide chains (Figure 3.32bii). It would be difficult to experimentally test these options. Comparing the localisation and abundance of fluorescently-tagged DacB enzymes at the mid-cell with HADA staining of septal PG in Δ*bd3285* rod-shaped bdelloplasts could be informative. Unfortunately, previous attempts by Dr Thomas Lerner to tag the DacB enzymes were unsuccessful – probably due to protein product toxicity to *E. coli* cloning strains (this was also observed for Bd3285 when protein expression was not controlled by an arabinose-inducible promoter).

Bd3285-mCherry was visible inside prey bdelloplasts but fluorescence intensity was low (Figure 3.13). The western blot band of Bd3285-mCherry was also faint (Figure 3.15), suggesting that only small concentrations of enzyme are secreted. This was also observed for the LD-transpeptidase Bd1176 which is secreted into the prey periplasm[33]. It could be important that only low and tightly controlled concentrations of PG-modifying enzymes are secreted into prey to avoid 'over-modification' and potential damage to the structure of the bdelloplast niche. The Bd3285-mCherry signal was only observed from 1.5 h into predation which was surprising for an enzyme that almost certainly functions at 15-30 min during prey shape conversion. The fusion protein Bd1904-mCherry was also only observed from 1.5 h despite early transcriptional upregulation at 15 min (pers. comm. from Dr Carey Lambert). Western blot analysis to detect the mCherry fusions showed that Bd1904-mCherry was present in bdelloplasts from 30 min – 3 h and Bd3285-mCherry was only present at 30 min (Figure 3.15). This suggests that folding of the mCherry fluorophore may be inhibited in the environment of the early prey periplasm. Subsequent enzyme activity that may change the environmental conditions may be more conducive to mCherry folding, resulting in later visualisation of the two fusion proteins. It would be interesting to examine the oxidising and pH conditions of 'early' and 'late' prey bdelloplasts to test this hypothesis – perhaps utilising pH-sensitive fluorescent probes. It is nonetheless surprising that Bd3285-mCherry was detected only at 30 min by western blot and not also at later time points when fluorescence was observed. This may be due to low Bd3285 concentration (the 30 min band was faint) which may have been difficult to detect by western blot later timepoints. The western blot was also only performed once and would benefit from repeats to test this.

Under arabinose-inducible overexpression, Bd3285-mCherry localised most strongly to the outer cell edges of *E. coli* TOP10, indicative of periplasmic localisation, and in dividing cells Bd3285-mCherry localised most strongly to the septum (Figure 3.23). The probable periplasmic

localisation of Bd3285 could be further verified via the construction of a Bd3285-mCitrine fluorescent fusion. The fluorophore mCitrine is incapable fluorescing in the bacterial periplasm, therefore if Bd3285 is periplasmic, then no signal would be observed for Bd3285-mCitrine in contrast to Bd3285-mCherry. This type of test of periplasmic localisation for another protein is demonstrated later in **Chapter 4 Section 4.3.6.2**. It is possible, however, that under overexpression conditions, some Bd3285-mCitrine foci could still be observed despite periplasmic localisation, therefore the fusion should also be tested during *B. bacteriovorus* predation on *E. coli*, where Bd3285-mCitrine fluorescence within prey bdelloplasts would not be expected. Moreover, although Bd3285 signal appears strongest at the *E. coli* septum, it is possible that this is due to additional cytoplasmic membrane being formed during cell division, therefore quantification of Bd3285 signal using image analysis software would be helpful to confirm specific localisation at the septum.

The predicted catalytic 3D domain residue D321 appears to be critical for Bd3285 enzymatic activity since a point mutation of D321A resulted in similar bdelloplast morphologies to the Δ*bd3285* deletion mutant (Figure 3.20). There is a small possibility, however, that the mutation may affect protein stability or folding instead of catalytic function, therefore it may be worth introducing a tag to the protein construct (for example a FLAG-tag) to confirm by western blot that D321A and wild-type protein levels are similar.

The residue D321 was not important for localisation as Bd3285 (D321A)-mCherry had a similar localisation pattern to the wild-type protein (data not shown). Bacterial LysM domains bind PG[239] (*E. coli* LT MltD contains multiple LysM domains) and SPOR domains specifically bind septal PG by recognising denuded (naked) glycans[219]. Bd3285 does not contain LysM nor SPOR domains that could bind PG. It does, however, contain an N-terminal disordered region of unknown function. The two other MltA family enzymes Bd0599 and Bd0519 are 130-140 amino acids shorter than Bd3285 and do not contain this disordered N-terminus (Figure 3.9).

Bd0599-mCherry also localised to the septum of dividing *E. coli* TOP10 cells, however, suggesting that the unique N-terminus of Bd3285 may not be essential for septal localisation (Figure 3.31).

Bd0599 did not have any discernible impact upon prey shape transformation; all rod-shaped *E. coli* preyed upon by Δ*bd0599* predators rounded into spheres as in wild-type predation (Figure 3.29), nor was there any contribution or additive effect in the double Δ*bd0599*Δ*bd3285* mutant (Figure 3.30). Bd0599 contains the three conserved aspartate residues, including the catalytic equivalent residue of D321 in Bd3285, therefore the absence of Δ*bd0599* phenotype may be due to very low enzyme concentrations or perhaps the lack of the Bd3285 N-terminal region which may fulfil an important role in protein-protein interactions or PG catalysis. Purifying the Bd0599 protein and testing its catalytic activity on PG would confirm whether the protein is enzymatically active or not. In *E. coli*, MltA interacts with PBP1b via the scaffolding protein MipA[210]. It is possible that Bd3285 interacts with PG enzymes such as PBP1b but there is no homologue of MipA in *B. bacteriovorus*, therefore such interactions may occur in a different way to those in *E. coli*. Due to the similarity of function, Bd3285 might interact with the DacB enzymes Bd0816 and Bd3459. This could be tested via protein interaction assays such as co-immunoprecipitation or bacterial two-hybrid experiments.

During my PhD, there was insufficient time to test the function of the third MltA homologue, Bd0519. It would be useful to make a single genetic deletion of *bd0519* and also combine this deletion with those of *bd0599* and *bd3285* to create a triple deletion mutant of Δ*bd0519*Δ*bd0599*Δ*bd3285*. As neither Δ*bd0599* nor Δ*bd0599*Δ*bd3285* had discernible phenotypes, and Bd0599 and Bd0519 are similar at the protein level, I would not necessarily expect a phenotype for the single nor triple Δ*bd0519* mutant but it is important to clarify this experimentally. It would also be helpful to fluorescently-tag Bd0519 with mCherry to

determine its subcellular localisation. Bd0519 will be characterised in the work of a current MSci project student Mr Cameron McLaughlin.

Bd3285 is a predicted lytic transglycosylase and while experimental data thus far support this prediction, purification and application of the enzyme to PG is important to confirm the predicted catalytic activity. The phenotype of Bd3285 is most similar to RlpA of *P. aeruginosa*; both localise to and cleave septal PG[112]. RlpA specifically cleaves septal PG that contains denuded glycans – PG that has been stripped of amino acid chains by amidase activity[112, 220]. It would be interesting to determine whether Bd3285 also has a preference for denuded PG via *in vitro* assays with purified protein and PG of differing compositions. Crystallisation of Bd3285 could also reveal novel features and insights into the catalytic mechanism of Bd3285, but this may prove challenging due to the highly disordered N-terminus and membrane-bound location of the lipoprotein.

Lerner *et al*. (2012) showed that the prey shape transformation of rods into spheres conferred two evolutionary fitness advantages to *B. bacteriovorus*[115]. Firstly, the double DacB ∆*bd0816*∆*bd3459* mutant entered prey significantly more slowly that the wild-type (7.4 min vs 4.4 min, respectively)[115]. Predator entry into *A. baumannii* prey was slower than entry into *E. coli* prey[115]. This is probably due to the difference in PG crosslinking proportions in each species: *A. baumannii* PG is 61% cross-linked whereas *E. coli* PG is 33% cross-linked, therefore a greater time-period of DacB DD-endopeptidase activity may be required to sufficiently de-crosslink *A. baumannii* PG and allow predator entry, resulting in slower entry times[115]. Moreover, unlike *E. coli* bdelloplasts, invaded *A. baumannii* bdelloplasts were malleable and could be deformed by contact with another cell[115]. Deformation could occur at the opposite PG side-wall to the location of *B. bacteriovorus* invasion, suggesting that DacB enzyme activity is not constrained to the entry porthole but may diffuse through the periplasm and around the prey bdelloplast during wild-type predation[115].

Secondly, the frequency of double invasions (two *B. bacteriovorus* predators entering prey instead of one) was significantly higher in the Δ*bd0816*Δ*bd3459* mutant than the wild-type (84% vs 27%, respectively) [115]. This suggested that conversion of rod-shaped prey into spheres may act as a signal to external *B. bacteriovorus* predators that the bdelloplast has already been occupied by another predator cell[115]. Lerner *et al*. (2012) hypothesised that DacB de-crosslinking (resulting in a softer and more malleable bdelloplast cell wall) by the first-invading predator may affect the efficiency of pili retraction by subsequent *B. bacteriovorus* predators against the cell wall[115]. Pili are likely to be involved in prey cell entry and therefore less efficient retraction of predator pili against a softer bdelloplast wall may inhibit the invasion of a second *B. bacteriovorus* predator[115]. It would be interesting to test whether it is the spherical shape change or softer prey PG wall (possibly affecting pili retraction) that reduces double invasion, however this may prove difficult to assay as this would require the generation of spherical prey that do not have an altered PG composition. Invasion by multiple *B. bacteriovorus* predators is wasteful since the resources available to generate new progeny within the prey bdelloplast remain the same[115]. This would introduce *B. bacteriovorus* intra-species competition and reduce the pool-size of attack-phase predators that are available to invade other prey cells[115].

Like the DacB enzymes, Bd3285 is also involved in prey cell invasion, however generation of a triple Δ*bd3285*Δ*bd0816*Δ*bd3459* mutant was not sufficient to abolish prey invasion (data not shown), therefore other enzymes must be involved in prey invasion. Since Bd3285 is a lytic transglycosylase which cleaves PG glycan strands during invasion, then like the DacB Δ*bd0816*Δ*bd3459* mutant, Δ*bd3285* may also enter prey more slowly than the wild-type. It would be useful to measure this experimentally through time-lapse microscopy of *B. bacteriovorus* invasion into prey (as determined for Δ*bd1075* in **Chapter 5 Section 5.3.3**). Measuring the frequency of double invasions for Δ*bd3285* would also be interesting since most Δ*bd3285*-invaded bdelloplasts do not

round up into spheres. If, however, PG-softening by DacB enzyme activity reduces double invasion events rather than prey shape change, then there may not be a difference between Δ*bd3285* and wild-type as the DacB enzymes are still present in the Δ*bd3285* mutant.

Approximately 4.3% of stationary phase *E. coli* S17-1 prey cells invaded by Δ*bd3285* form dumbbell-shaped bdelloplasts and these derive from dividing prey. From experiments thus far, it is not possible to determine whether the septum within dumbbell bdelloplasts is 'open', 'partially open' or 'closed'. The development of a new technique in which bacteria can be imaged in a vertical orientation upon their poles by super-resolution 3D-SIM microscopy[240] could help to answer this. This technique can allow visualisation of the progression of septal PG synthesis and therefore the degree to which the septum is open or closed.

If the septum is closed within dumbbell bdelloplasts then this may limit the growth and elongation of *B. bacteriovorus* if the predator cell is restricted to the compartment which it entered during invasion. Space and nutrient availability may therefore be limited, resulting in a reduction in predator fitness. This hypothesis could be tested experimentally by observing whether Δ*bd3285* predator cells can elongate across the septum separating both compartments (testing for space accessibility) or comparing the presence of DNA/protein markers at late timepoints between wild-type and Δ*bd3285* dumbbell bdelloplasts (testing for nutrient availability).

Bd3285 contains a lipoprotein signal peptide prediction that does not contain a lol-avoidance motif. A lol-avoidance motif (characterised by an aspartate residue after the lipobox cysteine) prevents lipoprotein transportation to the outer membrane. The absence of a lol avoidance motif suggests that Bd3285 may be inserted into the outer membrane. As Bd3285 cleaves the prey septum, it is possible that Bd3285 is inserted into the outer membrane of the prey, however, the mechanism of

secretion and possible insertion is unknown. The secretion mechanism of other prey-modifying enzymes such as the deacetylases, DD-endopeptidases and LD-transpeptidases is also unknown.

In *B. bacteriovorus*, most proteins are translocated into the periplasm via the sec secretory pathway, however there is also a twin-arginine translocation (Tat) pathway which potentially translocates 21 *B. bacteriovorus* proteins into the periplasm[241]. *B. bacteriovorus* only encodes genes for the general secretory pathway (type II secretion system) and does encode any classical delivery systems such as the type VI secretion system which are capable of injecting effector proteins into prey bacteria. *B. bacteriovorus* only encodes genes for the general secretory pathway (type II secretion system) and does not have classical delivery systems such as the type VI secretion system. One possibility is that Bd3285 may originally be inserted into the outer membrane of attack-phase predator cells. During predator-prey attachment and contact of predator and prey membranes, Bd3285 may be delivered into the prey membrane via membrane fusion or blebbing into outer membrane vesicles that then fuse with the prey membrane. The secretion and delivery of Bd3285 and other *B. bacteriovorus* effectors into prey would be interesting to study but would constitute a separate and challenging research project.

Chapter 4. The vibrioid cell shape-determinant of *B. bacteriovorus*

4.1. Chapter introduction

4.1.1. Determination of bacterial cell shape

Bacteria exist in an abundance of different shapes and sizes, ranging from common spheres and rods to corkscrews, squares, and stars[242] (Figure 4.1). Bacterial morphology is also of historical scientific importance since new bacterial species were initially classified based on their morphology until this practice was superseded by phylogenetics. Despite the early identification of the plethora of bacterial morphologies, the molecular and mechanistic bases that underpin the generation and maintenance of cell shape have only started to be understood in the last two decades.

4.1.1.1. Straight rods and spheres

Bacterial cell shape is most thoroughly understood for the two most common shapes of bacteria: spheres and rods. In nearly all bacteria, cell shape is determined by the peptidoglycan cell wall which surrounds the inner membrane of the cell[49]. The PG wall confers rigidity and robustness to the cell, maintaining cell shape, but is also dynamic to allow cell growth and division and can be modified and re-moulded by enzymatic action and mechanical forces[49]. Rod-shaped bacteria generate and maintain their cell shape via multiple different mechanisms which act together to maintain a constant cell width and lack of curvature during cell growth and division[56]. The cytoskeletal protein MreB is essential for the maintenance of rod shapes, localising to and directing PG synthesis at regions of negative curvature, resulting in cell straightening during elongation[90].

Spherical bacteria can be further subdivided into cocci, which are completely spherical (e.g. *Staphylococcus aureus*), and ovococci which are slightly elongated spheres (e.g. *Streptococcus pneumoniae*)[243]. Cocci generate their shape by just one mechanism: PG synthesis at the division septum, whereas ovococci additionally require a PG elongation complex to maintain cell shape[244, 245].

Interestingly, despite spheres appearing the simplest of bacterial shapes, spheres are probably not the 'default' shape; phylogenetics suggest that straight rod shapes were ancestral and that spheres were derived from rod-shaped bacteria which stopped elongating[246]. This possibility is supported by numerous experimental studies showing that rods can transform into spheres upon exposure to antibiotics[247].

Rods and spheres both utilise moderately complex mechanisms to generate and maintain their cell shape, however, more intricate shapes such as curved rods (e.g. *Bdellovibrio*) and helical bacteria require shape-generating mechanisms. These additional mechanisms and enzymes are of direct importance to this chapter which describes the discovery and characterisation of the first true cell shape determinant in *Bdellovibrio* bacteria. Thus far, shape generation of curved rods and helical bacteria has been most characterised in the bacteria *Caulobacter crescentus*, *Vibrio cholerae*, *Helicobacter pylori* and *Campylobacter jejuni* – each of which are individually introduced below.

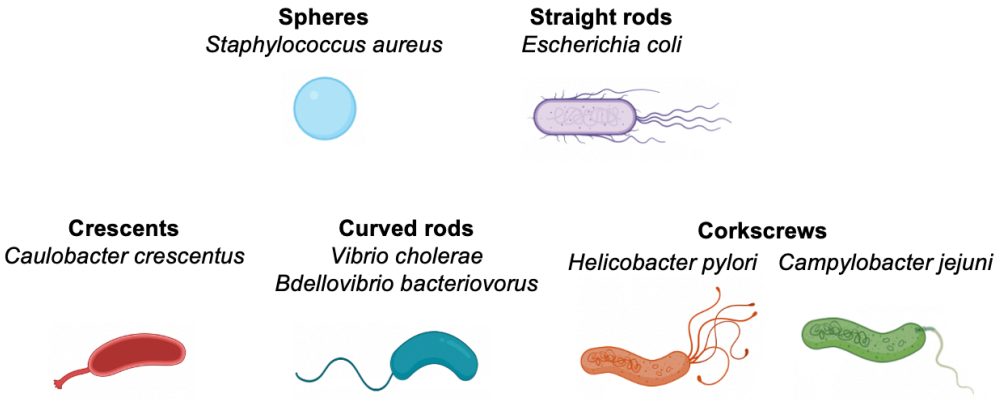

Figure 4.1. Common bacterial shapes

Cartoon drawings of the most common bacterial shapes: spheres, straight rods, crescentus, curved rods and corkscrews (helical bacteria). Example(s) of bacterial species are for each shape type are shown. Figure created in BioRender.

4.1.1.2. *Caulobacter crescentus*: a crescent-shaped curved rod

One of the first cell shape-determinants was identified in the Gram-negative curved rod (vibrioid-shaped) bacterium *Caulobacter crescentus* which is named for its crescent-like shape. *C. crescentus* is commonly found in freshwater lakes and streams and is most well-known for its unusual lifecycle[248]. The *C. crescentus* cell differentiates to produce a stalk at one pole ('stalked cell'), anchoring the cell to a surface[249]. Asymmetric cell elongation and division occurs, generating a new daughter cell with a polar flagellum ('swarmer cell')[249]. The stalked cell immediately re-enters the cell cycle and the new swarmer cell later differentiates into a stalked cell, also entering the cell cycle[249].

In *C. crescentus*, the protein crescentin generates cell curvature[250] (Figure 4.2b). Crescentin is a coiled-coil intermediate filament (IF)-like protein which localises to and polymerises at the cytoplasmic membrane of the inner concave cell face[250]. Exertion of mechanical force by crescentin polymers reduces the insertion of new PG subunits at the inner concave face during cell elongation, resulting in greater PG

insertion at the outer face[251]. The bias in new PG wall material insertion results in greater cell elongation at the outer face, generating cell curvature[251].

Cross-expression of crescentin in straight rod-shaped *E. coli* cells resulted in curved, often filamentous *E. coli*, indicating that curvature generation involves machinery that is conserved between the two species[251].

4.1.1.3. *Vibrio cholerae*: a curved rod

More recently, two cell shape determinants, CrvA and CrvB - which together form the curvature module CrvAB - were identified in the gram-negative curved rod *Vibrio cholerae*[252, 253] (Figure 4.2a). CrvA contains a signal peptide, two coiled-coil domains and a C-terminal PEGA (proline-glutamic acid-glycine-alanine) domain[252]. The protein is exported to the periplasm where it binds to the PG cell wall and forms periskeletal filaments at the inner concave cell face[252, 253]. Despite containing a putative catalytic PEGA domain (associated with carboxypeptidases in eukaryotes), the protein is not catalytically-active but instead exerts mechanical force on the PG wall to generate cell curvature in an analogous manner to crescentin[252]. CrvB, encoded downstream of CrvA, is also required for cell curvature, is non-enzymatic and localises to the concave face[253]. Interestingly, neither protein can cross-complement the deletion of the other, suggesting that each protein has a specialised role[253]. Further experiments revealed that CrvA is essential for the assembly of CrvB and that CrvB is required for the assembly of CrvA from short punctate filaments into higher-order long periskeletal filaments[253].

Cross-expression of CrvA and CrvB resulted in curvature of rod-shaped bacteria *E. coli* and *P. aeruginosa*[253]. CrvAB also caused modest curvature in a *C. crescentus* crescentin deletion mutant[253]. The rod-shaped bacterium *Agrobacterium tumefaciens* elongates from the cell

poles and does not require MreB for rod shape maintenance[254]. Expression of CrvA and CrvB in *A. tumefaciens* increased cell curvature, indicating that the curvature-inducing module does not require the MreB cytoskeletal machinery[253]. Further work revealed that CrvAB also generate curvature independently from the FtsZ divisome and the PG synthesis machinery PBP1a and PBP1b[253].

4.1.1.4. *Helicobacter pylori and Campylobacter jejuni*: helical bacteria

H. pylori and *C. jejuni* are both helical-shaped Gram-negative ε-proteobacteria. In *H. pylori*, cell shape has been studied extensively, leading to the identification of numerous proteins that coordinate the generation of helical shape (Figure 4.2c). Cell shape determinants in *H. pylori* include: the PG-modifying enzymes Csd1, Csd3, Csd4, Csd6 and Slt[255, 256, 257, 258]; the scaffolding proteins Csd2, Csd5 and Csd7[255, 258, 259]; and the cytoskeletal elements CcmA, Ccrp58, Ccrp59, Ccrp1142 and Ccrp1143[255, 260, 261]. Many of these shape determinants were identified through flow cytometry performed on a transposon mutant library of cells which could reveal transposon mutants with altered morphologies. Deletion of any of the four Ccrp proteins caused an increase in the proportion of straight rod-shaped cells, although the extent to which this occurred differed between *H. pylori* strains[260, 261]. The enzymatic proteins Csd1 and Csd3 are both DD-endopeptidases, cutting crosslinks between PG stem peptides, and Csd3 also has weak DD-carboxypeptidase activity, removing the terminal D-alanine from a pentapeptide to generate a tetrapeptide[255]. Deletion of Csd1 or Csd3 resulted in either completely curved rods or rods with varying degrees of curvature, respectively[255]. Csd2 and Csd7 are scaffolding proteins that interact with and stabilise Csd1, with Csd1 and Csd2 capable of forming heterodimers[258, 262]. Csd7 further interacts with Csd2 and the cytoskeletal element CcmA, connecting the inner membrane complex to the cytoskeleton and forming one part of a multi-protein shape complex[258]. CcmA localises to the outer convex face of spiral-shaped cells and is thus far the only *H. pylori* shape

protein for which specific localisation is known[263]. Deletion of either Csd2, Csd7 or CcmA results in *H. pylori* cells that are curved rods, indicating the importance of each protein[255, 258]. A final scaffolding protein Csd5 (deletion of which causes straight rods) directly binds PG and interacts with both CcmA and the PG precursor MurF to form a second part of the multi-protein shape complex[259].

Deletion of the lytic transglycosylase Slt resulted in curved rods and PG with a higher proportion of tripeptides, however, a mechanism to explain this remains unclear[258]. Δ*csd4* and Δ*csd6* mutants are straight rods and biochemical analysis showed that the two enzymes work sequentially: Csd6 is an LD-CPase that trims PG tetrapeptides to tripeptides and Csd4 is a DL-CPase that trims those tripeptides to dipeptides[256, 257]. The authors propose that the increase in dipeptides (which cannot participate in PG crosslinking) may contribute to helical cell shape generation[256, 257].

In contrast to the many characterised shape proteins of *H. pylori*, just three shape determinants have been identified in the related helical bacterium *C. jejuni*: Pgp1-3[264, 265, 266]. Deletion of either gene results in a population of straight rod-shaped *C. jejuni* cells[264, 265]. Pgp2 and Pgp1 are homologues of Csd6 and Csd4 and have LD-CPase and DL-CPase activity on PG, respectively[264, 265]. The more-recently identified Pgp3 has both DD-endopeptidase and DD-carboxypeptidase activity on PG and deletion results in curved rods[266].

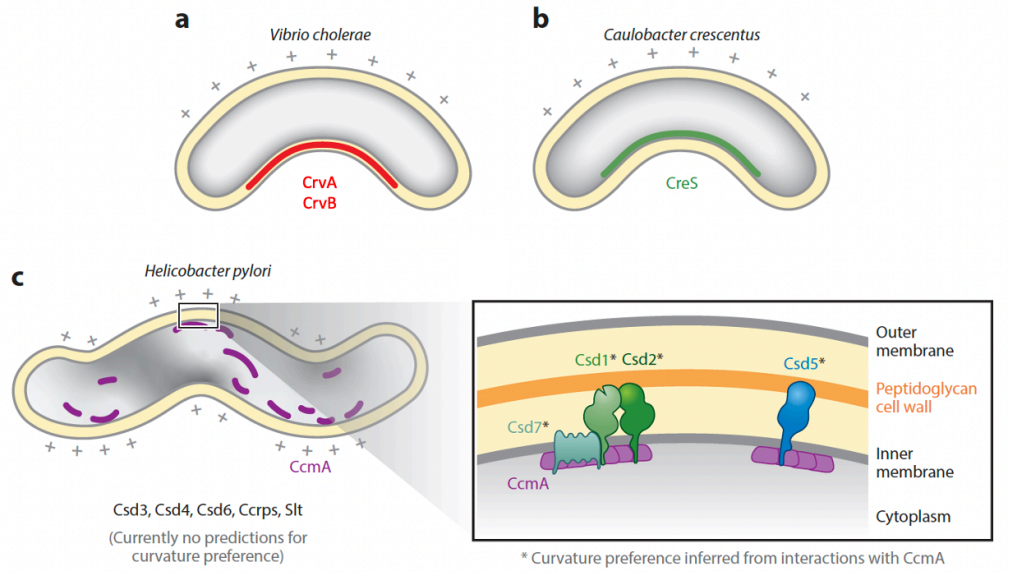

Figure 4.2. Characterised bacterial cell shape determinants

Illustrations of known bacterial cell shape determinants. **a**) *V. cholerae* proteins CrvA and CrvB form periskeletal polymers (red line) at the inner concave cell face, promoting more PG wall incorporation at the outer concave face. **b**) *C. crescentus* protein crescentin (Cres) forms cytoskeletal polymers (green line) at the inner face, also promoting greater PG wall incorporation at the outer face. **c**) *H. pylori* contains many cell shape determinants for form multimeric protein complexes. Cytoskeletal element CcmA localises to the outer concave face of spiral-shaped cells (purple lines) and may promote PG synthesis at the outer face. Csd7 interacts with CcmA, Csd1 and Csd2. Csd5 also interacts with CcmA. Diagram taken from Taylor *et al*., 2019[267]

4.1.1.5. *Bdellovibrio bacteriovorus*: a curved rod

The vibrioid cell shape of *B. bacteriovorus* has been little studied. Previous work by the PhD student Dr Andrew Fenton aimed to identify curvature determinants of *B. bacteriovorus* through searching the genome for homologues of crescentin-like coiled-coil proteins. One Ccrp protein was identified – deletion of which resulted in cells with minor membrane deformations but no severe cell shape defect[268].

The curvature-determinant of *Bdellovibrio* remained elusive until the discovery of Bd1075 during my MRes project[158].

4.1.2. My previous work on the protein Bd1075 leading up to this PhD project

The gene encoding the protein Bd1075 was selected as a genetic candidate for investigation during a short rotation project that I carried out as part of the MRes year of my 4-year Doctoral Training Programme. At the time, one of the ongoing projects in the lab was to study the roles of LD-transpeptidase (Ldt) proteins within *B. bacteriovorus*. In contrast to *E. coli* which contains 6 Ldts (LdtA-F), the genome of *B. bacteriovorus* HD100 encodes at least 19 potential Ldt or Ldt-family proteins. The role of several Ldts had been tested by gene deletions (single and multiple knockouts in combination), however rarely was a phenotypic difference observed. The Ldts Bd0886 and Bd1176 were an exceptional protein pair as a double deletion of these two genes resulted in bdelloplasts that incorporated less new cell wall material (demonstrated by pulsing with the fluorescent D-amino acid HADA) compared to wild-type bdelloplasts[33]. Δ*bd0886*Δ*bd1176* bdelloplasts were also less osmotically stable than wild-type bdelloplasts when subjected to osmotic shock[33]. These data suggested a role for the Ldts Bd0886 and Bd1176 in strengthening the bdelloplast structure following *B. bacteriovorus* invasion to confer osmotic stability and security during the growth and replication of *B. bacteriovorus* [33].

The 19 potential Ldt proteins of *B. bacteriovorus* were later classified into different groups based on phylogenetic analysis of their protein sequences (pers. comm. from Prof Andrew Lovering and Mr Christopher Graham - the latter being a former University of Nottingham MSci project student) (Figure 4.3). Three of the 6 groups had some degree of similarity to *E. coli* Ldts (Group 1 is LdtF-like, Group 2 is LdtA/B-like and Group 4 is LdtD-like), however, Groups 3, 5 and 6 appeared unique to *B. bacteriovorus*. Bd1075 formed a noticeable outlier as the only Ldt to comprise its own group and was phylogenetically divergent from the other Ldts (Figure 4.3).

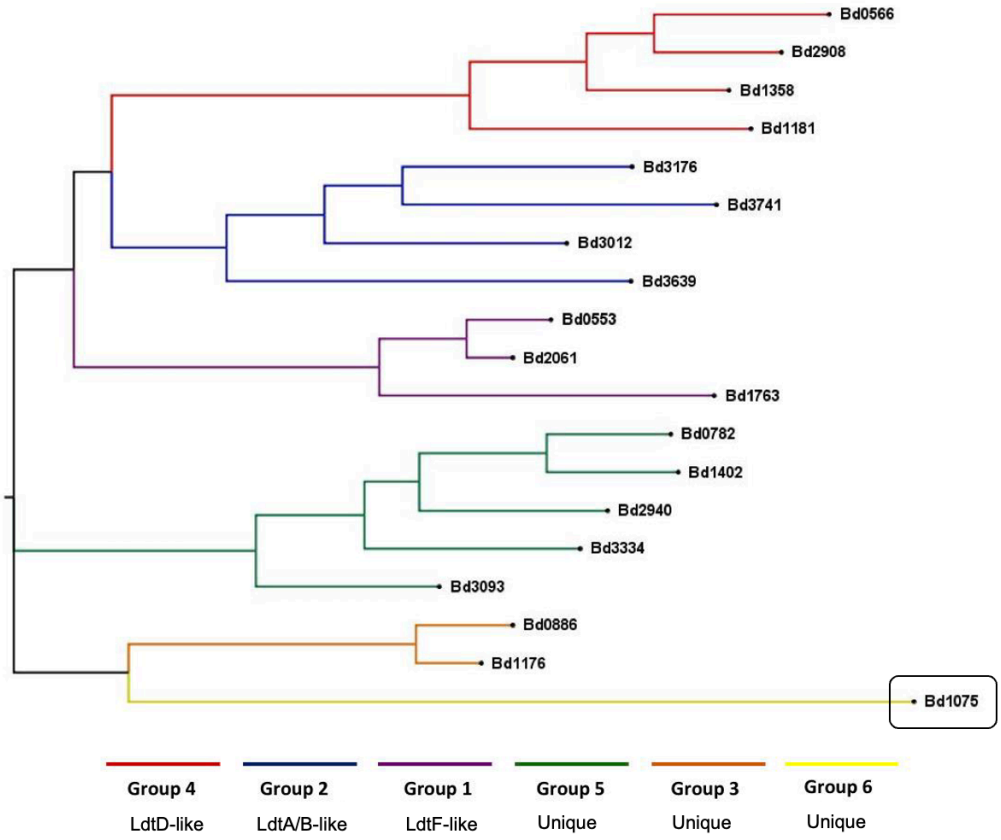

Figure 4.3. Phylogenetic tree of predicted LD-transpeptidase family genes in *B. bacteriovorus* HD100

Maximum likelihood unrooted phylogenetic tree generated from 19 predicted *B. bacteriovorus* LD-transpeptidase family protein sequences. Proteins are allocated to one of 6 different groups with any group similarity to *E. coli* homologues labelled below. Where there was no apparent homologue then the group was labelled as 'unique' to *Bdellovibrio*. Bd1075 (boxed in black) forms its own group: Group 6. Raw tree data were received from the former MSci student Mr Christopher Graham with gratitude. Phylogenetic analyses were carried out using MEGA7[269] with 1000 bootstrap replications. Figure shown previously in Banks (2018)[158].

Bd1075 therefore became a priority candidate for investigation, and I began to study this protein during my MRes short project. I will briefly summarise my key findings during that project since this laid essential groundwork for my PhD discoveries which were a continuation of the MRes project. Where a figure is replicated from my MRes thesis (Banks, 2018[158]), this is stated in the figure legend.

4.1.2.1. Introduction to the gene *bd1075*

Figure 4.4. Genomic context of the *bd1075* gene

A 5 kb genomic region of the *B. bacteriovorus* HD100 genome showing the genomic location of the *bd1075* gene which is monocistronic and flanked by the genes *futA* and *fliL* which are both divergently transcribed. The image was acquired and re-drawn from the xBASE server[179, 180].

Gene *bd1075* is a 999 bp monocistronic gene within the genome of *B. bacteriovorus* HD100 and encodes a 332 amino acid protein with a predicted molecular weight of 38 kDa (Figure 4.4). Gene *bd1075* is flanked by the genes *futA* and *fliL*. The gene *futA* - which is located 67 bp downstream from *bd1075* - is a putative iron ABC transporter and the gene *fliL* (which is located 163 bp upstream of *bd1075* and is one of three genomic copies) is a putative flagella rotor component[179, 180]. Both genes are divergently transcribed from *bd1075* and not contained within an operon.

Entering the protein sequence of Bd1075 into the signal peptide prediction server SignalP 5.0[183] reveals that Bd1075 contains a strongly predicted sec signal peptide (residues 1-19) (Figure 4.5). This indicates that the Bd1075 protein is probably either translocated into the periplasm or secreted from the cell.

Prediction: Signal peptide (Sec/SPI)

Cleavage site between pos. 19 and 20: VLA-GP. Probability: 0.9288

Protein type	Signal peptide (Sec/SPI)	TAT signal peptide (Tat/SPI)	Lipoprotein signal peptide (Sec/SPII)	Other
Likelihood	0.9925	0.0002	0.007	0.0004

Download: PNG / EPS / Tabular

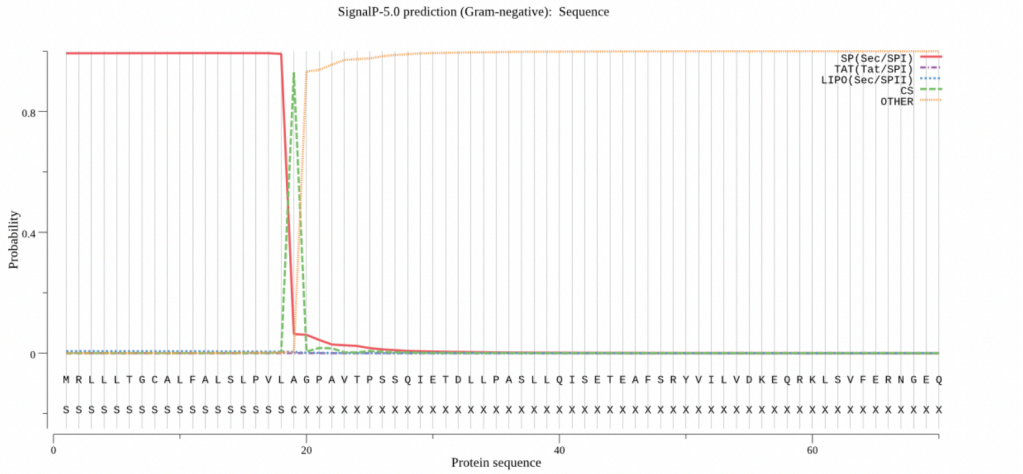

Figure 4.5. Bd1075 contains a sec signal peptide

Bd1075 contains a predicted sec signal peptide (likelihood of 0.99) which is predicted to be cleaved between the residues Ala-19 and Gly-20. Prediction obtained from the SignalP 5.0 server[183] .

In addition to a sec signal peptide, Bd1075 contains a predicted Ldt domain (residues 50-183) with a conserved catalytic triad comprising the amino acids H144, A145 and C159 (Figure 4.6a). Bd1075 also contains a C-terminal nuclear transport factor 2-like (NTF2) domain (residues 199-307) of unknown function (Figure 4.6a). The function of both predicted domains is interrogated later during this chapter. Despite containing a predicted Ldt catalytic domain, creation of a 3D model prediction of Bd1075 revealed a very strong similarity to the LD-CPase Csd6 from *H. pylori* (Figure 4.6b). As Csd6 had also been originally predicted to be an Ldt[270], this finding highlighted the necessity of verifying the true catalytic activity of Bd1075 (which is determined later in **Section 4.3.5**).

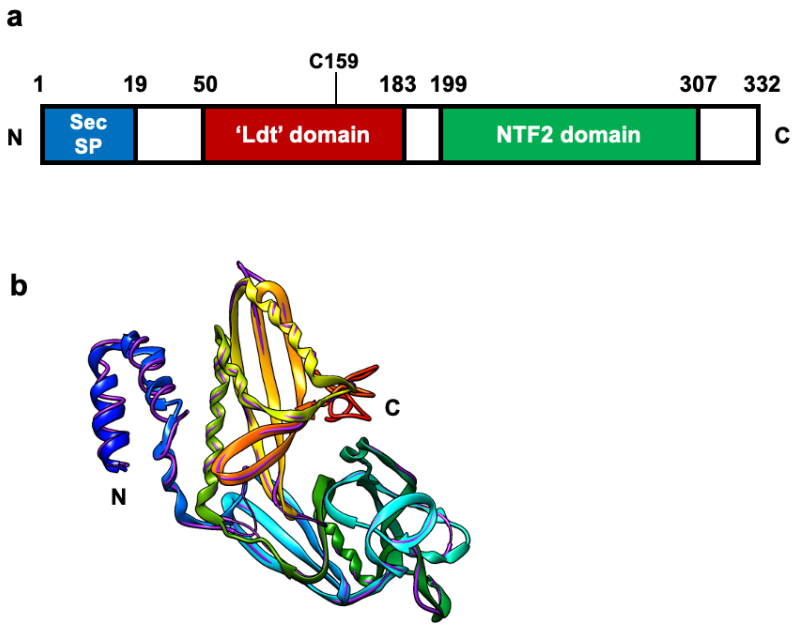

Figure 4.6. Bd1075 has a predicted Ldt domain but resembles an LD-CPase

a) Schematic of the predicted domain structure of Bd1075 prior to the start of my PhD. Numbers indicate amino acid position. Sec SP: sec signal peptide (blue), 'Ldt' domain: LD-transpeptidase catalytic domain (red), NTF2 domain: nuclear transport factor 2-like domain (green). The key catalytic residue C159 in the Ldt domain is annotated above the domain. **b)** 3D model alignment of the predicted model of Bd1075 (rainbow coloured from N to C-terminus) and the crystal structure of the most similar template in the PDB - *H. pylori* Csd6 (purple) (PDB: 4xzzA). Tm score = 0.889 where a score of 1.0 indicates a perfect match. The model prediction and alignment were generated using the server I-TASSER[271]

4.1.2.2. Transcription of *bd1075* across the predatory lifecycle

To determine whether Bd1075 was more likely to have a role within *B. bacteriovorus* predator cells as a 'house-keeping' gene or alternatively to have a secreted function during predation, RT-PCR was performed using *bd1075* primers on *B. bacteriovorus* HD100 total mRNA collected at timepoints across the predatory cycle. The RT-PCR showed that the expression level of *bd1075* was invariable across predatory cycle timepoints from attack-phase predator cells to prey lysis at 4 h (Figure 4.7). This result suggested that is more likely that *bd1075* has a house-keeping role within *B. bacteriovorus* cells as opposed to a secreted function during the predatory life cycle like Bd3285 (Figure 3.11).

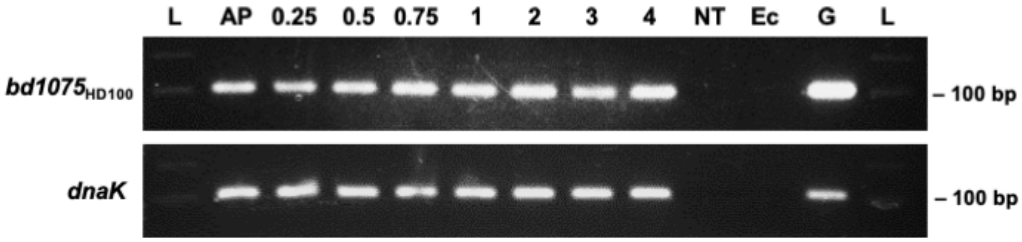

Figure 4.7. *bd1075* is constitutively transcribed across the predatory cycle of *B. bacteriovorus* HD100

Reverse-transcriptase PCR (RT-PCR) performed on RNA isolated from different timepoints across the life cycle of *B. bacteriovorus* HD100. Primers were designed to amplify an approximately 100 bp product internal to either *bd1075* or *dnaK* (a known constitutively transcribed control gene). L: 100 bp DNA ladder, AP: attack-phase, 0.25-4: h since predators and prey were mixed, NT: no-template control, Ec: *E. coli* S17-1 RNA, G: *B. bacteriovorus* HD100 genomic DNA. Image is representative of two biological repeats. Figure shown previously in Banks (2018)[158].

4.1.2.3. Deletion of *bd1075* results in rod-shaped *B. bacteriovorus* HD100 cells

To further investigate the function of Bd1075, an in-frame silent deletion of *bd1075* was constructed in the curved Type stain *B. bacteriovorus* HD100. The knockout was verified by Sanger sequencing and whole genome sequencing. Deletion of *bd1075* resulted in an immediately observable phenotype – *B. bacteriovorus* Δ*bd1075* cells were rod-shaped in contrast to the curved, vibrioid-shaped wild-type (Figure 4.8). The difference in cell morphology was additionally observed in more detail via electron micrographs taken during my PhD (Figure 4.9).

This key finding indicated that Bd1075 functions as a curvature cell shape-determinant within *B. bacteriovorus* HD100 itself.

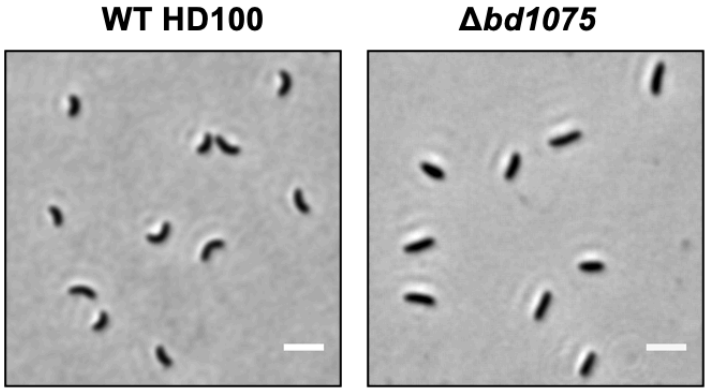

Figure 4.8. Phase-contrast images of *B. bacteriovorus* HD100 wild-type and Δ*bd1075* cells

Phase-contrast microscopy images showing the different cell morphology of attack-phase *B. bacteriovorus* HD100 curved wild-type (WT) and Δ*bd1075* rod-shaped mutant cells. Scale bars = 2 μm. Images are representative of five biological repeats. Figure shown previously in Banks (2018)[158].

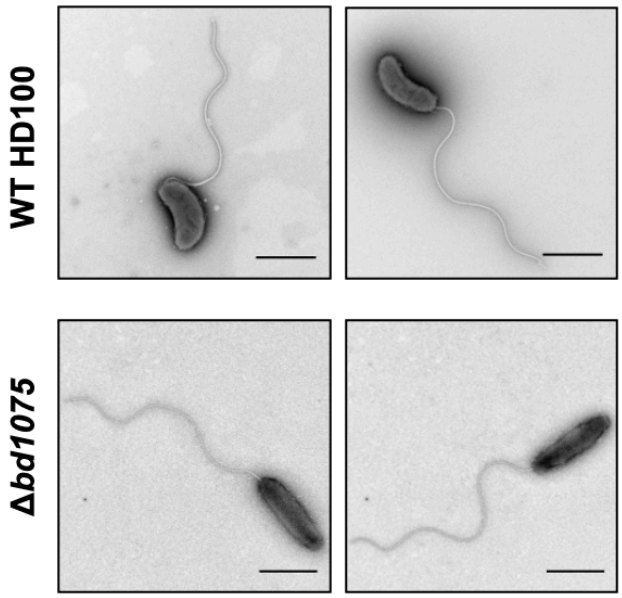

Figure 4.9. Transmission electron micrographs of *B. bacteriovorus* HD100 wild-type and Δ*bd1075* cells

Transmission electron micrographs showing the curved morphology of wild-type *B. bacteriovorus* HD100 cells in comparison to rod-shaped Δ*bd1075* mutant cells at high magnification. Cells were stained with 0.5% uranyl acetate. Scale bars = 1 μm. Images are representative of three biological repeats.

4.2. Research aims

- To further examine the *bd1075* gene product and study conservation of *bd1075* across other *Bdellovibrio* species.

- To complement the ∆*bd1075* deletion mutant and restore curvature.

- To investigate the absence of curvature in *B. bacteriovorus* strain 109J which contains a partial homologue of *bd1075*.

- With collaborators, to determine if Bd1075 is catalytically active on peptidoglycan and functions as an LD-transpeptidase as predicted.

- With collaborators, to crystallise and solve the protein structure of Bd1075 to provide deeper insights into protein composition and mechanism of action.

- To study the subcellular localisation of Bd1075 within *B. bacteriovorus* predator cells and elucidate the mechanism by which the protein is localised.

4.3. Chapter results

4.3.1. The start codon of *bd1075* was mis-annotated

Due to previous instances of *B. bacteriovorus* HD100 genes being mis-annotated (including Bd3285 as discovered in **Chapter 3 Section 3.3.2.4**), the transcriptional start site of *bd1075* was checked by aligning *B. bacteriovorus* HD100 RNA-Seq data to the HD100 genome.

Figure 4.10 reveals that the start codon of *bd1075* was probably mis-annotated. The mRNA transcript begins exactly at the predicted ATG start codon for *bd1075* (Figure 4.10). Moreover, a putative Shine-Dalgarno sequence (GAGA) is present 3 bases into the start of the gene instead of being located upstream from the start codon. This strongly indicates that the predicted ATG start codon is not the correct start codon. The next possible start codon is TTG, just three codons downstream from the original ATG codon and represents the most likely true start codon, following the Shine-Dalgarno sequence for ribosome binding (Figure 4.10).

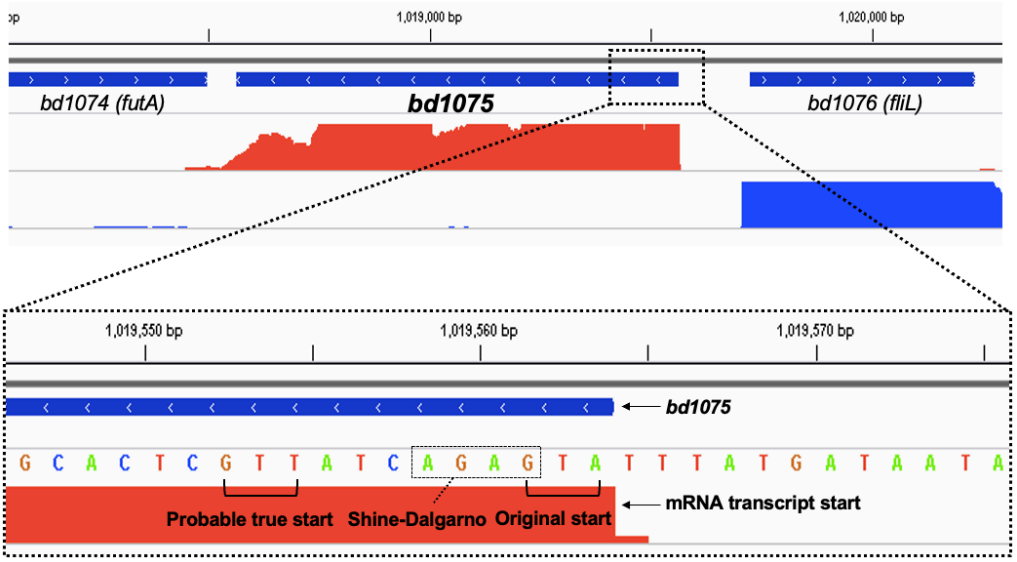

Figure 4.10. The transcriptional start site of *bd1075*

RNA-Seq reads[40] aligned to the genome of *B. bacteriovorus* HD100 with Rockhopper[192, 193]. Reads (red block) show the transcriptional initiation site of the *bd1075* gene (blue) which is encoded on the reverse strand. Transcription begins at the originally annotated ATG start codon, indicating that this is a mis-annotated start site. A probable Shine-Dalgarno site (GAGA) and the probable true start codon (TTG) are annotated. The DNA sequence was reverse-complemented for ease of viewing. Data were visualised in Integrative Genomics Viewer[225].

To assess the validity of the RNA-Seq data which suggests that the *bd1075* start codon was mis-annotated, RT-PCR primers were designed to further probe this possibility (Figure 4.11a). If the original prediction of ATG is the correct start codon, then the primer 1075_F1, which binds just upstream of ATG, should give a 331 bp product when paired with the reverse primer 1075_R. If, however, ATG is a mis-annotated start codon, then the primer 1075_F2, which binds at the ATG site, should give a 305 bp product when paired with 1075_R. The RT-PCR showed that only 1075_F2 and 1075_R produced a PCR product, providing additional evidence that ATG is not the start codon of *bd1075* (Figure 4.11b).

Due to this finding, the numbering of Bd1075 protein residues was adjusted to account for TTG being the likely true start codon of *bd1075*, reducing the total length of the protein from 332 amino acids to 329. It is important to note that this merely changes the start of the primary sequence from ‘MRL’ to ‘MLT’. This minor change has no obvious effect on the predicted domains or function of the protein itself and the sec signal peptide prediction is unchanged.

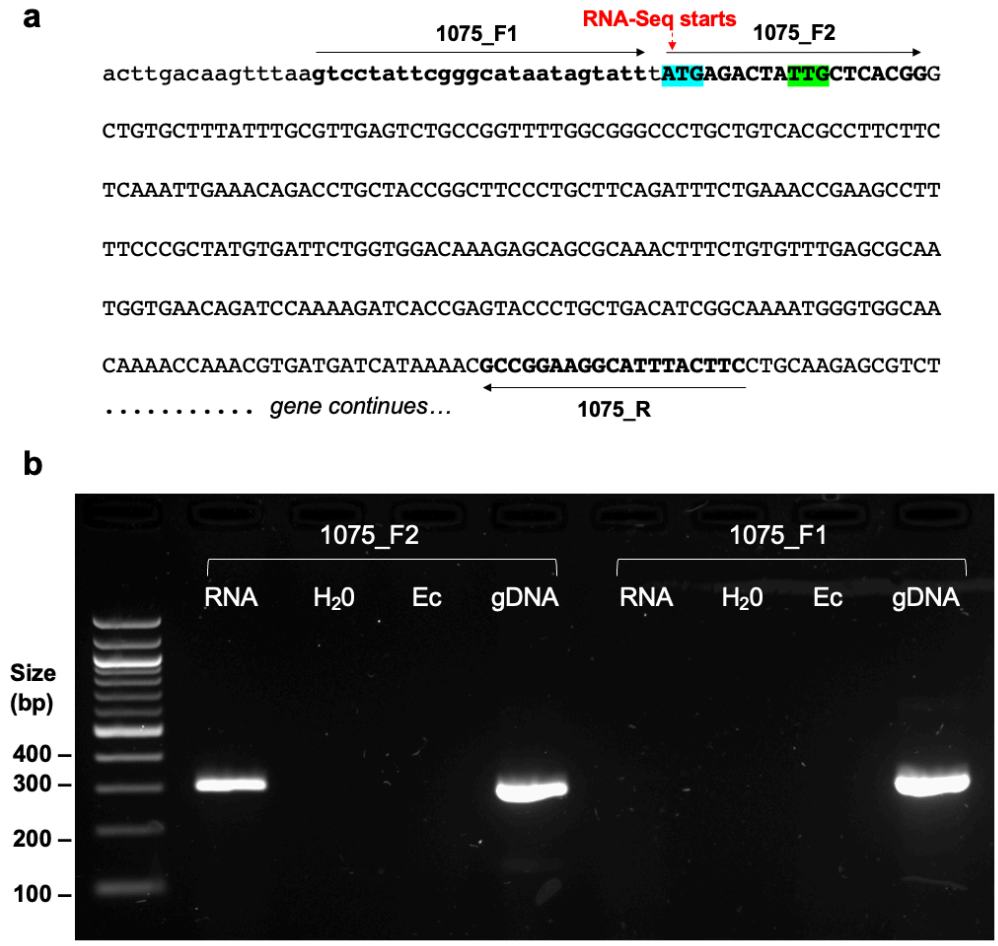

Figure 4.11. RT-PCR confirmation that the *bd1075* gene has an alternative start codon

a) N-terminus of the *bd1075* gene shown with 40 bp of upstream region prior to the originally annotated ATG start codon (highlighted in blue). The proposed true TTG start codon (highlighted in green) and the RNA-Seq transcription start site (indicated by red arrow) are also shown. **b)** RT-PCR designed to test the true start codon of *bd1075* using the primers 1075_F2 with 1075_R or 1075_F1 with 1075_R. The annealing site of each primer is indicated in **a.** No product was detected using the 1075_F_1 primer but a 305 bp product was detected using 1075_F2, indicating that the RNA-Seq data is correct and that TTG is most likely the true start codon. RNA: *B. bacteriovorus* HD100 AP RNA, H_20: negative water control, Ec: *E. coli* S17-1 negative control, gDNA: *B. bacteriovorus* HD100 genomic DNA positive control. The RT-PCR is representative of two biological repeats.

4.3.2. Conservation of vibrioid shape and Bd1075 across *Bdellovibrio*

All known strains of *Bdellovibrio* are vibrioid-shaped like *B. bacteriovorus* HD100 with one definite exception: *B. bacteriovorus* 109J, a common laboratory strain that has been in continuous laboratory culture since the 1960s and is rod-shaped[17]. It is also necessary to briefly discuss the recently discovered epibiotic strain *Bdellovibrio* sp. Qaytius[272]. There is only one publication describing *Bdellovibrio* sp. Qaytius and from the unclear electron micrographs, it is difficult to confidently ascertain the predator cell morphology which could appear curved, slightly curved or rod-shaped[272]. Due to this uncertainty, the shape of *Bdellovibrio* sp. Qaytius in not discussed further in this thesis and *B. bacteriovorus* 109J is referred to as the sole rod-shaped strain of *Bdellovibrio*.

To gain a broader understanding of the possible evolutionary importance of Bd1075, protein conservation was assessed across all known strains of *Bdellovibrio* from endobiotic intraperiplasmic predators (such as *B. bacteriovorus* strains) to predators that do not invade prey (such as *B. exovorus* and *Bdellovibrio* sp. Qaytius). Bd1075 homologues are present in all known strains of *Bdellovibrio* including endobiotic and epibiotic predators. The degree of conservation at the protein level is generally strong, with the two epibiotic predators *B. exovorus* and *Bdellovibrio* sp. Qaytius having the greatest phylogenetic distance from the Type strain *B. bacteriovorus* HD100 (Figure 4.12). This is not surprising as the genome of *B. bacteriovorus* HD100 has more differences to epibiotic strains than other intraperiplasmic strains.

It is notable, however, that while intraperiplasmic *Bdellovibrio* predators contain just one copy of Bd1075, epibiotic *B. exovorus* and *Bdellovibrio* sp. Qaytius contain two copies of Bd1075. Of these two copies, one in each strain (indicated by '_2' in Figure 4.12) is particularly divergent from other Bd1075 sequences. In *B. exovorus*_2, the Bd1075 protein does not contain a predicted signal peptide. Due to the functional importance of

Bd1075 periplasmic localisation (detailed in later sections), the absence of a signal peptide could render this protein copy redundant. The second copy of Bd1075 in *Bdellovibrio* sp. Qaytius ('*Bdellovibrio* sp. Qaytius_2') is much shorter (212 residues) than that of other Bd1075 sequences (generally 275-338 residues in length). Critically, the protein terminates immediately after the predicted 'Ldt' domain and therefore does not contain a C-terminal NTF2 domain which I show later to be essential for Bd1075 function (**Section 4.3.7.2**). Thus, the Bd1075 homologues in these two epibiotic strains might possibly be on a pathway to removal from the genome.

The final strain that contained a significant difference to *B. bacteriovorus* $HD100_{Bd1075}$ is the rod-shaped intraperiplasmic strain *B. bacteriovorus* 109J. Despite sharing 100% sequence identity with $Bd1075_{HD100}$ and therefore appearing closely related phylogenetically (Figure 4.12), the protein $Bd1075_{109J}$ contains a 57 amino acid truncation towards the N-terminus. The morphology of *B. bacteriovorus* 109J and the significance of this truncation is examined in detail in **Section 4.3.4.**

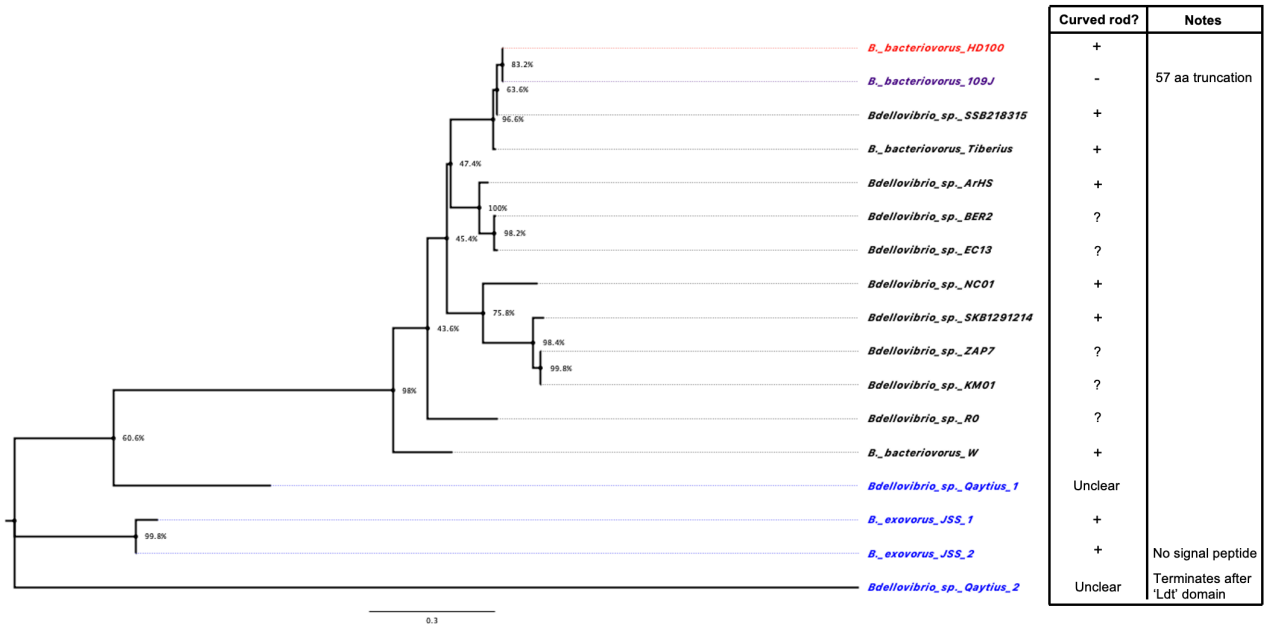

Figure 4.12. Phylogenetic tree showing broad conservation and differences in Bd1075 across *Bdellovibrio* strains

Maximum likelihood unrooted phylogenetic tree constructed from Bd1075 protein sequences in different *Bdellovibrio* strains. Red label: *B. bacteriovorus* HD100 (Type strain). Purple label: *B. bacteriovorus* 109J – the only definitively rod-shaped *Bdellovibrio* strain. Blue labels: Epibiotic predators *B. exovorus* and *Bdellovibrio* sp. Qaytius (each strain contains two copies of Bd1075 indicated by '_1' and '_2'). Strain shape (if known) and striking differences in Bd1075 are noted in columns 1 and 2, respectively. Protein sequences were aligned with ClustalW[189]. The tree was constructed in MEGA-X[190] with 500 bootstrap replications and visualised in FigTree.

4.3.3. Complementation of Δ*bd1075* morphology

The Δ*bd1075* mutant cells appeared rod-shaped, therefore the image analysis software MicrobeJ was used to quantitatively measure the difference in curvature between wild-type and Δ*bd1075* cells using large numbers of *B. bacteriovorus* attack-phase cells (>1900 cells across multiple biological repeats). As expected, curved wild-type cells were significantly ($p<0.0001$) more curved (median 0.64 A.U., 95% CI [0.63, 0.66]) than the Δ*bd1075* mutant strain (median 0.11 A.U., 95% CI [0.10, 0.12]) (Figure 4.13).

To eliminate the possibility that factors other than a clean genetic deletion of *bd1075* resulted in this phenotype, the Δ*bd1075* deletion was complemented. To achieve this, the $bd1075_{HD100}$ gene with 100 bp of flanking DNA (to include the native gene promoter region) was cloned into the replicative plasmid pMQBAD (the only plasmid that can stably replicate within *Bdellovibrio*). Both the complementation plasmid containing the *bd1075* gene and an empty plasmid (negative control) were conjugated into *B. bacteriovorus* Δ*bd1075* and maintained under a gentamicin selection pressure. Plasmid-based trans-complementation of Δ*bd1075* with the wild-type $bd1075_{HD100}$ gene resulted in an increase in cell curvature compared to Δ*bd1075* (Figure 4.13). Trans-complementation was partial and did not completely restore curvature to a wild-type level. This is probably due to aberrant plasmid copy number and the difficulty of plasmid maintenance and segregation in *B. bacteriovorus* which divides as a filament. Later cis-complementation (**Section 4.3.7.2** and **Section 5.3.3**) achieved via genetic crossover into the *B. bacteriovorus* genome resulted in much stronger complementation back to wild-type levels. Nonetheless, partial trans-complementation here indicates that it is Bd1075 which generates cell curvature in *B. bacteriovorus* HD100 predator cells.

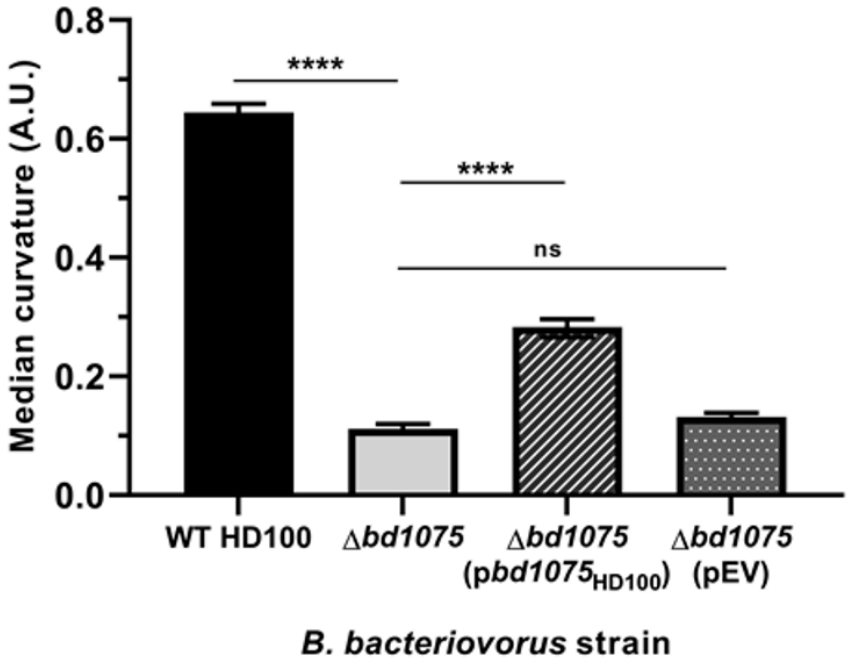

Figure 4.13. Plasmid-based trans-complementation of rod-shaped *B. bacteriovorus* Δ*bd1075* cells

Measurements of cell curvature for *B. bacteriovorus* HD100 attack-phase cells determined using MicrobeJ. The Δ*bd1075* mutant was complemented with the wild-type HD100 *bd1075* gene (p*bd1075*$_{HD100}$) expressed *in trans* on the plasmid pMQBAD. The empty plasmid vector (pEV) served as a negative control. n = 1920-2503 cells per strain from three biological repeats. Error bars represent 95% confidence intervals of the median. ns: non-significant ($p>0.05$), **** ($p<0.0001$); Kruskal-Wallis test.

4.3.4. Investigating absence of curvature in *B. bacteriovorus* strain 109J

The only *Bdellovibrio* strain that is definitively not curved is *B. bacteriovorus* 109J which is rod-shaped (Figure 4.14). Despite being rod-shaped, *B. bacteriovorus* 109J contains a truncated copy of Bd1075 which has now been demonstrated to be the curvature-determinant of *B. bacteriovorus*. Why, then, is *B. bacteriovorus* 109J not curved? Through BLAST analysis in **Section 4.3.2**, it was discovered that despite sharing otherwise 100% sequence identity with $Bd1075_{HD100}$, the $Bd1075_{109J}$ protein contains a deletion of 171 bp (57 amino acids) (Figure 4.15a). This predicted N-terminal truncation can also be observed by aligning raw *B. bacteriovorus* 109J DNA reads to the *B. bacteriovorus* HD100 genome (Figure 4.15b). The N-terminal truncation runs from DNA encoding Proline-21 to Tyrosine-74, encompassing a region that begins just after the signal peptide and stretches 27 residues into the 'Ldt' catalytic domain (Figure 4.15c).

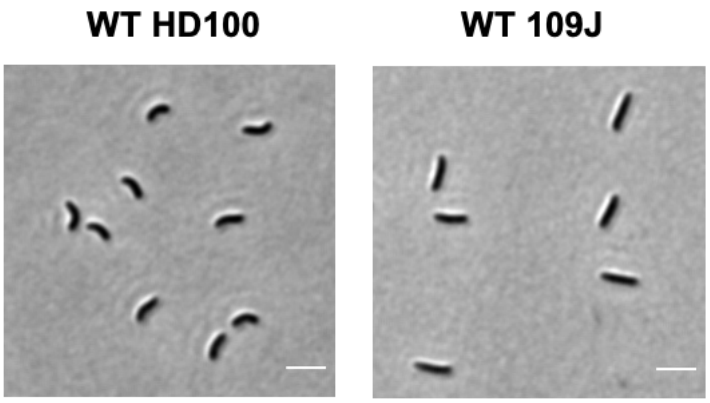

Figure 4.14. Morphology of *B. bacteriovorus* HD100 compared to *B. bacteriovorus* 109J

Phase-contrast microscopy images showing the different cell morphology of wild-type attack-phase *B. bacteriovorus* HD100 - a curved rod, and *B. bacteriovorus* 109J - a straight rod. Scale bars = 2 μm. Images are representative of three biological repeats.

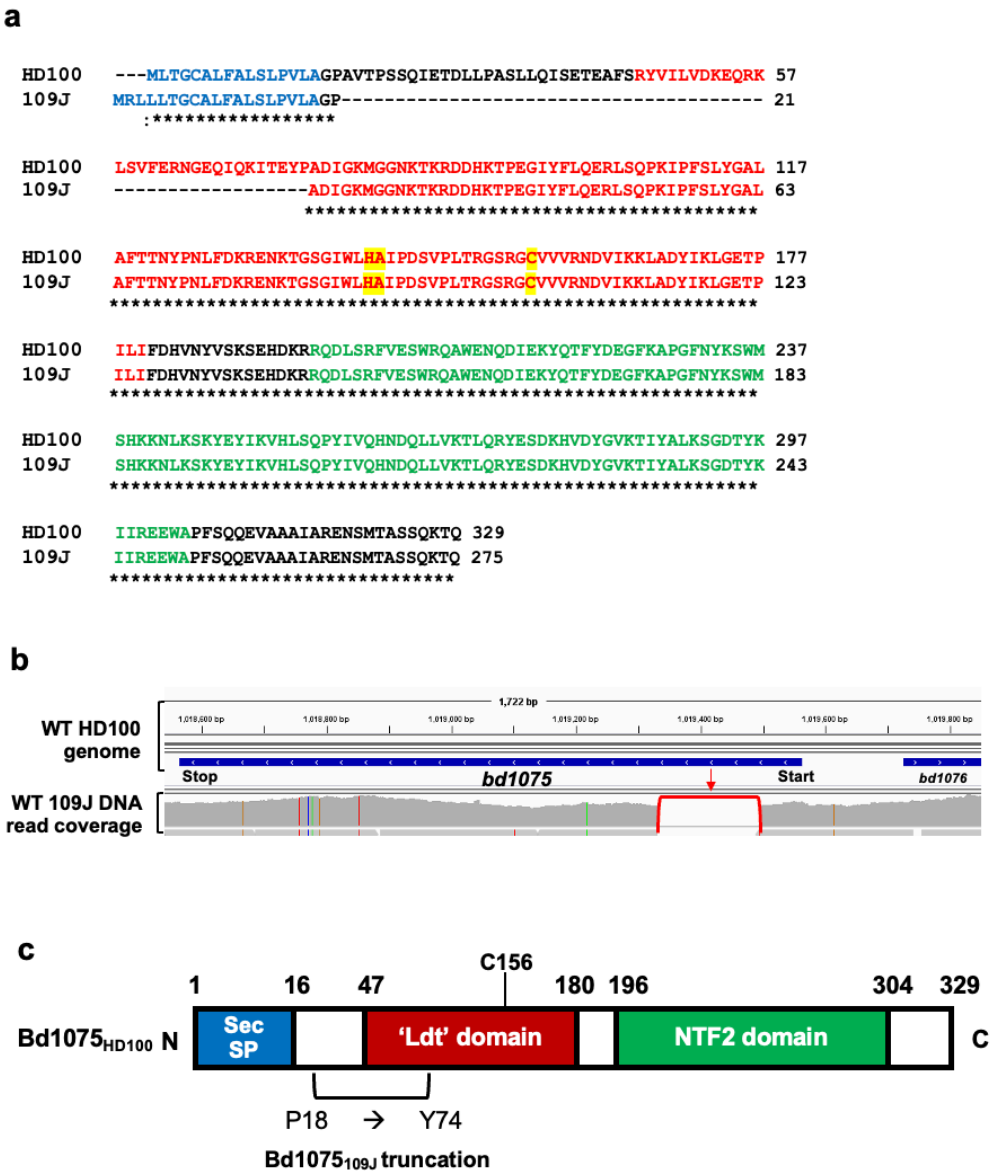

Figure 4.15. Bd1075$_{109J}$ contains a predicted N-terminal truncation

a) Pairwise amino acid alignment of *B. bacteriovorus* proteins Bd1075$_{HD100}$ and Bd1075$_{109J}$. Asterisks represent identical amino acids and dashes indicate the 57 residue truncation in Bd1075$_{109J}$. Blue residues: signal peptide, red residues: 'Ldt' domain with the catalytic triad highlighted in yellow. Green residues: NTF2 domain. **b)** Wild-type 109J DNA sequence reads mapped to the genome of wild-type HD100. The truncation in Bd1075$_{109J}$ can be seen as an absence of read coverage (red arrow). Reads were mapped with Rockhopper[192, 193] and visualised in Integrative Genomics Viewer[225]. **c)** Schematic of the protein Bd1075$_{HD100}$, indicating the 57 amino acid truncation present from P18 to Y74 in Bd1075$_{109J}$. Sec SP: sec signal peptide, 'Ldt' domain: predicted LD-transpeptidase domain with key catalytic residue C156 indicated above, NTF2 domain: nuclear transport factor 2-like domain of unknown function.

To determine whether the *bd1075*$_{109J}$ gene is still expressed in *B. bacteriovorus* 109J despite the genetic truncation, RNA was isolated from *B. bacteriovorus* 109J attack-phase cells for RT-PCR. Figure 4.16a shows that *bd1075*$_{109J}$ is still transcribed in *B. bacteriovorus* 109J attack-phase cells. In addition, to experimentally verify the predicted truncation, RT-PCR primers were designed to specifically bind to each side of the truncation (Figure 4.16b). For wild-type HD100 RNA which does not contain the truncation, a 298 bp product would be expected. In contrast, if the truncation is present in the wild-type 109J RNA transcript, then a 127 bp product would be expected. RT-PCR confirmed the presence of the *bd1075*$_{109J}$ truncation in the transcribed mRNA (Figure 4.16c). Moreover, the presence of a specific 8 bp repeat (CCCTGCTG) was observed immediately flanking the deleted region (blue bases in Figure 4.16b). This is suggestive of the deletion occurring by a process such as replication slippage. This has been observed previously for *B. bacteriovorus* gene *bd0108* in which 10 bp flanking repeats resulted in an internal genetic deletion[39].

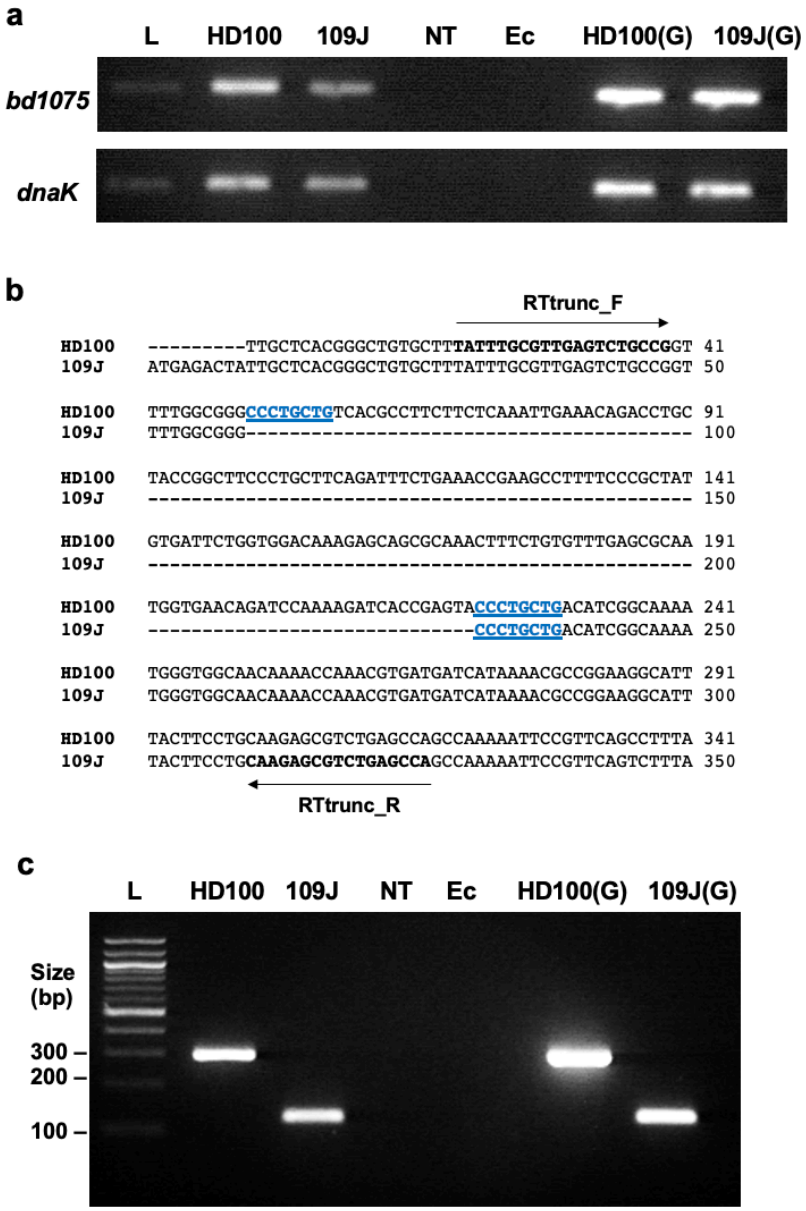

Figure 4.16. The *bd1075*$_{109J}$ gene is transcribed and contains the predicted truncation

a) Reverse-transcriptase PCR performed on RNA isolated from attack-phase *B. bacteriovorus* HD100 and 109J strains using primers designed to amplify a 100 bp product from either *bd1075* or *dnaK* (control gene). NT: no template negative control, Ec: *E. coli* S17-1 negative control, HD100(G) and 109(G): genomic DNA positive controls. Two biological repeats were performed. **b)** Pairwise DNA alignment of *bd1075*$_{HD100}$ and *bd1075*$_{109J}$ showing the *bd1075*$_{109J}$ truncation (dashes) and 8 bp flanking repeats (emboldened, blue and underlined). **c)** Reverse-transcriptase PCR performed on *B. bacteriovorus* attack-phase RNA with primers binding either side of the predicted truncation (as shown in **b**). Expected product sizes of 298 bp (HD100) and

127 bp (109J) confirmed the presence of the *bd1075*$_{109J}$ truncation. Two biological repeats were performed.

Since *B. bacteriovorus* 109J produces an mRNA transcript of *bd1075* which encodes the predicted 57 amino acid truncation, it is likely that the resulting protein also contains this mutation. To test whether the N-terminal truncation in *bd1075*$_{109J}$ is the cause of rod-shaped wild-type 109J cells, a cross-complementation experiment was devised. I observed previously that the Δ*bd1075* mutant can be trans-complemented by plasmid-based expression of the wild-type HD100 copy of *bd1075* (Figure 4.13). Therefore, to test the function (or lack of) of *bd1075*$_{109J,}$ the *bd1075*$_{109J}$ gene was cloned into the replicative plasmid pMQBAD using the method described previously in **Section 4.3.3**. The p*bd1075*$_{109J}$ plasmid was then conjugated into the HD100 Δ*bd1075* mutant alongside an empty vector control (pEV) and the curvature of the resulting strains was measured.

In contrast to the *bd1075*$_{HD100}$ gene which can complement the rod-shaped Δ*bd1075* mutant, the new strain Δ*bd1075* (p*bd1075*$_{109J}$) remained completely rod-shaped (Figure 4.17). Cross-expression of *bd1075*$_{HD100}$ in the normally rod-shaped strain 109J, however, resulted in a significant increase ($p<0.0001$) in cell curvature compared with the morphology of wild-type 109J (Figure 4.17).

Together, these cross-complementation experiments indicate that, while Bd1075 is a curvature-determinant of *B. bacteriovorus*, strain 109J contains a truncated version of Bd1075 with an inactivating mutation which renders the strain incapable of generating cell curvature. This truncation may have arisen and been selected for during the long laboratory culture history of strain 109J, as discussed in **Section 4.4**.

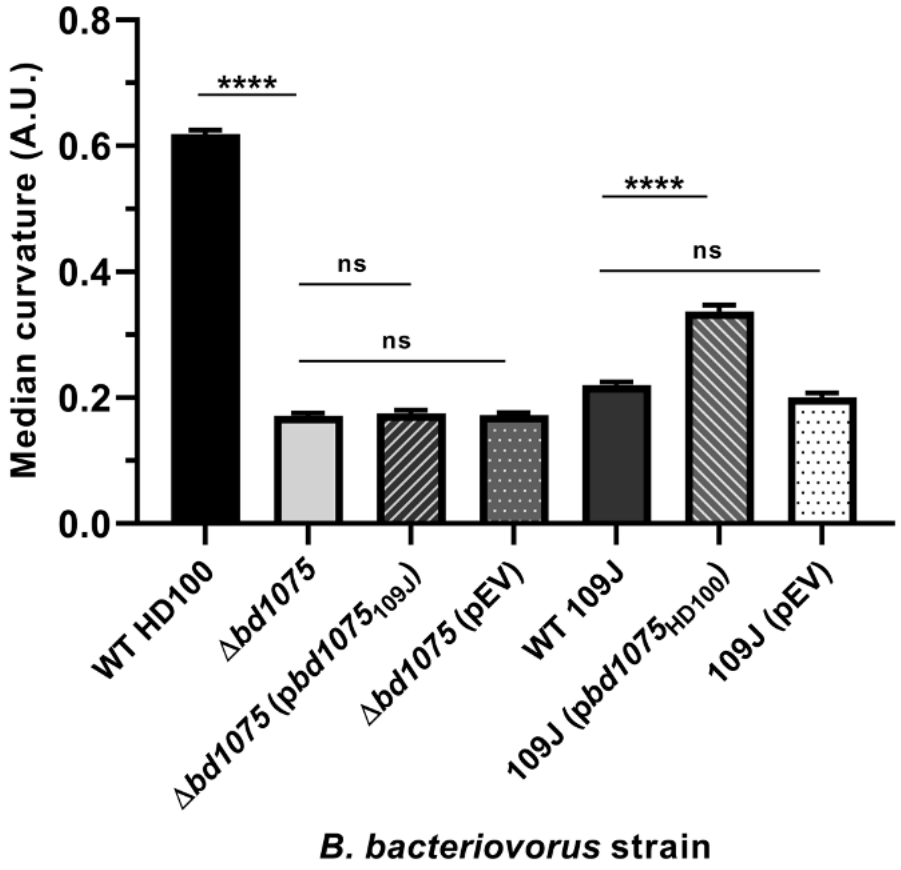

Figure 4.17. Curvature of *B. bacteriovorus* 109J and cross-complementation strains

Cell curvature measurements of attack-phase *B. bacteriovorus* wild-type HD100, wild-type 109J and cross-complementation strains. WT HD100, Δ*bd1075* and Δ*bd1075* (pEV) bars are reproduced from Figure 4.13 to allow comparison with new cross-complementation strains. Δ*bd1075 (*p*bd1075*$_{109J}$) = the *bd1075*$_{109J}$ gene copy expressed *in trans* in the HD100 Δ*bd1075* mutant. 109J (p*bd1075*$_{HD100}$) = the *bd1075*$_{HD100}$ gene copy expressed *in trans* in the wild-type 109J. n = 757-2503 cells per strain from three biological repeats. Error bars represent 95% confidence intervals of the median. ns: non-significant ($p>0.05$), **** ($p<0.0001$; Kruskal-Wallis test).

4.3.5. Bd1075 functions as an LD-carboxypeptidase

4.3.5.1. Bd1075 has LD-carboxypeptidase activity on PG *in vivo*

Bd1075 is a curvature-determinant of *B. bacteriovorus* but until now the mechanistic function of the protein had not been investigated. Cell shape determinants do not necessarily have enzymatic activity. As discussed earlier, crescentin (*C. crescentus*) and CrvA/B (*V. cholerae*) generate curvature through self-polymerisation into cyto- or peri-skeletal filaments that bias insertion of new PG wall material towards one lateral side[251, 252]. Alternatively, proteins such as Csd5 (*H. pylori*) can contribute to cell shape via interactions with periplasmic cell shape machinery[259].

Bd1075 contains a predicted LD-transpeptidase (Ldt) domain, thus a catalytic function for the protein appeared more likely than non-enzymatic activity. Nevertheless, it was very important to ascertain whether Bd1075 was a true Ldt enzyme since the similar cell shape proteins Csd6 (*H. pylori*) and Pgp2 (*C. jejuni*) were originally annotated as Ldts (catalysing *m*-Dap^3-*m*-Dap^3 bond formation) but instead had LD-carboxypeptidase activity, cleaving the terminal D-Ala^4 from PG tetrapeptides to generate tripeptides[257, 265].

To verify the catalytic activity of Bd1075, I collaborated with peptidoglycan experts at Newcastle University: Professor Waldemar Vollmer and postdoctoral researcher Dr Jacob Biboy. Prof Vollmer's lab has extensive experience in extraction and analysis of bacterial cell wall sacculi – which is a gold-standard technique for investigating PG enzyme activity.

Therefore, to investigate Bd1075, cell wall sacculi from *B. bacteriovorus* strains were prepared for muropeptide analysis. Large volumes of culture (1 l) of curved wild-type *B. bacteriovorus* HD100 and rod-shaped Δ*bd1075* were grown and filtered to remove any prey debris. Each culture

was pelleted by centrifugation and the pellet was boiled in 8% SDS to lyse the membranes of the cells. The samples were shipped to Newcastle University for PG extraction and analysis by HPLC. HPLC produces a chromatogram for the muropeptides of the PG from each strain and peaks can be assigned to individual PG muropeptides (e.g. dipeptide, tripeptide, tetra-tetrapeptide) based on standard known elution times. This process is illustrated in Figure 4.18.

For *B. bacteriovorus*, peaks 1-7 (shown in chromatogram figures) were annotated based on known *E. coli* muropeptide retention times. Smaller peaks (which are not important or discussed further in this thesis) were identified by mass spectrometry. Wild-type *B. bacteriovorus* HD100 PG had been previously analysed and compared to *E. coli* PG during the PhD of Dr Thomas Lerner[123]. This revealed some similarities such as the degree of cross-linkage (~33% in *B. bacteriovorus* vs 25-35% in *E. coli*) and some differences such as a higher proportion of pentapeptides and tripeptides and a lower proportion of tetrapeptides in *B. bacteriovorus* compared to *E. coli*[123].

In this study, however, the aim was to compare PG profiles of different *B. bacteriovorus* strains to each other, not *E. coli*. By comparing the muropeptide peaks of different strains (e.g. wild-type vs ∆*bd1075*), any changes caused to PG by Bd1075 can be observed and the corresponding enzyme class assigned to the protein.

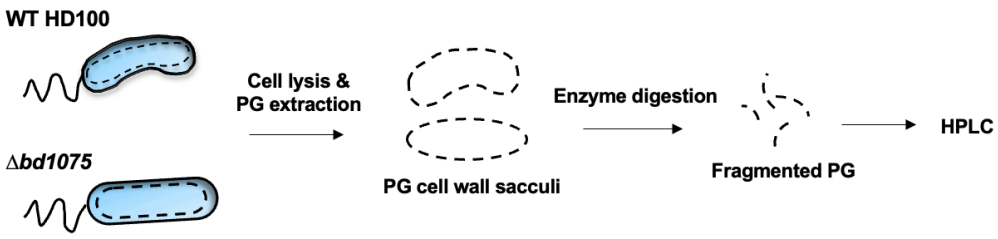

Figure 4.18. Method to isolate and analyse bacterial cell wall PG sacculi

Schematic to briefly illustrate the method of bacterial cell wall sacculi isolation and analysis which is detailed more thoroughly in methods **Section 2.14.1**. *B. bacteriovorus* cultures were grown and then lysed by boiling in 8% SDS. PG sacculi were isolated through further boiling and centrifugation, followed by incubation with the enzyme cellosyl to fragment the PG. PG muropeptides were further reduced with sodium borohydride and then analysed by HPLC to obtain chromatogram profiles.

The muropeptide profile of curved attack-phase *B. bacteriovorus* wild-type cells is shown in Figure 4.19a. Importantly, 9.6% ± 0.8% of wild-type PG consisted of monomeric tetrapeptides and 18.6% ± 0.6% consisted of cross-linked tetra-tetrapeptides (Figure 4.19a and Table 4.1). In contrast, the PG of the rod-shaped ∆*bd1075* mutant contained a much higher proportion of monomeric tetrapeptides (23.7% ± 0.8%) and crosslinked tetra-tetrapeptides (33.2% ± 0.7%) compared to the wild-type (Figure 4.19b and Table 4.1). Moreover, ∆*bd1075* did not contain any monomeric tripeptides and had negligible levels of crosslinked tetra-tripeptides (0.5% ± 0.7%) unlike the curved wild-type (14.4% ± 1% and 14.9% ± 0.7%, respectively) (Figure 4.19b and Table 4.1).

To confirm that the differences in the PG wall structure were caused by Bd1075, PG sacculi were also isolated from the *B. bacteriovorus* complementation strain Δ*bd1075* (p*bd1075*$_{HD100}$) and the control strain Δ*bd1075 (*pEV) (Figure 4.19c-d). Complementing ∆*bd1075* with the *bd1075*$_{HD100}$ gene expressed on a plasmid *in trans* was previously shown to partially restore cell curvature (Figure 4.13). The PG of Δ*bd1075* (p*bd1075*$_{HD100}$) had a negligible level of monomeric tetrapeptides (0.6% ± 0.9%) in contrast to the ∆*bd1075* mutant (Figure 4.19c and Table 4.1). In addition, the strain contained 14.8% ± 1.2% tripeptides and 7.2% ± 0.5% dipeptides (Figure 4.19c and Table 4.1). This suggests that re-introducing the *bd1075*$_{HD100}$ gene into the ∆*bd1075* mutant may have resulted in excess enzymatic activity beyond wild-type levels since all monomeric tetrapeptides were converted to tripeptides, with some further conversion to dipeptides.

Earlier experiments suggested the copy of *bd1075* present in rod-shaped *B. bacteriovorus* strain 109J may not be enzymatically active due to an N-terminal truncation in the gene (**Section 4.3.4**). To test this further, PG of the cross-expression strain Δ*bd1075* (p*bd1075*$_{109J}$) – in which curvature was not complemented (Figure 4.17) – was analysed. The PG muropeptide profile did not significantly differ from that of the ∆*bd1075* mutant (Figure 4.23a and Table 4.2), providing further evidence that the Bd1075$_{109J}$ protein is catalytically-inactive.

Wild-type strain 109J PG was found to be very similar to that of the ∆*bd1075* mutant, containing a complete absence of tripeptides and a negligible level of tetra-tripeptides along with a high proportion of monomeric tetrapeptides (28.0% ± 4.3%) and cross-linked tetra-tetrapeptides (33.8% ± 1.1%) (Figure 4.23b and Table 4.2).

The alternative cross-expression strain 109J (p*bd1075*$_{HD100}$) which had a higher curvature than the wild-type strain 109J (Figure 4.17) contained tripeptides (18.7% ± 3.0%) and cross-linked tetra-tripeptides (26.2% ± 0.6%) unlike wild-type 109J, as well as a reduction in monomeric tetrapeptides and cross-linked tetra-tetrapeptides (Figure 4.23c and Table 4.2). Therefore, the cross-expression of the functional *bd1075*$_{HD100}$ gene in rod-shaped wild-type 109J can increase the curvature of the normally rod-shaped strain through enzymatic activity on the cell wall.

Taken together, this *in vivo* analysis of PG sacculi isolated from *B. bacteriovorus* strains suggests that Bd1075 enzymatically cleaves both monomeric and cross-linked tetrapeptides to tripeptides in the PG wall, functioning as an LD-CPase and not an Ldt as originally predicted.

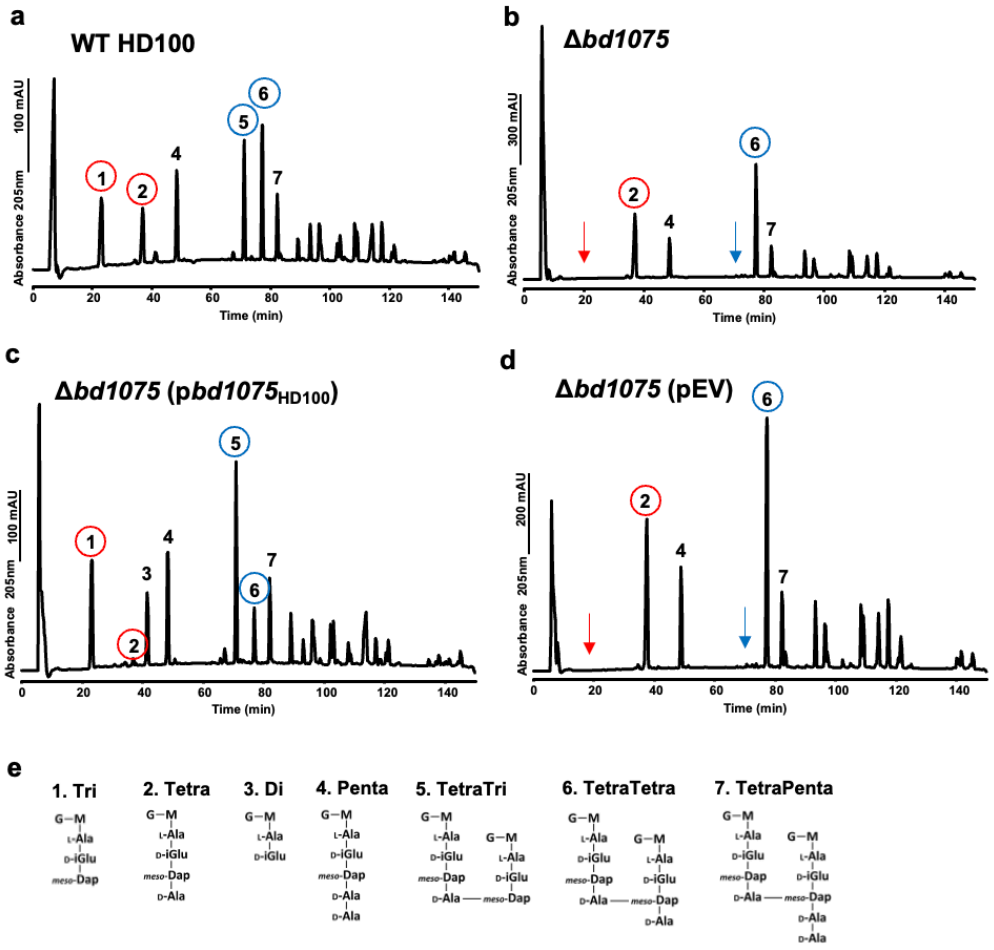

Figure 4.19. Muropeptide composition of *B. bacteriovorus* HD100 strains. HPLC muropeptide chromatograms for PG sacculi isolated from attack-phase *B. bacteriovorus* HD100 strains: **a)** wild-type, **b)** Δ*bd1075* mutant, **c)** Δ*bd1075* complemented with $bd1075_{HD100}$ and **d)** Δ*bd1075* containing an empty vector control. Circles and arrows indicate important muropeptides affected by Bd1075. Coloured red are tripeptides (1) and tetrapeptides (2). Circles denote the presence of the peak and arrows indicate the absence of the peak. Tetra-tripeptide (5) and tetra-tetrapeptide (6) peaks are coloured blue and highlighted in the same manner. Chromatograms are representative of two biological repeats. **e)** Structures of the seven main muropeptide fractions. Numbers correspond to those above peaks in **a-d** and were assigned based on the retention times of known muropeptides. G: *N*-acetylglucosamine, M: *N*-acetylmuramitol, L-Ala: L-alanine, D-Glu: D-glutamic acid, *meso*-Dap: *meso*-diaminopimelic acid, D-Ala: D-alanine. **Data were collected by Dr Jacob Biboy**.

Table 4.1. Quantification of muropeptides released from *B. bacteriovorus* HD100 strains

Numbers represent the relative percentage area of each muropeptide peak in Figure 4.19. Values with an asterisk differ from WT HD100 by more than 30%. Values in bold with an asterisk differ from WT HD100 by more than 50%. **Data were collected by Dr Jacob Biboy.**

Muropeptide	Relative peak area (%)[1] in *B. bacteriovorus* strain			
	WT HD100	**Δ*bd1075***	**Δ*bd1075* (p*bd1075*$_{HD100}$)**	**Δ*bd1075* (pEV)**
Monomers				
Tri	14.4 ± 1.0	**n.d.*[2]**	14.8 ± 1.2	**n.d.***
Tetra	9.6 ± 0.8	**23.7 ± 0.8***	**0.6 ± 0.9***	**23.1 ± 2.7***
Di	2.1 ± 0.1	**n.d.***	**7.2 ± 0.5***	**n.d.***
Penta	12.8 ± 2.5	11.9 ± 3.6	12.2 ± 4.2	14.8 ± 0.0
Monomer anhydroMurNAc	2.2 ± 3.0	2.3 ± 3.2	2.6 ± 3.7	2.5 ± 3.6
Monomers (Total)	38.9 ± 0.5	35.6 ± 4.3	34.9 ± 2.6	37.8 ± 2.6
Dimers				
TetraTri	14.9 ± 0.7	**0.5 ± 0.7***	**26.4 ± 1.5***	**n.d.***
TetraTetra	18.6 ± 0.6	**33.2 ± 0.7***	**7.8 ± 1.4***	**29.6 ± 4.7***
TetraPenta	12.2 ± 1.0	12.5 ± 0.3	14.7 ± 2.9	13.1 ± 0.2
Dimer anhydroMurNAc	17.3 ± 0.8	16.4 ± 0.6	20.5 ± 4.4	17.0 ± 0.3
Dimers (total)	45.6 ± 2.3	46.1 ± 0.6	48.9 ± 2.9	42.7 ± 4.5
Trimers				
TetraTetraTri	1.6 ± 0.4	**n.d.***	**3.8 ± 0.2***	**n.d.***
TetraTetraTetra	6.9 ± 0.5	**11.2 ± 0.8***	4.9 ± 1.0	**10.6 ± 2.2***
TetraTetraPenta	6.9 ± 3.6	7.1 ± 3.2	7.4 ± 4.3	8.8 ± 4.0
Trimer anhydroMurNAc	7.0 ± 0.3	9.5 ± 1.0*	6.2 ± 1.3	10.3 ± 1.0*
Trimers (total)	15.4 ± 2.8	18.3 ± 4.0	16.2 ± 5.5	19.4 ± 1.8
Dipeptides (total)	2.1 ± 0.1	**n.d.***	**7.2 ± 0.5***	**n.d.***
Tripeptides (total)	22.4 ± 0.6	**0.2 ± 0.3***	29.3 ± 0.5*	**n.d.***
Tetrapeptides (total)	54.3 ± 1.1	79.3 ± 2.0*	41.4 ± 4.2	75.7 ± 1.4*
Pentapeptides (total)	19.0 ± 1.3	18.2 ± 0.9	19.5 ± 0.6	21.8 ± 5.0
AnhydroMurNAc (total)	13.1 ± 3.3	13.6 ± 2.6	14.9 ± 5.4	14.5 ± 3.8
Average chain length	7.9 ± 2.0	7.5 ± 1.4	7.2 ± 2.6	7.1 ± 1.9
Degree of cross-linkage	33.1 ± 0.7	35.3 ± 2.8	35.3 ± 2.2	34.3 ± 1.0
% peptides in cross-links	61.1 ± 0.5	64.4 ± 4.3	65.1 ± 2.6	62.2 ± 2.6

[1] values are mean ± variation of two biological replicates.

[2] n.d., not detected.

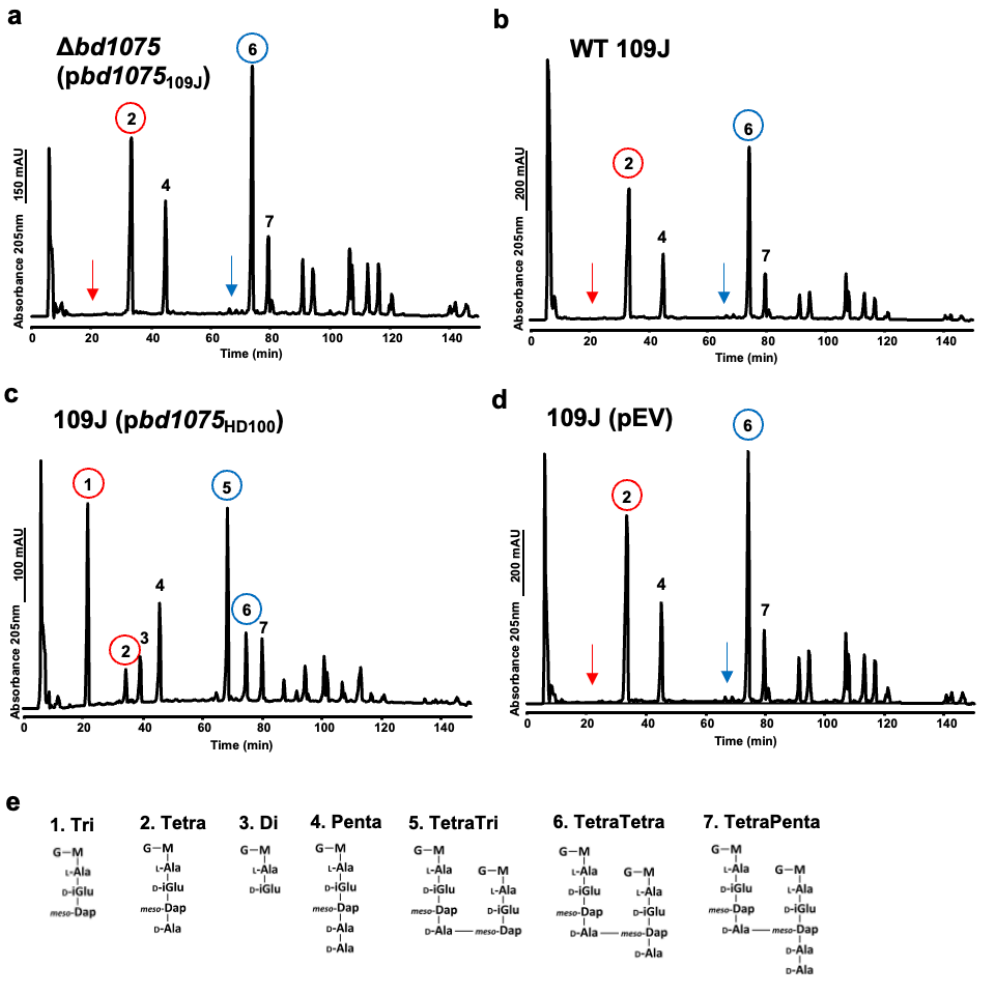

Figure 4.20. Muropeptide composition of further *B. bacteriovorus* strains

HPLC muropeptide chromatograms for PG sacculi isolated from attack-phase *B. bacteriovorus* strains: **a)** Δ*bd1075* expressing *bd1075*$_{109J}$, **b)** wild-type 109J, **c)** 109J complemented with *bd1075*$_{HD100}$ and **d)** 109J containing and empty vector control. Circles and arrows indicate important muropeptides affected by Bd1075. Coloured red are tripeptides (1) and tetrapeptides (2). Circles denote peak presence and arrows indicate peak absence. Tetra-tripeptide (5) and tetra-tetrapeptide (6) peaks are coloured blue and highlighted in the same manner. Chromatograms are representative of two biological repeats. **e)** Structures of the seven main muropeptide fractions. Numbers correspond to those above peaks in **a-d** and were assigned based on the retention times of known muropeptides. G: *N*-acetylglucosamine, M: *N*-acetylmuramitol, L-Ala: L-alanine, D-Glu: D-glutamic acid, *meso*-Dap: *meso*-diaminopimelic acid, D-Ala: D-alanine. **Data were collected by Dr Jacob Biboy.**

Table 4.2. Quantification of muropeptides released from further *B. bacteriovorus* strains

Numbers represent the relative percentage area of each muropeptide peak in Figure 4.20. For the strain Δ*bd1075* (p*bd1075*$_{109J}$), values with an asterisk differ from WT HD100 by more than 30% and values that are additionally emboldened differ by more than 50%. Values for strains 109J (p*bd1075*$_{HD100}$) and 109J (pEV) are compared to WT 109J in identical manner. **Data were collected by Dr Jacob Biboy.**

Muropeptide	Relative peak area (%)[1] in *B. bacteriovorus* strain			
	Δ*bd1075* (p*bd1075*$_{109J}$)	**WT 109J**	**109J (p*bd1075*$_{HD100}$)**	**109J (pEV)**
Monomers				
Tri	**n.d.*[2]**	n.d.	**18.7 ± 3.0***	0.3 ± 0.4
Tetra	**22.2 ± 1.5***	28.0 ± 4.3	**3.0 ± 0.8***	26.4 ± 0.5
Di	**n.d.***	n.d.	**6.2 ± 0.8***	n.d.
Penta	12.8 ± 5.9	13.1 ± 4.1	14.0 ± 1.9	14.6 ± 2.5
Monomer anhydroMurNAc	2.8 ± 4.0*	2.5 ± 3.5	2.2 ± 3.2	3.1 ± 4.3
Monomers (Total)	35.1 ± 7.4	41.0 ± 8.4	42.0 ± 4.8	41.3 ± 2.7
Dimers				
TetraTri	**0.5 ± 0.7***	0.3 ± 0.4	**26.2 ± 0.6***	0.2 ± 0.2*
TetraTetra	**33.4 ± 0.9***	33.8 ± 1.1	**8.8 ± 0.8***	34.3 ± 1.5
TetraPenta	12.6 ± 0.5	11.4 ± 1.4	13.2 ± 0.5	12.1 ± 0.9
Dimer anhydroMurNAc	17.2 ± 1.3	15.1 ± 1.3	16.2 ± 1.1	15.2 ± 0.4
Dimers (total)	46.5 ± 0.6	45.5 ± 0.7	48.2 ± 1.0	46.6 ± 0.3
Trimers				
TetraTetraTri	**n.d.***	n.d.	**2.3 ± 0.6***	n.d.
TetraTetraTetra	**11.6 ± 2.6***	7.9 ± 1.9	**2.5 ± 0.4***	7.2 ± 0.9
TetraTetraPenta	6.9 ± 5.4	5.6 ± 5.8	5.1 ± 4.8	4.9 ± 4.0
Trimer anhydroMurNAc	10.4 ± 2.8*	6.6 ± 2.5	**2.9 ± 1.0***	5.9 ± 0.7
Trimers (total)	18.4 ± 8.0	13.5 ± 7.7	9.8 ± 5.8	12.1 ± 3.0
Dipeptides (total)	**n.d.***	n.d.	**6.2 ± 0.8***	n.d.
Tripeptides (total)	**0.2 ± 0.3***	0.1 ± 0.2	**32.6 ± 3.1***	**0.3 ± 0.5***
Tetrapeptides (total)	78.3 ± 4.0*	79.3 ± 1.3	**38.9 ± 2.3***	77.4 ± 0.3
Pentapeptides (total)	18.6 ± 0.3	18.1 ± 2.0	20.0 ± 3.2	19.2 ± 3.6
AnhydroMurNAc (total)	14.9 ± 2.4	12.3 ± 2.1	11.3 ± 3.4	12.6 ± 4.8
Average chain length	6.8 ± 1.1	8.3 ± 1.4	9.2 ± 2.8	8.5 ± 3.2
Degree of cross-linkage	35.5 ± 5.0	31.7 ± 5.5	30.7 ± 3.4	31.4 ± 1.9
% peptides in cross-links	64.9 ± 7.4	59.0 ± 8.4	58.0 ± 4.8	58.7 ± 2.7

[1] values are mean ± variation of two biological replicates.

[2] n.d., not detected.

4.3.5.2. Purification of Bd1075 and activity on PG *in vitro*

Analysis of *B. bacteriovorus* wild-type, Δ*bd1075* mutant and cross-expression strains suggested that Bd1075 acts as an LD-CPase on PG. To additionally verify this activity, I collaborated with my co-supervisor Prof Andrew Lovering's group at the University of Birmingham who routinely purify and crystallise proteins from *Bdellovibrio*. PhD student Ms Amber Wilson (with help from student Ms Chloe Hudson and postdoctoral researcher Dr Ian Cadby) successfully cloned a recombinant version of the *bd1075*$_{HD100}$ gene (with an N-terminal His-tag and no signal peptide) into *E. coli* expression strain BL21 and purified the recombinant protein by both Ni-NTA IMAC chromatography and size exclusion gel filtration chromatography. Homogenous purification of Bd1075 can be visualised in Figure 4.21 which was kindly provided by the PhD student Mr Mauricio Valdivia-Delgado who assumed subsequent protein and crystallographic work on Bd1075.

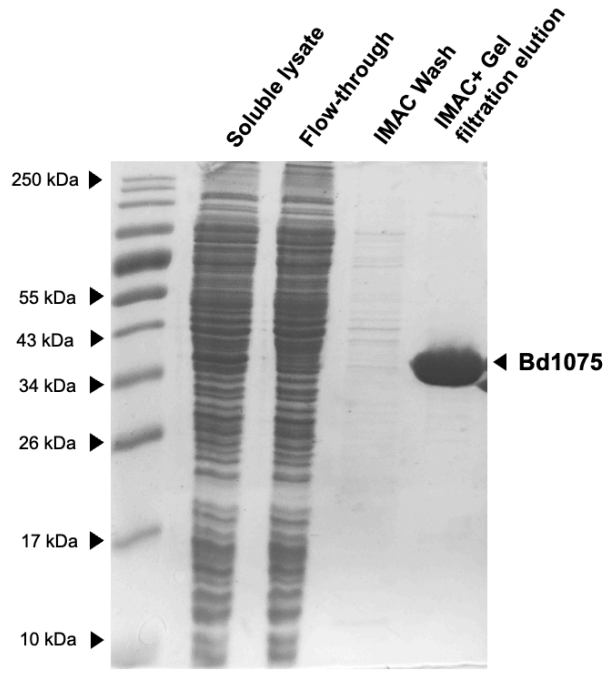

Figure 4.21. Purification of Bd1075 protein

Recombinant Bd1075 (35 kDa) was purified by IMAC Ni-NTA chromatography followed by gel filtration chromatography. The purity of the Bd1075 protein was observed by running the protein sample on a 15% SDS-PAGE gel followed by staining with Coomassie blue. **The gel image was kindly provided by Mr Mauricio Valdivia-Delgado who performed the purification.**

To test the activity of purified Bd1075$_{HD100}$ enzyme *in vitro*, our collaborators at Newcastle University then applied the purified enzyme to Δ*bd1075* PG that had previously been isolated for *in vivo* studies and compared this to a no-treatment buffer control. The resulting PG muropeptides were analysed by HPLC. Addition of Bd1075$_{HD100}$ enzyme to Δ*bd1075* PG resulted in complete conversion of monomeric tetrapeptides (peak 2 in Figure 4.22a) to tripeptides (peak 1) and complete conversion of cross-linked tetra-tetrapeptides (peak 6) to tetra-tripeptides (peak 5). This demonstrated that Bd1075$_{HD100}$ also possesses LD-CPase enzymatic activity *in vitro*. Further application of purified Bd1075$_{HD100}$ enzyme to either wild-type *B. bacteriovorus* 109J PG or wild-type *E. coli* BW25113 PG resulted in identical muropeptide peak conversions (Figure 4.23), indicating that the Bd1075$_{HD100}$ protein can also function on PG from both a different bacterial strain (wild-type 109J) and species (*E. coli*) *in vitro*.

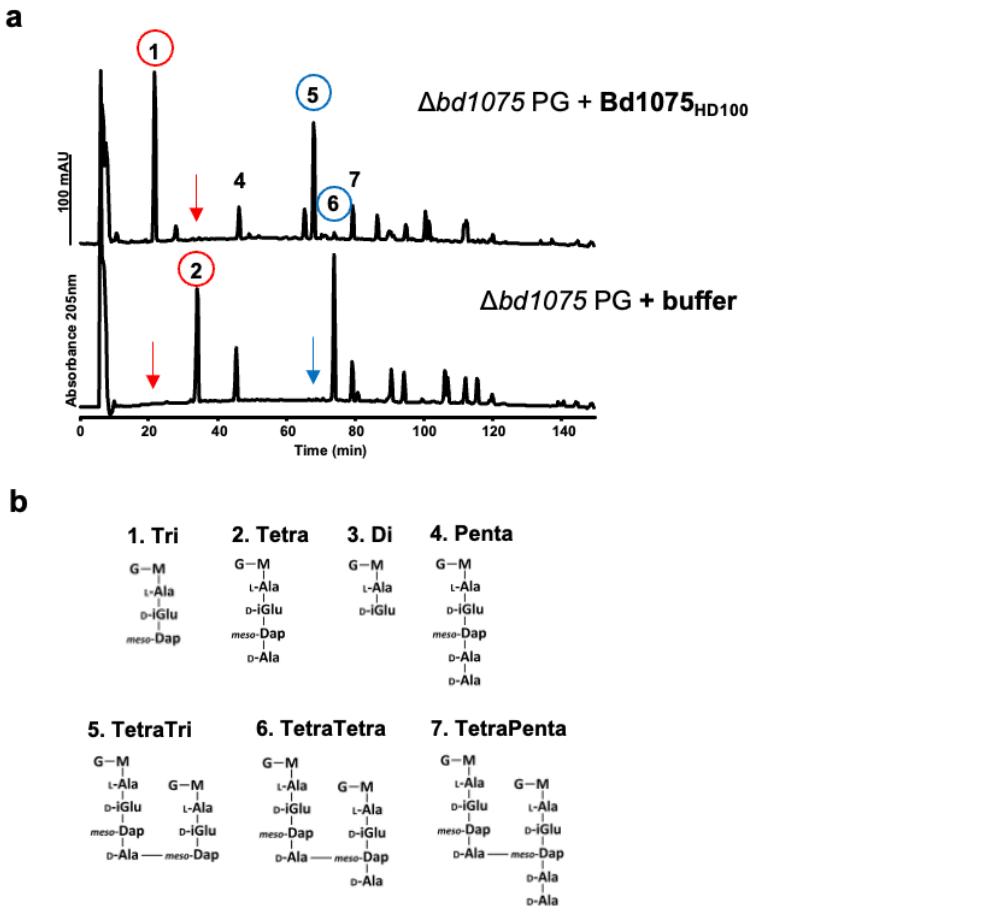

Figure 4.22. Muropeptide analysis of Δ*bd1075* PG treated with purified Bd1075 enzyme

a) HPLC muropeptide chromatograms for Δ*bd1075* PG sacculi treated with purified Bd1075 enzyme (top row) or a buffer control (bottom row). Circles and arrows indicate important muropeptides affected by Bd1075. Coloured red are tripeptides (1) and tetrapeptides (2), with circles denoting presence of the peak and arrows indicating absence. Tetra-tripeptide (5) and tetra-tetrapeptide (6) peaks are coloured blue and highlighted in the same manner. Data are from one biological repeat. **b)** Structures of the seven main muropeptide fractions. Numbers correspond to those above peaks in **a-b** and were assigned based on the retention times of known muropeptides. G: *N*-acetylglucosamine, M: *N*-acetylmuramitol, L-Ala: L-alanine, D-Glu: D-glutamic acid, *meso*-Dap: *meso*-diaminopimelic acid, D-Ala: D-alanine. **Data were collected by Dr Jacob Biboy.**

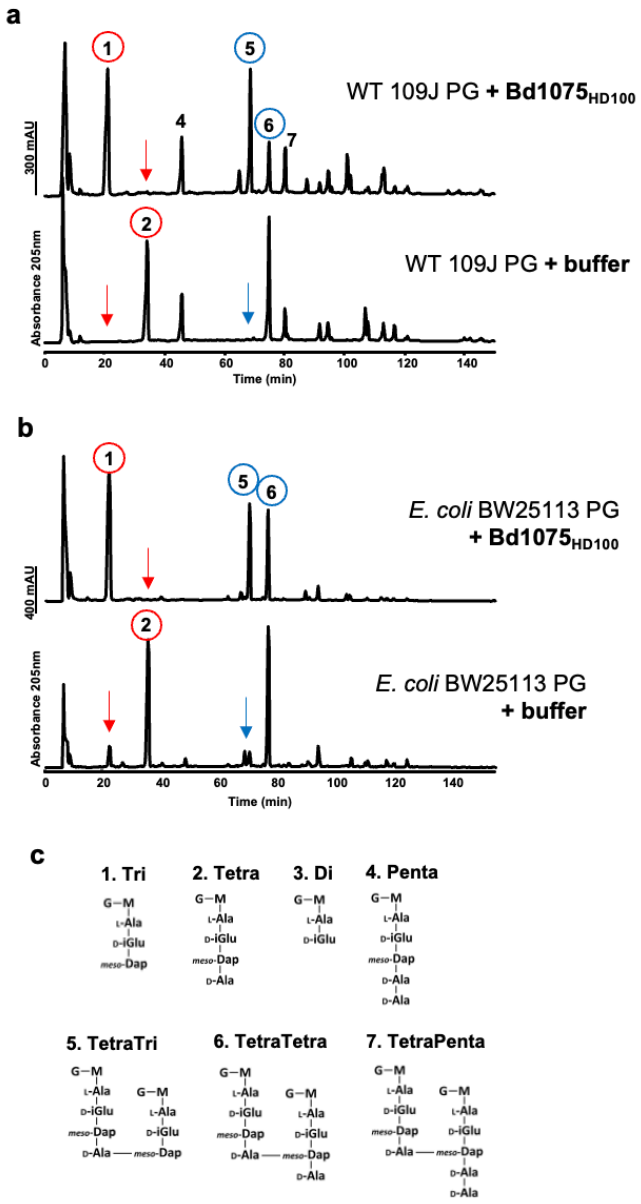

Figure 4.23. Muropeptide analysis of WT 109J and *E. coli* BW25113 PG treated with purified Bd1075 enzyme

HPLC muropeptide chromatograms for **a)** WT 109J and **b)** *E. coli* BW25113 PG sacculi treated with purified Bd1075 enzyme (top row) or a buffer control (bottom row). Circles and arrows indicate important muropeptides affected by Bd1075. Coloured red are tripeptides (1) and tetrapeptides (2), with circles denoting presence of the peak and arrows indicating a very small or absent peak. Tetra-tripeptide (5) and tetra-tetrapeptide (6) peaks are coloured blue and highlighted in the same manner. Data are from one biological repeat. **c)** Structures of the seven main muropeptide fractions. Numbers correspond to those above peaks in **a-b** and were assigned based on the retention times of known muropeptides. G: *N*-acetylglucosamine, M: *N*-acetylmuramitol, L-Ala: L-alanine, D-Glu: D-glutamic acid, *meso*-Dap: *meso*-diaminopimelic acid, D-Ala: D-alanine. **Data were collected by Dr Jacob Biboy**.

Cumulatively, the *in vivo* analysis of *B. bacteriovorus* PG and *in vitro* analysis of purified $Bd1075_{HD100}$ protein on different bacterial PG provide strong evidence that the protein Bd1075 is 1) enzymatically-active and 2) functions as an LD-CPase class of PG-modifying protein as opposed to the original prediction of an Ldt. These data inform on the mechanistic role of Bd1075 which cuts down both monomeric and cross-linked tetrapeptides in the PG wall to tripeptides by cleaving the terminal D-Alanine[4] from the stem peptide (Figure 4.24).

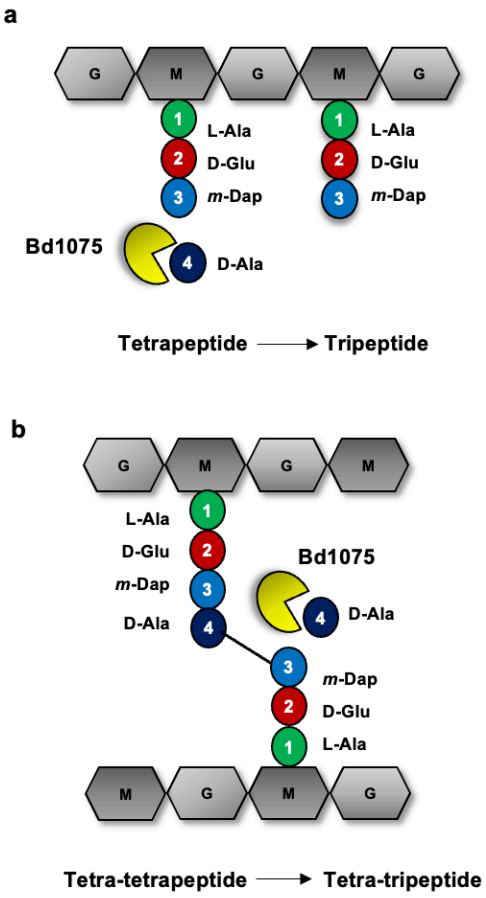

Figure 4.24. Schematic of Bd1075 LD-CPase activity on peptidoglycan

Schematic demonstrating the mechanism of LD-CPase action by Bd1075. LD-CPase-mediated cleavage by Bd1075 of the terminal D-alanine from the stem peptide of either **a)** a monomeric tetrapeptide, converting it to a tripeptide or **b)** a cross-linked tetra-tetrapeptide, converting it to a cross-linked tetra-tripeptide. G: *N*-acetylglucosamine, M: *N*-acetylmuramitol, L-Ala: L-alanine, D-Glu: D-glutamic acid, *m*-Dap: *meso*-diaminopimelic acid, D-Ala: D-alanine.

4.3.6. Bd1075 localises to the outer convex face of curved *B. bacteriovorus* cells

4.3.6.1. Localisation of Bd1075-mCherry to the convex face of *B. bacteriovorus*

During my MRes rotation project, I constructed a double-crossover chromosomal fusion of mCherry to the C-terminus of Bd1075. Due to time constraints, there was limited opportunity to examine this fluorescent fusion. I did note, however, that Bd1075-mCherry was visible within *B. bacteriovorus* HD100 predator cells and did not appear to be secreted into prey bdelloplasts during predation[158].

Closer examination of Bd1075-mCherry during my PhD revealed a particular subcellular localisation of Bd1075 within *B. bacteriovorus* predator cells – the protein appeared to specifically localise to the outer, convex cell face (Figure 4.25a). To visualise this more clearly, a single-crossover fusion of the cytoplasmic protein Bd0064-mCerulean3 was introduced into the existing Bd1075-mCherry double-crossover background to label the predator cytoplasm blue. This double-coloured *B. bacteriovorus* strain provided clearer visual evidence that Bd1075-mCherry localised to the outer curve (Figure 4.25b).

To determine whether Bd1075-mCherry localised to the convex face of attack-phase *B. bacteriovorus* cells only or remained at the convex face throughout the predatory life cycle, images were taken across a synchronous predatory timecourse using the double-coloured strain. This experiment revealed that Bd1075-mCherry (although not particularly bright – especially at later timepoints of 2 and 3 hours) did not appear to move away from the outer convex face during predatory growth (Figure 4.26).

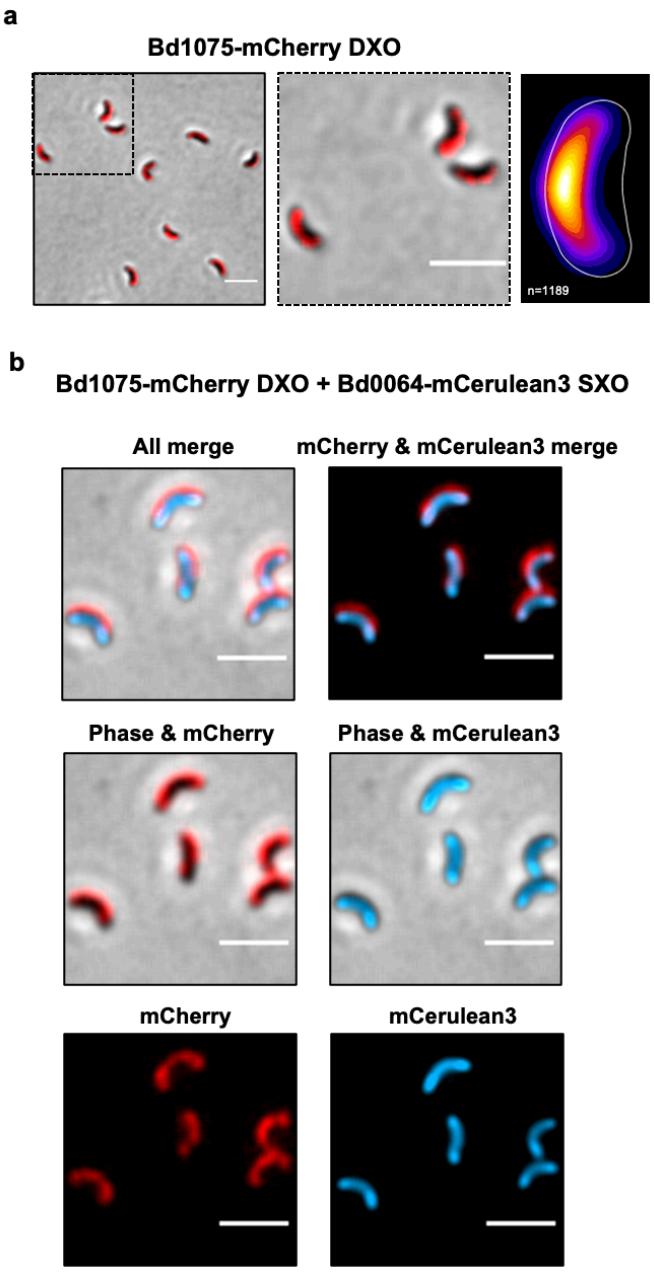

Figure 4.25. Bd1075 localises to the outer convex face of *B. bacteriovorus*

Fluorescence microscopy images of *B. bacteriovorus* attack-phase cells showing localisation of Bd1075-mCherry to the outer convex face of predator cells. Fluorescent strains contain either a double-crossover (DXO) genomic copy of Bd1075-mCherry **(a)** or a single-crossover (SXO) copy of cytoplasmic protein Bd0064-mCerulean3 in addition to a double-crossover genomic copy of Bd1075-mCherry **(b)**. In **a)** the dashed box region (left image) is shown as a magnified close-up (middle image) and the heatmap (right image) generated in MicrobeJ shows the distribution of Bd1075-mCherry foci detected in n = 1189 cells from three biological repeats. White-yellow: greatest foci intensity, purple-black: lowest foci intensity. Scale bars = 2 μm and images are representative of three biological repeats.

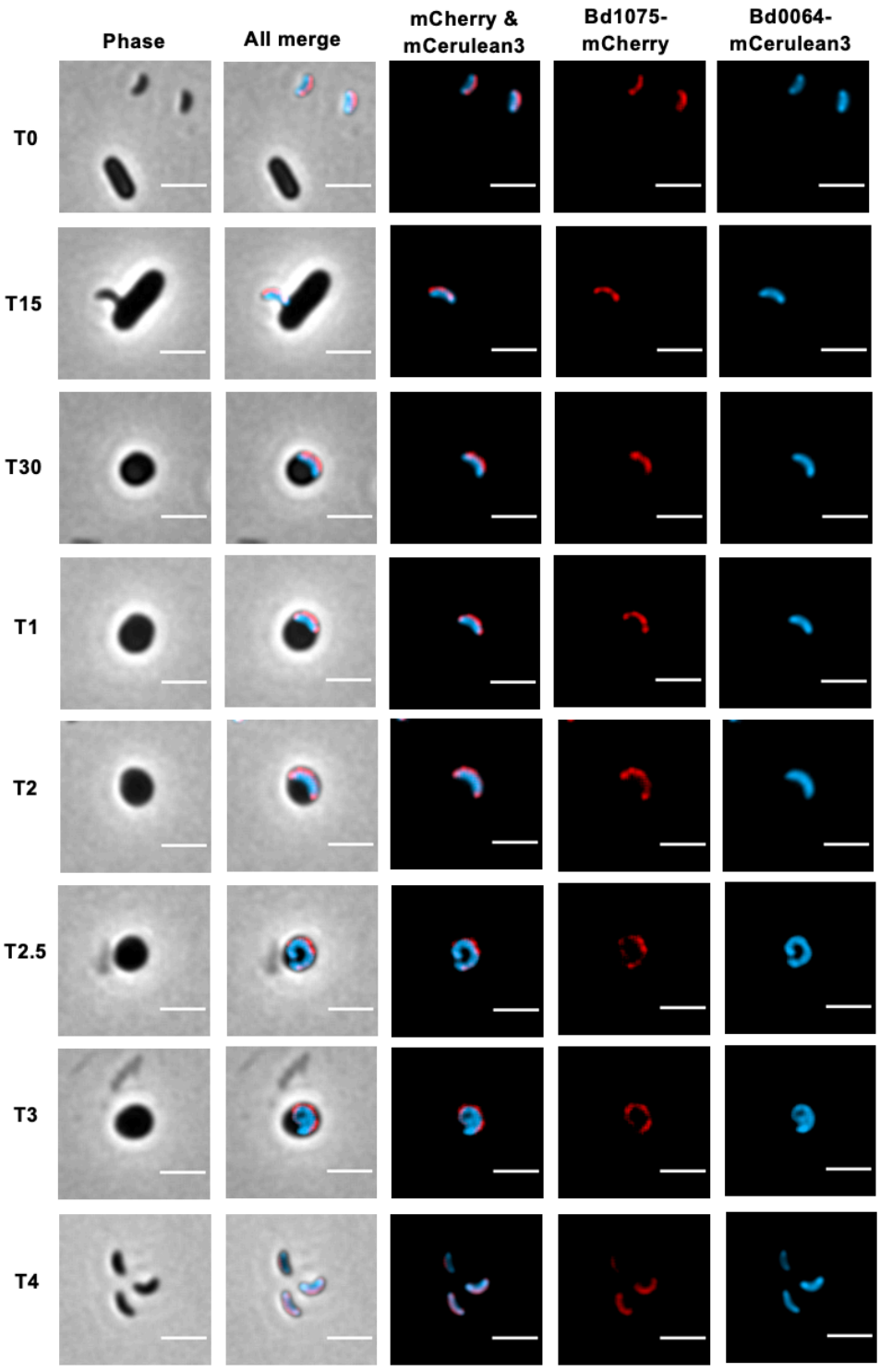

Figure 4.26. Bd1075 localises to the convex face throughout predation

Fluorescence microscopy images of a *B. bacteriovorus* strain containing chromosomal fluorescent fusions of both Bd1075-mCherry (double-crossover) and cytoplasmic protein fusion Bd0064-mCerulean3 (single-crossover) during a synchronous predatory cycle with *E. coli* (pZMR100) prey. T = min (0-30) or hours (1-4) since initial mixing of predators and prey. Scale bars = 2 μm and images are representative of three biological repeats.

4.3.6.2. Bd1075 localises to the periplasm of *B. bacteriovorus*

Thus far the data have shown that Bd1075 functions as an LD-CPase on the PG cell wall and that the fluorescent fusion Bd1075-mCherry localises to the outer convex cell face of *B. bacteriovorus* cells. Since the PG cell wall is in the bacterial periplasm and Bd1075 is predicted to contain a sec signal (Figure 4.5), Bd1075 should be translocated into the *B. bacteriovorus* periplasm. To test this experimentally, I decided to utilise the fact that there is a paucity of fluorophores that can fold and fluoresce within the bacterial periplasm. The fluorophore mCitrine is one of many fluorescent proteins that cannot fold in the periplasm in contrast to mCherry. To test the potential localisation of Bd1075 to the periplasm, two new strains were constructed: 1) Bd1075-mCitrine (single-crossover) and 2) Bd0064-mCitrine (single-crossover). If Bd1075 is periplasmic, then a fusion of Bd1075 to mCitrine should be unable to fluoresce whereas Bd0064-mCitrine should be fluorescent since Bd0064 is a cytoplasmic protein. Both strains were verified by Sanger sequencing to confirm correct insertion of the fusion protein and that no mutations had occurred which could affect fluorophore viability. While Bd0064-mCitrine was visible within attack-phase cells, the fusion Bd1075-mCitrine was not (in contrast to Bd1075-mCherry), indicating that Bd1075 localises to the bacterial periplasm (Figure 4.27). It would be helpful to further verify this by performing a western blot to confirm that the Bd1075-mCitrine fusion is successfully expressed and able to fold correctly.

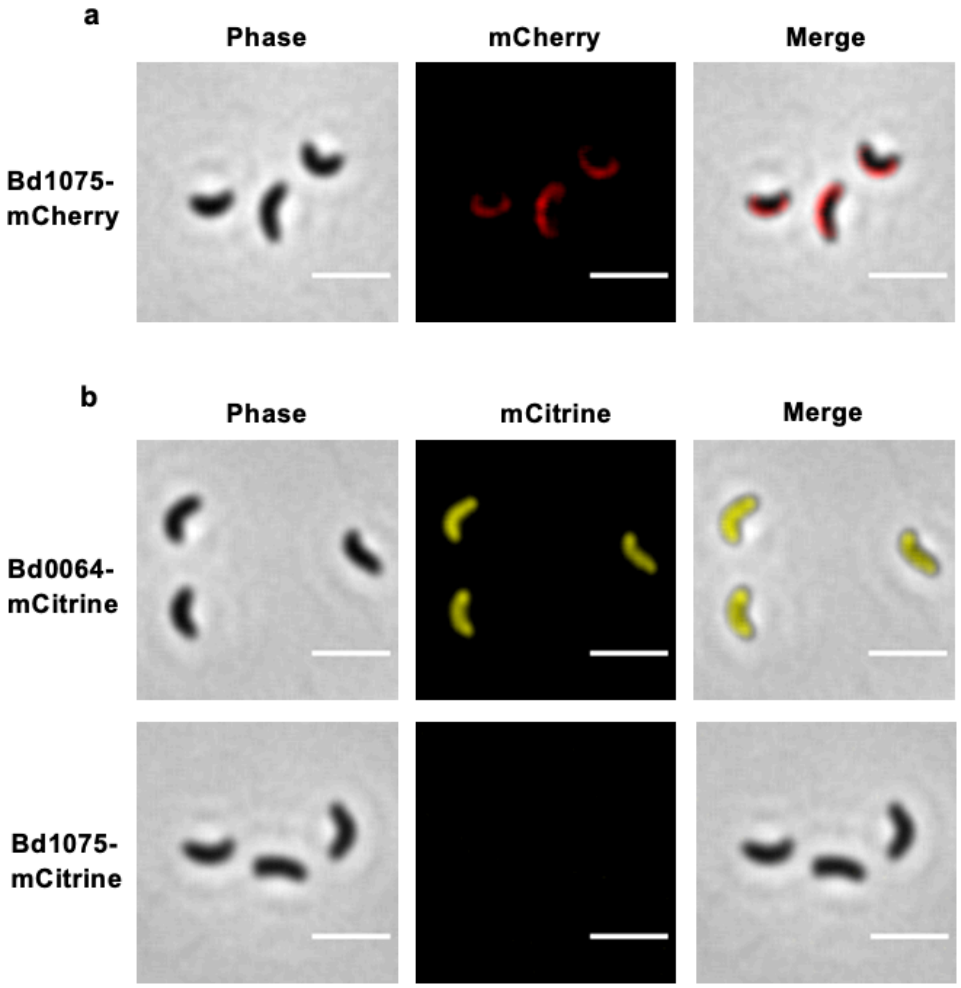

Figure 4.27. Periplasmic destination of Bd1075

Fluorescence microscopy images of *B. bacteriovorus* attack-phase cells containing either a Bd1075-mCherry single-crossover fusion **(a)** which is known to localise to the convex face of predator cells or a single-crossover fusion of the fluorophore mCitrine (which cannot fluoresce in the bacterial periplasm) to either the cytoplasmic protein Bd0064 or Bd1075 **(b)**. All *B. bacteriovorus* strains were sequenced to confirm the correct construction of each fluorescent fusion. Scale bars = 2 μm and images are representative of three biological repeats.

4.3.7. Bd1075 is targeted to the outer convex face by its NTF2-like domain

4.3.7.1. Targeting of Bd1075 to the convex face by its NTF2 domain

Periplasmic localisation of Bd1075-mCherry to the outer convex face of *B. bacteriovorus* predator cells raised the question of how the protein is targeted to just one lateral side of the cell. Unlike proteins which are targeted to the cell poles such as PopZ[273] and DivIVA[274], no mechanistic basis for protein targeting to a lateral side-wall could be found when searching the literature. Intrigued by this knowledge gap in bacterial protein localisation, I decided to use Bd1075 to provide some insight into how bacterial proteins may be targeted to just one lateral side-wall.

Hypothesising that the Bd1075 protein may contain a secondary targeting sequence or domain (in addition to the sec signal peptide which allows translocation into the periplasm), the fluorophore mCherry was fused to the C-terminus of five different Bd1075 protein variants (Figure 4.28). Each genetic construct contained 1 kb of DNA upstream from the *bd1075* gene. The protein variants were then introduced into the curved wild-type HD100 strain background via single-crossover recombination. Due to the presence of upstream DNA in each construct, homologous recombination resulted in new strains of *B. bacteriovorus* containing two copies of *bd1075*: the original untagged wild-type copy and the newly-introduced *bd1075* copy fused to mCherry. This ensured that the original wild-type copy was present and functional, thus generating curved predator cells. Following strain confirmation by Sanger sequencing, the subcellular localisation of each Bd1075-mCherry fusion was examined by fluorescence microscopy.

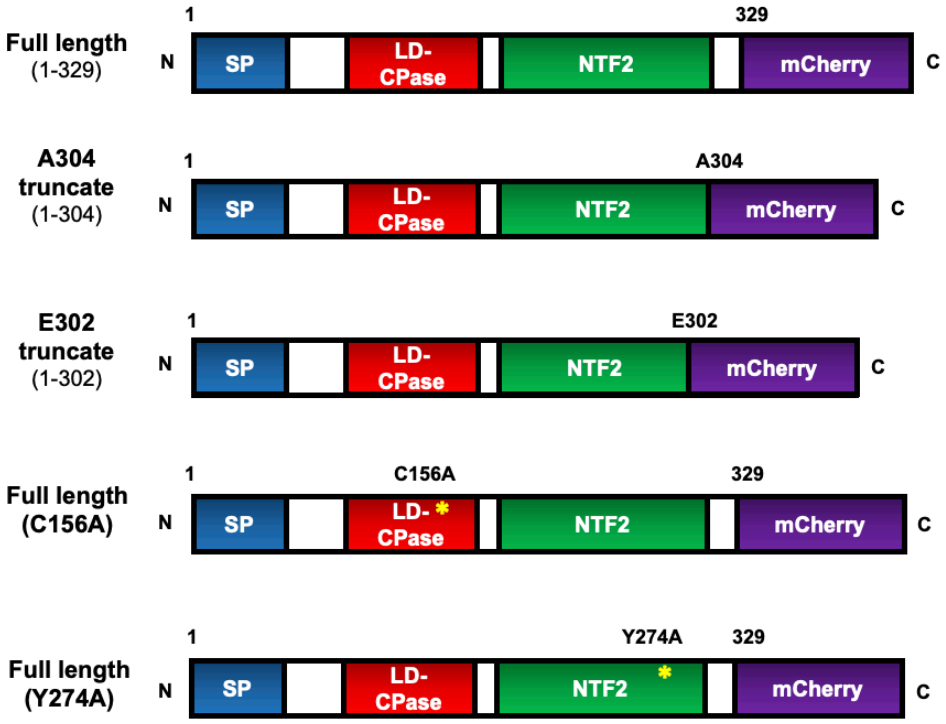

Figure 4.28. Bd1075-mCherry domain and point mutants

Schematics to show the five different variants of Bd1075 that were designed to test the localisation of Bd1075 to the outer convex face of *B. bacteriovorus* cells. Full length: The wild-type full length Bd1075 protein (residues 1-329) fused to mCherry. A304 truncate: Bd1075 protein which terminates at residue A304 fused to mCherry. E302 truncate: Bd1075 protein which terminates at residue E302 fused to mCherry. C156A: Full length Bd1075 protein containing a point mutation of C156A in the LD-CPase domain fused to mCherry. Y274A: Full length Bd1075 protein containing a point mutation of Y274A in the NTF2 domain fused to mCherry. Yellow asterisks indicate each point mutation. SP: sec signal peptide, LD-CPase: catalytic LD-carboxypeptidase domain, NTF2: nuclear transport factor 2-like domain, mCherry: fluorophore to which each protein variant was fused.

As expected, the full length Bd1075-mCherry protein localised to the outer convex face (Figure 4.29) and no deleterious effects were observed from the presence of two genomic copies of *bd1075*. The LD-CPase domain of Bd1075 contains three residues that form a catalytic triad: H141, A142 and C156. The catalytic triad cysteine (C156 of Bd1075) is critical for PG catalysis in Ldts[275, 276] some LD-CPases[270, 277]. To test whether the LD-CPase domain had a secondary role in protein targeting, the important C156 residue was mutated to alanine, creating the protein variant C156A-mCherry. The mutated protein variant was still capable of localisation to the outer curve, however, which indicates that the LD-CPase domain is not involved in protein localisation (Figure 4.29).

In addition to the catalytic LD-CPase domain, Bd1075 also contains a nuclear transport factor 2-like (NTF2) domain at the C-terminus (residues 196-304). NTF2 is a nuclear envelope protein that transports molecules into eukaryotic nuclei[278]. The NTF2-like domain protein superfamily is extremely broad, however, comprising many proteins from across the 3 domains of life and which are associated with over 200 different biological pathways[279]. Due to such diverse functions across species, it was not possible to predict a putative function for the NTF2-like domain of Bd1075 based on homology alone. Lacking an ascribed role, I hypothesised that the NTF2-like domain could function in protein targeting and therefore constructed three additional mCherry fusions:

1. Full length Bd1075 containing a point mutation (Y274A) in the NTF2 domain (the equivalent residue in the Csd6 NTF2 domain formed a key residue of the substrate-binding pocket).
2. A Bd1075 truncated variant which terminates at the residue E302 (two residues prior to completion of the NTF2 domain).
3. A Bd1075 truncated variant which terminates at the residue A304 (the natural end of the NTF2 domain).

Interestingly, neither the NTF2 point mutated variant Y274A-mCherry nor the NTF2 truncated variant E302-mCherry could localise to the outer

convex face and the fluorescence remained diffuse throughout the cell (Figure 4.29). In contrast, the variant A304-mCherry, which contains a complete wild-type NTF2 domain, localised correctly to the convex face (Figure 4.29).

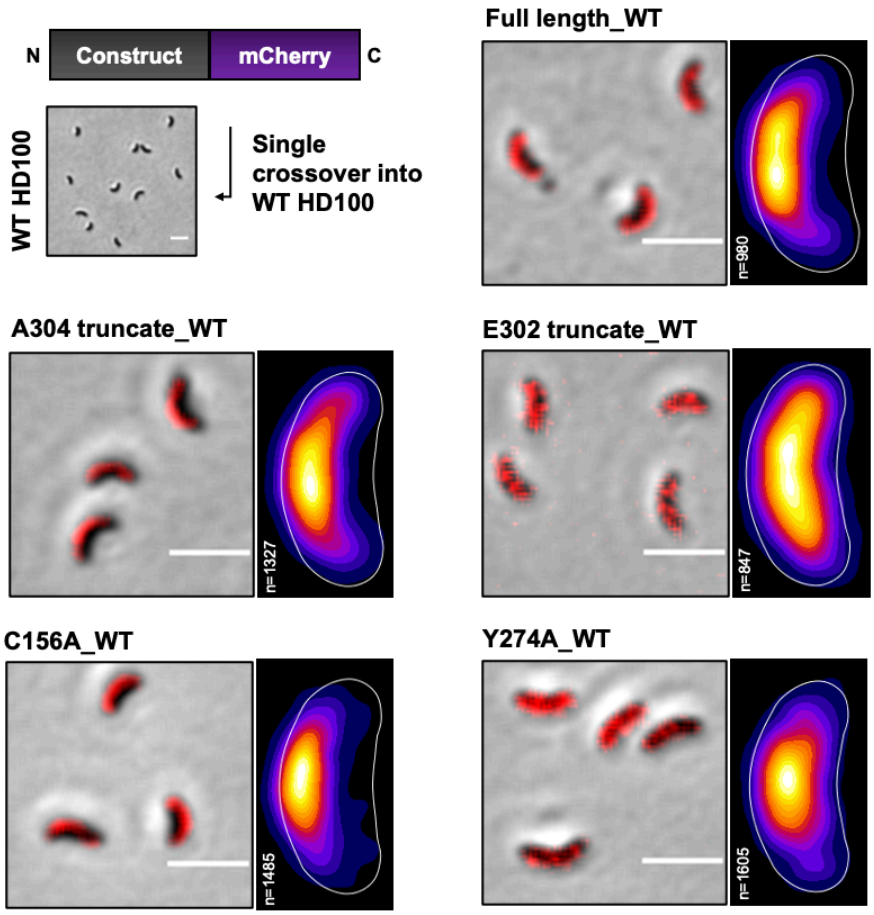

Figure 4.29. The NTF2 domain of Bd1075 targets the protein to the convex face

Top left: schematic of the construction of each *B. bacteriovorus* fluorescent strain. Fluorescent microscopy images of *B. bacteriovorus* attack-phase cells show the localisation of each Bd1075 protein variant. Adjacent heatmaps depict a representation of both the strain cell shape and location of Bd1075 foci across many cells (n = number of cells analysed). White-yellow: greatest foci intensity, purple-black: lowest foci intensity. Scale bars = 2 μm. Images and data to construct heatmaps were generated from three biological repeats.

These initial results strongly suggested that the previously cryptic NTF2 domain may have a role in the subcellular targeting of Bd1075 to the convex cell face.

4.3.7.2. Correct targeting to the convex face is required to generate cell curvature

I subsequently tested whether the specific localisation of Bd1075 at the outer curve of *B. bacteriovorus* cells is essential to generate cell curvature. To test this, the same five Bd1075-mCherry protein variants were introduced into the rod-shaped ∆*bd1075* mutant, resulting in strains that contain just one copy of *bd1075* - the newly introduced protein variant. Two outcomes were measured: subcellular localisation of the Bd1075-mCherry variant and whether rod-shaped morphology was cis-complemented.

The full length Bd1075-mCherry protein localised correctly to the outer curve (Figure 4.30) and also completely complemented the shape of ∆*bd1075*, restoring curvature to near wild-type levels (Figure 4.31). The LD-CPase domain point mutation C156A-mCherry failed to complement curvature as it was catalytically-inactive (Figure 4.31) and therefore had no convex face at which to localise, remaining diffuse within the cell (Figure 4.30). Importantly, neither the NTF2 domain point mutation Y274A-mCherry nor the NTF2 truncated variant E302-mCherry could localise to the outer convex cell face (Figure 4.30) and neither could complement the curvature of rod-shaped ∆*bd1075* cells (Figure 4.31).

Together, these experiments reveal that the C-terminal NTF2 domain of Bd1075 is responsible for the asymmetric targeting of Bd1075 to the convex face of *B. bacteriovorus* cells, and that correct targeting is required for the generation of cell curvature at one lateral side-wall.

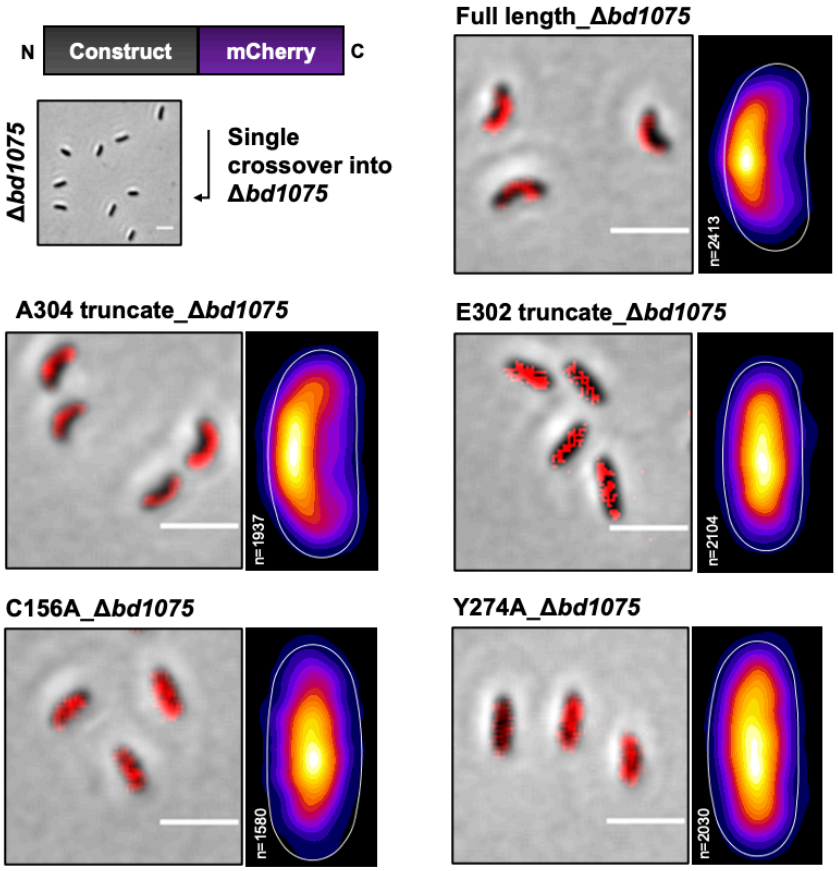

Figure 4.30. Bd1075 NTF2 domain mutants cannot localise to the convex cell face

Top left: schematic of the construction of each *B. bacteriovorus* fluorescent strain. Fluorescent microscopy images of *B. bacteriovorus* attack-phase cells show the localisation of each Bd1075 protein variant. Adjacent heatmaps depict a representation of both the strain cell shape and location of Bd1075 foci across many cells (n= number of cells analysed). White-yellow: greatest foci intensity, purple-black: lowest foci intensity. Scale bars = 2 μm. Images and data to construct heatmaps were generated from three biological repeats.

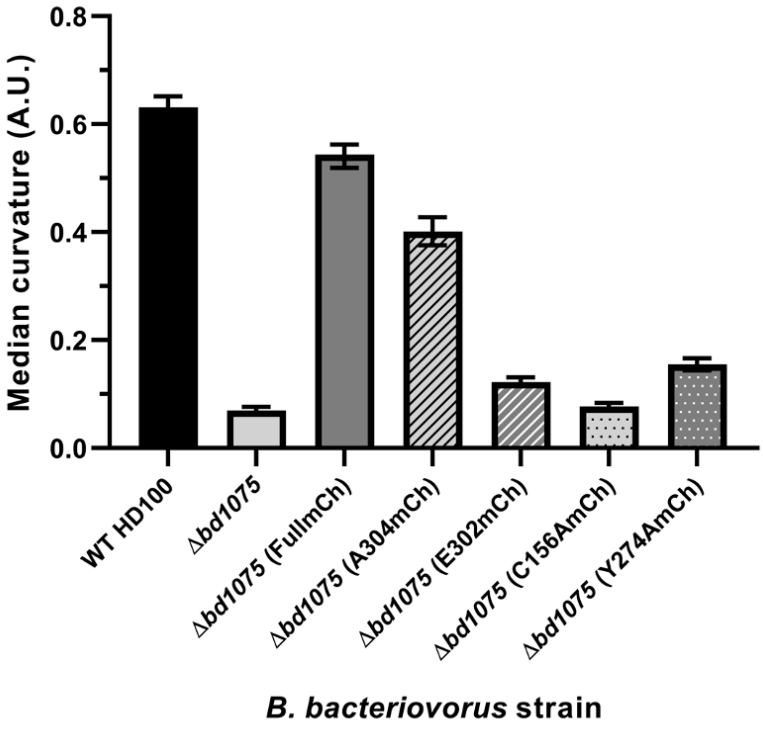

Figure 4.31. Bd1075 NTF2 domain mutants cannot restore Δ*bd1075* curvature by single-crossover cis-complementation

Curvature measurements of *B. bacteriovorus* Δ*bd1075* attack-phase cells containing different Bd1075-mCherry protein variants. n =1886-2812 cells per strain from three biological repeats. All comparisons between strains (except for Δ*bd1075* vs Δ*bd1075* (C156A-mCherry) were significant ($p<0.0001$, Kruskal-Wallis test).

4.3.8. Crystal structure of Bd1075

To understand the mechanism by which Bd1075 functions, I collaborated with Prof Andrew Lovering and his PhD student Mr Mauricio Valdivia-Delgado who succeeded in crystallising and solving the structure of Bd1075. The protein was first purified by Ni-NTA chromatography and then by size-exclusion chromatography which additionally revealed that the Bd1075 protein is monomeric (Figure 4.32). This contrasts with the LD-CPase cell shape proteins Csd6 from *H. pylori* and Pgp2 from *C. jejuni* which both form dimers[270, 277].

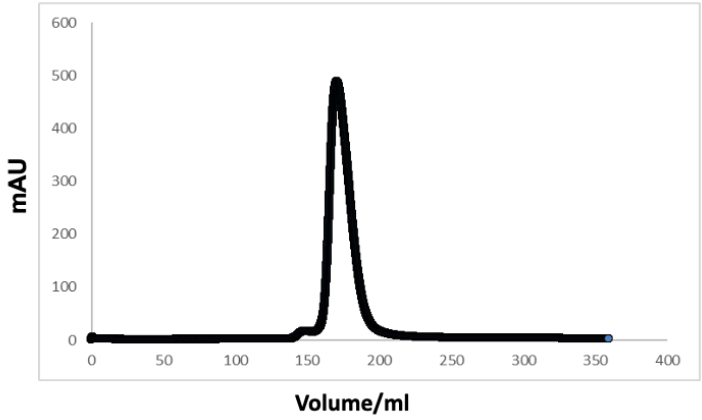

Figure 4.32. Bd1075 is a monomeric protein

Size-exclusion chromatography trace of Bd1075 protein purified on a Superdex 75 26/60 column. The profile shows a monodisperse peak at 170 ml corresponding to a monomeric Bd1075 protein. **Figure kindly provided by Mr Mauricio Valdivia-Delgado.**

The structure of Bd1075 was solved to a resolution of 1.34 Å and comprised residues 29-308 of the protein (Figure 4.33a), except for a highly flexible region (residues 82-91) which could not be seen in the structure and was termed the active site 'lid'. The crystal structure confirmed the presence of a consensus LD-CPase active site with the predicted and conserved catalytic triad residues H141, A142 and C156 present in expected orientations (Figure 4.33b).

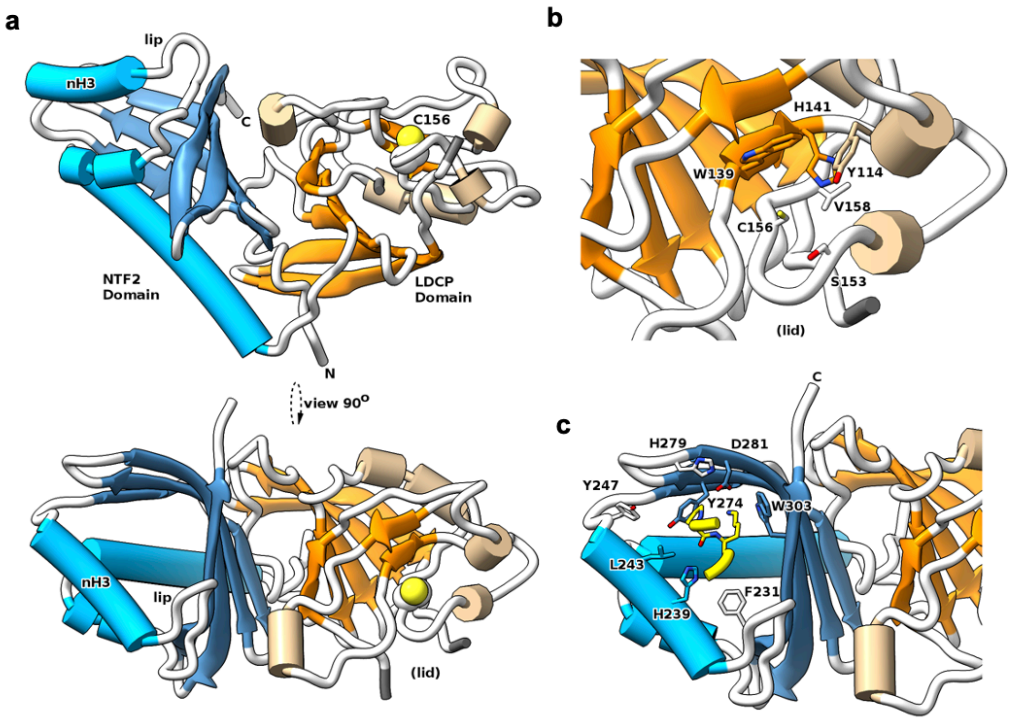

Figure 4.33. Crystal structure of Bd1075

a) Crystal structure of Bd1075 in two orthogonal views. The LD-CPase domain (orange), catalytic LD-CPase residue C156 (yellow space-fill form) and the NTF2 domain (blue) are shown. **b)** Close-up of the catalytic LD-CPase domain showing selected pocket-forming residues in stick-form. **c)** Close-up of the C-terminal NTF2 domain showing NTF2 residues packing around Y274 which forms the base of the domain pocket. **Figure kindly provided by Prof Andrew Lovering.**

Despite sharing an overall agreement in fold with the structures of Csd6 and Pgp2, the structure of Bd1075 contained several differences – particularly at the termini of the protein.

Firstly, the structure confirmed the previous size-exclusion data, showing that Bd1075 does not have a dimerisation domain at the protein N-terminus unlike Csd6 and Pgp2.

Secondly, Bd1075 has an extended C-terminus, with the NTF2 domain finishing with a longer beta strand (residues 295-306) which forms part of the NTF2 binding pocket (Figure 4.34a-b). The C-terminus continues for a further 21 amino acids but unfortunately these could not be crystallised as part of the structure – most probably due to being highly disordered. In **Section 4.3.7,** it was predicted (based on homology to Csd6) that Y274 may be an important NTF2 pocket residue and I showed that mutating Y274 to an alanine disrupted the targeting of Bd1075 to the outer convex cell face. The structure showed NTF2 domain amino acids packing around Y274 which forms the base of the NTF2 binding pocket, confirming the importance of this residue (Figure 4.33c).

Thirdly, and most importantly however, was the presence of a tryptophan residue (W303) within the pocket of the NTF2 domain (Figure 4.34b). This tryptophan is unusual as, despite being highly conserved among *Bdellovibrio* homologues, it is not found in the LD-CPase structures of Csd6 or Pgp2 since these proteins terminate that the residue equivalent to Bd1075^{E302}. The presence of this important W303 tryptophan within the crystal structure of Bd1075 helps to explain why the targeting test protein A304-mCherry could localise correctly to the outer curve but the E302-mCherry variant could not (Figure 4.29). W303 is evidently an essential residue for the function of the NTF2 domain, and consequently protein localisation and activity.

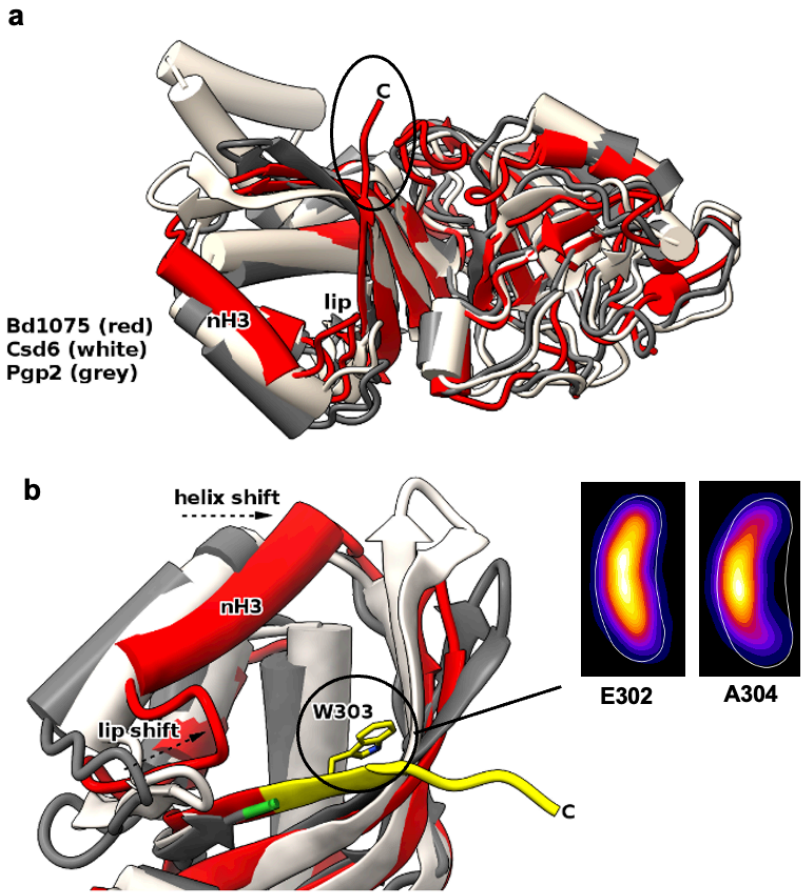

Figure 4.34. The NTF2 domain is extended and contains the important residue W303

a) Overall fold of Bd1075 (red, PDB: 7O21) overlaid onto the structures of Csd6 (white, PDB: 4XZZ) and Pgp2 (grey, PDB: 6XJ6). The unique, extended C-terminus of Bd1075 is circled in black. **b)** Close-up of the overlaid structure from **a** showing the Bd1075 NTF2 domain C-terminus (yellow) which is extended in comparison to the termini of Csd6 and Pgp2 (coloured green). The unique and critical NTF2 domain pocket residue W303 is circled in black. Bd1075-mCherry fluorescence heat maps are taken from Figure 4.29, highlighting that A302-mCherry can localise to the outer convex cell face but not E302-mCherry (which lacks the residue W303). The relative shifts of the Bd1075 nH3 helix and lip loop which constrict the NTF2 pocket are denoted by dashed arrows. **Figure kindly provided by Prof Andrew Lovering.**

4.4. Chapter discussion

Bd1075 is the first cell shape determinant to be discovered in predatory bacteria. In this chapter, the conservation, shape phenotype, enzymatic activity, localisation and crystal structure of Bd1075 were characterised, revealing new insights into the mechanism by which curvature is generated in *B. bacteriovorus* HD100.

Bd1075 is widely conserved across the *Bdellovibrio* genera which is suggestive of evolutionary importance (Figure 4.12). There are key differences in just three strains: the two epibiotic species *B. exovorus* and *Bdellovibrio* sp. Qaytius, and the closely-related strain *B. bacteriovorus* 109J. The epibiotic strains are distantly-related to intraperiplasmic *B. bacteriovorus* HD100 and contain two copies of *bd1075* – one of which is likely to be non-functional due to the absence of either a signal peptide or NTF2 domain (Figure 4.12). Phylogenetic studies suggest that epibiotic predation was the ancestral form of predation and that an invasive intraperiplasmic lifestyle derived from this[272]. It is therefore possible that the putative non-functional copy of *bd1075* was lost from the genome during the evolution of intraperiplasmic invasion.

B. bacteriovorus 109J is the only definitely non-curved strain of *Bdellovibrio* and contains a 57 amino acid truncation towards the N-terminus of Bd1075 (Pro21-Tyr74) (Figure 4.15). Genetic cross-complementation experiments and PG analysis revealed that $Bd1075_{109J}$ is an inactive enzyme and unable to generate cell curvature in strain 109J (Figure 4.17 and Figure 4.20). Historically, the strain was originally named *B. bacteriovorus* 109 but was re-designated as strain 109J following an observation by *Bdellovibrio* researcher Sydney Rittenberg[280]. Rittenberg noted that strain 109 used in Mortimer Starr's laboratory in Davis, California, USA had a curved morphology, but in Moshe Shilo's laboratory in Jerusalem, Israel, strain 109 was rod-shaped[280]. Mazal Varon, a researcher within Shilo's Jerusalem lab, suggested that the rod-shaped Jerusalem strain was a variant of the

original 109 strain and was “selected for by the procedures used in Shilo’s laboratory for maintaining the stock culture” [280]. Consequently, the curved strain was renamed 109D (for Davis) and the rod-shaped strain was renamed 109J (for Jerusalem)[280]. Unfortunately, stocks of strain 109D were eventually lost but 109J continues to be cultured by other *Bdellovibrio* labs around the world. While it is not possible to confidently conclude on the origins of rod-shaped 109J, if the mutation in *bd1075* arose due to long-term laboratory culture without regular freezing, then it is possible that laboratory conditions may favour rod-shaped predators over curved predators. The contribution of cell shape to *Bdellovibrio* predation is addressed in the next chapter.

In vibrio-shaped bacteria like *C. crescentus* and *V. cholerae*, vibrioid cell shape is determined by IF-like polymers that generate mechanical stress at the inner concave face to generate a bias in new PG insertion at the outer face[251, 252, 253]. Although *B. bacteriovorus* is also vibrio-shaped, Bd1075 functions differently to crescentin and CrvAB to generate cell curvature. Bd1075 had a predicted Ldt catalytic domain but instead functions as an LD-CPase, cleaving both crosslinked and uncrosslinked PG tetrapeptides to tripeptides (Figure 4.19 and Figure 4.22). A similar discrepancy was previously noted for LD-CPase shape proteins Csd6 (*H. pylori*) and Pgp2 (*C. jejuni*), highlighting the importance of biochemical validation of protein domain predictions[265, 270]. It is unclear exactly how LD-CPase activity leads to the generation of curvature or helicity, however, the reduction in tetrapeptides could reduce the availability of peptides for crosslinking reactions. This may reduce localised PG crosslinking, weaking the side-wall at which the enzyme localises and allowing either internal or external mechanical pressure to push upon the wall and create curvature. This idea is discussed further following the results of the next chapter.

Interestingly, while plasmid-based complementation of ∆*bd1075* by *bd1075*$_{HD100}$ only partially restored cell curvature (Figure 4.13), plasmid-based complementation also resulted in ‘over-complementation’ of the

Δ*bd1075* PG cell wall profile 'beyond wild-type', causing complete conversion of tetrapeptides to tripeptide and further conversion into dipeptides (Figure 4.19). This discrepancy was also observed for Csd6 and was due to an overabundance (2.1X increase) of the protein compared to the wild-type[257]. An excess of enzymatic activity resulting in 'over-complementation' of the PG wall profile but 'under-complementation' of cell curvature may cause imbalance and dysregulation of shape-generating enzymes like Csd6 and Bd1075.

Bd1075 localises to the periplasm of *B. bacteriovorus* (Figure 4.27). This is unsurprising for an LD-CPase that is catalytically-active on PG peptides which are located in the periplasm. It was surprisingly, however, that Bd1075 specifically localises to the outer convex face of *B. bacteriovorus* cells since the three vibrio shape-determinants crescentin, CrvA and CrvB all localise to the inner concave face[250, 252, 253]. CcmA, the cytoplasmic and non-enzymatic bactofilin of *H. pylori* is the only other shape protein known to localise to the outer face[263]. The previously cryptic NTF2 domain (for which no function could be predicted bioinformatically) targets Bd1075 to the outer convex face and targeting is essential for LD-CPase activity and the consequent generation of cell curvature (Figure 4.30 and Figure 4.31). Solving the structure of Bd1075 revealed key differences to the LD-CPase enzymes Csd6 and Pgp2 including divergent N- and C-termini and the unique NTF2 pocket residue W303 which is essential for localisation (Figure 4.30 and Figure 4.34).

NMR studies with the LD-CPase protein Pgp2 showed that Pgp2 could bind PG and that upon PG-binding, the major feature within the protein that shifted was a particular helix[277]. The corresponding helix in the structure of Bd1075 is labelled 'nH3' and it is the third helix within the NTF2 domain (residues 233-248). Interestingly, in comparison to Csd6 and Pgp2, both the nH3 helix of Bd1075 and an associated loop (called the 'lip', residues 226-232) are already shifted in relation to Pgp2 and Csd6 (Figure 4.34b). Due to overall similarities between Bd1075 and Pgp2, and the observation that the solved structure of Bd1075 exists in

a similar ‘PG-bound’ state to Pgp2, it is possible that Bd1075 might also bind PG. This would help to further explain how Bd1075 exerts LD-CPase activity on the PG wall, generating the curvature of *B. bacteriovorus*.

Chapter 5. The importance of *B. bacteriovorus* vibrioid cell shape

5.1. Chapter introduction

Bacteria exist in an extensive variety of shapes and sizes. In the previous chapter, the protein Bd1075 was identified and characterised as the cell curvature-determinant of *B. bacteriovorus*. Bd1075 generates the curvature of vibrio-shaped *B. bacteriovorus* predator cells and is highly conserved across *Bdellovibrio* bacteria, but why are *Bdellovibrio* predators curved? In this chapter, I will firstly introduce the benefits of cell shape in non-predatory bacteria and then describe my experiments which determine the unique roles of *B. bacteriovorus* cell curvature within bacterial predation.

5.1.1. Why do bacteria have different shapes?

Bacterial shape is evolutionary conserved which indicates that specific cell shapes have evolutionary importance and confer some fitness advantage(s) to bacterial species[281]. The benefits of different cell shapes (such as crescent-shaped *C. crescentus* and helical *H. pylori*) have been studied experimentally but there is much that remains unknown (Table 5.1). The four most well-characterised fitness advantages conferred by a specific cell shape or morphological transition between shapes are introduced below.

Table 5.1. The evolutionary importance of different bacterial shapes

The consequences of different bacterial shapes or shape transitions are detailed adjacent to example organisms which are representative of each morphology. The figure was adapted from Yang *et al*. (2016)[243] and icons were created in BioRender.

Morphology/feature	Examples	Shape consequence
Curvature		
	*Vibrio cholerae*	Increased swimming motility through dense gels. Increased colonisation during pathogenesis
	*Caulobacter crescentus*	Adapted to the force of moderate liquid flows, promoting microcolony formation
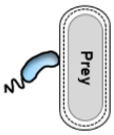	*Bdellovibrio bacteriovorus*	Unknown – to be studied in this chapter
Helicity		
	*Helicobacter pylori*	Increased swimming motility through viscous environments. Increased colonisation during pathogenesis
	*Campylobacter jejuni*	
Cell size increase/decrease		
	*Legionella pneumophila* Uropathogenic *E. coli*	Increased adherence to epithelia and stronger resistance against phagocytosis
	*Streptococcus pneumoniae*	Increased adherence to epithelia and stronger resistance against phagocytosis (size increase) or better resistance against complement-mediated killing (size decrease)

5.1.1.1. Adaptation to environmental conditions

The crescent-shaped *C. crescentus* - which is commonly found in freshwater lakes and streams - appears to have adopted a curved morphology to enhance fitness in these flowing environments[282]. In lakes and streams, *C. crescentus* cells adhere to cell surfaces via a strong holdfast at the tip of a stalked appendage, allowing *C. crescentus* cells to harvest dilute nutrients from the environment as they flow by[282].

Deletion of the shape-determinant crescentin, resulting in straight rods, does not cause any phenotypic disadvantage to the shape mutant under standard laboratory conditions[250]. Simulation of moderate flow against the stalked bacterium, however, revealed a difference between the curved wild-type and rod-shaped mutant[282]. When curved *C. crescentus* cells were exposed to the force of moderate liquid flow, the asymmetrically-dividing daughter cell could bend towards the cell surface, facilitating attachment of the new swarmer cell to the surface and preventing dispersal[282]. This also promotes the formation of microcolonies[282]. In contrast, the rod-shaped mutant did not display enhanced surface attachment[282]. This experiment suggested that curved *C. crescentus* cells can attach to surfaces more efficiently, perhaps better withstanding the pressure of water flow within freshwater streams and thus harvesting nutrients more efficiently[282].

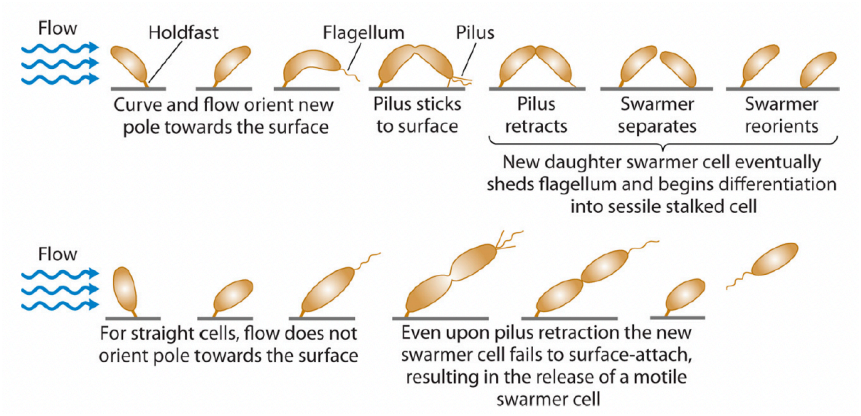

Figure 5.1. The shape of *Caulobacter crescentus* enhances surface colonisation under flow conditions

Under conditions of moderate flow, the curvature of crescent-shaped *C. crescentus* cells allows the dividing cell to re-orientate the new daughter cell towards the surface to which the stalked cell is attached. Pilus retraction then facilitates surface attachment of the new swarmer cell. The swarmer eventually differentiates into a stalked cell. Rod-shaped *C. crescentus* mutant cells are unable to re-orientate the daughter cell towards the surface and the new swarmer cell is instead released and dispersed. Figure reproduced from Yang *et al*. (2016)[243].

5.1.1.2. Efficiency of locomotion

For motile bacteria, the efficiency of different modes of motility can be important for survival. The impact of cell shape upon locomotion has been most studied for swimming motility but research progress thus far has been limited by the added complexity of bacterial appendages such as flagella – the number and placement of which can have major impacts upon swimming speeds. For example, the peritrichously-flagellated straight rod *E. coli* can reach higher swimming speeds in viscous media than the straight rod *Pseudomonas aeruginosa* (polar flagellum) or the straight rod *Spirillum serpens* (bipolar flagella)[283].

Separating the contribution of flagella placement and number towards swimming efficiency from cell shape had therefore been difficult until the isolation of genetic deletion shape mutants with wild-type flagellation patterns within the last decade. The straight rod mutants *H. pylori* Δ*csd4* and *C. jejuni* Δ*pgp1* both showed slower swimming motility through soft agar[256, 264] and the straight rod *H. pylori* Δ*csd6* mutant also had reduced motility through viscous gastric mucin solutions[284]. These studies suggested that helical shape contributes towards faster swimming speeds through more viscous media. This finding was not limited to helical bacteria; the *V. cholerae crvA* straight rod mutant also swam more slowly through high-density soft agar[252]. Swimming speeds in LB liquid or low-density soft agar gels did not differ from the wild-type, indicating that cell curvature facilitates traversal through viscous environments[252].

The straight rod morphology of both *Proteus mirabilis* and the archaeon *Haloferax volcanii* also appear advantageous for cell motility. A curved rod mutant of *P. mirabilis* retains its ability to differentiate into elongated swarmer cells, however the curved swarmer cells have poor swarming motility compared to wild-type straight rods[285]. *H. volcanii* cells are generally pleomorphic, existing in a variety of disc/plate shapes, but the archaeon can also differentiate into rod-shaped cells[286]. Deletion of the tubulin-like gene *cetZ1* disrupted this shape-differentiation and cells had

lower swimming speeds, suggesting that the differentiated rod-shaped form is most optimal for swimming[286].

A recent study hypothesised that cell shape may result from a trade-off between three different factors: swimming efficiency, chemotaxis and the cost of cell construction[287]. Using a simulation to test this hypothesis, the authors discovered that straight but slightly elongated rods were most efficient at swimming, however, slightly curved rods were most chemotactic and spherical bacteria had the lowest cell construction cost[287]. Although interesting, the study was limited to specific cell shapes and draws generalisations that may not apply to all bacteria – many of which will be influenced by their own unique properties and environmental niche.

5.1.1.3. Colonisation of the host during pathogenesis

Cell shape can also have an important impact on the virulence potential of animal and human bacterial pathogens. *H. pylori* and *C. jejuni* are helical pathogens which colonise the human gastrointestinal system[288]. The curved rod mutants Δ*csd1* and Δ*csd3* both showed reduced colonisation of the stomach[255, 289] and the straight rod mutant Δ*csd4* was out-competed by the helical wild-type in a mouse infection model[256]. Together, these data suggested that the helical shape of *H. pylori* facilitates colonisation of the stomach. Similarly to *H. pylori*, the straight rod mutants of *C. jejuni*, Δ*pgp1* and Δ*pgp2,* had reduced fitness in a chick colonisation model with the Δ*pgp1* mutant showing a 3-fold decrease in colonisation compared to the helical wild-type[264, 265].

To successfully establish an infection, *H. pylori* must escape from the highly acidic gastric lumen and traverse the gastric mucus layer to colonise the epithelial surface of the stomach[243]. It has been theorised that the helical shape of *H. pylori* may facilitate traversal through the mucus layer via a corkscrew motility model, however further studies are required to substantiate this assertion[243]. There is also considerable

heterogeneity in the shape of *H. pylori* cells from different clinical isolates which can vary in length and the degree of helicity[255]. This heterogeneity may allow *H. pylori* to optimally adapt its cell shape and tailor infection to individual gastric environments[255].

The human pathogen *V. cholerae* also causes gastrointestinal infection and the rod-shaped *crvA* mutant showed reduced colonisation of infant mice small intestines 20 h post-infection compared to the curved wild-type, demonstrating that cell curvature is important for virulence[252].

5.1.1.4. Morphological adaptations during pathogenesis

Bacteria can also undergo morphological changes to adapt their shape during infection such as alterations to cell size. Bacterial pathogens such as *Legionella pneumophila* can form filaments during infection which are more difficult for the human immune system to phagocytose[290]. Uropathogenic *E. coli* can also form filaments which are more resistant to immune system killing than single bacillus-shaped cells[291]. An increase in surface area can also facilitate bacterial attachment and adherence to host surfaces[292]. For example, the spherical Gram-positive bacterium *Streptococcus pneumoniae* can polymerise to form chains, with longer chains better adhering to respiratory epithelial cells than shorter chains[293]. Conversely, during systemic infection, *S. pneumoniae* reduces its chain length to aid in the avoidance of complement-mediated killing by the immune system[294]. This can, however, be counteracted by antibody-mediated agglutination of small chains into larger targets for presentation to the complement system[294].

5.1.1.5. Potential cell shape benefits in *B. bacteriovorus*

The predatory bacterium, *B. bacteriovorus* is not a pathogen, however, and it is possible that in this organism, cell curvature has consequences that are different to those discussed above. Due to the unusual predatory lifestyle of *B. bacteriovorus*, I hypothesised that curvature may have evolved to contribute some advantage(s) to predatory fitness. This hypothesis is investigated in the following sections.

5.2. Research aims

- To examine whether curvature confers an overall fitness benefit to curved wild-type *B. bacteriovorus* by comparing the ability of wild-type and Δ*bd1075* strains to prey on *E. coli* in forms of either liquid cultures or as a pre-grown biofilm.

- To determine whether curvature influences the rate at which the curved wild-type and the rod-shaped Δ*bd1075* mutant invade prey bacteria.

- To visualise the growth and replication of wild-type and Δ*bd1075* *B. bacteriovorus* predators inside prey bdelloplasts, assessing whether curved predators grow differently to rod-shaped predators within a spherical niche.

- To examine any differences in the stability of prey bdelloplasts containing either curved wild-type or rod-shaped Δ*bd1075* predator cells.

5.3. Chapter results

5.3.1. Predation on *E. coli* in liquid culture

Since cell shape is known to confer evolutionary fitness advantages in other bacteria, I speculated that the curvature of *B. bacteriovorus* cells may somehow be beneficial. As *B. bacteriovorus* is not a pathogen but instead a predator that can prey on pathogens by close access, I hypothesised that the specific vibrioid shape of *B. bacteriovorus* may increase the predatory efficiency of *B. bacteriovorus*.

To investigate this, the initial experiment simply aimed to compare the overall rate at which curved wild-type and rod-shape Δ*bd1075* predators kill *E. coli* prey within a liquid culture environment. The experimental design was based on an assay designed and optimised previously by Lambert *et al.* (2003)[166]. In brief, different dilutions of predator strains were mixed with a luminescent *E. coli* S17-1 strain in a 96 well plate format. The plate was incubated at 29 °C shaking inside a spectrophotometer which took luminescence readings each hour for 21 h. The luminescence of the *E. coli* prey initially increased for about 4 h as *E. coli* utilises the medium nutrients. After approximately 4 h, luminescence decreased due to *B. bacteriovorus* prey killing. Heat-killed predators mixed with *E. coli* served as a negative control and luminescence also decreased within these wells due to a general reduction in nutrient availability over time. Prey killing by the curved wild-type and the rod-shaped Δ*bd1075* mutant is shown in
Figure 5.2a.

5.3.1.1. Trialling assays to match *B. bacteriovorus* cell numbers between strains

One of the greatest challenges in *Bdellovibrio* research is to ensure that, for experiments which directly compare *B. bacteriovorus* strains, the concentration of each *B. bacteriovorus* strain is as closely matched as

possible. This is important because if one strain is much more concentrated than another, then it is difficult to draw any confident conclusions from the experimental outcome. For other bacteria, this is simply achieved by matching strains by optical density at OD_{600} prior to the experiment, however, due to the small size of *B. bacteriovorus* prey-dependent cells, optical density readings cannot be used to determine or match predator cell concentrations. Previously, our lab group has generally used the total protein content of *B. bacteriovorus* cells measured by a Markwell detergent-modified Lowry assay[162, 163] to match the concentration of predator strains. This method has limitations but was used in this luminescence experiment to match wild-type and Δ*bd1075* strains. The concentration of each strain is ultimately verified by plaque counts but these take approximately a week to appear following conclusion of the experiment.

5.3.1.2. Conclusions of predation on *E. coli* in liquid culture

The plaque count concentrations were plotted against the rate of luminescence decrease due to predator killing. The luminescence decrease was calculated by measuring the area under the prey death curve and normalising this to the maximum luminescence value reached (as this varied between samples). This created a graph which could be used to directly compare wild-type and Δ*bd1075* killing rates at different predator concentrations (
Figure 5.2b). The results were very variable (in part due to plaque count variation which is a normal phenomenon in *Bdellovibrio* research) despite performing five biological repeats. Nevertheless, it could be concluded that there was no significant difference between the rate at which curved wild-type and rod-shaped Δ*bd1075* predators kill *E. coli* in liquid culture.

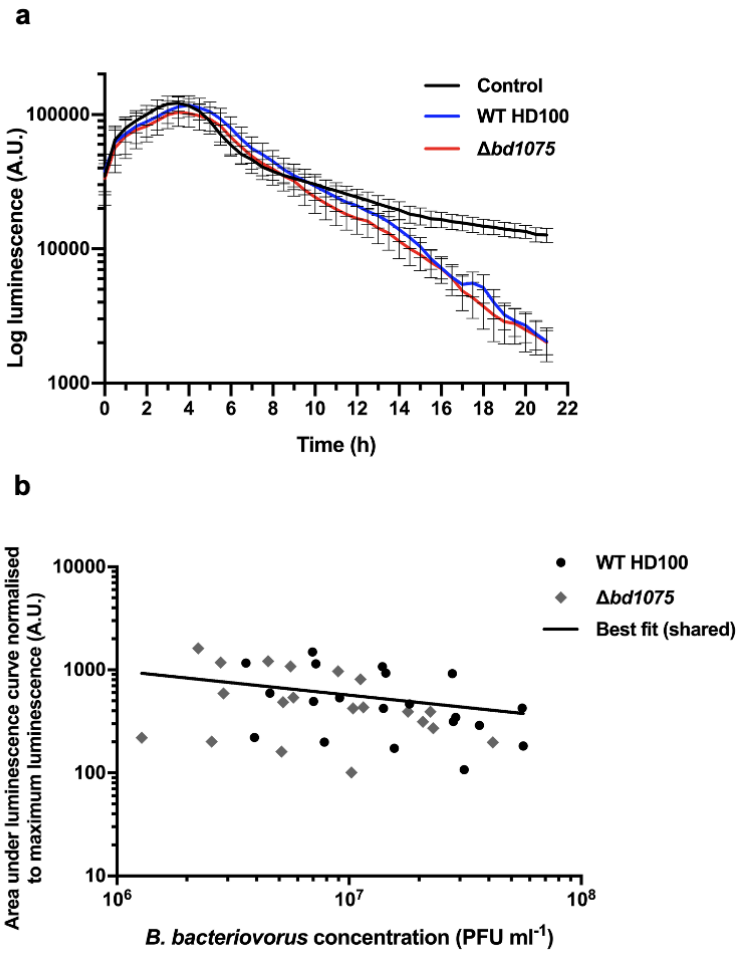

Figure 5.2. Predation on *E. coli* in liquid culture by *B. bacteriovorus* wild-type and Δ*bd1075*

Comparison of the rate at which *B. bacteriovorus* HD100 curved wild-type and rod-shaped Δ*bd1075* strains prey on a luminescent strain of *E. coli* S17-1 in liquid culture. **a)** Representative prey death curve showing WT HD100 (blue), Δ*bd1075* (red) and the heat-killed predator control (black). Prey death was measured by reduction in log luminescence readings which were taken every 30 min for 21 h. Error bars represent standard error of the mean. **b)** The area under each prey death curve was measured and normalised to the maximum luminescence value reached by each strain. This value is plotted against the concentration of each predator strain as determined by plaque counts. Black circles: WT HD100, grey diamonds: Δ*bd1075*. A line of best fit is shared between the two strains indicating that there was no significant difference in prey killing between the two ($p=0.70$). Data are taken from five biological repeats.

5.3.2. Predation on *E. coli* biofilms

Although there did not appear to be an immediate difference between the predation efficiency of wild-type and Δ*bd1075* strains in liquid culture, I could not exclude the possibility of a difference in a different predatory culture condition. Prey biofilms represent a different culture environment to liquid media as *Bdellovibrio* swimming motility for prey location may be more important in liquid, whereas predation on biofilms could involve a combination of swimming and gliding. The shape of *B. bacteriovorus* cells might also affect the ability of predator cells to penetrate layers of the prey biofilm. To investigate any potential difference, an experiment was performed to test the ability of curved wild-type and rod-shaped Δ*bd1075* predators to prey on pre-grown *E. coli* S17-1 biofilms. The experimental design was based on an assay developed by Lambert & Sockett (2013)[167] which was inspired by *Bdellovibrio* biofilm predation studies by the Kadouri group[168]. Briefly, *E. coli* S17-1 was grown as a biofilm a 96-well PV microtiter plate for 24 h. Different dilutions (10^0, 10^{-1}, 10^{-2} and 10^{-3}) of wild-type and Δ*bd1075* predators were then added to each well and incubated at 29 °C in a static incubator for a further 24 h. Plates were washed and stained with crystal violet dye which binds to biofilm material. Levels of remaining biofilm were quantified by readings taken at OD_{600} nm. *B. bacteriovorus* cells filtered through a 0.22 μm membrane (which does not let any bacterial cells through) served as a negative predation control. *B. bacteriovorus* cells were pre-matched by total protein content again but this time using a NanoOrange™ Protein Quantitation Kit to test whether this showed any improvement over the Lowry method. Generally, the accuracy was slightly improved with a less time-intensive protocol, representing a small improvement over the Lowry assay.

The results from this experiment did not signal any difference between the efficiency of wild-type and Δ*bd1075* predation on *E. coli* biofilms (Figure 5.3).

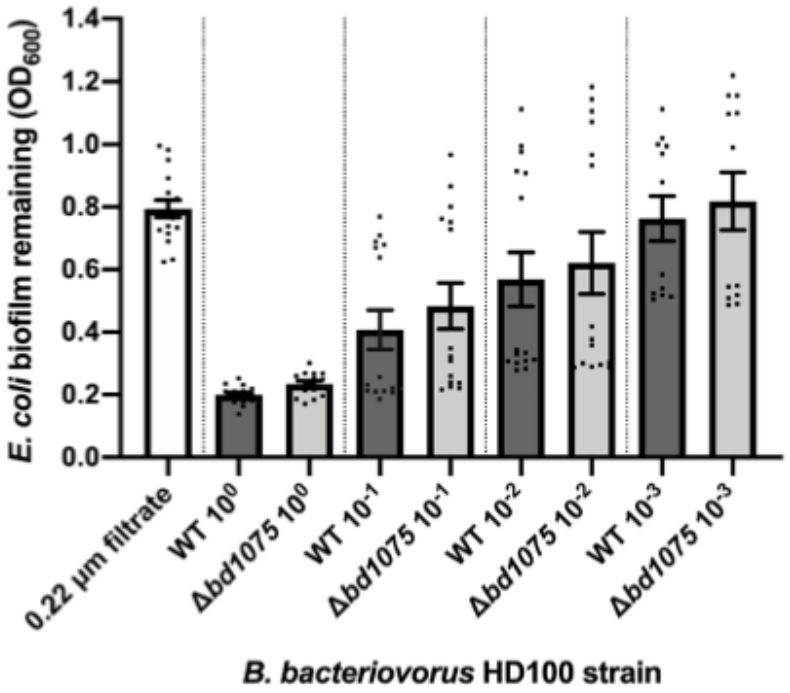

Figure 5.3. Predation on pre-grown *E. coli* biofilms by *B. bacteriovorus* wild-type and Δ*bd1075*

Comparison of *B. bacteriovorus* HD100 curved wild-type and rod-shaped Δ*bd1075* strain preying on pre-grown *E. coli* S17-1 biofilms in 96-well PVC microtiter plates. Predation was measured by the amount of *E. coli* biofilm (OD_{600}) remaining after incubation with predators for 24 h. 0.22 μm filtrate: A no-predator negative control. Neat (10^0), and diluted (10^{-1}, 10^{-2} and 10^{-3}) concentrations of *B. bacteriovorus* were tested and the two strains compared against each other. Data points show 15 technical replicates from 3 biological repeats. There was a small significant difference between WT and Δ*bd1075* at 10^0 (p=0.01, unpaired t-test), however, plaque counts showed that 1.4-2X more WT than Δ*bd1075* was added, therefore this was not considered biologically meaningful. No other comparisons were significant (p>0.05, Mann-Whitney test).

5.3.3. Rod-shaped predators enter prey more slowly than the curved wild-type

The previous two experiments were informative in showing that there was no difference between the efficiency with which curved wild-type and rod-shaped mutant predators preyed on *E. coli*. It is important to note, however, that these experiments compared the overall gross predation rate between strains which is affected by multiple factors: prey location, invasion, growth, and replication.

I wondered whether a more subtle phenotype – for example a difference in the individual stages of prey invasion or intracellular growth might be masked by simple comparisons of overall gross predation which is a four-hour process affected by many enzymes. Considering this, I decided to study predator-prey encounters at the single-cell level. This involved the use of time-lapse microscopy to measure two different parameters: 1) duration of predator-prey attachment and 2) duration of prey entry – which together comprise the prey invasion stage of the predatory lifecycle (Figure 5.4). Curved wild-type or rod-shaped Δ*bd1075* predators were mixed with *E. coli* S17-1 and applied to an agarose slide. Six regions of view were re-visited by the microscope each minute to create a time-lapse video of predators invading prey. From these videos, attachment and entry times were measured. Attachment time was defined as the number of frames (where 1 frame = 1 min) between initial predator-prey contact and the predator starting to physically move into the prey cell. Entry time was defined as the number of frames between initial traversal into prey and completion of prey entry which was signified by the predator residing completely inside the prey bdelloplast. As predation occurs in 3 dimensions but can only be visualised in 2D on an agarose pad, there is the possibility that some predator cells may not be within the focal imaging plane during prey invasion. To mitigate this possibility, only invasion events in which the *B. bacteriovorus* predator cell was continuously within the focal plane were analysed. Examples of predatory invasion time-lapse stills are shown in Figure 5.5.

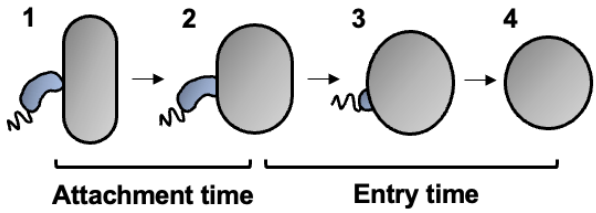

Figure 5.4. Schematic to show how rates of *B. bacteriovorus* prey invasion were measured

Schematic detailing how *B. bacteriovorus* attachment time and entry time into *E. coli* were measured by time-lapse microscopy. Attachment time was defined as the number of frames (1 frame = 1 min) between initial predator contact with the prey surface and the predator beginning to visibly move into the prey (stages 1-2). Entry time was defined as the number of frames between initial traversal into prey and the predator residing completely inside the rounded prey bdelloplast without any visible predatory tail extruding from the bdelloplast (stages 2-3).

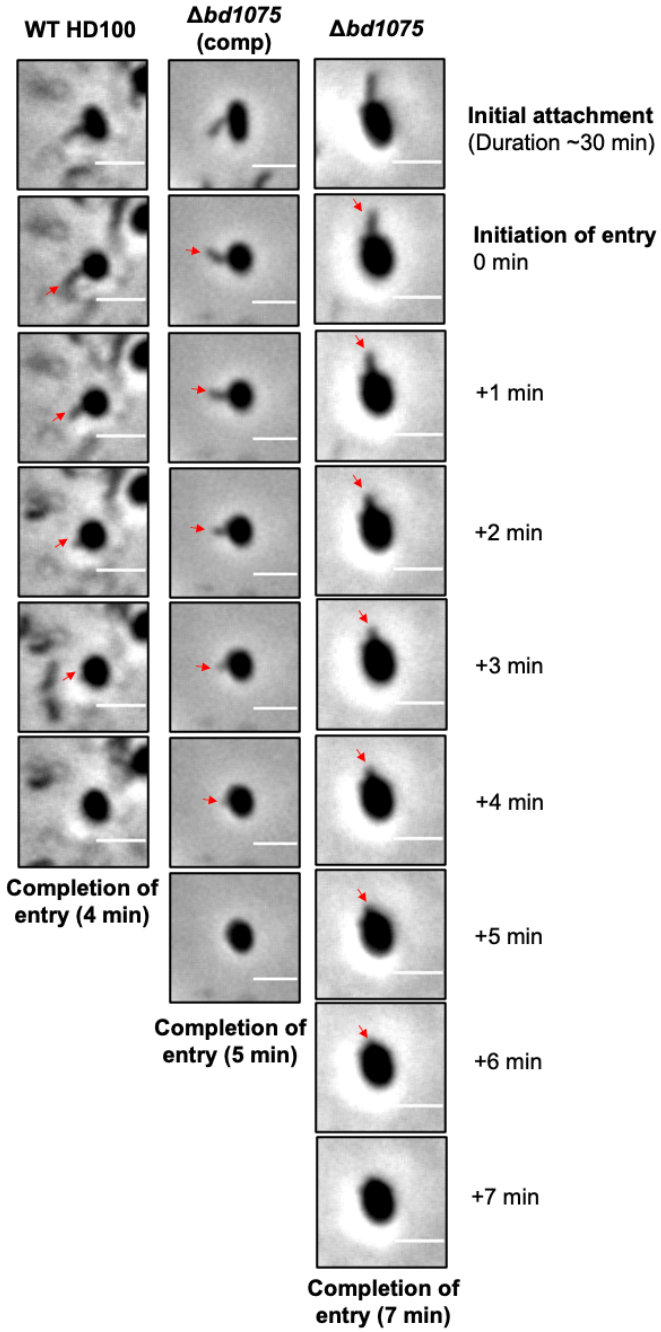

Figure 5.5. Time-lapse microscopy stills of prey invasion by different *B. bacteriovorus* strains

Time-lapse microscopy frame stills of a single prey invasion by three different strains of *B. bacteriovorus* HD00: 1) wild-type, 2) Δ*bd1075* complemented with a chromosomal copy of *bd1075* and 3) Δ*bd1075* deletion mutant. The frame at which initial predator-prey attachment occurred is shown on the top row. Each frame below shows predator entry into prey, lasting from 4 min (wild-type) up to 7 min (Δ*bd1075*). Red arrows indicate the visibility of the predator cell outside of the prey. Invasion events are representative of 90 total invasions from 3 biological repeats with 30 cells analysed from each repeat.

There was no significant difference (p=0.46) in the attachment time between the wild-type (median 28.5 min, 95% CI [28.0, 29.0]) and Δ*bd1075* (median 29.5 min, 95% CI [29.0, 30.0]) (Figure 5.6a). There was, however, a significant difference (p<0.0001) between the entry time of curved wild-type predators (median 4.0 min, 95% CI [4.0, 5.0]) and rod-shaped Δ*bd1075* predators (median 6.0 min, 95% CI [5.0, 6.0]) (Figure 5.6b). Moreover, 35.6% of Δ*bd1075* invasions lasted ≥ 7 min and the longest measured 14 min. In comparison, just one wild-type invasion lasted ≥ 7 min.

Despite the significant difference between the strains, the difference in minutes is relatively small. Therefore, to fairly test our confidence in this finding, the Δ*bd1075* deletion mutant was complemented by re-introduction of the *bd1075* gene via single-crossover homologous recombination into the Δ*bd1075* chromosome. The cell curvature of this new strain Δ*bd1075* (cis-comp) returned to near-wild-type levels (Figure 5.7), again indicating that cis-complementation by re-introducing the gene into the genome was more effective than the plasmid-based trans-complementation carried out previously (Figure 4.13). The *B. bacteriovorus* strain Δ*bd1075* (cis-comp) did not significantly differ in attachment time from either the wild-type or Δ*bd1075* (Figure 5.6a). The complemented strain entered prey in a median time of 5.0 min (95% CI [4.0, 5.0]) which was significantly faster than Δ*bd1075* and not significantly different from the wild-type (Figure 5.6b).

These data suggest that the curvature of *B. bacteriovorus* predator cells facilitates a more rapid invasion of predators into the intraperiplasmic compartment of rounded prey.

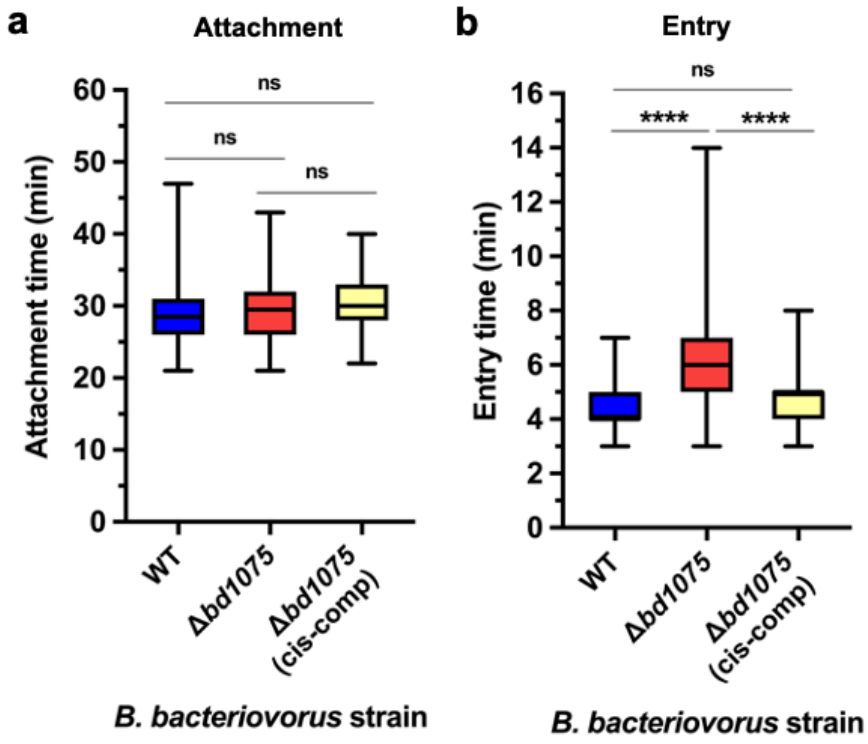

Figure 5.6. Prey attachment and entry times for different *B. bacteriovorus* strains

Duration of *B. bacteriovorus* attachment to **(a)** and entry into **(b)** *E. coli* S17-1 prey measured by time-lapse microscopy for wild-type, Δ*bd1075*, and Δ*bd1075* (cis-comp) – the Δ*bd1075* mutant complemented with a chromosomal copy of *bd1075* by single-crossover homologous recombination into the Δ*bd1075* genome. Attachment time was defined as the number of frames (each frame = 1 min) between initial predator-prey attachment and the predator starting to enter prey. Entry time was defined as the number of frames between the predator starting to enter prey and residing completely inside the prey bdelloplast. Box: 25th-75th percentiles, whiskers: range min-max, box line: median. ns: non-significant ($p>0.05$; Kruskal-Wallis test), **** ($p<0.0001$; Kruskal-Wallis test). n = 90 prey cell invasion events from three biological repeats where 30 cells were analysed from each repeat.

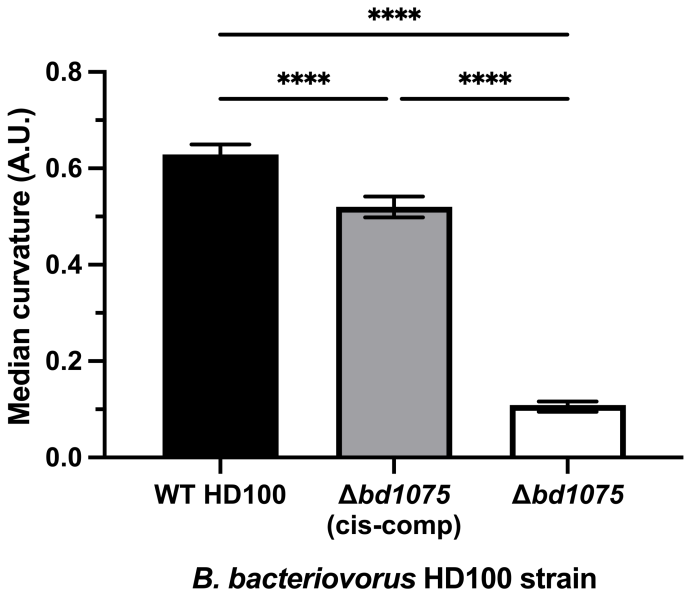

Figure 5.7. Single-crossover cis-complementation of Δ*bd1075* restores curvature to near-wild-type levels

Cell curvature measurements of *B. bacteriovorus* attack-phase cells of the strain Δ*bd1075* (cis-comp) – a strain of Δ*bd1075* complemented by single-crossover re-introduction of the *bd1075* gene into the genome by homologous recombination – compared to wild-type and Δ*bd1075* strains. n = 1129-1664 cells per strain from three biological repeats. Error bars represent 95% confidence intervals of the median. **** ($p<0.0001$; Kruskal-Wallis test).

5.3.4. Rod-shaped predators become curved inside bdelloplasts but exit as rods

Following invasion into prey, *B. bacteriovorus* predator cells grow inside the prey cell, elongating for approximately 3.5 hours. As rod-shaped prey like *E. coli* are sculpted into spherical bdelloplasts during prey invasion, I was intrigued to know how the non-curved Δ*bd1075 B. bacteriovorus* strain would grow inside prey in comparison to the curved wild-type.

To investigate this, each *B. bacteriovorus* strain had to be visible inside prey bdelloplasts during a timecourse of predation, therefore the cytoplasmic-labelling construct Bd0064-mCerulean3 was generated and introduced by single-crossover recombination into the genomes of both the wild-type and Δ*bd1075* strains.

The fluorescently-labelled *B. bacteriovorus* strains were mixed with *E. coli* S17-1 (pZMR100) and incubated at 29 °C, shaking, commencing a synchronous predatory cycle. Images were taken at different timepoints to visualise predator growth inside prey. Curved wild-type predators slowly elongated as a curved filament inside prey, before septating at 3 h and lysing the prey at 4 h (Figure 5.8a). Interestingly, rod-shaped Δ*bd1075* predators entered prey as rods but after 1 h, as the predator begins to grow, the cellular filament started to become curved inside the prey (Figure 5.8a). Despite a visible increase in curvature during intra-bdelloplast growth, the Δ*bd1075* strain did not curve as tightly as the wild-type strain (Figure 5.8b) and the Δ*bd1075* filament septated to give rod-shaped progeny which lysed the prey host at 4 h, producing attack-phase rod-shaped predators (Figure 5.8a).

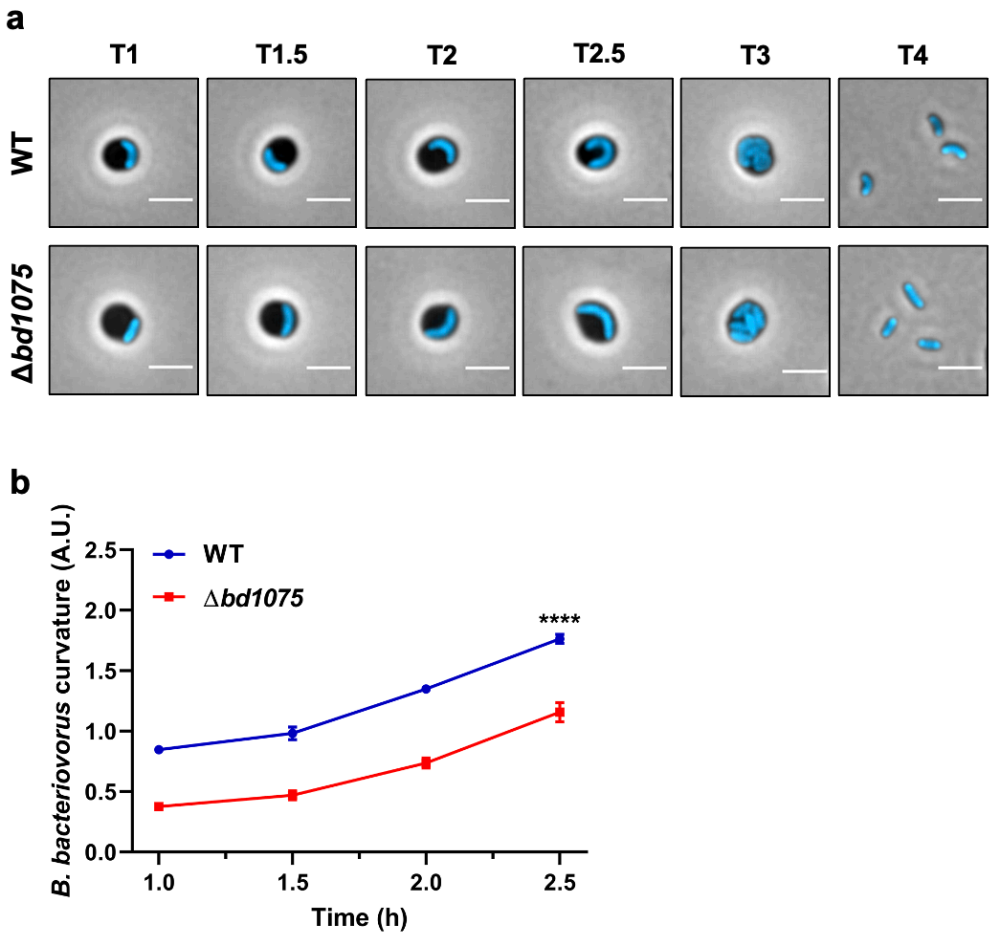

Figure 5.8. Growth of *B. bacteriovorus* wild-type and Δ*bd1075* inside *E. coli* prey

a) Images of *B. bacteriovorus* curved wild-type (top) and rod-shaped Δ*bd1075* mutant (below) predators growing inside *E. coli* S17-1 (pZMR100) prey bdelloplasts. *B. bacteriovorus* strains contain a cytoplasmic fusion of Bd0064-mCerulean3 to allow visualisation of predators inside prey. T = hours elapsed since predator-prey mixing. Scale bars = 2 μm and images are representative of three biological repeats. **b)** Curvature of wild-type (blue line) and Δ*bd1075* (red line) *B. bacteriovorus* strains inside prey bdelloplasts during predation as show in **a**. T = hours elapsed since predator-prey mixing. n = 134-250 cells per strain and per timepoint from three biological repeats. Error bars represent standard error of the mean. **** ($p<0.0001$; Mann-Whitney test).

5.3.5. Rod-shaped predators can stretch and deform prey bdelloplasts

The most striking visible difference, however, was the presence of a sub-set of *E. coli* prey bdelloplasts containing Δ*bd1075* predators that appeared particularly stretched and deformed by the growing *B. bacteriovorus* filament 2.5 h after predators and prey were mixed (Figure 5.9). To estimate the proportion of Δ*bd1075* cells that generated stretched bdelloplasts, the sub-set was defined as prey bdelloplasts with a circularity value of ≤0.96. This cut-off value was chosen based on visual observation of many bdelloplasts and the fact that no prey containing the wild-type strain had a circularity of ≤0.96. This classification system revealed that approximately 9.2% of Δ*bd1075* predator cells stretched and deformed the prey bdelloplast.

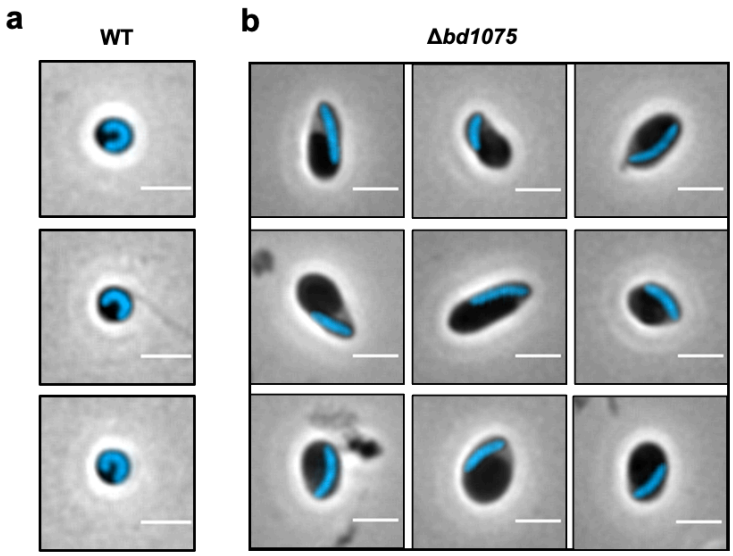

Figure 5.9. Bdelloplasts stretched by Δ*bd1075* predator cells compared to wild-type-invaded bdelloplasts at 2.5 h into predation

Examples of *E. coli* S17-1 (pZMR100) prey bdelloplasts containing either **a**) *B. bacteriovorus* wild-type predators or **b**) Δ*bd1075* predator cells where the bdelloplasts appeared particularly stretched and deformed by the growing Δ*bd1075* filament 2.5 h after predators and prey were mixed. *B. bacteriovorus* strains contain a fusion of Bd0064-mCerulean3 to label the predator cytoplasm and allow visualisation of intraperiplasmic predator cells. Scale bars = 2 μm and images are taken from three biological repeats.

To determine whether the overall population of bdelloplasts containing Δ*bd1075* predators was misshapen by the elongated predator filament, measurements of area, circularity, length, and width were taken from 1 h to 2.5 h during predation (Figure 5.10). Between 1 h and 2 h, the shapes of bdelloplasts containing either the wild-type or Δ*bd1075* strain did not markedly differ. However, at 2.5 h, when the *B. bacteriovorus* cell filament is nearing maximal elongation, the area of bdelloplasts containing Δ*bd1075* predators was significantly higher than bdelloplasts containing wild-type predators ($p<0.01$; Figure 5.10a), and the circularity was significantly lower ($p<0.05$; Figure 5.10b). In addition, the length of prey bdelloplasts containing Δ*bd1075* predators was significantly longer ($p<0.01$; Figure 5.10c) and the width did not significantly change (Figure 5.10a), consistent with the appearance of stretched bdelloplasts.

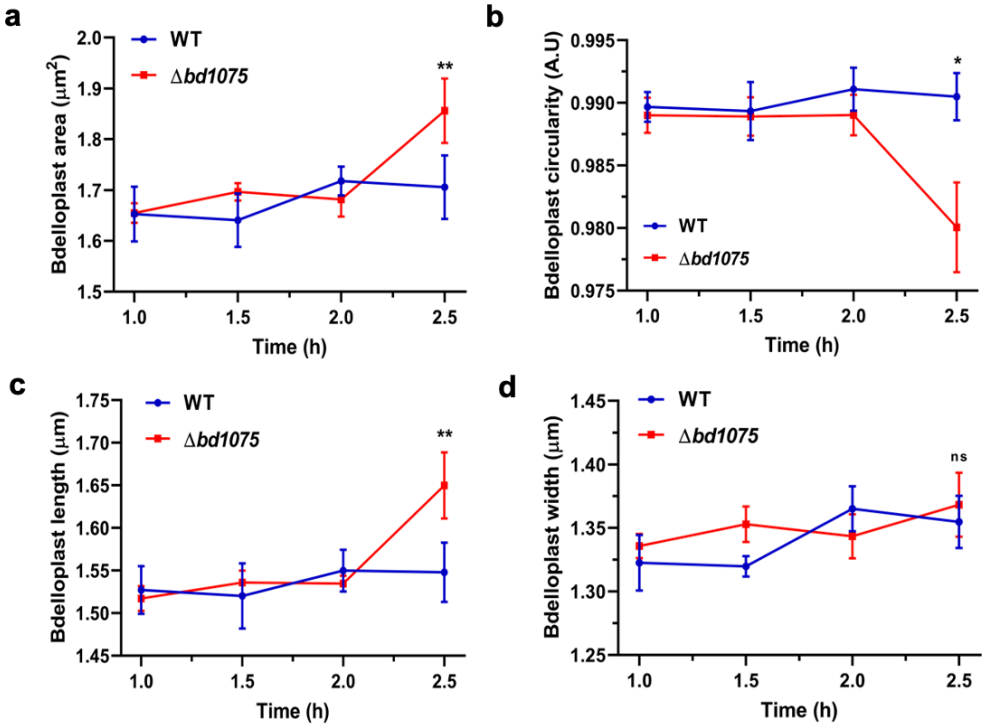

Figure 5.10. Morphology of bdelloplasts containing wild-type or Δ*bd1075* predators as the predatory lifecycle progresses

Area (**a**), circularity (**b**), length (**c**) and width (**d**) measurements of *E. coli* S17-1 (pZMR100) prey bdelloplasts containing either *B. bacteriovorus* wild-type (blue line) or Δ*bd1075* mutant (red line) predators. T = hours elapsed since predator-prey mixing. n = 134-250 cells per strain and per timepoint from three biological repeats. Error bars represent standard error of the mean. ns: non-significant ($p>0.05$), * ($p<0.05$), ** ($p<0.01$); Mann-Whitney tests.

From these observations, it appears that Δ*bd1075* adopts a temporary curvature inside the bdelloplast which may be generated by the inward mechanical forces imposed upon the predator cell by growth inside a confined spherical environment. This was most visible in the first 2 h of the predatory lifecycle. Later at 2.5 h (in ~ 9.2% of cases), however, the elongated Δ*bd1075* predator filament appears to be generating outward mechanical pressure upon the bdelloplast wall, causing the prey bdelloplast to become stretched and misshapen.

Collectively, the data suggest that curved wild-type predators may more optimally ‘fit into’ a spherical prey niche than rod-shaped predators.

5.3.6. Investigating the stability of bdelloplasts containing rod-shaped predators

5.3.6.1. Previous work showed that LD-transpeptidases reinforce the prey bdelloplast by utilising a bdelloplast damage assay

Stretching of prey bdelloplasts by rod-shaped Δ*bd1075* predators could potentially damage the prey cell. This would probably be deleterious to *B. bacteriovorus* predators which require a stable niche within which to replicate and complete their lifecycle. Stability of prey bdelloplasts has been studied by Kuru, Lambert *et al*., (2017) who discovered that the PG wall of prey bdelloplasts is altered during predation, with maximal modification occurring at 45 min (measured via incorporation of HADA pulses)[33].

B. bacteriovorus HD100 encodes at least 19 LD-transpeptidases but the Ldts *bd0886* and *bd1176* were both upregulated at 15-30 min and therefore strong candidates for this action on the prey wall at 45 min[33, 295]. During predation by a double Δ*bd0886*Δ*bd1176* deletion mutant, approximately 2-4 fold less HADA signal was incorporated into the prey bdelloplast at 45 min compared to the wild-type strain, suggesting that these two Ldt enzymes were largely responsible for Ldt-mediated PG modification of prey cells[33].

Hypothesising that Ldt activity may confer rigidity to bdelloplasts, the authors tested the stability of prey bdelloplasts at 1 h during predation and compared the wild-type strain and mutant strain Δ*bd0886*Δ*bd1176* by using the β-galactosidase substrate chlorophenyl red-β-D-galactopyranoside (CPRG). β-galactosidase hydrolyses the yellow-orange CPRG substrate into the dark red product chlorophenol red. Addition of CPRG therefore acts as a read-out for leakage of bdelloplast contents including β-galactosidase into the surrounding culture medium. When subjected to either osmotic upshock, downshock, or centrifugal/resuspension shock alone, bdelloplasts invaded by

∆*bd0886*∆*bd1176* produced significantly more chlorophenol red – as measured by absorbance at 574 nm[33]. This suggested that the two Ldts strengthen prey bdelloplasts at an early stage during predation.

5.3.6.2. Construction of a triple *B. bacteriovorus* deletion mutant to test bdelloplast stability

To test whether rod-shaped ∆*bd1075* predators damage bdelloplasts, a similar methodology was employed. A new strain was also constructed for the experiment: a triple deletion mutant of ∆*bd1075*∆*bd0886*∆*bd1176* since this strain may potentially produce weaker and less stable bdelloplasts than the single ∆*bd1075* mutant alone.

To obtain a deletion mutant in *B. bacteriovorus*, it is very uncommon to require PCR screening of greater than 100 kanamycin-sensitive exconjugant clones (the single ∆*bd1075* deletion was obtained following 50 PCR reactions) and can indicate that the gene is essential for predation and is therefore impossible to delete. To confirm if this was the case for this triple deletion attempt, further extensive screening of potential mutants was performed, and after 350 PCR reactions, a triple deletion mutant of ∆*bd1075*∆*bd0886*∆*bd1176* was obtained (Figure 5.11). Due to the difficulty of generating the genetic knockout, the new strain was verified by whole-genome sequencing in addition to standard Sanger sequencing.

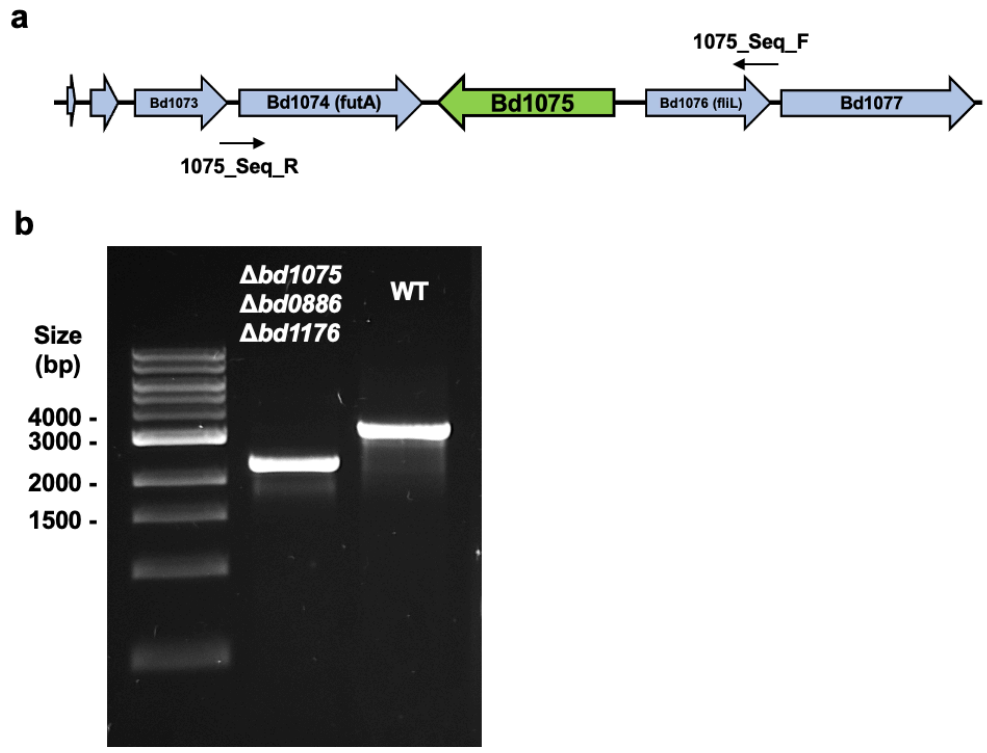

Figure 5.11. Deletion of *bd1075* from the double deletion mutant *B. bacteriovorus* HD100 Δ*bd0886*Δ*bd1176*

a) Amplification across the chromosomal region containing the *bd1075* gene showing the primers 1075_Seq_F and 1075_Seq_R used to confirm the deletion of *bd1075*. **b)** Agarose gel confirming the successful deletion of *bd1075* from the genome of *B. bacteriovorus* HD100 Δ*bd0886*Δ*bd1176*, generating the triple knockout Δ*bd1075*Δ*bd0886*Δ*bd1176*. Bands show PCR products amplified from the genomic DNA of Δ*bd1075*Δ*bd0886*Δ*bd1176* and wild-type (WT) *B. bacteriovorus* HD100. Primers (annotated in **a**) were designed to anneal approximately 200 bp either side of the site of homologous recombination. The triple mutant band (2,334 bp) was 985 bp smaller than the wild-type (3,319 bp), indicating successful deletion of *bd1075*.

Surprisingly, there was no obvious predatory defect for the triple mutant (hereafter referred to as Δ*bd1075*Δ2*ldt*) in comparison to the wild-type, however the strain was examined in the following CPRG bdelloplast damage assay.

5.3.6.3. Bdelloplast damage assay design

The complex methodology of the CPRG assay is illustrated in Figure 5.12. It is important to note that it was necessary to use β-galactosidase as a reporter for bdelloplast damage as a simpler assay such as live/dead staining would not be informative (prey cells stain 'dead' within 30 minutes of predator invasion). *E. coli* S17-1 (the standard prey strain in our laboratory and which has been used throughout this thesis) could also be used in this assay as it contains a functional β-galactosidase gene and can therefore convert CPRG into chlorophenol red, resulting in a colour change from yellow to red.

E. coli S17-1 was incubated with IPTG for 2 h at 37 °C shaking to stimulate the production of β-galactosidase, then washed and adjusted to an OD of 1.0. Four *B. bacteriovorus* HD100 strains were cultured and adjusted to a starting cell count of $5x10^9$ cells using a haemocytometer counting chamber: wild-type, Δ*bd1075*, Δ2*ldt (*Δ*bd0886*Δ*bd1176)*, and Δ*bd1075*Δ2*ldt*. Predators and prey were then mixed and incubated for 2.5 h at 29 °C shaking. This timepoint was chosen as maximal bdelloplast deformation by Δ*bd1075* was previously observed at 2.5 h. Predatory cultures were then either subjected to:

1. No osmotic shock (centrifugal and resuspension alone).
2. Osmotic upshock (resuspension in 750 mM NaCl).
3. Osmotic downshock (resuspension in 750 mM NaCl, followed by 29 °C static incubation for 30 min, followed by a final resuspension in H_2O).

CPRG was then added to each treatment tube, followed by static incubation at 29 °C for 30 min, centrifugation and isolation of the supernatant which would contain any bdelloplast leakage products.

Chlorophenol red concentration were measured by absorbance at 574 nm after incubation at 29 °C for 24 h. Higher absorbance values corresponded with a stronger colour change, representing greater leakage of β-galactosidase from prey bdelloplasts.

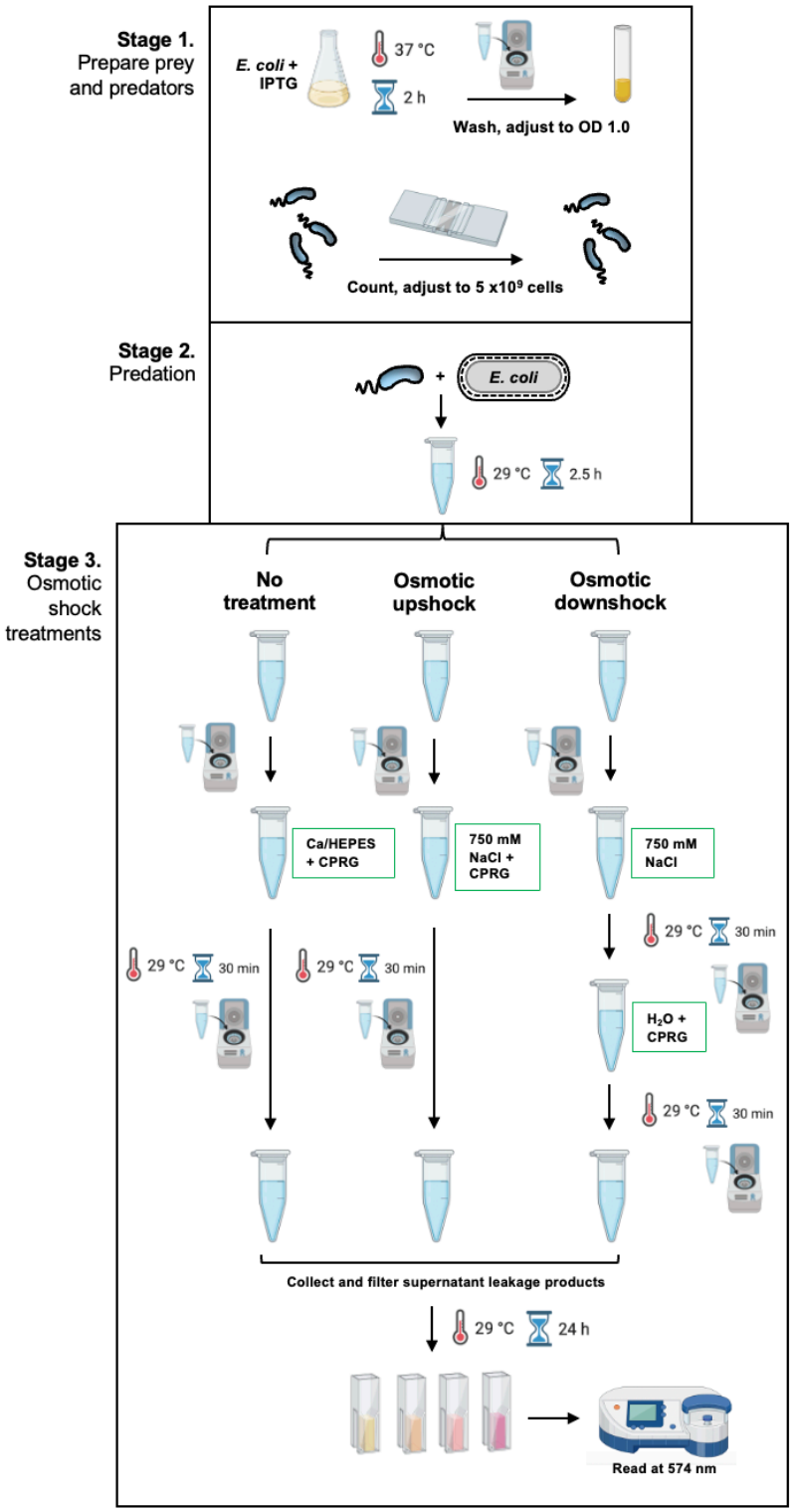

Figure 5.12. Experimental design of bdelloplast damage assay

Detailed experimental diagram illustrating the methodology of the bdelloplast damage assay. The experiment comprises three stages: Stage 1 – preparation of *B. bacteriovorus* predator strains and *E. coli* S17-1 prey, Stage 2 – mixing of predators and prey and predation for 2.5 h, and Stage 3 – osmotic shock treatments and measurement of bdelloplast damage. Diagram created using icons from BioRender.

5.3.6.4. Bdelloplast damage assay results

The control samples of *B. bacteriovorus* strains or *E. coli* alone did not produce any detectable signal (Figure 5.13) which was expected since no predation could occur. When subjected to osmotic upshock, the Δ2*ldt* strain showed significantly more bdelloplast damage than the wild-type ($p<0.0001$), confirming the previous observation by Kuru, Lambert *et al*. (2017)[33] (Figure 5.13). No significant difference was detected between the wild-type and Δ*bd1075* in either upshock or downshock treatments (Figure 5.13). Bdelloplasts invaded by the triple mutant Δ*bd1075*Δ2*ldt* were noticeably less damaged than the Δ2*ldt* strain during osmotic upshock ($p<0.01$) and slightly (but not significantly) more damaged during osmotic downshock (Figure 5.13).

This result was slightly surprisingly as the initial hypothesis was that rod-shaped Δ*bd1075* mutants might cause more bdelloplast damage in both shock treatments. Osmotic upshock is caused by addition of the salt NaCl which causes water to leave the bdelloplast. It is possible that shrinkage of the bdelloplast membrane may be better tolerated by a rod-shaped predator helping to scaffold and maintain the original shape than a curved wild-type predator. This might explain why bdelloplasts containing rod-shaped Δ*bd1075*Δ2*ldt* predators were less damaged than curved Δ2*ldt* predators during upshock. Osmotic downshock is caused by addition of NaCl followed by water, presumably resulting in bdelloplasts that initially shrink then expand as water re-enters the cell. Although rod-shaped predators may have initially stabilised the bdelloplast during NaCl-induced upshock, the sudden expansion of the bdelloplast during re-entry of water may result in over-expansion of an already-strained bdelloplast, causing damage. This may explain the small degree of extra bdelloplast damage in prey containing rod-shaped Δ*bd1075*Δ2*ldt* predators compared to curved Δ2*ldt* predators during osmotic downshock.

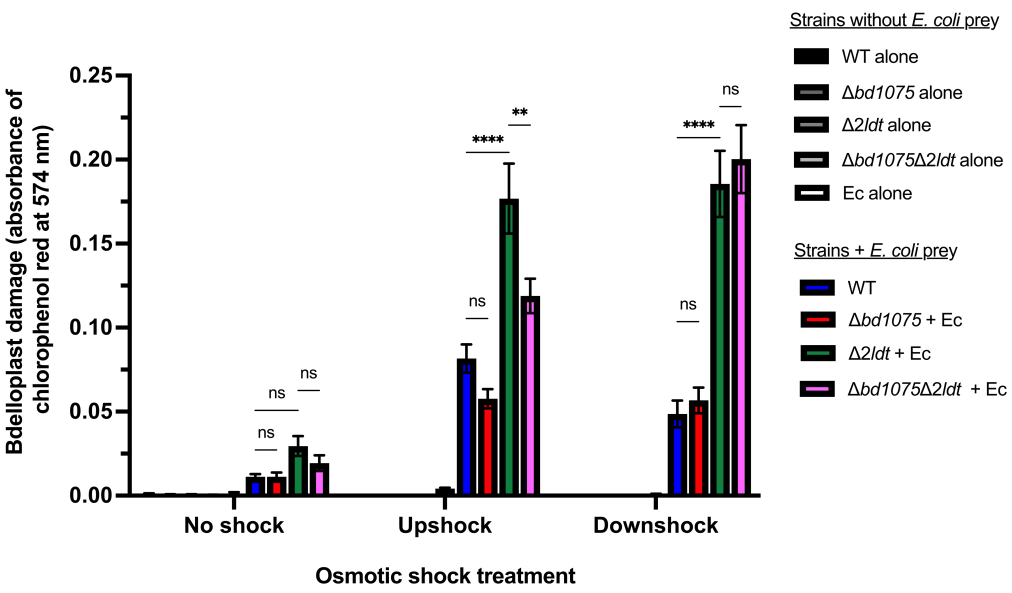

Figure 5.13. Bdelloplast damage assay

Damage to *E. coli* S17-1 prey bdelloplasts caused by the curved *B. bacteriovorus* HD100 strains wild-type (WT) and Δ2*ldt* and the rod-shaped strains Δ*bd1075* and Δ*bd1075*Δ2*ldt*. Damage was determined by the measurement of β-galactosidase leakage from prey bdelloplasts. β-galactosidase leakage was quantified by detecting the concentration of a coloured chlorophenol red product. Following 2.5 h of predation, predatory cultures were either subjected to no shock (centrifugation and resuspension alone), osmotic upshock (750 mM NaCl) or osmotic downshock (750mM NaCl followed by H_2O). Bdelloplast leakage products were incubated with CPRG substrate for 24 h and absorbance at 574 nm was measured. *B. bacteriovorus* strains alone without the addition of prey, or *E. coli* S17-1 alone, were negative controls for damage (values were around 0.00 and therefore bars are barely visible). Error bars represent standard error of the mean and data are from five biological repeats. ns: non-significant, **: $p<0.01$, ****: $p<0.0001$ (2-way ANOVA with Tukey's multiple comparisons test).

5.4. Chapter discussion

In some bacteria, cell shape is intrinsically linked to a particular physiological function and confers an evolutionary fitness advantage[242, 281]. This would likely explain the strong conservation of different bacterial morphologies throughout evolution and selection for the most advantageous shapes. In this chapter, possible fitness advantages conferred by the vibrioid cell shape of *B. bacteriovorus* were investigated. Initial experiments revealed that there was no significant difference between the ability of curved wild-type predators and rod-shaped Δ*bd1075* mutant predators to prey on *E. coli* in either liquid culture (Figure 5.2) or on pre-grown *E. coli* biofilms (Figure 5.3). It is possible that no difference was detected as the overall predation rate would be affected by numerous factors such as prey location, invasion, and replication.

Studying encounters between *B. bacteriovorus* predators and prey at the single-cell level using time-lapse microscopy to observe individual prey invasion events showed that rod-shaped predators invaded prey more slowly than the curved wild-type (Figure 5.6b). Although the difference in entry time appears small (4.0 min *versus* 6.0 min), this represents a 50% increase in Δ*bd1075* entry time. The phenotypic difference was also completely complemented via re-introduction of the *bd1075* gene into Δ*bd1075*. Together, these data suggested that curved predators can more efficiently traverse the outer membrane and wall of prey, most likely curving into the inner periplasmic compartment. During invasion, it is likely that *B. bacteriovorus* must overcome opposing physical forces exerted upon the predator cell by the turgid prey membrane and wall. Curved predators may deflect these opposing forces as a ‘glancing blow’ along the outer curved edge of the cell, facilitating an efficient curved trajectory into prey. In contrast, forces exerted on rod-shaped predators entering prey ‘head-on’ may be concentrated upon the invasive cell pole, slowing prey entry.

Inside prey bdelloplasts, the curvature of the elongating, initially-rod-shaped Δ*bd1075* predator filament increased over time, however, the curved predator filament nevertheless divided to yield rod-shaped progeny cells (Figure 5.8). The adoption of a temporary curvature inside the bdelloplast is interesting and showed that mechanical pressure resulting from growth within a restricted niche can physically deform the shape of *B. bacteriovorus* cells. Even more interestingly, *B. bacteriovorus* rod-shaped predators could also deform the shape of the prey bdelloplast, resulting in a sub-population of bdelloplasts that were considerably stretched and deformed by the elongated predator (Figure 5.9 and Figure 5.10).

Some bacterial proteins such as PopZ[273] and DivIVA[274] can sense the curvature of cell poles. It is possible that Bd1075 (which localises the outer convex face of *B. bacteriovorus*) may sense the temporary curvature adopted inside the bdelloplast and localise to the newly-generated outer face. This localisation may be mediated by the NTF2 domain which is involved in the asymmetrical targeting of Bd1075. Bd1075 could exert localised LD-CPase activity on the PG wall to enzymatically 'fix' and make permanent the curvature of *B. bacteriovorus*. Unfortunately, this potential model is incredibly difficult to test experimentally due to both the lack of genetic induction tools in *Bdellovibrio* and the complex 'chicken-and-egg' nature of *Bdellovibrio* curvature generation. Hypothetically, this model could be tested by inducing Bd1075-mCherry expression within the rod-shaped Δ*bd1075* mutant and visualising protein localisation and curvature formation. Unfortunately, it has not proven possible to engineer a functional genetic induction system within predatory bacteria such as *Bdellovibrio* thus far.

The stretching and deformation of a sub-set of bdelloplasts at 2.5 h into predation by rod-shaped *B. bacteriovorus* predators suggested that curved predators may more optimally 'fit into' spherical prey bdelloplasts. Possible damage to bdelloplasts caused by rod-shaped Δ*bd1075*

predators was tested by utilising an existing bdelloplast damage which uses the coloured substrate CPRG as a marker for damage. The assay previously demonstrated that the Ldt enzymes Bd0886 and Bd1176 strengthen the integrity of bdelloplasts[33]. Nonetheless, the CPRG assay can produce very variable results, often necessitating many biological repeats and normalisation of each experiment. Unfortunately, despite carrying out five biological repeats, the CPRG experiment performed during my PhD produced highly variable data points and it was not possible to conclude that rod-shaped predators caused any significant damage to prey bdelloplasts (Figure 5.13). Due to the limitations of this assay, it would however, be interesting to perform time-lapse microscopy to determine whether any overly-stretched Δ*bd1075* bdelloplasts are weakened and prematurely lyse. Alternatively, it is possible that bdelloplast deformation may have a detrimental effect upon the efficiency of *B. bacteriovorus* growth and division within bdelloplasts, but this has not been examined experimentally.

Collectively, this chapter has shown complex relationships between predator shape and predatory growth processes. During intra-bdelloplast growth, a curved shape is imposed upon the *B. bacteriovorus* cell by the confines of the spherical prey bdelloplast niche. There is also an important enzymatic element, however, to the 'chicken-and-egg' nature of *B. bacteriovorus* curvature generation. This is dependent upon Bd1075 (as shown in Chapter 4) – the localised LD-CPase activity of which may result in permanent fixation of *B. bacteriovorus* curvature.

Chapter 6. Concluding remarks

Bdellovibrio bacteriovorus is a bacterium that has fascinated microbiologists for 60 years. Over this time there have been numerous excellent and insightful studies on *B. bacteriovorus* – from the early biochemical experiments and beautiful electron microscopy of the 1960s-1980s to the genomic revolution of the early 2000s which re-invigorated the field of research, inspiring new studies that have characterised the roles of specific predatory proteins at the molecular level.

The primary aim of my PhD research was to expand our current knowledge of bacterial predation by *B. bacteriovorus*. Despite the impressive volume of previous publications, there is still an enormous amount that is unknown about the predatory cycle which is exciting for *Bdellovibrio* researchers. This is also relevant to my Antimicrobials and Antimicrobial Resistance (AAMR) Wellcome Trust DTP PhD since furthering our knowledge of predatory bacteria may lead to the much-needed development of novel antibacterials. During my PhD I worked on two main projects testing the roles of unstudied PG-modifying enzymes of *B. bacteriovorus*: the first (chronologically in my PhD) was cell shape determination in *B. bacteriovorus*, described in Chapters 4 and 5, and the second was prey cell shape transformation, described in Chapter 3.

6.1. Curvature generation in a bacterial predator

During a previous short project, I identified the protein Bd1075 as the cell curvature-determinant of vibrioid *B. bacteriovorus* HD100 predator cells. I started my PhD by characterising this shape determinant in greater detail, discovering that the protein is broadly conserved across *Bdellovibrio* and that the only rod-shaped *B. bacteriovorus* strain, strain 109J, contained a significant mutation in Bd1075 (a deletion of 57 amino acids). Cross-complementation experiments suggested that the *bd1075* copy in 109J is non-functional, explaining the lack of curvature generation

in strain 109J. Through a collaboration with Prof Waldemar Vollmer's group (Newcastle University), I learned that Bd1075 exerts LD-carboxypeptidase activity upon the PG cell wall, cutting tetrapeptides to tripeptides. A further collaboration with my co-supervisor Prof Andrew Lovering's group (University of Birmingham) produced the protein used in those PG activity assays and resulted in the determination of the crystal structure of Bd1075. This allowed comparison of Bd1075 to other known shape enzymes, highlighting unique differences such as its monomeric structure and important extended C-terminus. I also determined the subcellular address of Bd1075, which surprisingly localised to the outer convex face instead of the concave face (as noted for *C. crescentus* crescentin[250] and *V. cholerae* CrvA[252] and CrvB[253]). Using a combination of site-directed mutagenesis and fluorescence microscopy, I identified the cryptic nuclear transport factor 2-like (NTF2) domain of Bd1075 as responsible for protein targeting to the convex face and required for curvature generation.

It is worth noting that only Bd1075 has been identified as a *B. bacteriovorus* curvature-determinant thus far, however, in other vibrioid and helical bacteria, more than one enzyme is involved in shape generation (2 in *V. cholerae*[252, 253], 3 in *C. jejuni*[264, 265, 266] and at least 8 in *H. pylori*[255, 256, 257, 258, 259]). It is therefore possible that Bd1075 does not function in isolation but may interact with other unknown enzymes to generate *B. bacteriovorus* cell curvature.

Bacterial shapes are not only fascinatingly diverse but also evolutionarily conserved in related bacteria, suggesting that specific shapes confer fitness benefits; these have been identified for other non-predatory bacteria[252, 255, 265, 282]. I discovered that the cell curvature of *B. bacteriovorus* facilitated faster invasion into prey which may protect predators from the potentially dangerous prey cell surface where type VI toxin secretion could damage predator cells. I also observed that rod-shaped mutant predators did not appear to grow optimally inside prey

bdelloplasts - although I could not detect any bdelloplast damage in the laboratory conditions used in my studies.

My collected work on Bd1075 as detailed in Chapter 4 and Chapter 5 is currently in the final stages of peer review at the journal Nature Communications.

6.2. Modifying walls to invade prey

In the second half of my PhD, I started to work on *B. bacteriovorus* lytic transglycosylases. Just before the first COVID-19 lockdown, my MSci project student Mr Samuel Mason and I identified Bd3285 as a *B. bacteriovorus* LT that is involved in prey shape transformation during invasion. All *E. coli* prey invaded by wild-type predators completely round up into spherically-shaped bdelloplasts, however prey invaded by Δ*bd3285* predators formed three different shapes: spheres, straight rods, and rods with a constriction at the mid-cell ('dumbbells'). I continued this work after lockdown, showing that dumbbell bdelloplasts were derived from prey cells that were in the process of dividing at the moment of invasion by *B. bacteriovorus*. I also discovered that Bd3285 is secreted into the prey bdelloplast and can localise to the septum of dividing *E. coli* cells. Pre-labelling the prey bdelloplast wall with the fluorescent D-amino acid dye HADA (by labelling the *E. coli* prey prior to predation) revealed that the septum remains intact in dividing *E. coli* that were invaded by Δ*bd3285* predators and formed dumbbell bdelloplasts. This was an important result, strongly suggesting that Bd3285 specifically cleaves the septal PG of *E. coli* prey and that in the absence of septal cleavage, prey cells do not round up into spheres.

Previous work by Lerner *et al*. (2012)[115] showed that when two DD-endopeptidase DacB enzymes, Bd0816 and Bd3459 were deleted, rod-shaped prey did not transform into spherical bdelloplasts. In **Chapter 3 Section 3.4**, I proposed an updated model for prey invasion, combining existing DacB knowledge with my new Bd3285 data (Figure 3.32). Lerner *et al*. (2012)[115] discovered that rod-shaped bdelloplasts had a significantly higher frequency of double invasions by *B. bacteriovorus* predators which is wasteful of prey resources. It is possible that this is also true for rod-shaped Δ*bd3285* bdelloplasts and that conversion of prey bdelloplast shape confers a fitness advantage to predators. The unique dumbbell-shaped bdelloplasts in the Δ*bd3285* mutant might also

be a sub-optimal niche for *B. bacteriovorus* if the elongating predator cell is restricted to the space of just one compartment and/or cannot access nutrients from the opposite compartment. Further work would be required to test this idea experimentally.

Bd3285 is a homologue of the *E. coli* LT MltA. Two other homologues of MltA are encoded within the genome of *B. bacteriovorus*: Bd0599 and Bd0519. In my PhD, I characterised Bd0599, determining that it is also secreted into the prey bdelloplast and can localise to the *E. coli* septum. Deletion of *bd0599* did not result in a bdelloplast shape phenotype, however, suggesting that Bd0599 does not play a critical role in prey invasion. There was insufficient time to elucidate the function of Bd0519, however I have designed some experiments for a current MSci student in our laboratory, Mr Cameron McLaughlin, who will characterise this protein. Ultimately, the work on *B. bacteriovorus* MltA-like LTs in prey invasion will be submitted for publication.

Taken together, my projects have demonstrated two discrete mechanisms by which *B. bacteriovorus* self-shape and predatory sculping of prey shape is achieved, providing greater insight into the complexity and co-ordination of bacterial predation.

References

1. Perez J, Moraleda-Munoz A, Marcos-Torres FJ, Munoz-Dorado J. Bacterial predation: 75 years and counting! *Environ. Microbiol.* **18**, 766-779 (2016).

2. Bratanis E, Andersson T, Lood R, Bukowska-Faniband E. Biotechnological potential of *Bdellovibrio* and like organisms and their secreted enzymes. *Front. Microbiol.* **11**, 662 (2020).

3. Atterbury RJ, Tyson J. Predatory bacteria as living antibiotics - where are we now? *Microbiology (Reading)* **167**, (2021).

4. Sohngen NL. Heterobacteriolyse en Bacteriophagie. *Kon. Akad. Wet. Amsterdam*, 1-6 (1927).

5. Schatz A, Bugie E, Waksman SA. Streptomycin, a substance exhibiting antibiotic activity against gram-positive and gram-negative bacteria. 1944. *Clin Orthop Relat Res*, 3-6 (2005).

6. Welsch M. Bacteriolytic enzymes from Streptomycetes. A review. *J. Gen. Physiol.* **45(4)Pt 2**, 115-124 (1962).

7. Beebe JM. The morphology and cytology of *Myxococcus xanthus*, N. Sp. *J. Bacteriol.* **42**, 193-223 (1941).

8. Oxford AE, Singh BN. Factors contributing to the bacteriolytic effect of species of myxococci upon viable eubacteria. *Nature* **158**, 745 (1946).

9. Berleman JE, Kirby JR. Deciphering the hunting strategy of a bacterial wolfpack. *FEMS Microbiol. Rev.* **33**, 942-957 (2009).

10. Berleman JE*, et al.* The lethal cargo of *Myxococcus xanthus* outer membrane vesicles. *Front. Microbiol.* **5**, 474 (2014).

11. Velicer GJ, Mendes-Soares H. Bacterial predators. *Curr. Biol.* **19**, R55-56 (2009).

12. Davidov Y, Huchon D, Koval SF, Jurkevitch E. A new alpha-proteobacterial clade of *Bdellovibrio*-like predators: implications for the mitochondrial endosymbiotic theory. *Environ. Microbiol.* **8**, 2179-2188 (2006).

13. Koval SF, Hynes SH, Flannagan RS, Pasternak Z, Davidov Y, Jurkevitch E. *Bdellovibrio exovorus* sp. nov., a novel predator of *Caulobacter crescentus*. *Int J Syst Evol Microbiol* **63**, 146-151 (2013).

14. Guerrero R, Pedros-Alio C, Esteve I, Mas J, Chase D, Margulis L. Predatory prokaryotes: predation and primary consumption evolved in bacteria. *Proc. Natl. Acad. Sci. U. S. A.* **83**, 2138-2142 (1986).

15. Starr MP, Baigent NL. Parasitic interaction of *Bdellovibrio bacteriovorus* with other bacteria. *J. Bacteriol.* **91**, 2006-2017 (1966).

16. Stolp H, Petzold H. Untersuchungen über einen obligat parasitischen Mikroorganismus mit lytischer Aktivität für Pseudomonas -Bakterien. *J. Phytopathol.* **45**, 364-390 (1962).

17. Stolp H, Starr MP. *Bdellovibrio bacteriovorus* gen. et sp. n., a predatory, ectoparasitic, and bacteriolytic microorganism. *Antonie Van Leeuwenhoek* **29**, 217-248 (1963).

18. Waite DW*, et al.* Proposal to reclassify the proteobacterial classes Deltaproteobacteria and Oligoflexia, and the phylum Thermodesulfobacteria into four phyla reflecting major functional capabilities. *Int J Syst Evol Microbiol* **70**, 5972-6016 (2020).

19. Rendulic S*, et al.* A predator unmasked: life cycle of *Bdellovibrio bacteriovorus* from a genomic perspective. *Science* **303**, 689-692 (2004).

20. Hespell RB, Thomashow MF, Rittenberg SC. Changes in cell composition and viability of *Bdellovibrio bacteriovorus* during starvation. *Arch. Microbiol.* **97**, 313-327 (1974).

21. Stolp H. Film: Lysis von bacterien durch den parasiten *Bdellovibrio bacteriovorus*. (ed Medien IWFWu) (1967).

22. Seidler RJ, Starr MP. Structure of the flagellum of *Bdellovibrio bacteriovorus*. *J. Bacteriol.* **95**, 1952-1955 (1968).

23. Thomashow LS, Rittenberg SC. Waveform analysis and structure of flagella and basal complexes from *Bdellovibrio bacteriovorus* 109J. *J. Bacteriol.* **163**, 1038-1046 (1985).

24. Thomashow LS, Rittenberg SC. Isolation and composition of sheathed flagella from *Bdellovibrio bacteriovorus* 109J. *J. Bacteriol.* **163**, 1047-1054 (1985).

25. Nan B. Bacterial gliding motility: rolling out a consensus model. *Curr. Biol.* **27**, R154-R156 (2017).

26. Lambert C, Fenton AK, Hobley L, Sockett RE. Predatory *Bdellovibrio* bacteria use gliding motility to scout for prey on surfaces. *J. Bacteriol.* **193**, 3139-3141 (2011).

27. Wadhams GH, Armitage JP. Making sense of it all: bacterial chemotaxis. *Nat. Rev. Mol. Cell Biol.* **5**, 1024-1037 (2004).

28. Straley SC, Conti SF. Chemotaxis in *Bdellovibrio bacteriovorus*. *J. Bacteriol.* **120**, 549-551 (1974).

29. LaMarre AG, Straley SC, Conti SF. Chemotaxis toward amino acids by *Bdellovibrio bacteriovorus*. *J. Bacteriol.* **131**, 201-207 (1977).

30. Straley SC, Conti SF. Chemotaxis by *Bdellovibrio bacteriovorus* toward prey. *J. Bacteriol.* **132**, 628-640 (1977).

31. Jashnsaz H*, et al.* Hydrodynamic hunters. *Biophys. J.* **112**, 1282-1289 (2017).

32. Shilo M. Morphological and physiological aspects of the interaction of *Bdellovibrio* with host bacteria. *Curr Top Microbiol Immunol* **50**, 174-204 (1969).

33. Kuru E*, et al.* Fluorescent D-amino-acids reveal bi-cellular cell wall modifications important for *Bdellovibrio bacteriovorus* predation. *Nat Microbiol* **2**, 1648-1657 (2017).

34. Matin A, Rittenberg SC. Kinetics of deoxyribonucleic acid destruction and synthesis during growth of *Bdellovibrio bacteriovorus* strain 109D on *Pseudomonas putida* and *Escherichia coli*. *J. Bacteriol.* **111**, 664-673 (1972).

35. Hespell RB, Miozzari GF, Rittenberg SC. Ribonucleic acid destruction and synthesis during intraperiplasmic growth of *Bdellovibrio bacteriovorus*. *J. Bacteriol.* **123**, 481-491 (1975).

36. Ruby EG, McCabe JB, Barke JI. Uptake of intact nucleoside monophosphates by *Bdellovibrio bacteriovorus* 109J. *J. Bacteriol.* **163**, 1087-1094 (1985).

37. Sockett RE. Predatory lifestyle of *Bdellovibrio bacteriovorus*. *Annu. Rev. Microbiol.* **63**, 523-539 (2009).

38. Harding CJ*, et al.* A lysozyme with altered substrate specificity facilitates prey cell exit by the periplasmic predator *Bdellovibrio bacteriovorus*. *Nat Commun* **11**, 4817 (2020).

39. Cotter TW, Thomashow MF. Identification of a *Bdellovibrio bacteriovorus* genetic locus, *hit*, associated with the host-independent phenotype. *J. Bacteriol.* **174**, 6018-6024 (1992).

40. Capeness MJ*, et al.* Activity of *Bdellovibrio* hit locus proteins, Bd0108 and Bd0109, links type IVa pilus extrusion/retraction status to prey-independent growth signalling. *PLoS One* **8**, e79759 (2013).

41. Hobley L*, et al.* Genome analysis of a simultaneously predatory and prey-independent, novel *Bdellovibrio bacteriovorus* from the River Tiber, supports *in silico* predictions of both ancient and recent lateral gene transfer from diverse bacteria. *BMC Genomics* **13**, 670 (2012).

42. Collaborators AR. Global burden of bacterial antimicrobial resistance in 2019: a systematic analysis. *The Lancet*, (2022).

43. Gupta S, Tang C, Tran M, Kadouri DE. Effect of predatory bacteria on human cell lines. *PLoS One* **11**, e0161242 (2016).

44. Monnappa AK, Bari W, Choi SY, Mitchell RJ. Investigating the responses of human epithelial cells to predatory bacteria. *Sci. Rep.* **6**, 33485 (2016).

45. Atterbury RJ*, et al.* Effects of orally administered *Bdellovibrio bacteriovorus* on the well-being and *Salmonella* colonization of young chicks. *Appl Environ Microbiol* **77**, 5794-5803 (2011).

46. Shatzkes K*, et al.* Predatory bacteria attenuate *Klebsiella pneumoniae* burden in rat lungs. *MBio* **7**, (2016).

47. Willis AR*, et al.* Injections of predatory bacteria work alongside host immune cells to treat *Shigella* infection in zebrafish larvae. *Curr. Biol.* **26**, 3343-3351 (2016).

48. Raghunathan D*, et al.* Engulfment, persistence and fate of *Bdellovibrio bacteriovorus* predators inside human phagocytic cells informs their future therapeutic potential. *Sci. Rep.* **9**, 4293 (2019).

49. Silhavy TJ, Kahne D, Walker S. The bacterial cell envelope. *Cold Spring Harb. Perspect. Biol.* **2**, a000414 (2010).

50. Vollmer W, Blanot D, de Pedro MA. Peptidoglycan structure and architecture. *FEMS Microbiol. Rev.* **32**, 149-167 (2008).

51. Sun J, Rutherford ST, Silhavy TJ, Huang KC. Physical properties of the bacterial outer membrane. *Nat. Rev. Microbiol.*, (2021).

52. Lovering AL, Safadi SS, Strynadka NC. Structural perspective of peptidoglycan biosynthesis and assembly. *Annu. Rev. Biochem.* **81**, 451-478 (2012).

53. Barreteau H, Kovac A, Boniface A, Sova M, Gobec S, Blanot D. Cytoplasmic steps of peptidoglycan biosynthesis. *FEMS Microbiol. Rev.* **32**, 168-207 (2008).

54. Bouhss A, Trunkfield AE, Bugg TD, Mengin-Lecreulx D. The biosynthesis of peptidoglycan lipid-linked intermediates. *FEMS Microbiol. Rev.* **32**, 208-233 (2008).

55. Ruiz N. Lipid flippases for bacterial peptidoglycan biosynthesis. *Lipid Insights* **8**, 21-31 (2015).

56. Typas A, Banzhaf M, Gross CA, Vollmer W. From the regulation of peptidoglycan synthesis to bacterial growth and morphology. *Nat. Rev. Microbiol.* **10**, 123-136 (2011).

57. Yousif SY, Broome-Smith JK, Spratt BG. Lysis of *Escherichia coli* by beta-lactam antibiotics: deletion analysis of the role of penicillin-binding proteins 1A and 1B. *J. Gen. Microbiol.* **131**, 2839-2845 (1985).

58. Bertsche U*, et al.* Interaction between two murein (peptidoglycan) synthases, PBP3 and PBP1B, in *Escherichia coli*. *Mol. Microbiol.* **61**, 675-690 (2006).

59. Paradis-Bleau C*, et al.* Lipoprotein cofactors located in the outer membrane activate bacterial cell wall polymerases. *Cell* **143**, 1110-1120 (2010).

60. Typas A*, et al.* Regulation of peptidoglycan synthesis by outer-membrane proteins. *Cell* **143**, 1097-1109 (2010).

61. Magnet S, Dubost L, Marie A, Arthur M, Gutmann L. Identification of the L,D-transpeptidases for peptidoglycan cross-linking in *Escherichia coli*. *J. Bacteriol.* **190**, 4782-4785 (2008).

62. Wietzerbin J, Das BC, Petit JF, Lederer E, Leyh-Bouille M, Ghuysen JM. Occurrence of D-alanyl-(D)-meso-diaminopimelic acid and meso-diaminopimelyl-meso-diaminopimelic acid interpeptide linkages in the peptidoglycan of Mycobacteria. *Biochemistry* **13**, 3471-3476 (1974).

63. Pisabarro AG, de Pedro MA, Vazquez D. Structural modifications in the peptidoglycan of *Escherichia coli* associated with changes in the state of growth of the culture. *J. Bacteriol.* **161**, 238-242 (1985).

64. Glauner B, Holtje JV, Schwarz U. The composition of the murein of *Escherichia coli*. *J. Biol. Chem.* **263**, 10088-10095 (1988).

65. Holtje JV. Growth of the stress-bearing and shape-maintaining murein sacculus of *Escherichia coli*. *Microbiol Mol Biol Rev* **62**, 181-203 (1998).

66. Mainardi JL*, et al.* A novel peptidoglycan cross-linking enzyme for a beta-lactam-resistant transpeptidation pathway. *J. Biol. Chem.* **280**, 38146-38152 (2005).

67. Mainardi JL, Legrand R, Arthur M, Schoot B, van Heijenoort J, Gutmann L. Novel mechanism of beta-lactam resistance due to bypass of DD-transpeptidation in *Enterococcus faecium*. *J. Biol. Chem.* **275**, 16490-16496 (2000).

68. Hugonnet JE*, et al.* Factors essential for L,D-transpeptidase-mediated peptidoglycan cross-linking and beta-lactam resistance in *Escherichia coli*. *elife* **5**, (2016).

69. Magnet S*, et al.* Identification of the L,D-transpeptidases responsible for attachment of the Braun lipoprotein to *Escherichia coli* peptidoglycan. *J. Bacteriol.* **189**, 3927-3931 (2007).

70. More N*, et al.* Peptidoglycan Remodeling Enables *Escherichia coli* To Survive Severe Outer Membrane Assembly Defect. *MBio* **10**, (2019).

71. Geiger T, Pazos M, Lara-Tejero M, Vollmer W, Galan JE. Peptidoglycan editing by a specific LD-transpeptidase controls the muramidase-dependent secretion of typhoid toxin. *Nat Microbiol* **3**, 1243-1254 (2018).

72. Egan AJF, Errington J, Vollmer W. Regulation of peptidoglycan synthesis and remodelling. *Nat. Rev. Microbiol.* **18**, 446-460 (2020).

73. Meeske AJ*, et al.* SEDS proteins are a widespread family of bacterial cell wall polymerases. *Nature* **537**, 634-638 (2016).

74. Rohs PDA*, et al.* A central role for PBP2 in the activation of peptidoglycan polymerization by the bacterial cell elongation machinery. *PLoS Genet.* **14**, e1007726 (2018).

75. Legaree BA, Clarke AJ. Interaction of penicillin-binding protein 2 with soluble lytic transglycosylase B1 in *Pseudomonas aeruginosa*. *J. Bacteriol.* **190**, 6922-6926 (2008).

76. van den Ent F, Johnson CM, Persons L, de Boer P, Lowe J. Bacterial actin MreB assembles in complex with cell shape protein RodZ. *EMBO J.* **29**, 1081-1090 (2010).

77. Morgenstein RM, Bratton BP, Nguyen JP, Ouzounov N, Shaevitz JW, Gitai Z. RodZ links MreB to cell wall synthesis to mediate MreB rotation and robust morphogenesis. *Proc. Natl. Acad. Sci. U. S. A.* **112**, 12510-12515 (2015).

78. van den Ent F, Amos LA, Lowe J. Prokaryotic origin of the actin cytoskeleton. *Nature* **413**, 39-44 (2001).

79. Shi H, Bratton BP, Gitai Z, Huang KC. How to build a bacterial cell: MreB as the foreman of *E. coli* construction. *Cell* **172**, 1294-1305 (2018).

80. Kawai Y, Asai K, Errington J. Partial functional redundancy of MreB isoforms, MreB, Mbl and MreBH, in cell morphogenesis of *Bacillus subtilis*. *Mol. Microbiol.* **73**, 719-731 (2009).

81. Ursell TS*, et al.* Rod-like bacterial shape is maintained by feedback between cell curvature and cytoskeletal localization. *Proc. Natl. Acad. Sci. U. S. A.* **111**, E1025-1034 (2014).

82. Daniel RA, Errington J. Control of cell morphogenesis in bacteria: two distinct ways to make a rod-shaped cell. *Cell* **113**, 767-776 (2003).

83. Jones LJ, Carballido-Lopez R, Errington J. Control of cell shape in bacteria: helical, actin-like filaments in *Bacillus subtilis*. *Cell* **104**, 913-922 (2001).

84. Carballido-Lopez R, Errington J. The bacterial cytoskeleton: in vivo dynamics of the actin-like protein Mbl of *Bacillus subtilis*. *Dev. Cell* **4**, 19-28 (2003).

85. Dominguez-Escobar J, Chastanet A, Crevenna AH, Fromion V, Wedlich-Soldner R, Carballido-Lopez R. Processive movement of MreB-associated cell wall biosynthetic complexes in bacteria. *Science* **333**, 225-228 (2011).

86. van Teeffelen S*, et al.* The bacterial actin MreB rotates, and rotation depends on cell-wall assembly. *Proc. Natl. Acad. Sci. U. S. A.* **108**, 15822-15827 (2011).

87. Garner EC, Bernard R, Wang W, Zhuang X, Rudner DZ, Mitchison T. Coupled, circumferential motions of the cell wall synthesis machinery and MreB filaments in *B. subtilis*. *Science* **333**, 222-225 (2011).

88. Olshausen PV, Defeu Soufo HJ, Wicker K, Heintzmann R, Graumann PL, Rohrbach A. Superresolution imaging of dynamic MreB filaments in *B. subtilis*--a multiple-motor-driven transport? *Biophys. J.* **105**, 1171-1181 (2013).

89. Reimold C, Defeu Soufo HJ, Dempwolff F, Graumann PL. Motion of variable-length MreB filaments at the bacterial cell membrane influences cell morphology. *Mol. Biol. Cell* **24**, 2340-2349 (2013).

90. Errington J. Bacterial morphogenesis and the enigmatic MreB helix. *Nat. Rev. Microbiol.* **13**, 241-248 (2015).

91. Billaudeau C, Yao Z, Cornilleau C, Carballido-Lopez R, Chastanet A. MreB forms subdiffraction nanofilaments during active growth in *Bacillus subtilis*. *MBio* **10**, (2019).

92. Kruse T, Bork-Jensen J, Gerdes K. The morphogenetic MreBCD proteins of *Escherichia coli* form an essential membrane-bound complex. *Mol. Microbiol.* **55**, 78-89 (2005).

93. Divakaruni AV, Baida C, White CL, Gober JW. The cell shape proteins MreB and MreC control cell morphogenesis by positioning cell wall synthetic complexes. *Mol. Microbiol.* **66**, 174-188 (2007).

94. Adams DW, Errington J. Bacterial cell division: assembly, maintenance and disassembly of the Z ring. *Nat. Rev. Microbiol.* **7**, 642-653 (2009).

95. Mukherjee A, Dai K, Lutkenhaus J. *Escherichia coli* cell division protein FtsZ is a guanine nucleotide binding protein. *Proc. Natl. Acad. Sci. U. S. A.* **90**, 1053-1057 (1993).

96. McCausland JW*, et al.* Treadmilling FtsZ polymers drive the directional movement of sPG-synthesis enzymes via a Brownian ratchet mechanism. *Nat Commun* **12**, 609 (2021).

97. Whitley KD*, et al.* FtsZ treadmilling is essential for Z-ring condensation and septal constriction initiation in *Bacillus subtilis* cell division. *Nat Commun* **12**, 2448 (2021).

98. Schoenemann KM, Margolin W. Bacterial division: FtsZ treadmills to build a beautiful wall. *Curr. Biol.* **27**, R301-R303 (2017).

99. Pichoff S, Lutkenhaus J. Unique and overlapping roles for ZipA and FtsA in septal ring assembly in *Escherichia coli*. *EMBO J.* **21**, 685-693 (2002).

100. Hale CA, de Boer PA. Direct binding of FtsZ to ZipA, an essential component of the septal ring structure that mediates cell division in *E. coli*. *Cell* **88**, 175-185 (1997).

101. Gueiros-Filho FJ, Losick R. A widely conserved bacterial cell division protein that promotes assembly of the tubulin-like protein FtsZ. *Genes Dev* **16**, 2544-2556 (2002).

102. Pazos M*, et al.* Z-ring membrane anchors associate with cell wall synthases to initiate bacterial cell division. *Nat Commun* **9**, 5090 (2018).

103. Buddelmeijer N, Beckwith J. A complex of the *Escherichia coli* cell division proteins FtsL, FtsB and FtsQ forms independently of its localization to the septal region. *Mol. Microbiol.* **52**, 1315-1327 (2004).

104. Gerding MA, Liu B, Bendezu FO, Hale CA, Bernhardt TG, de Boer PA. Self-enhanced accumulation of FtsN at Division Sites and Roles for Other Proteins with a SPOR domain (DamX, DedD, and RlpA) in *Escherichia coli* cell constriction. *J. Bacteriol.* **191**, 7383-7401 (2009).

105. Vollmer W, Joris B, Charlier P, Foster S. Bacterial peptidoglycan (murein) hydrolases. *FEMS Microbiol. Rev.* **32**, 259-286 (2008).

106. Heidrich C, Ursinus A, Berger J, Schwarz H, Holtje JV. Effects of multiple deletions of murein hydrolases on viability, septum cleavage, and sensitivity to large toxic molecules in *Escherichia coli*. *J. Bacteriol.* **184**, 6093-6099 (2002).

107. Heidrich C*, et al.* Involvement of N-acetylmuramyl-L-alanine amidases in cell separation and antibiotic-induced autolysis of *Escherichia coli*. *Mol. Microbiol.* **41**, 167-178 (2001).

108. Peters NT, Morlot C, Yang DC, Uehara T, Vernet T, Bernhardt TG. Structure-function analysis of the LytM domain of EnvC, an activator of cell wall remodelling at the *Escherichia coli* division site. *Mol. Microbiol.* **89**, 690-701 (2013).

109. Uehara T, Parzych KR, Dinh T, Bernhardt TG. Daughter cell separation is controlled by cytokinetic ring-activated cell wall hydrolysis. *EMBO J.* **29**, 1412-1422 (2010).

110. Priyadarshini R, Popham DL, Young KD. Daughter cell separation by penicillin-binding proteins and peptidoglycan amidases in *Escherichia coli*. *J. Bacteriol.* **188**, 5345-5355 (2006).

111. Weaver AI, Jimenez-Ruiz V, Tallavajhala SR, Ransegnola BP, Wong KQ, Dorr T. Lytic transglycosylases RlpA and MltC assist in *Vibrio cholerae* daughter cell separation. *Mol. Microbiol.* **112**, 1100-1115 (2019).

112. Jorgenson MA, Chen Y, Yahashiri A, Popham DL, Weiss DS. The bacterial septal ring protein RlpA is a lytic transglycosylase that contributes to rod shape and daughter cell separation in *Pseudomonas aeruginosa*. *Mol. Microbiol.* **93**, 113-128 (2014).

113. Egan AJF. Bacterial outer membrane constriction. *Mol. Microbiol.* **107**, 676-687 (2018).

114. Dik DA, Marous DR, Fisher JF, Mobashery S. Lytic transglycosylases: concinnity in concision of the bacterial cell wall. *Crit Rev Biochem Mol Biol* **52**, 503-542 (2017).

115. Lerner TR*, et al.* Specialized peptidoglycan hydrolases sculpt the intra-bacterial niche of predatory *Bdellovibrio* and increase population fitness. *PLoS Pathog.* **8**, e1002524 (2012).

116. Vermassen A, Leroy S, Talon R, Provot C, Popowska M, Desvaux M. Cell wall hydrolases in bacteria: insight on the diversity of cell wall amidases, glycosidases and peptidases toward peptidoglycan. *Front. Microbiol.* **10**, 331 (2019).

117. Evans KJ, Lambert C, Sockett RE. Predation by *Bdellovibrio bacteriovorus* HD100 requires type IV pili. *J. Bacteriol.* **189**, 4850-4859 (2007).

118. Mahmoud KK, Koval SF. Characterization of type IV pili in the life cycle of the predator bacterium *Bdellovibrio*. *Microbiology* **156**, 1040-1051 (2010).

119. Abram D, Castro e Melo J, Chou D. Penetration of *Bdellovibrio bacteriovorus* into host cells. *J. Bacteriol.* **118**, 663-680 (1974).

120. Varon M, Shilo M. Interaction of *Bdellovibrio bacteriovorus* and host bacteria. I. Kinetic studies of attachment and invasion of *Escherichia coli* B by *Bdellovibrio bacteriovorus*. *J. Bacteriol.* **95**, 744-753 (1968).

121. Lambert C*, et al.* Characterizing the flagellar filament and the role of motility in bacterial prey-penetration by *Bdellovibrio bacteriovorus*. *Mol. Microbiol.* **60**, 274-286 (2006).

122. Burnham JC, Hashimoto T, Conti SF. Electron microscopic observations on the penetration of *Bdellovibrio bacteriovorus* into gram-negative bacterial hosts. *J. Bacteriol.* **96**, 1366-1381 (1968).

123. Lerner TR. Modification of prey peptidoglycan by *Bdellovibrio bacteriovorus*.). University of Nottingham (2012).

124. Rittenberg SC, Shilo M. Early host damage in the infection cycle of *Bdellovibrio bacteriovorus*. *J. Bacteriol.* **102**, 149-160 (1970).

125. Varon M, Drucker I, Shilo M. Early effects of *Bdellovibrio* infection on the syntheses of protein and RNA of host bacteria. *Biochem Biophys Res Commun* **37**, 518-525 (1969).

126. Snellen JE, Starr MP. Ultrastructural aspects of localized membrane damage in *Spirillum serpens* VHL early in its association with *Bdellovibrio bacteriovorus* 109D. *Arch. Microbiol.* **100**, 179-195 (1974).

127. Thomashow MF, Rittenberg SC. Intraperiplasmic growth of *Bdellovibrio bacteriovorus* 109J: solubilization of *Escherichia coli* peptidoglycan. *J. Bacteriol.* **135**, 998-1007 (1978).

128. Li GW, Burkhardt D, Gross C, Weissman JS. Quantifying absolute protein synthesis rates reveals principles underlying allocation of cellular resources. *Cell* **157**, 624-635 (2014).

129. Hantke K, Braun V. Covalent binding of lipid to protein. Diglyceride and amide-linked fatty acid at the N-terminal end of the murein-lipoprotein of the *Escherichia coli* outer membrane. *Eur. J. Biochem.* **34**, 284-296 (1973).

130. Braun V, Bosch V. Repetitive sequences in the murein-lipoprotein of the cell wall of *Escherichia coli*. *Proc. Natl. Acad. Sci. U. S. A.* **69**, 970-974 (1972).

131. Suzuki H, Nishimura Y, Yasuda S, Nishimura A, Yamada M, Hirota Y. Murein-lipoprotein of *Escherichia coli*: a protein involved in the stabilization of bacterial cell envelope. *Mol Gen Genet* **167**, 1-9 (1978).

132. Sanders AN, Pavelka MS. Phenotypic analysis of *Escherichia coli* mutants lacking L,D-transpeptidases. *Microbiology* **159**, 1842-1852 (2013).

133. Cohen EJ, Ferreira JL, Ladinsky MS, Beeby M, Hughes KT. Nanoscale-length control of the flagellar driveshaft requires hitting the tethered outer membrane. *Science* **356**, 197-200 (2017).

134. Asmar AT*, et al.* Communication across the bacterial cell envelope depends on the size of the periplasm. *PLoS Biol.* **15**, e2004303 (2017).

135. Thomashow MF, Rittenberg SC. Intraperiplasmic growth of *Bdellovibrio bacteriovorus* 109J: attachment of long-chain fatty acids to *Escherichia coli* peptidoglycan. *J. Bacteriol.* **135**, 1015-1023 (1978).

136. Ruby EG, Rittenberg SC. Attachment of diaminopimelic acid to bdelloplast peptidoglycan during intraperiplasmic growth of *Bdellovibrio bacteriovorus* 109J. *J. Bacteriol.* **158**, 597-602 (1984).

137. Araki Y, Ruby EG. A soluble enzyme activity that attaches free diaminopimelic acid to bdelloplast peptidoglycan. *Biochemistry* **27**, 2624-2629 (1988).

138. Thomashow MF, Rittenberg SC. Intraperiplasmic growth of *Bdellovibrio bacteriovorus* 109J: N-deacetylation of *Escherichia coli* peptidoglycan amino sugars. *J. Bacteriol.* **135**, 1008-1014 (1978).

139. Lambert C*, et al.* Interrupting peptidoglycan deacetylation during *Bdellovibrio* predator-prey interaction prevents ultimate destruction of prey wall, liberating bacterial-ghosts. *Sci. Rep.* **6**, 26010 (2016).

140. Lambert C*, et al.* Ankyrin-mediated self-protection during cell invasion by the bacterial predator *Bdellovibrio bacteriovorus*. *Nat Commun* **6**, 8884 (2015).

141. Talley BG, McDade RL, Jr., Diedrich DL. Verification of the protein in the outer membrane of *Bdellovibrio bacteriovorus* as the OmpF protein of its *Escherichia coli* prey. *J. Bacteriol.* **169**, 694-698 (1987).

142. Diedrich DL, Duran CP, Conti SF. Acquisition of *Escherichia coli* outer membrane proteins by *Bdellovibrio* sp. strain 109D. *J. Bacteriol.* **159**, 329-334 (1984).

143. Rayner JR, Cover WH, Martinez RJ, Rittenberg SC. *Bdellovibrio bacteriovorus* synthesizes an OmpF-like outer membrane protein during both axenic and intraperiplasmic growth. *J. Bacteriol.* **163**, 595-599 (1985).

144. Beck S, Schwudke D, Strauch E, Appel B, Linscheid M. *Bdellovibrio bacteriovorus* strains produce a novel major outer membrane protein during predacious growth in the periplasm of prey bacteria. *J. Bacteriol.* **186**, 2766-2773 (2004).

145. Barel G, Sirota A, Volpin H, Jurkevitch E. Fate of predator and prey proteins during growth of *Bdellovibrio bacteriovorus* on *Escherichia coli* and *Pseudomonas syringae* prey. *J. Bacteriol.* **187**, 329-335 (2005).

146. Tudor JJ, Karp MA. Translocation of an outer membrane protein into prey cytoplasmic membranes by bdellovibrios. *J. Bacteriol.* **176**, 948-952 (1994).

147. Hespell RB, Odelson DA. Metabolism of RNA-ribose by *Bdellovibrio bacteriovorus* during intraperiplasmic growth on *Escherichia coli*. *J. Bacteriol.* **136**, 936-946 (1978).

148. Rosson RA, Rittenberg SC. Regulated breakdown of *Escherichia coli* deoxyribonucleic acid during intraperiplasmic growth of *Bdellovibrio bacteriovorus* 109J. *J. Bacteriol.* **140**, 620-633 (1979).

149. Fenton AK, Kanna M, Woods RD, Aizawa SI, Sockett RE. Shadowing the actions of a predator: backlit fluorescent microscopy reveals synchronous nonbinary septation of predatory *Bdellovibrio* inside prey and exit through discrete bdelloplast pores. *J. Bacteriol.* **192**, 6329-6335 (2010).

150. Kessel M, Shilo M. Relationship of *Bdellovibrio* elongation and fission to host cell size. *J. Bacteriol.* **128**, 477-480 (1976).

151. Milner DS*, et al.* DivIVA controls progeny morphology and diverse ParA proteins regulate cell division or gliding motility in *Bdellovibrio bacteriovorus*. *Front. Microbiol.* **11**, 542 (2020).

152. Fenton AK, Lambert C, Wagstaff PC, Sockett RE. Manipulating each MreB of *Bdellovibrio bacteriovorus* gives diverse morphological and predatory phenotypes. *J. Bacteriol.* **192**, 1299-1311 (2010).

153. Wurtzel O, Dori-Bachash M, Pietrokovski S, Jurkevitch E, Sorek R. Mutation detection with next-generation resequencing through a mediator genome. *PLoS One* **5**, e15628 (2010).

154. Hanahan D. Studies on transformation of *Escherichia coli* with plasmids. *J. Mol. Biol.* **166**, 557-580 (1983).

155. Simon R, Preifer U, Puhler A. A broad host range mobilisation system for *in vivo* genetic engineering: transposon mutagenesis in gram negative bacteria. *Biotechnology* **9**, 184-191 (1983).

156. Rogers M, Ekaterinaki N, Nimmo E, Sherratt D. Analysis of Tn7 transposition. *Mol Gen Genet* **205**, 550-556 (1986).

157. Studier FW, Moffatt BA. Use of bacteriophage T7 RNA polymerase to direct selective high-level expression of cloned genes. *J. Mol. Biol.* **189**, 113-130 (1986).

158. Banks EJ. Molecular investigation of *Bdellovibrio bacteriovorus* envelope processes associated with bacterial predation.). University of Nottingham (2018).

159. Schafer A, Tauch A, Jager W, Kalinowski J, Thierbach G, Puhler A. Small mobilizable multi-purpose cloning vectors derived from the *Escherichia coli* plasmids pK18 and pK19: selection of defined deletions in the chromosome of *Corynebacterium glutamicum*. *Gene* **145**, 69-73 (1994).

160. Guzman LM, Belin D, Carson MJ, Beckwith J. Tight regulation, modulation, and high-level expression by vectors containing the arabinose PBAD promoter. *J. Bacteriol.* **177**, 4121-4130 (1995).

161. Mukherjee S, Brothers KM, Shanks RMQ, Kadouri DE. Visualizing *Bdellovibrio bacteriovorus* by using the tdTomato fluorescent protein. *Appl Environ Microbiol* **82**, 1653-1661 (2015).

162. Lowry OH, Rosebrough NJ, Farr AL, Randall RJ. Protein measurement with the Folin phenol reagent. *J. Biol. Chem.* **193**, 265-275 (1951).

163. Markwell MA, Haas SM, Bieber LL, Tolbert NE. A modification of the Lowry procedure to simplify protein determination in membrane and lipoprotein samples. *Anal. Biochem.* **87**, 206-210 (1978).

164. Williams LE*, et al.* Variation in genome content and predatory phenotypes between *Bdellovibrio* sp. NC01 isolated from soil and *B. bacteriovorus* type strain HD100. *Microbiology* **165**, 1315-1330 (2019).

165. Remy O, Lamot T, Santin Y, Kaljevic J, de Pierpont C, Laloux G. An optimized workflow to measure bacterial predation in microplates. *STAR Protoc* **3**, 101104 (2022).

166. Lambert C, Smith MCM, Sockett RE. A novel assay to monitor predator-prey interactions for *Bdellovibrio bacteriovorus* 109J reveals a role for methyl-accepting chemotaxis proteins in predation. *Environ. Microbiol.* **5**, 127-132 (2003).

167. Lambert C, Sockett RE. Nucleases in *Bdellovibrio bacteriovorus* contribute towards efficient self-biofilm formation and eradication of preformed prey biofilms. *FEMS Microbiol. Lett.* **340**, 109-116 (2013).

168. Medina AA, Shanks RM, Kadouri DE. Development of a novel system for isolating genes involved in predator-prey interactions using host

independent derivatives of *Bdellovibrio bacteriovorus* 109J. *BMC Microbiol.* **8**, 33 (2008).

169. Ye J, Coulouris G, Zaretskaya I, Cutcutache I, Rozen S, Madden TL. Primer-BLAST: a tool to design target-specific primers for polymerase chain reaction. *BMC Bioinformatics* **13**, 134 (2012).

170. Gibson DG, Young L, Chuang RY, Venter JC, Hutchison CA, 3rd, Smith HO. Enzymatic assembly of DNA molecules up to several hundred kilobases. *Nat. Methods* **6**, 343-345 (2009).

171. Glauner B. Separation and quantification of muropeptides with high-performance liquid chromatography. *Anal. Biochem.* **172**, 451-464 (1988).

172. Kabsch W. XDS. *Acta Crystallogr. D Biol. Crystallogr.* **66**, 125-132 (2010).

173. Winter G. xia2: an expert system for macromolecular crystallography data reduction. *Journal of Applied Crystallography* **43**, 186-190 (2010).

174. Skubak P, Pannu NS. Automatic protein structure solution from weak X-ray data. *Nat Commun* **4**, 2777 (2013).

175. Emsley P, Cowtan K. Coot: model-building tools for molecular graphics. *Acta Crystallogr. D Biol. Crystallogr.* **60**, 2126-2132 (2004).

176. Zwart PH*, et al.* Automated structure solution with the PHENIX suite. *Methods Mol. Biol.* **426**, 419-435 (2008).

177. Schindelin J*, et al.* Fiji: an open-source platform for biological-image analysis. *Nat. Methods* **9**, 676-682 (2012).

178. Ducret A, Quardokus EM, Brun YV. MicrobeJ, a tool for high throughput bacterial cell detection and quantitative analysis. *Nat Microbiol* **1**, 16077 (2016).

179. Chaudhuri RR, Pallen MJ. xBASE, a collection of online databases for bacterial comparative genomics. *Nucleic Acids Res.* **34**, D335-337 (2006).

180. Chaudhuri RR, Loman NJ, Snyder LA, Bailey CM, Stekel DJ, Pallen MJ. xBASE2: a comprehensive resource for comparative bacterial genomics. *Nucleic Acids Res.* **36**, D543-546 (2008).

181. Howe KL*, et al.* Ensembl Genomes 2020-enabling non-vertebrate genomic research. *Nucleic Acids Res.* **48**, D689-D695 (2020).

182. Altschul SF, Gish W, Miller W, Myers EW, Lipman DJ. Basic local alignment search tool. *J. Mol. Biol.* **215**, 403-410 (1990).

183. Almagro Armenteros JJ*, et al.* SignalP 5.0 improves signal peptide predictions using deep neural networks. *Nat. Biotechnol.* **37**, 420-423 (2019).

184. Sonnhammer EL, Eddy SR, Durbin R. Pfam: a comprehensive database of protein domain families based on seed alignments. *Proteins* **28**, 405-420 (1997).

185. Mitchell AL*, et al.* InterPro in 2019: improving coverage, classification and access to protein sequence annotations. *Nucleic Acids Res.* **47**, D351-D360 (2019).

186. Needleman SB, Wunsch CD. A general method applicable to the search for similarities in the amino acid sequence of two proteins. *J. Mol. Biol.* **48**, 443-453 (1970).

187. Sievers F*, et al.* Fast, scalable generation of high-quality protein multiple sequence alignments using Clustal Omega. *Mol. Syst. Biol.* **7**, 539 (2011).

188. Robert X, Gouet P. Deciphering key features in protein structures with the new ENDscript server. *Nucleic Acids Res.* **42**, W320-324 (2014).

189. Thompson JD, Higgins DG, Gibson TJ. CLUSTAL W: improving the sensitivity of progressive multiple sequence alignment through sequence weighting, position-specific gap penalties and weight matrix choice. *Nucleic Acids Res.* **22**, 4673-4680 (1994).

190. Kumar S, Stecher G, Li M, Knyaz C, Tamura K. MEGA X: Molecular Evolutionary Genetics Analysis across Computing Platforms. *Mol Biol Evol* **35**, 1547-1549 (2018).

191. Jones DT, Taylor WR, Thornton JM. The rapid generation of mutation data matrices from protein sequences. *Comput. Appl. Biosci.* **8**, 275-282 (1992).

192. McClure R*, et al.* Computational analysis of bacterial RNA-Seq data. *Nucleic Acids Res.* **41**, e140 (2013).

193. Tjaden B. De novo assembly of bacterial transcriptomes from RNA-seq data. *Genome Biol.* **16**, 1 (2015).

194. Cloud KA, Dillard JP. A lytic transglycosylase of *Neisseria gonorrhoeae* is involved in peptidoglycan-derived cytotoxin production. *Infect Immun* **70**, 2752-2757 (2002).

195. Cookson BT, Tyler AN, Goldman WE. Primary structure of the peptidoglycan-derived tracheal cytotoxin of *Bordetella pertussis*. *Biochemistry* **28**, 1744-1749 (1989).

196. Knilans KJ, Hackett KT, Anderson JE, Weng C, Dillard JP, Duncan JA. *Neisseria gonorrhoeae* lytic transglycosylases LtgA and LtgD reduce host innate immune signaling through TLR2 and NOD2. *ACS Infect Dis* **3**, 624-633 (2017).

197. Thunnissen AM, Rozeboom HJ, Kalk KH, Dijkstra BW. Structure of the 70-kDa soluble lytic transglycosylase complexed with bulgecin A. Implications for the enzymatic mechanism. *Biochemistry* **34**, 12729-12737 (1995).

198. van Asselt EJ, Thunnissen AM, Dijkstra BW. High resolution crystal structures of the *Escherichia coli* lytic transglycosylase Slt70 and its complex with a peptidoglycan fragment. *J. Mol. Biol.* **291**, 877-898 (1999).

199. Templin MF, Edwards DH, Holtje JV. A murein hydrolase is the specific target of bulgecin in *Escherichia coli*. *J. Biol. Chem.* **267**, 20039-20043 (1992).

200. Cho H, Uehara T, Bernhardt TG. Beta-lactam antibiotics induce a lethal malfunctioning of the bacterial cell wall synthesis machinery. *Cell* **159**, 1300-1311 (2014).

201. Romeis T, Holtje JV. Specific interaction of penicillin-binding proteins 3 and 7/8 with soluble lytic transglycosylase in *Escherichia coli*. *J. Biol. Chem.* **269**, 21603-21607 (1994).

202. von Rechenberg M, Ursinus A, Holtje JV. Affinity chromatography as a means to study multienzyme complexes involved in murein synthesis. *Microb. Drug Resist.* **2**, 155-157 (1996).

203. Artola-Recolons C*, et al.* Structure and cell wall cleavage by modular lytic transglycosylase MltC of *Escherichia coli*. *ACS Chem. Biol.* **9**, 2058-2066 (2014).

204. Artola-Recolons C*, et al.* High-resolution crystal structure of MltE, an outer membrane-anchored endolytic peptidoglycan lytic transglycosylase from *Escherichia coli*. *Biochemistry* **50**, 2384-2386 (2011).

205. Artola-Recolons C, Llarrull LI, Lastochkin E, Mobashery S, Hermoso JA. Crystallization and preliminary X-ray diffraction analysis of the lytic transglycosylase MltE from *Escherichia coli*. *Acta Crystallogr. Sect. F Struct. Biol. Cryst. Commun.* **67**, 161-163 (2011).

206. Santin YG, Cascales E. Domestication of a housekeeping transglycosylase for assembly of a Type VI secretion system. *EMBO Rep* **18**, 138-149 (2017).

207. Dominguez-Gil T*, et al.* Activation by allostery in cell-wall remodeling by a modular membrane-bound lytic transglycosylase from *Pseudomonas aeruginosa*. *Structure* **24**, 1729-1741 (2016).

208. van Straaten KE, Dijkstra BW, Vollmer W, Thunnissen AM. Crystal structure of MltA from *Escherichia coli* reveals a unique lytic transglycosylase fold. *J. Mol. Biol.* **352**, 1068-1080 (2005).

209. Lee M*, et al.* Reactions of all *Escherichia coli* lytic transglycosylases with bacterial cell wall. *J. Am. Chem. Soc.* **135**, 3311-3314 (2013).

210. Vollmer W, von Rechenberg M, Holtje JV. Demonstration of molecular interactions between the murein polymerase PBP1B, the lytic transglycosylase MltA, and the scaffolding protein MipA of *Escherichia coli*. *J. Biol. Chem.* **274**, 6726-6734 (1999).

211. Jennings GT*, et al.* GNA33 from *Neisseria meningitidis* serogroup B encodes a membrane-bound lytic transglycosylase (MltA). *Eur. J. Biochem.* **269**, 3722-3731 (2002).

212. Lommatzsch J, Templin MF, Kraft AR, Vollmer W, Holtje JV. Outer membrane localization of murein hydrolases: MltA, a third lipoprotein lytic transglycosylase in *Escherichia coli*. *J. Bacteriol.* **179**, 5465-5470 (1997).

213. Adu-Bobie J*, et al.* GNA33 of *Neisseria meningitidis* is a lipoprotein required for cell separation, membrane architecture, and virulence. *Infect Immun* **72**, 1914-1919 (2004).

214. Cloud KA, Dillard JP. Mutation of a single lytic transglycosylase causes aberrant septation and inhibits cell separation of *Neisseria gonorrhoeae*. *J. Bacteriol.* **186**, 7811-7814 (2004).

215. van Asselt EJ, Dijkstra AJ, Kalk KH, Takacs B, Keck W, Dijkstra BW. Crystal structure of *Escherichia coli* lytic transglycosylase Slt35 reveals a lysozyme-like catalytic domain with an EF-hand. *Structure* **7**, 1167-1180 (1999).

216. Ehlert K, Holtje JV, Templin MF. Cloning and expression of a murein hydrolase lipoprotein from *Escherichia coli*. *Mol. Microbiol.* **16**, 761-768 (1995).

217. Yunck R, Cho H, Bernhardt TG. Identification of MltG as a potential terminase for peptidoglycan polymerization in bacteria. *Mol. Microbiol.* **99**, 700-718 (2016).

218. Sassine J, Pazos M, Breukink E, Vollmer W. Lytic transglycosylase MltG cleaves in nascent peptidoglycan and produces short glycan strands. *Cell Surf* **7**, 100053 (2021).

219. Yahashiri A, Jorgenson MA, Weiss DS. Bacterial SPOR domains are recruited to septal peptidoglycan by binding to glycan strands that lack stem peptides. *Proc. Natl. Acad. Sci. U. S. A.* **112**, 11347-11352 (2015).

220. Alcorlo M*, et al.* Structural basis of denuded glycan recognition by SPOR domains in bacterial cell division. *Nat Commun* **10**, 5567 (2019).

221. Arends SJ, Williams K, Scott RJ, Rolong S, Popham DL, Weiss DS. Discovery and characterization of three new *Escherichia coli* septal ring proteins that contain a SPOR domain: DamX, DedD, and RlpA. *J. Bacteriol.* **192**, 242-255 (2010).

222. Somers H. Charactering *Bdellovibrio bacteriovorus* HD100 peptidoglycan modification genes during distinct cell cycle events.). University of Nottingham (2016).

223. Kovacs-Simon A, Titball RW, Michell SL. Lipoproteins of bacterial pathogens. *Infect Immun* **79**, 548-561 (2011).

224. Lowry RC*, et al.* Evolutionary diversification of the RomR protein of the invasive deltaproteobacterium, *Bdellovibrio bacteriovorus*. *Sci. Rep.* **9**, 5007 (2019).

225. Robinson JT*, et al.* Integrative genomics viewer. *Nat. Biotechnol.* **29**, 24-26 (2011).

226. Powell AJ, Liu ZJ, Nicholas RA, Davies C. Crystal structures of the lytic transglycosylase MltA from *N. gonorrhoeae* and *E .coli:* insights into interdomain movements and substrate binding. *J. Mol. Biol.* **359**, 122-136 (2006).

227. van Straaten KE, Barends TR, Dijkstra BW, Thunnissen AM. Structure of *Escherichia coli* lytic transglycosylase MltA with bound chitohexaose: implications for peptidoglycan binding and cleavage. *J. Biol. Chem.* **282**, 21197-21205 (2007).

228. Kelley LA, Sternberg MJ. Protein structure prediction on the Web: a case study using the Phyre server. *Nat. Protoc.* **4**, 363-371 (2009).

229. Madeira F*, et al.* The EMBL-EBI search and sequence analysis tools APIs in 2019. *Nucleic Acids Res.* **47**, W636-W641 (2019).

230. Coenye T. Do results obtained with RNA-sequencing require independent verification? *Biofilm* **3**, 100043 (2021).

231. Everaert C*, et al.* Benchmarking of RNA-sequencing analysis workflows using whole-transcriptome RT-qPCR expression data. *Sci. Rep.* **7**, 1559 (2017).

232. Amikam D, Galperin MY. PilZ domain is part of the bacterial c-di-GMP binding protein. *Bioinformatics* **22**, 3-6 (2006).

233. Ryjenkov DA, Simm R, Romling U, Gomelsky M. The PilZ domain is a receptor for the second messenger c-di-GMP: the PilZ domain protein YcgR controls motility in enterobacteria. *J. Biol. Chem.* **281**, 30310-30314 (2006).

234. Pratt JT, Tamayo R, Tischler AD, Camilli A. PilZ domain proteins bind cyclic diguanylate and regulate diverse processes in *Vibrio cholerae*. *J. Biol. Chem.* **282**, 12860-12870 (2007).

235. Christen M*, et al.* DgrA is a member of a new family of cyclic diguanosine monophosphate receptors and controls flagellar motor function in *Caulobacter crescentus*. *Proc. Natl. Acad. Sci. U. S. A.* **104**, 4112-4117 (2007).

236. Benach J*, et al.* The structural basis of cyclic diguanylate signal transduction by PilZ domains. *EMBO J.* **26**, 5153-5166 (2007).

237. Costantini LM, Snapp EL. Fluorescent proteins in cellular organelles: serious pitfalls and some solutions. *DNA Cell Biol* **32**, 622-627 (2013).

238. Kuru E*, et al. In situ* probing of newly synthesized peptidoglycan in live bacteria with fluorescent D-amino acids. *Angew. Chem. Int. Ed. Engl.* **51**, 12519-12523 (2012).

239. Steen A*, et al.* Cell wall attachment of a widely distributed peptidoglycan binding domain is hindered by cell wall constituents. *J. Biol. Chem.* **278**, 23874-23881 (2003).

240. Perez AJ*, et al.* Organization of peptidoglycan synthesis in nodes and separate rings at different stages of cell division of Streptococcus pneumoniae. *Mol. Microbiol.* **115**, 1152-1169 (2021).

241. Chang CY*, et al.* The *Bdellovibrio bacteriovorus* twin-arginine transport system has roles in predatory and prey-independent growth. *Microbiology* **157**, 3079-3093 (2011).

242. Young KD. The selective value of bacterial shape. *Microbiol Mol Biol Rev* **70**, 660-703 (2006).

243. Yang DC, Blair KM, Salama NR. Staying in shape: the impact of cell shape on bacterial survival in diverse environments. *Microbiol Mol Biol Rev* **80**, 187-203 (2016).

244. Zapun A, Vernet T, Pinho MG. The different shapes of cocci. *FEMS Microbiol. Rev.* **32**, 345-360 (2008).

245. Pinho MG, Kjos M, Veening JW. How to get (a)round: mechanisms controlling growth and division of coccoid bacteria. *Nat. Rev. Microbiol.* **11**, 601-614 (2013).

246. Siefert't JL, Fox GE. Phylogenetic mapping of bacterial morphology. *Microbiology (Reading)* **144 (Pt 10)**, 2803-2808 (1998).

247. Zou J*, et al.* Non-walled spherical *Acinetobacter baumannii* is an important type of persister upon beta-lactam antibiotic treatment. *Emerg Microbes Infect* **9**, 1149-1159 (2020).

248. Poindexter JS. Biological properties and classification of the *Caulobacter* group. *Bacteriol. Rev.* **28**, 231-295 (1964).

249. Skerker JM, Laub MT. Cell-cycle progression and the generation of asymmetry in *Caulobacter crescentus*. *Nat. Rev. Microbiol.* **2**, 325-337 (2004).

250. Ausmees N, Kuhn JR, Jacobs-Wagner C. The bacterial cytoskeleton: an intermediate filament-like function in cell shape. *Cell* **115**, 705-713 (2003).

251. Cabeen MT*, et al.* Bacterial cell curvature through mechanical control of cell growth. *EMBO J.* **28**, 1208-1219 (2009).

252. Bartlett TM*, et al.* A periplasmic polymer curves *Vibrio cholerae* and promotes pathogenesis. *Cell* **168**, 172-185 e115 (2017).

253. Martin NR, Blackman E, Bratton BP, Chase KJ, Bartlett TM, Gitai Z. CrvA and CrvB form a curvature-inducing module sufficient to induce cell-shape complexity in Gram-negative bacteria. *Nat Microbiol* **6**, 910-920 (2021).

254. Brown PJ*, et al.* Polar growth in the Alphaproteobacterial order Rhizobiales. *Proc. Natl. Acad. Sci. U. S. A.* **109**, 1697-1701 (2012).

255. Sycuro LK*, et al.* Peptidoglycan crosslinking relaxation promotes *Helicobacter pylori's* helical shape and stomach colonization. *Cell* **141**, 822-833 (2010).

256. Sycuro LK*, et al.* Multiple peptidoglycan modification networks modulate *Helicobacter pylori*'s cell shape, motility, and colonization potential. *PLoS Pathog.* **8**, e1002603 (2012).

257. Sycuro LK*, et al.* Flow cytometry-based enrichment for cell shape mutants identifies multiple genes that influence *Helicobacter pylori* morphology. *Mol. Microbiol.* **90**, 869-883 (2013).

258. Yang DC*, et al.* A genome-wide *Helicobacter pylori* morphology screen uncovers a membrane-spanning helical cell shape complex. *J. Bacteriol.* **201**, (2019).

259. Blair KM*, et al.* The *Helicobacter pylori* cell shape promoting protein Csd5 interacts with the cell wall, MurF, and the bacterial cytoskeleton. *Mol. Microbiol.* **110**, 114-127 (2018).

260. Waidner B*, et al.* A novel system of cytoskeletal elements in the human pathogen *Helicobacter pylori*. *PLoS Pathog.* **5**, e1000669 (2009).

261. Specht M, Schatzle S, Graumann PL, Waidner B. *Helicobacter pylori* possesses four coiled-coil-rich proteins that form extended filamentous structures and control cell shape and motility. *J. Bacteriol.* **193**, 4523-4530 (2011).

262. An DR*, et al.* Structural basis of the heterodimer formation between cell shape-determining proteins Csd1 and Csd2 from *Helicobacter pylori*. *PLoS One* **11**, e0164243 (2016).

263. Taylor JA*, et al.* Distinct cytoskeletal proteins define zones of enhanced cell wall synthesis in *Helicobacter pylori*. *elife* **9**, (2020).

264. Frirdich E*, et al.* Peptidoglycan-modifying enzyme Pgp1 is required for helical cell shape and pathogenicity traits in *Campylobacter jejuni*. *PLoS Pathog.* **8**, e1002602 (2012).

265. Frirdich E*, et al.* Peptidoglycan LD-carboxypeptidase Pgp2 influences *Campylobacter jejuni* helical cell shape and pathogenic properties and provides the substrate for the DL-carboxypeptidase Pgp1. *J. Biol. Chem.* **289**, 8007-8018 (2014).

266. Min K*, et al.* Peptidoglycan reshaping by a noncanonical peptidase for helical cell shape in *Campylobacter jejuni*. *Nat Commun* **11**, 458 (2020).

267. Taylor JA, Sichel SR, Salama NR. Bent bacteria: a comparison of cell shape mechanisms in Proteobacteria. *Annu. Rev. Microbiol.* **73**, 457-480 (2019).

268. Fenton AK, Hobley L, Butan C, Subramaniam S, Sockett RE. A coiled-coil-repeat protein 'Ccrp' in *Bdellovibrio bacteriovorus* prevents cellular indentation, but is not essential for vibroid cell morphology. *FEMS Microbiol. Lett.* **313**, 89-95 (2010).

269. Kumar S, Stecher G, Tamura K. MEGA7: molecular evolutionary genetics analysis version 7.0 for bigger datasets. *Mol Biol Evol* **33**, 1870-1874 (2016).

270. Kim HS*, et al.* The cell shape-determining Csd6 protein from *Helicobacter pylori* constitutes a new family of L,D-carboxypeptidase. *J. Biol. Chem.* **290**, 25103-25117 (2015).

271. Zhang Y. I-TASSER server for protein 3D structure prediction. *BMC Bioinformatics* **9**, 40 (2008).

272. Deeg CM, Le TT, Zimmer MM, Suttle CA. From the inside out: an epibiotic *Bdellovibrio* predator with an expanded genomic complement. *J. Bacteriol.*, (2020).

273. Bowman GR*, et al.* A polymeric protein anchors the chromosomal origin/ParB complex at a bacterial cell pole. *Cell* **134**, 945-955 (2008).

274. Lenarcic R*, et al.* Localisation of DivIVA by targeting to negatively curved membranes. *EMBO J.* **28**, 2272-2282 (2009).

275. Biarrotte-Sorin S*, et al.* Crystal structure of a novel beta-lactam-insensitive peptidoglycan transpeptidase. *J. Mol. Biol.* **359**, 533-538 (2006).

276. Aliashkevich A, Cava F. LD-transpeptidases: the great unknown among the peptidoglycan cross-linkers. *FEBS J.*, (2021).

277. Sheng-Huei Lin C*, et al.* Peptidoglycan binding by a pocket on the accessory NTF2-domain of Pgp2 directs helical cell shape of *Campylobacter jejuni*. *J. Biol. Chem.*, 100528 (2021).

278. Corbett AH, Silver PA. The NTF2 gene encodes an essential, highly conserved protein that functions in nuclear transport *in vivo*. *J. Biol. Chem.* **271**, 18477-18484 (1996).

279. Eberhardt RY*, et al.* Filling out the structural map of the NTF2-like superfamily. *BMC Bioinformatics* **14**, 327 (2013).

280. Rittenberg SC. Nonidentity of *Bdellovibrio bacteriovorus* strains 109D and 109J. *J. Bacteriol.* **109**, 432-433 (1972).

281. Young KD. Bacterial morphology: why have different shapes? *Curr. Opin. Microbiol.* **10**, 596-600 (2007).

282. Persat A, Stone HA, Gitai Z. The curved shape of *Caulobacter crescentus* enhances surface colonization in flow. *Nat Commun* **5**, 3824 (2014).

283. Greenberg EP, Canale-Parola E. Motility of flagellated bacteria in viscous environments. *J. Bacteriol.* **132**, 356-358 (1977).

284. Martinez LE*, et al. Helicobacter pylori* strains vary cell shape and flagellum number to maintain robust motility in viscous environments. *Mol. Microbiol.* **99**, 88-110 (2016).

285. Hay NA, Tipper DJ, Gygi D, Hughes C. A novel membrane protein influencing cell shape and multicellular swarming of *Proteus mirabilis*. *J. Bacteriol.* **181**, 2008-2016 (1999).

286. Duggin IG*, et al.* CetZ tubulin-like proteins control archaeal cell shape. *Nature* **519**, 362-365 (2015).

287. Schuech R, Hoehfurtner T, Smith DJ, Humphries S. Motile curved bacteria are Pareto-optimal. *Proc. Natl. Acad. Sci. U. S. A.* **116**, 14440-14447 (2019).

288. Kelly DJ. The physiology and metabolism of *Campylobacter jejuni* and *Helicobacter pylori*. *Symp Ser Soc Appl Microbiol*, 16S-24S (2001).

289. Bonis M, Ecobichon C, Guadagnini S, Prevost MC, Boneca IG. A M23B family metallopeptidase of *Helicobacter pylori r*equired for cell shape, pole formation and virulence. *Mol. Microbiol.* **78**, 809-819 (2010).

290. Prashar A*, et al.* Filamentous morphology of bacteria delays the timing of phagosome morphogenesis in macrophages. *J. Cell Biol.* **203**, 1081-1097 (2013).

291. Horvath DJ, Jr.*, et al.* Morphological plasticity promotes resistance to phagocyte killing of uropathogenic *Escherichia coli*. *Microbes Infect* **13**, 426-437 (2011).

292. Weiser JN. The battle with the host over microbial size. *Curr. Opin. Microbiol.* **16**, 59-62 (2013).

293. Rodriguez JL, Dalia AB, Weiser JN. Increased chain length promotes pneumococcal adherence and colonization. *Infect Immun* **80**, 3454-3459 (2012).

294. Dalia AB, Weiser JN. Minimization of bacterial size allows for complement evasion and is overcome by the agglutinating effect of antibody. *Cell Host Microbe* **10**, 486-496 (2011).

295. Lambert C, Chang CY, Capeness MJ, Sockett RE. The first bite--profiling the predatosome in the bacterial pathogen *Bdellovibrio*. *PLoS One* **5**, e8599 (2010).